Copyright ©

Temporal and geochemical evolution of the Madeira and Selvagen Islands and associated seamounts (eastern North Atlantic): Implications for the size and structure of mantle plumes

Dissertation
zur Erlangung des Doktorgrades
der Mathematisch-Naturwissenschaftlichen Fakultät
der Christian-Albrechts-Universität
zu Kiel

vorgelegt von

Jörg Geldmacher

Kiel 2000

Referent: Prof. Dr. K. Hoernle

Koreferent: Prof. Dr. H.-U. Schmincke

Tag der mündlichen Prüfung: 14.06.2000

Zum Druck genehmigt: Kiel, den 14.06.2000

Der Dekan

gez. H. König

Hiermit erkläre ich an Eides statt, daß die vorliegende Abhandlung, abgesehen von der Beratung durch meine akademischen Lehrer, nach Inhalt und Form meine eigene Arbeit darstellt.

Jörg Geldmacher

Table of contents

Summary

This study reports $^{40}Ar/^{39}Ar$ age determinations, major element, trace element and Sr-Nd-Pb isotope compositions from volcanic rocks of the Madeira and Selvagen Island groups and associated seamounts to the east and northeast. Evidence for the recycling of oceanic crust over short time scales and the attribution of islands and seamounts to separate hotspot systems are presented.

The volcanic evolution of Madeira can be divided into a voluminous tholeiitic to basanitic shield stage (> 4.6-0.7 Ma) and a subsequent low-volume basanitic post-erosional stage (< 0.7-0 Ma). Volcanism during the shield stage originated from a two-armed rift system, composed of the E-W oriented Madeira Rift Arm and the NNW-SSE oriented Desertas Rift Arm. Madeira is interpreted as the present location of a > 70 Ma old hotspot which formed Porto Santo Island, Seine, Ampère, Coral Patch and Ormond Seamounts, and the Serra de Monchique complex in southern Portugal. The large and variable age gaps between the individual volcanoes of the hotspot track and the relatively low magmatic productivity can be best explained by a weak hotspot, which is only intermittently active. Age and spatial relationships result in a calculated absolute African plate motion above the hotspot of about 12 mm/a and a rotation pole located at 43° N/ 24° W.

Although the Sr and Nd isotopic ratios of volcanic rocks from the Madeira archipelago are similar to those of normal mid-ocean ridge basalt (N-MORB), the incompatible element signatures and Pb isotopic compositions show similarities to the HIMU (high time-integrated $^{238}U/^{204}Pb$) mantle component. All samples plot below the Northern Hemisphere Reference Line (NHRL; Δ 7/4 = -1.0 to -7.2) on the $^{206}Pb/^{204}Pb$ versus $^{207}Pb/^{204}Pb$ isotope correlation diagram and form a 400 Ma isochron. These data suggest the presence of recycled Palaeozoic oceanic crust in the Madeira magma source. Variations in major element and isotope geochemistry point to a heterogeneous plume source containing both upper (primarily altered basaltic) and lower (primarily unaltered gabbroic) ocean crust in a discrete blob of upwelling plume material. The more enriched basaltic upper crustal component is preferentially sampled during the shield stage of volcanism, whereas the depleted gabbroic lower crustal component is primarily sampled during the post-erosional stage of volcanism. Therefore, the plume material becomes progressively depleted through melt extraction in the plume pulse as it is sheared northeastward (direction of plate motion) by lithospheric drag. Systematic decrease in $^{143}Nd/^{144}Nd$ and increase in $^{207}Pb/^{204}Pb$ isotopic ratios along the Madeira hotspot track with increasing age and proximity to Iberia is interpreted as increased contamination by continental lithosphere.

The Selvagen Islands are older than the Madeira archipelago. Evolution of the Selvagens can be divided into a basanitic to phonolitic subaerial shield stage (30-24 Ma), followed by an around 12 Ma volcanic hiatus during the Early Miocene, resulting in extensive erosion and sedimentation of marine carbonates on Selvagen Grande, and a rejuvenated or post-erosional stage. The latter started Mid-Miocene with the emplacement of alkali basaltic and basanitic dikes (8-12 Ma) and continued in the Pliocene by the eruption of subaerial alkali basaltic and basanitic pyroclastics and lava flows (3.4 Ma). Trace elements and isotopic ratios of the Selvagen Islands and neighboring seamounts to the east are consistent with a mantle plume origin but differ significantly from the Madeira Islands in their isotope composition. The isotopic ratios are similar to the nearby Canary Islands suggesting a common plume source. Spatial distribution and age propagation of the volcanism in the region, however, can not be explained by a simple narrow hotspot track. Either a continuous plume (300-400 km in diameter) sheared by lithospheric drag and/or asthenospheric wind or interaction of a lower mantle plume with the 660 km discontinuity resulting in formation of individual diapirs could explain the poorly-defined, broad hotspot track. The proposed >800 km long and ca. 450 km wide hotspot track includes the Canary Islands, the Selvagen Islands and associated seamounts, corresponding to an absolute plate velocity of approximately 12 mm/a.

Zusammenfassung

In dieser Arbeit werden $^{40}Ar/^{39}Ar$ Altersdatierungen, Haupt- und Spurenelementzusammensetzungen sowie Sr-, Nd- und Pb-Isotopenverhältnisse von vulkanischen Gesteinen der Madeira und Selvagen Inselgruppen sowie der östlich und nordöstlich gelegenen untermeerischern Vulkane präsentiert. Aufgrund der Ergebnisse können die einzelnen Inseln und untermeerischen Vulkane zwei verschiedenen, pulsierenden Hotspot-System zugeordnet werden. Für Madeira wird ein schnelles Recycling von ozeanischer Kruste in der Magmenquelle angenommen.

Die vulkanische Entwicklung Madeiras kann in ein voluminöses tholeiitisches bis basanitisches Schildstadium (> 4,6 - 0,7 Mill. J.) und ein nachfolgendes kleinräumiges basanitisches Posterosionsstadium (< 0,7 Mill. J.) unterteilt werden. Während des Schildstadiums war der Vulkanismus entlang eines zweiarmigen Riftsystems angeordnet, bestehend aus einem E-W orientierten Madeira Riftarm und einem NNW-SSE orientierten Desertas Riftarm. Die Lage Madeiras zeigt die heutige Position eines mehr als 70 Mill. Jahre alten Hotspots an, der auch für die Entstehung von Porto Santo, der untermeerischen Vulkane Seine, Ampère, Coral Patch und Ormonde sowie des Serra de Monchique Komplex in Südportugal verantwortlich ist. Große und unregelmäßig lange zeitliche Lücken zwischen den einzelnen Vulkanen und die relativ geringe Eruptionssrate lassen sich durch ein nur zeitweilig aktives (pulsierendes) relativ schwaches Hotspot-System erklären. Aufgrund des Alters und der räumliche Anordnung der Vulkankomplexe ergibt sich eine absolute Bewegung der afrikanischen Platte von ca. 12 mm/a in der Region Madeira um einen Rotationspol bei 43° N/ 24° W.

Die Sr- und Nd-Isotopenverhältnisse der vulkanischen Gesteine von Madeira sind weitgehend identisch mit entsprechenden Verhältnissen in Basalten von Mittelozeanischen Rücken (N-MORB). Die Pb-Isotopenverhältnisse und die Spurenelementsignaturen der Gesteine zeigen aber große Ähnlichkeit mit einer HIMU Mantelkomponente (HIMU= „ high time-integrated $^{238}U/^{204}Pb$“). Im $^{206}Pb/^{204}Pb$ gegen $^{207}Pb/^{204}Pb$ Korrelationsdiagram liegen alle untersuchten Proben unterhalb der Northern Hemisphere Reference Linie (NHRL; $\Delta 7/4 = -1,0 - 7,2$) und bilden eine Isochrone, die einem Alter von etwa 400 Mill. Jahre entspricht. Die besondere geochemische Zusammensetzung deutet auf recycelte paläozoische Ozeankruste in der Magmenquelle von Madeira hin. Die Magmen entstehen in einem relativ kleinen, begrenzten Puls aus aufsteigendem Plumematerial, der beim Auftreffen auf die Lithosphere in Richtung der Plattenbewegung abgelenkt wird. Die Variationen der Haupt- und Spurenelementzusammensetzung deuten auf eine heterogene Plumequelle hin, in der sowohl

obere (stärker alterierte basaltische) als auch untere (weniger stark alterierte gabbroische) Ozeankruste vorkommt. Während des Aufstiegs schmilzt zunächst die isotopisch radiogenere obere Ozeankruste bevorzugt auf und bildet daher den Hauptanteil in den frühen Vulkaniten des Schildstadiums. Der diskrete Plumepuls verarmt zunehmend an radiogenen Komponenten aus der ehemaligen oberen Ozeankruste. Durch diesen Prozeß werden die Isotopenverhältnisse der vulkanischen Gesteine Madeiras im Laufe der Zeit immer unradiogener. Während des Posterosionsstadiums entstammen die Magmen daher überwiegend aus der weniger radiogenen ehemaligen unteren Ozeankruste. Die vulkanischen Gesteine der Madeira Hotspotspur zeigen mit zunehmendem Alter der Vulkankomplexe und abnehmender Entfernung zum iberischen Kontinent eine systematische Abnahme in ihren $^{143}Nd/^{144}Nd$ bei gleichzeitiger Zuname ihrer $^{207}Pb/^{204}Pb$ Verhältnisse. Diese Entwicklung wird durch zunehmende Kontamination der jeweiligen Plumepluse durch kontinentale Lithosphere erklärt.

Die Selvagen Inseln sind älter als die Madeira Inselgruppe. Auf ein basanitisch bis phonolitisches Schildstadium (30-24 Mill. Jahre) folgt eine etwa 12 Mill. Jahre andauernder vulkanischer Hiatus, in der die Gesteine des Schildstadiums erodiert wurden und zumindest Selvagem Grande unter den Meeresspiegel absank und von Karbonatsedimenten bedeckt wurde. Mit dem Wiederaufleben des Vulkanismus vor 8-12 Mill. Jahren begann das Posterosionsstadium. In diesem Stadium entstanden alkalibasaltische und basanitische Gänge. Vor 3,4 Mill. Jahren setzte sich das Posterosionsstadium mit der Förderung von subaerischen Pyroclastika und Lavaströmen fort. Die Spurenelementzusammensetzungen und Isotopenverhältnisse der vulkanischen Gesteine von den Selvagen Inseln und den untermeerischen Vulkanen östlich der Inselgruppe weisen ebenfalls auf Mantelplumes als Ursache des Magmatismus hin. Die Isotopenverhältnisse unterscheiden sich jedoch deutlich von denen auf Madeira und zeigen stattdessen eine starke Ähnlichkeit mit den vulkanischen Gesteinen der Kanarischen Inseln, was auf eine gemeinsame Hotspotquelle schließen läßt. Die räumliche und zeitliche Anordnung des Vulkanismus in dieser Region läßt sich nicht mit einer klassischen Hotspotspur erklären. Stattdessen wird ein breiter, kontinuierlicher Plume vorgeschlagen, der von der Lithosphärendrift und der Mantelströmung in Richtung der Plattenbewegung abgelenkt wird. Alternativ ist auch eine Interaktion von aufsteigendem Plumematerial mit der 660 km Phasengrenze denkbar, an der sich der Plume zu einem großräumigen Schirm verbreitert von dem aus sekundäre, kleine Diapiere aufsteigen können. Die resultierende unregelmäßige, 800 km lange und ca. 450 km breite Hotspotspur umfaßt demnach die Kanarischen Inseln, die Selvagen Inseln und die benachbarten untermeerischen Vulkane und deckt sich mit einer regionalen Plattengeschwindigkeit von ungefähr 12 mm/a.

Chapter 1: Introduction

General introduction

Mantle plumes have become an important topic of geodynamic research during the last three decades of the past century. The general idea was first developed to explain the age progression of the narrow chain of islands, seamounts and banks of the Hawaiian Ridge. Wilson (1963) proposed that the Hawaiian Ridge was formed by the Pacific plate overriding a stationary lava source in the asthenosphere - a so-called "hotspot". Expanding this hypothesis, Morgan (1972) postulated that the Hawaiian island chain and other hotspots reflect thermal plumes of mantle material, that convectively upwells from the deep mantle to the base of the moving lithosphere forming linear volcanic chains on the earth's surface. Since most hotspot tracks are linear and relatively small (100-200 km wide), upwelling zones must be relatively narrow (classical plume model). However, geophysical observations (e.g., geoid, topographical and seismic velocity anomalies) and theoretical models also support large-scale zones of mantle upwelling. White and McKenzie (1989) proposed that upwelling plume material can form a large, mushroom-shaped plume head spreading out laterally when a cylindrical plume enters the base of the lithosphere. Such a plume head can reach 1000 to 2000 km in diameter but is believed to develop only during the initial stages of a starting plume (Campbell and Griffiths, 1990). Linear volcanic hotspot tracks forming in the advanced stage of a plume, originate directly over the relatively narrow plume stem. As shown in seismic tomography studies, areas of mantle upwelling could be significantly larger and may not have a cylindrical shape. Seismic tomography and isotope geochemistry in the upper mantle suggest a large region of upwelling extending from the eastern Atlantic Ocean to central Europe (Hoernle et al., 1995).

A broad belt of volcanism including three island groups (Canary, Selvagen and Madeira Islands) and more than 20 large seamounts occur between 23° and 38° N above the postulated region of large-scale mantle upwelling (Fig. 3.1). An unresolved question concerns the origin of this ≈ 1700 km long and 800 km wide volcanic province. Proposed models include volcanism from decompression melting beneath rising lithospheric blocks due to tectonic shortening (Araña and Ortiz, 1991), along an extension of the South Atlas fault (Anguita and Hernan, 1975), or due to a mantle plume (e.g. Morgan, 1972; Holik and Rabinowitz, 1991; Hoernle and Schmincke 1993a; Hoernle and Schmincke, 1993b). Models to explain the distribution of the volcanic islands range from volcanism along a suture zone running along the Atlantic margin of NW Africa (Schmincke, 1982) to multiple hotspots (Morgan, 1972). However, the large-scale upwelling proposed by Hoernle et al. (1995) seems to originate under this region in the East Atlantic and is observed to depths > 500 km strongly

supporting a mantle plume origin. Due to the insufficient resolution of global seismic tomography models, it is unclear whether this large upwelling zone represents a single continuous anomaly ("mega plume") or multiple smaller, isolated plumes, forming individual hotspot tracks along the plate surface (e.g., two or three individual hotspot tracks). Better knowledge of age relationships and geochemical composition of the seamounts and islands in this region will help to distinguish between the different models. Establishing the geochronological evolution of the individual islands is important because of the often long-lasting activities of volcanic islands on slow-moving plates. Only the oldest available ages are used for the reconstruction of hotspot tracks as they should be relatively close to the first plume material arrival at a given site. The geochemical composition of the volcanic rocks gives additional valuable information. Variations of geochemical signatures during the evolution of a volcanic island can reflect changes in depths of melting or mixing of multiple magma sources, allowing conclusions to be made about the size, shape and structure of the mantle plume. In general, plume-related magmas show characteristic trace and isotopic signatures that often point to the endmember composition in the mantle source, e.g. recycled crustal components. Consequently, the geochemical signature can also be used to assign individual islands to different hotspot tracks if they originate from geochemically different mantle plumes.

Mantle plumes play an important role in the geodynamic recycling of material subducted to the mantle. It is widely accepted that the source of mantle plumes could be ancient, subducted oceanic crust (e.g. Chase, 1981; Hofmann and White, 1982). The geochemical evidence for recycling of oceanic crust largely comes from ocean island basalt (OIB). Some of these rocks are characterized by elevated $^{206}Pb/^{204}Pb$ isotope ratios (reflecting high time-integrated $^{238}U/^{204}Pb$ ratios (μ) ="high μ" or called: HIMU). The HIMU component is characterized by the trace element enrichment of highly incompatible elements, in particular Nb and Ta, relative to other incompatible elements (e.g. Weaver, 1991) and the enrichment of U and Th relative to Pb, resulting in radiogenic Pb isotope ratios after a certain amount of time. It is still a matter of debate whether the observed U/Pb fractionation is produced by hydrothermal alteration of the former oceanic crust shortly after creation near the ancient ridge axis (e.g. Hoernle, 1998; Staudigel et al., 1995) or by fluid mobilization during subduction (e.g. Hart and Staudigel, 1989; Kogiso et al., 1997). However, the specific radiogenic lead isotope ratios in HIMU source volcanic rocks are commonly believed to reflect ancient (~2 Ga) recycled oceanic crust in the plume (e.g. Zindler and Hart, 1986; Chauvel et al., 1992). In contrast, recent studies provide evidence that recycling times can be significantly shorter (e.g. Hanan and Graham, 1996; Hauff et al., 2000). Thirlwall (1997)

argues that OIB with intermediate $^{206}Pb/^{204}Pb$ in combination with relatively low $^{207}Pb/^{204}Pb$ represents recycled oceanic crust with ages between 400 and 1400 Ma.

Primitive volcanic rocks from the Madeira Islands show characteristic HIMU trace element compositions but seem to show normal mid-ocean-ridge-basalt (N-MORB) Sr- and Nd, as well as intermediate Pb isotope ratios. Therefore, the rare isotopic ratios of Madeira volcanic rocks reported until now, indicate relatively young trace element fractionation (Halliday et al., 1992; Halliday et al., 1993). A possible process for explaining the unusual geochemical signature of volcanic rocks from Madeira would be the recycling of relatively young oceanic crust in an upwelling mantle plume. Evidence for young recycled crust in the Madeira magma source is of great importance for establishing the idea of recycling over short time scales and contributes to the on-going debate of recycling times in the system earth.

Outline and aims of this study

The temporal and geochemical evolution of the Madeira and Selvagen Islands and associated seamounts was studied in combination with existing data from the Canary Islands. Thc study contributes to the understanding of the geodynamic evolution of the East Atlantic and in particular the relationship of Islands and seamounts to separate hotspot tracks.

The principal aims of this study were to:

1) Establish the geochronological history of the Madeira and Selvagen archipelagoes, which is largely unknown.

2) Compare the data of the Island groups with age data from neighboring seamounts of the East Atlantic volcanic province, dated for the first time in this study.

3) Develop a geodynamic model for the region by assigning the volcanism to one or more possible hotspot tracks and to discuss the implications for plume size and structure and absolute African Plate motion.

4) Characterize the geochemical evolution of the Madeira Islands and revising the observed young HIMU trace element enrichment by using the idea of young recycling times for subducted oceanic crust.

5) Establish the temporal and geochemical evolution of the Selvagen Islands and neighboring seamounts.

6) Evaluate a possible Canary hotspot track by comparing the geochemical and age data with existing data from the Canary Islands.

This study is divided in separate chapters focussing on the different aims outlined above. Following a common chapter about material and methods (Chapter 2), the chapters represent individual papers that have been recently published (Chapter 3: $^{40}Ar/^{39}Ar$ age dating of the Madeira archipelago and hotspot track), submitted (Chapter 4: The geochemical evolution of the Madeira hotspot) or are in preparation for submission (Chapter 5: Age dating and geochemical evolution of the Selvagen archipelago and neighboring seamounts). Final conclusions of the complete work are summarized in Chapter 6.

Chapter 2: Material and Methods

The samples obtained in this study have been collected during four field trips to Madeira and the Selvagen Islands. Samples from the submarine seamounts were dredged during POSEIDON cruise POS 235. Three additional submarine samples were made available from cruise VICTOR HENSEN-97.

After removing weathered surfaces (submarine samples were hand-picked under a binocular microscope), samples were crushed and ground to fine powder in an agate-mill. Glassy samples were crushed to fragments of about 0.5-1.5 mm diameter and then hand-chosen. Rock powders were dried in a furnace at 110°C for 12 hours to drive-off moisture. H_2O and CO_2 were analyzed in an infra-red photometer (Rosemount CSA 5003).

Whole rock major/minor element data were determined at GEOMAR by X-ray fluorescence spectroscopy (XRF) on fused beads using a Phillips X'Unique PW1480 X-ray fluorescence spectrometer, equipped with a Rh-tube and calibrated with international standards. Glass analyses were carried out at GEOMAR on a Cameca SX-50 electron microprobe. Standard operating conditions were 15 kV accelerating voltage and beam current of 10 nA. Concentrations of the oxides were calculated following the Pouchou and Pichoir model. The measurements were calibrated with natural mineral standards for the specific elements.

Trace elements (Cs, Hf, Tl, Y, Rb, Ba, Th, Nb, Ta, U, Pb and all REE) were determined from mixed acid (HF-aqua regia-$HClO_4$) pressure digests by inductively coupled plasma-mass spectrometry (ICP-MS) at the Department of Geology, University of Kiel, using a VG Plasmaquad PQ1. Details of the analytical procedure are described by (Garbe-Schönberg, 1993). The accuracy of the reference material BHVO-1, BE-N and Ja 2, measured with the samples, is better than 10% except for Ta, Pb and Y (up to15%) and Cs and Tl (up to 25%). REE were generally better than 4 %. Comparisons between duplicate digests of the same samples showed a precision better than 3%, except for Tl (< 15%).

Sr, Nd and Pb isotopic ratios were determined on a Finnigan MAT 262 thermal ionization mass spectrometer at GEOMAR and on a Finnigan MAT 261 mass spectrometer at the Department of Geological Sciences at the University of California in Santa Barbara (UCSB). Subaerial samples were leached for 20 minutes with 3N HNO_3, whereas submarine samples and samples which may have been under submarine conditions or exposed to sea spray (including all samples from the Selvagen Islands) were leached with hot 6N HCL for 1 h. A subset of submarine samples were leached for 3.5 h in a mix of hot 6N HCL and 8N HNO_3 for

Sr analyses. The chemical separation techniques are described in Hoernle and Tilton (1991). Replicate analyses of Sr-Nd-Pb isotopes on the same samples were within the analytical uncertainties. All isotope ratios were measured in static mode, except Nd at UCSB which was analyzed in dynamic mode. $^{87}Sr/^{86}Sr$ was fractionation-corrected within-run to $^{86}Sr/^{88}Sr$ of 0.1194 and NBS987 yielded 0.710254±11 (n=7) at GEOMAR. The $^{143}Nd/^{144}Nd$ ratio was normalized within-run to $^{146}Nd/^{144}Nd$= 0.7219 and La Jolla gave 0.511844± 9 (n=9) at GEOMAR. The UCSB data were normalized to the average GEOMAR standard values.

Analyses of Pb standard NBS981 (N=19) at GEOMAR gave $^{206}Pb/^{204}Pb$= 16.893± 4, $^{207}Pb/^{204}Pb$= 15.433± 5 and $^{208}Pb/^{204}Pb$= 36.513± 16. All Pb isotope analyses were fractionation-corrected to the NBS981 values of Todt et al. (1996). Total chemistry blanks in both labs were negligible (≤ 200 pg). Replicate analyses yielded an external reproducibility better than 0.025 % per amu for Pb and < 0.000015 for $^{143}Nd/^{144}Nd$ and $^{87}Sr/^{86}Sr$.

$^{40}Ar/^{39}Ar$ laser total-fusion analyses were conducted at the GEOMAR Geochronology Laboratory using a 25 W Spectra Physics argon ion laser and a MAP 216 Series mass spectrometer fitted with a Baur-Signer ion source and a Johnson electron multiplier. Details of the analytical procedure and measuring parameters are described in Chapter 3.

Chapter 3

$^{40}Ar/^{39}Ar$ age dating of the Madeira archipelago and hotspot track

This chapter consists of an individual paper that is published in Geochemistry, Geophysics, Geosystems, Volume 1, 2000. The large data set presented in the Appendix of the original paper is given in the Appendix of this thesis.

$^{40}Ar/^{39}Ar$ Age Dating of the Madeira Archipelago and Hotspot Track (eastern North Atlantic)

Jörg Geldmacher, Paul van den Bogaard, Kaj Hoernle
and Hans-Ulrich Schmincke

GEOMAR, Wischhofstrasse 1-3, D-24148 Kiel, Germany

Abstract

$^{40}Ar/^{39}Ar$ ages for 35 volcanic rocks and ^{14}C ages for two charcoal samples from the Madeira Archipelago and Ampère Seamount (eastern North Atlantic) are presented. The volcanic evolution of Madeira can be divided into a voluminous Shield Stage (>4.6-0.7 Ma) and a subsequent low-volume Post-erosional stage (<0.7-0 Ma). Volcanism during the Shield Stage originated from a two-armed rift system, composed of the E-W oriented Madeira Rift Arm and the N-S oriented Desertas Rift Arm. Average growth rates for the submarine (5500 km^3/Ma) and subaerial (100-150 km^3/Ma) Shield Stages on Madeira are among the lowest found for ocean island volcanoes. It is proposed that Madeira represents the present location of a > 70 Ma old hotspot which formed Porto Santo Island (11.1-14.3 Ma), Seine, Ampère (31 Ma), Corral Patch and Ormond (65-67 Ma; Feraud et al., 1982, 1986) Seamounts, and the Serra de Monchique (70-72 Ma; McIntyre and Berger, 1982) complex in southern Portugal. Age and spatial relationships result in a calculated absolute African Plate motion above the hotspot of 1.2 cm/a around a rotation pole located at 43°36' N/ 24°33' W.

3.1 Introduction

A long-standing question concerns the origin of the ≈ 1700 km belt of volcanism in the eastern North Atlantic located off the coast of Iberia and western Africa between 23° and 38° N (Figure 3.1)(Schmincke, 1982). The belt consists of three island groups (Canary, Selvagen and Madeira Archipelagoes) and more than 20 large seamounts. Global seismic tomographic studies provide evidence for large-scale upwelling from depths of > 500 km beneath the region (Zhang and Tanimoto, 1992; Hoernle et al., 1995), supporting a mantle plume origin as previously suggested (e.g. Morgan, 1972; Holik and Rabinowitz, 1991; Hoernle et al., 1991; Hoernle and Schmincke, 1993a,b).

The Madeira archipelago (Figure 3.2) is located near the southwestern termination of a broad alignment of scattered seamounts and volcanic ridges extending from the Iberian shelf almost 900 km to the southwest (Figure 3.1). Based on its spatial orientation, it has been

proposed that this belt of volcanoes could represent a hotspot track (Morgan, 1981). Morgan proposes that the trace of this hotspot extends into the Mesozoic, at which time the hotspot was

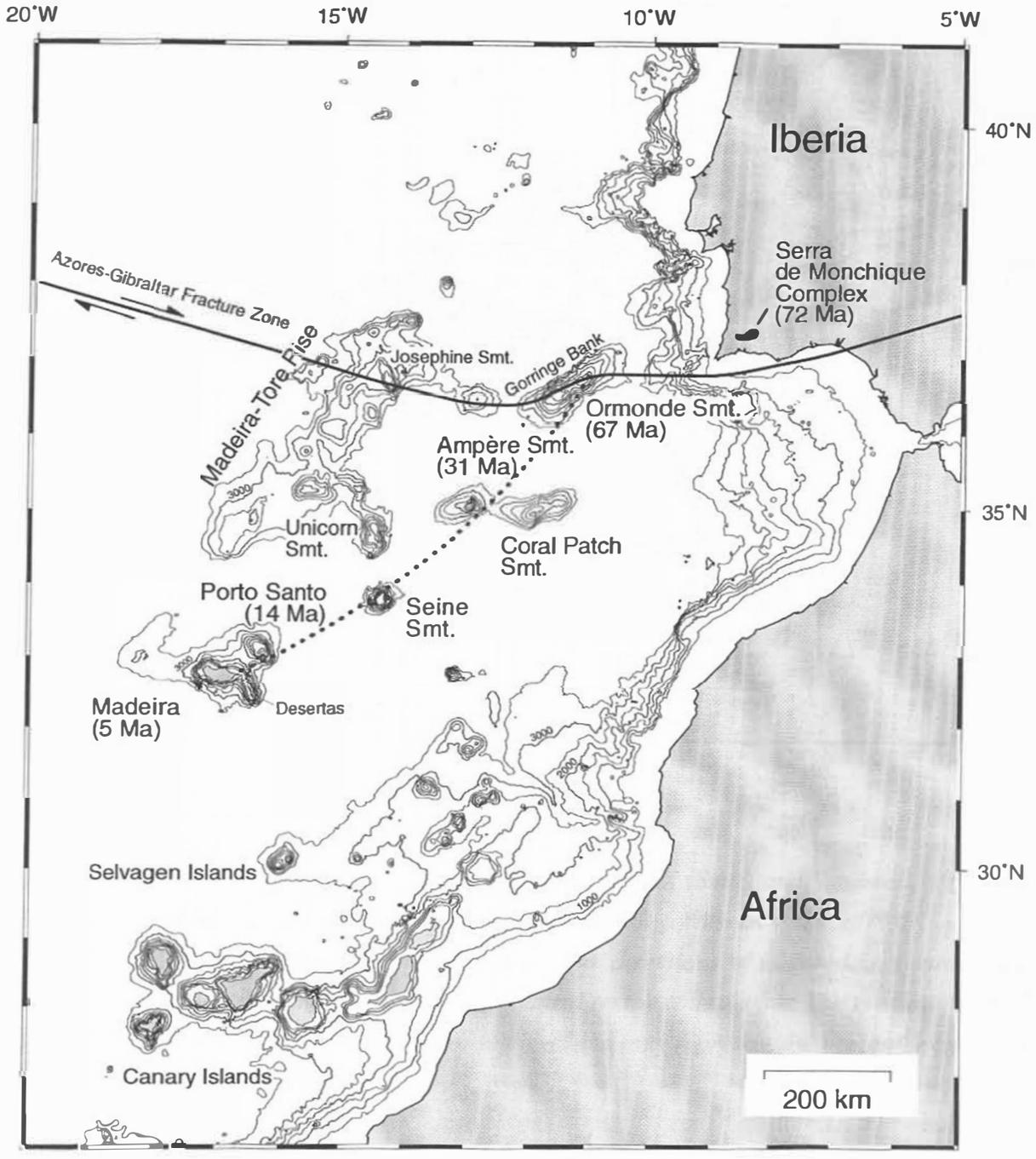

Figure 3.1:

Bathymetric map of seamounts and island groups in the eastern North Atlantic (only depth contours above 3500 meters below sea level are shown). Source: TOPEX (Smith and Sandwell, 1997). Azores-Gibraltar Fracture Zone after Verhbitsky and Zolotarev (1989). Proposed Madeira hotspot track shown as thin dotted line (oldest available radiometric ages for each volcano are given in Ma; see text for details).

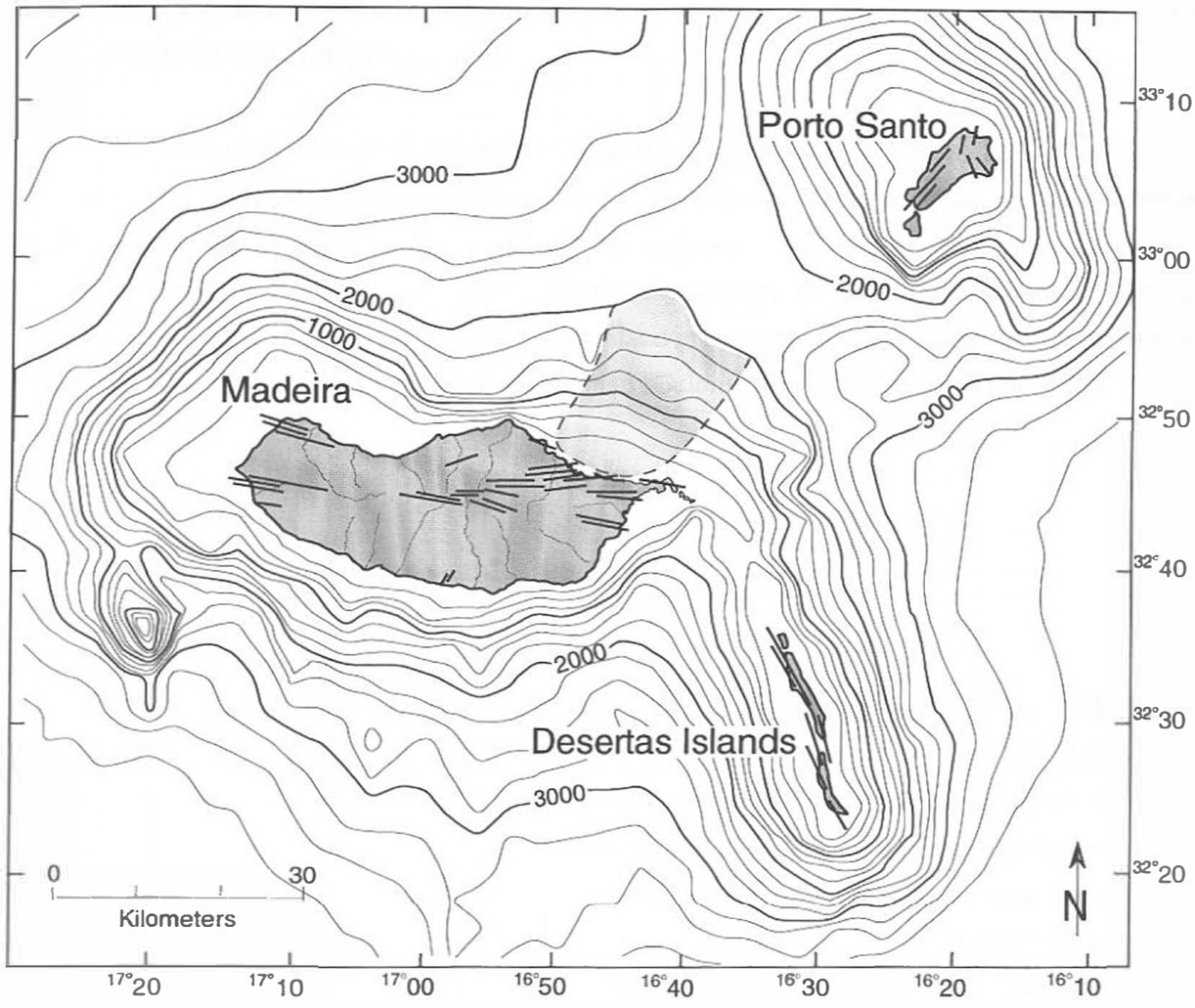

Figure 3.2:

Bathymetric map of the Madeira Archipelago. Source: TOPEX (Smith and Sandwell, 1997). At the eastern tip of Madeira, the E-W oriented Madeira Rift forms an angle of 110° with the narrower NNW-SSE oriented Desertas Rift Arm. The directions of major dike swarms are shown schematically, as is the location of a postulated sector collapse fan. The seamount SW of Madeira extends to a height of 500 m below sea level and may represent the present location of the Madeira hotspot.

located between Labrador and Greenland. The entire belt can be divided into a western complex of seamounts on the NE-SW trending Madeira-Tore Rise and an eastern chain of large, isolated seamounts forming a slightly curved track towards Madeira Island, which we will henceforth refer to as the Madeira volcanic chain. Gravimetric studies of Josephine Seamount, located at the northern end of the Madeira-Tore rise, have shown that this seamount is in isostatic equilibrium with the underlying oceanic crust, leading to the interpretation that the entire rise structure originated on young lithosphere adjacent to the Mid-Atlantic Ridge (Peirce and Barton, 1991). The eastern chain of isolated volcanoes includes Madeira with the small Desertas Islands, Porto

Santo, Seine Seamount, possibly Unicorn Seamount, Ampère Seamount, Coral Patch Seamount and Ormonde Seamount/Gorringe Bank.

We have undertaken volcanological, geochronological and geochemical studies on the Madeira Island group and associated seamounts, in order to elucidate the origin of the volcanism in the eastern North Atlantic and to constrain the magmatic evolution of the Madeira/Desertas volcanic system. In this study we summarize the results of field studies and present $^{40}Ar/^{39}Ar$ age data from volcanic rocks from the Madeira Island group and Ampére Seamount. The results of geochemical studies will be presented elsewhere (Geldmacher and Hoernle, in prep.).

3.2 Geological setting of islands and seamounts in the Madeira chain

Madeira and Desertas Islands

The Madeira archipelago consists of five principal islands: the main island of Madeira (728 km^2), the three narrow Desertas Islands (15 km^2) extending more than 60 km SSE of the eastern end of Madeira, and Porto Santo Island (69 km^2) 45 km to the northeast of Madeira (Figure 3.2). The archipelago is located on 140 Ma old oceanic crust (Pitman and Talwani, 1972) and rises from more than 4000 m water depths up to 1862 m above sea level (summit of Pico Ruivo). Previous geological studies (Carvalho and Brandão, 1991), geological mapping (Zbyszewski et al., 1973; Zbyszewski et al., 1975) and palaeontological work (summarized in Mitchel-Thomé, 1976) have outlined a long and complex volcanic history.

Using lithostratigraphic criteria, the geology of Madeira can be divided into four units: 1) The submarine shield, about which little is known. 2) The late Miocene to Pliocene basal unit consisting primarily of volcanic breccias and pyroclastic deposits with minor lava flows (unit β1 of Zbyszewski et al., 1975). Locally this unit is extensively cut by dikes which approach dike swarms in some regions, in particular in the central part of the island. 3) The middle unit, composed primarily of Pliocene to Pleistocene alkalic basalt lava flows (units β 2-4 of Zbyszewski et al., 1975). This unit covers most of the island (Figure 3.3) and forms lava sequences > 500 m in thickness locally cut by dike swarms. 4) The upper unit consists of scoria cones and intra-canyon flows, which were for the most part erupted after considerable erosion of the island. Published radiometric age data focus on the younger volcanic rocks yielding K/Ar ages ranging from 0.7-3 Ma (Watkins and Abdel-Monem, 1971; Ferreira et al., 1975; Feraud et al., 1981; Mata et al., 1995) except for two from lava flows with ages of 3.9 Ma (Ferreira et al., 1975) and 4.4 Ma (average of duplicate analyses from Mata et al., 1995). Ages and stratigraphic

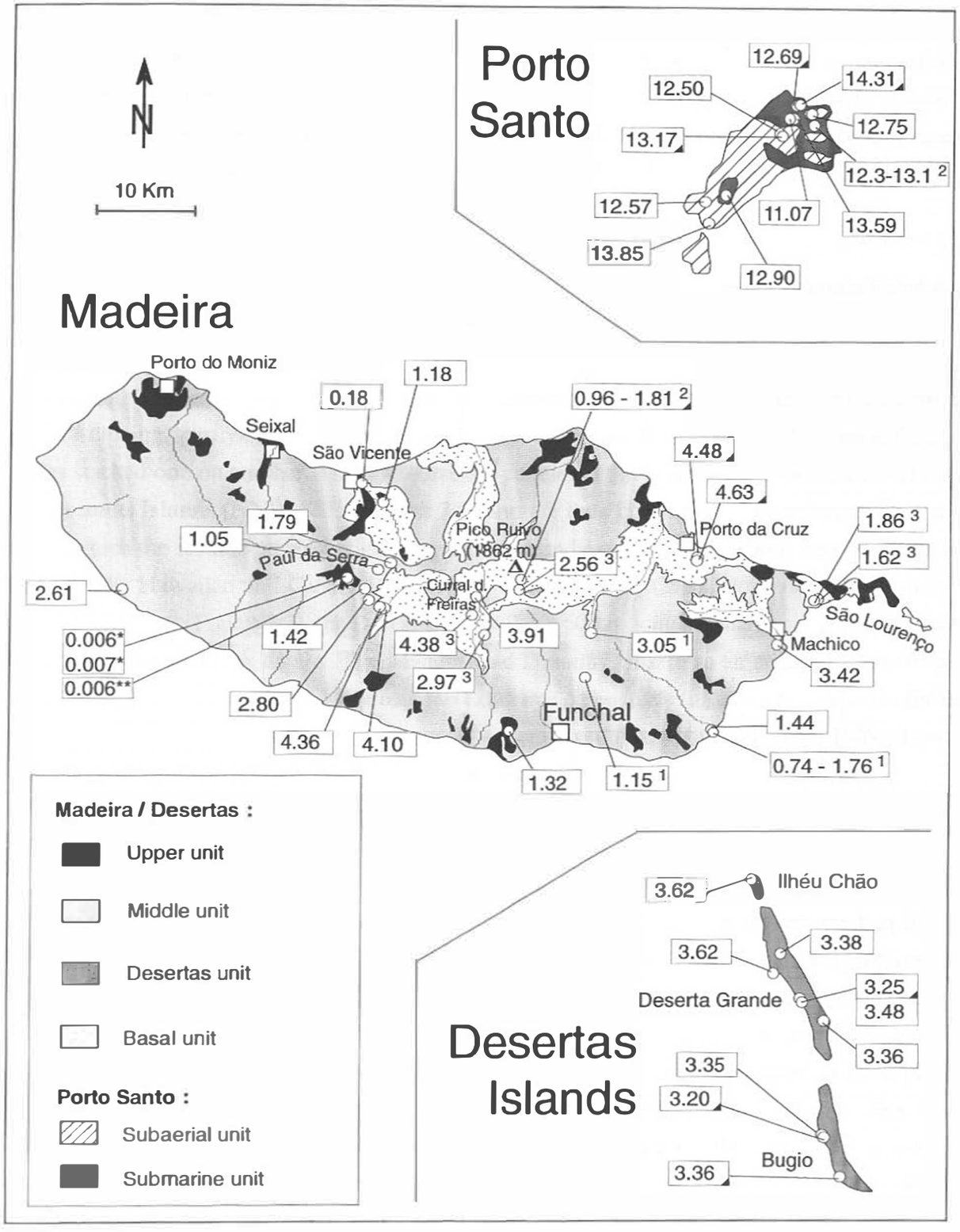

Figure 3.3:

Geological map of Madeira, Desertas and Porto Santo based on Zbyszewski et al. (1975) and Ferreira and Cotelo Neiva (1997). White circles mark sampling sites for age determination. Numbers are in million years. Superscript numbers identify K/Ar dates from [1] Watkins and Abdel-Monem (1971), [2] Feraud et al. (1981), and [3] Mata et al. (1995). From Mata et al. (1995)

*averages of replicate analyses are shown when replicates are within 2 σ error of each other. If not, the age with smallest error is used. Black triangles in the lower right hand corner of boxes around the ages mark samples from dikes. Numbers with * are from ^{14}C radiocarbon ages of charcoal from this study and ** Schmincke (1998). All other numbers without superscript indicators are $^{40}Ar/^{39}Ar$ age determinations from this study.*

relationships of the oldest rocks (> 3 Ma) are poorly understood. No age or compositional data have been published from the Desertas Islands.

Both Madeira and the Desertas are characterized in their central regions by swarms of steeply-dipping, partly-sheeted dikes, normal faults and graben structures and abundant cinder cones stacked one on another. These features are parallel to the long axes of Madeira (E-W) and the Desertas Islands (NNW-SSE) (Figure 3.2) and are thus characteristic of volcanic rift zones, along which the islands preferably grew by intrusion and extrusion as has been described for rift zones in the Hawaiian and Canary Islands (e.g. Walker, 1987; Carracedo, 1994). As seen on a bathymetric map (Figure 3.2), the Desertas rift builds a 60 km long submarine ridge, rising from more than 4000 m water depths. The Madeira and Desertas rifts form an angle of ca. 110° and intersect near the eastern tip of Madeira (São Lourenço peninsula). In summary, we consider the Madeira and Desertas ridges to form a single volcanic complex, consisting of an E-W oriented Madeira Rift arm and a NNW-SSE oriented Desertas Rift arm.

Porto Santo

Porto Santo is located 45 km to the northeast of Madeira; the two islands are separated by water depths of ca. 2000 m. Porto Santo is lower in elevation (with its highest peak at 517m) and more uniform in relief compared to Madeira. A large basaltic to trachytic, mainly submarine, clastic cone makes up the core of the NE part of the island (seamount stage) (Schmincke and Staudigel, 1976; Schmidt et al., in prep). Intercalated with the volcanic rocks are shallow water carbonates. The cone is dissected by voluminous trachytic and basaltic intrusions. A thick pile of submarine to subaerial alkali basaltic to hawaiitic lava flows and associated pillows forms the western part of the island. All units are cut by minor trachytic and basaltic intrusions and dikes, which form most hill tops and ridge crests on the island. Dikes show a preferred NE-SW orientation in the western part of the island and a more radial arrangement in the east (Ferreira and Cotelo Neiva, 1997). Published K/Ar ages of Porto Santo range from 12.3 to 13.1 Ma (Feraud et al., 1981).

Seine, Unicorn, Ampère and Coral Patch Seamounts

Seine Seamount is located ≈ 200 km NE of Porto Santo, rising from more than 4000 m to less than 200 m water depths. This round seamount has steep sides and a flat top characteristic of a guyot. Unicorn Seamount lies ≈100 km due north of Seine Seamount. Ampère and Coral Patch Seamounts are located at ≈ 190 km NE of Seine Seamount. Bathymetric data shows that the shape of Ampère Seamount is also similar to a guyot with a summit that extends to 59 m below sea level (Litvin et al., 1982; Marova and Yevsyukov, 1987). Alkaline and nepheline basaltoids have been described from two short drill holes on the top of the seamount (Matveyenkov et al., 1994). The neighboring Coral Patch Seamount forms an elongated E-W orientated structure rising up to 900 m below sea level.

Ormonde Seamount

The 250 km long Gorringe Bank, which lies along the Azores-Gibraltar fracture zone (the Eurasia-African Plate boundary), is dominated by two summits, the Gettysburg (west) and Ormonde (east) Seamounts which almost reach sea level. Except for the Ormonde summit, the rest of Gorringe Bank consists primarily of altered tholeiitic basalt and serpentinized peridotite (Auzende et al., 1978; Cyagor II Group, 1984; Matveyenkov et al., 1994) and is considered to be a fragment of oceanic lithosphere of early Cretaceous age (Féraud et al., 1986) uplifted and slightly tilted along the Azores-Gibraltar fracture zone (Auzende et al., 1978). In contrast, the younger volcanic rocks on top of Ormonde Seamount comprise a wide range of alkaline rocks, including alkali basalts, nephelinites and phonolites (Cornen, 1982). $^{40}Ar/^{39}Ar$ age dating of Ormonde alkaline volcanic rocks yielded ages between 65 and 67 Ma (Féraud et al., 1982; Féraud et al., 1986).

3.3 Sample description and analytical procedures

Samples from the Madeira archipelago (locations shown in Figure 3.3) were collected from all stratigraphic units (brief description and sampling sites are given in the Appendix). From Madeira Island, five samples from the basal unit, eight samples from the middle unit and two samples from the upper unit were dated. At the center of Madeira, a continuous section was sampled extending from the basal unit through the middle and upper units on the eastern slope of Paul da Serra plateau (Figure 3.4, 3.5). Desertas' samples comprise rocks from the upper and lower parts of the successions of all three islands. On Porto Santo, samples were taken from the NE and SW parts of the island and come from all stratigraphic units.

Rock samples from Madeira and Desertas islands choosen for age-dating range from tholeiites to alkali basalt to basanite and hawaiite. Olivine is the dominant phenocryst phase. Ti-augite and/or plagioclase also occur as phenocrysts. The groundmass consists of plagioclase, Ti-

augite, olivine, and Fe/Ti-oxides. Two glass samples from tholeiitic dike rims from the basal unit on Madeira were also dated. Six samples of plagioclase crystals were separated from thin trachytic pumice deposits and from one small rhyolitic intrusion. In contrast to Madeira and the Desertas, differentiated rocks are more common on Porto Santo. Plagioclase crystals from Porto Santo were separated from two benmoreitic dikes and two trachytic intrusions. Whole rock samples range from basanites to trachytes. Ampère Seamount sample DS 797-1 is a rounded beach cobble of hawaiitic composition and was recovered during F.S. Poseidon cruise 235. Descriptions and locations of land and dredge samples are compiled in the Appendix.

Following removal of altered surfaces, pieces of selected rock samples were crushed in a jaw crusher to < 1 mm and < 0.5 mm size and sieved. Matrix chips, fresh glass or plagioclase phenocrysts were hand-picked under a binocular microscope and cleaned with distilled H_2O in an ultrasonic disintegrator. Plagioclase crystals (250-1000 µm) were treated in 5% HF for 5 min. Plagioclase crystals and rock matrix chip samples were placed in drill holes in 99.95% pure aluminum disks. Sample disks with a 3-dimensional array of 27.92 Ma TCR (batch #85G003) sanidine monitor (Duffield and Dalrymple, 1990), were secured together, sealed in an aluminum can and irradiated with 1 mm Cd shielding at the Geesthacht Research Center (Germany). J-values and associated errors were interpolated for each sample position using a 3-dimensional least-squares cosine plane fit. $^{40}Ar/^{39}Ar$ laser total fusion analyses were conducted at the Geomar Geochronology Laboratory using a 25 W Spectra Physics argon ion laser and a MAP 216 series mass spectrometer fitted with a Baur-Signer ion source and a Johnson electron multiplier. Between 5-13 single grains (rock/glass fragments or plagioclase crystals) of each samples were completely fused (see Table 3.1 for number of single particles analyzed). Raw mass spectrometer peaks were corrected for mass discrimination, background values (determined between every 4 or 5 analyses), and interfering neutron reactions on Ca and K using optical grade CaF_2 and K_2SO_4 salts that had been irradiated together with the samples. Age uncertainties were calculated by partial differentiation of the age equation (Dalrymple and Duffield, 1988) and include uncertainties in the determination of the flux monitor, J, the blank determination, the regression of the intensities of the individual isotopes, and the mass discrimination correction (1.0083 per AMU). Ages and error estimates were determined by calculating the mean apparent age of each population (single fusion ages weighted by the inverse of their variance following the method described by Young, 1962), assuming an initial 'atmospheric' $^{40}Ar/^{39}Ar$ ratio of 295.5. Isochrons have been calculated as inverse isochrons using York's least squares fit that accommodates errors in both ratios and correlation of errors (York, 1969). Mean squared weighted deviates (MSWD) were determined for the mean apparent ages and isochron ages in order to test the scatter of the single fusion data (Wendt and Carl, 1991). If the scatter was greater than predicted from the analytical uncertainties (MSWD > 1), the analytical error has been expanded by multiplying by the square root of the MSWD (York, 1969). Errors are quoted at the 2σ level. Mean apparent ages, isochron ages and mean square weighted deviates (MSWD)

are reported in Table 3.1. Due to the reasonable good control of the initial $^{40}Ar/^{36}Ar$ ratios in isotope correlation diagrams (see Appendix III 1-3) inherited or excess ^{40}Ar can be ruled out for samples within 2σ error from the accepted initial value of 295.5 or slightly lower. If the isotope correlation give atmospheric initial Ar isotope ratios (within error), a relatively inaccurate determination of the initial ratio for the isochron age would rather tend to adulterate than to improve the absolute age. Therefore, except for sample K 48, the mean apparent age is accepted instead of the isochron age to represent the age of crystallization. Because sample K 48 has an elevated initial $^{40}Ar/^{36}Ar$ ratio (outside of 2σ error from the accepted value), the isochron age is accepted for this sample instead of the apparent age.

Table 3.1: Radiometric ages

Sample	N	Mean apparent age (Ma)	MSWD	Isochron age (Ma)	MSWD (isochron)	Initial $^{40}Ar/^{36}Ar$
Madeira						
MA 85 (wr)	10	**0.18 ± 0.08**	1.96	0.34 ± 0.34	1.77	286 ± 16
MA 19 (plag)	8	**1.05 ± 0.16**	0.4	1.08 ± 0.22	0.44	288 ± 38
MA 82c (plag)	9	**1.18 ± 0.10**	0.28	1.21 ± 0.28	0.31	293 ± 19
MA 146 (plag)	10	**1.32 ± 0.30**	0.6	1.22 ± 0.82	0.66	300 ± 34
MA 37 (wr)	10	**1.42 ± 0.08**	3.01	1.13 ± 0.56	2.92	309 ± 28
MA 107 (plag)	12	**1.44 ± 0.06**	0.57	1.45 ± 0.12	0.67	295 ± 4
MA 75 (wr)	6	**1.79 ± 0.36**	2.65	1.26 ± 1.60	3.05	297 ± 7
MA 152 (wr)	6	**2.61 ± 0.10**	1.87	2.36 ± 0.38	1.74	301 ± 9
MA 44 (plag)	11	**2.80 ± 0.06**	0.40	2.83 ± 0.08	0.37	295 ± 2
MA 170 (wr)	6	**3.42 ± 0.10**	0.54	3.34 ± 1.20	0.67	298 ± 71
MA 227 (wr)	7	**3.91 ± 0.08**	0.80	3.96 ± 0.24	0.89	294 ± 4
MA 208 (wr)	6	**4.10 ± 0.06**	0.35	3.93 ± 0.52	0.36	300 ± 20
MA 203 (plag)	7	**4.36 ± 0.40**	1.51	4.20 ± 0.62	1.45	292 ± 16
13-7-96-1 (glass)	7	**4.48 ± 0.18**	1.19	4.47 ± 0.48	1.41	295 ± 6
13-7-96-3 (glass)	6	**4.63 ± 0.10**	1.09	4.56 ± 0.32	1.38	295 ± 4
Desertas Islands						
Ilhéu Chão						
K 22 (wr)	10	**3.62 ± 0.24**	0.55	3.43 ± 1.50	0.62	298 ± 50
Deserta Grande						
DGR 9 (wr)	6	**3.25 ± 0.08**	1.46	3.34 ± 0.20	1.80	289 ± 10
6302B (amph)	7	**3.36 ± 0.12**	3.27	3.42 ± 0.52	3.83	279 ± 82
DGR 47 (wr)	6	**3.38 ± 0.12**	0.89	3.14 ± 1.30	1.08	301 ± 40
DGR 2 (wr)	4	**3.48 ± 0.18**	1.41	3.83 ± 0.36	0.60	288 ± 6
K 31 (wr)	5	**3.62 ± 0.14**	1.72	3.14 ± 1.84	2.13	313 ± 74
Ilhéu do Bugio						
K 15 (wr)	5	**3.20 ± 0.94**	3.26	3.35 ± 0.68	3.95	290 ± 19
K 5 (plag)	9	**3.36 ± 0.2**	1.08	3.19 ± 0.48	1.17	291 ± 31

K 11 (wr)	7	**3.35 ± 0.06**	0.89	3.47 ± 0.44	0.86	286 ± 24
Porto Santo K 43 (wr)	8	**11.07 ± 0.10**	1.27	10.98 ± 0.46	1.52	298 ± 20
K 38 (plag)	11	**12.50 ± 0.30**	1.14	12.35 ± 0.54	1.28	296 ± 4
K 67a (wr)	8	**12.57 ± 0.12**	0.81	12.51 ± 0.26	0.84	296 ± 9
K 48 (wr)	6	15.40 ± 0.90	22.1	**12.69 ± 0.82**	2.05	309 ± 4
K 47 (plag)	11	**12.75 ± 0.26**	0.70	12.67 ± 0.46	0.80	294 ± 19
K 68 (wr)	7	**12.90 ± 0.08**	0.80	12.05 ± 1.10	0.28	359 ± 82
K 42 (plag)	11	**13.17 ± 0.58**	1.55	13.39 ± 1.06	1.74	291 ± 9
K 46 (plag)	10	**13.59 ± 0.58**	1.37	13.56 ± 1.08	1.49	292 ± 12
K 55 (wr)	7	**13.85 ± 0.34**	2.90	12.90 ± 4.10	3.37	302 ± 30
K 49 (plag)	11	**14.31 ± 0.22**	1.0	14.45 ± 0.32	0.88	291 ± 4
Ampére Seamount DS 797-1 (wr)	13	31.20 ± 0.20	1.33	32.70 ± 0.92	0.69	285 ± 6

Radiometric ages calculated from $^{40}Ar/^{39}Ar$ isotope composition of whole rocks (wr), plagioclase (plag) and amphibole phenocrysts (amph). N = Number of single crystals / whole rock particles fused. Errors are quoted at the 2 σ-level. Accepted ages in bold letters. MSWD = Mean square weighted deviates.

Two samples of charcoal, at the base of a pyroclastic fallout deposit on top of Paul da Serra plateau on Madeira, were selected for radiocarbon dating (Table 3.2). Samples were leached in 1 % HCL, 1% NaOH and again with 1% HCL at 60° C. The graphitisized samples were analyzed for ^{14}C ratios with an accelerator mass spectrometer (AMS) at the Leibniz Laboratory at Christian Albrechts University in Kiel. The measured ^{14}C ratios are corrected for mass fractionation and converted into calibrated age after Stuiver and Reimer (1993).

Table 3.2: Radiocarbon ages of charcoal

Sample	Conventional age (a)	Corrected FMC	$\delta^{13}C$ (‰)	Calibrated age (a)*
KIA 685	5670 ± 60 BP	0.4936 ± 0.0038	-20.49 ± 0.26	6407-6496 BP
KIA 686	6270 ± 60 BP	0.4584 ± 0.0033	-19.50 ± 0.20	7159-7216 BP

*Translation into Calibrated age according to Stuiver and Reimer (1993). * Ages referred to before present (1950). Errors at 1 σ-level.*

3.4 Results

Madeira

The oldest dated rocks on Madeira occur in the vicinity of Porto da Cruz (NE Madeira, Figure 3). Fresh glass rims of tholeiitic dikes, cross-cutting volcanic breccia and pyroclastic rocks, gave $^{40}Ar/^{39}Ar$ ages of 4.48± 0.18 and 4.63± 0.10 Ma (Sample 13-7-96-1 and 13-7-96-3). Lavas from the basal unit in Curral das Freiras valley and near the base of the eastern slope of Paul da Serra plateau (Figure 4) produced ages between 3.9 and 4.4 Ma (MA 227, MA 208, MA 203). Only one flow from Madeira dated in this study has an age between 2.8-3.9 Ma. Sample MA 170 with an age of 3.42± 0.10 Ma was taken from a lava flow at Machico near the easternmost tip of Madeira, where Madeira joins the Desertas submarine ridge (see Figure 3.2).

Samples from the middle unit range in age from 1.0-2.8 Ma. At Paul da Serra (Figure 3.5), the middle unit fills in a paleo canyon in the basal unit, reaching a thickness of up to 500 m. Plagioclase crystals (MA 44) from a pumice layer, just above this unconformity on the paleo-hill forming part of the southern wall of the canyon, yielded an age of 2.80± 0.06 Ma. The unconformity separates this pumice layer from basal unit samples MA 208 and MA 203 with ages of 4.10± 0.06 and 4.36± 0.40 Ma sampled about 300 m below the unconformity at the same locality. A lava flow (MA 37) and pumice layer (MA 19), stratigraphically overlying the 2.8 Ma old pumice layer, were dated at 1.42± 0.08 and 1.05 ± 0.16 Ma respectively. Additional samples from the middle unit (MA 75, MA 152, MA 146 and MA 107) fall within the range found at Paul da Serra (1.0-2.8 Ma). In the southeastern part of the island (at the coast half-way between Funchal and Machico), Watkins and Abdel-Monem (1971) report K/Ar ages between 1.76 Ma at the base and 0.74 Ma at the top of a road profile (Figure 3.3). Plagioclase crystals (MA 107) from a pumice layer between the second (1.64 Ma) and the third (1.05 Ma) lowest flow produced an $^{40}Ar/^{39}Ar$ age of 1.44± 0.06 Ma in good agreement with the K/Ar ages of (Watkins and Abdel-Monem, 1971).

The upper unit on Madeira consists of numerous cinder cones and intra-canyon lava flows, for example at Porto do Moniz, Seixal, and São Vicente (Figure 3.3). Sample MA 85 from the pahoehoe lava sequence at São Vicente, which originates from the top of Paul da Serra, yields a young age of 0.18 ± 0.08 Ma. Two charcoal samples were collected beneath a tephra layer on top of Paul da Serra. The samples have calibrated ^{14}C ages of 6407 to 6496 a BP (KIA 685) and 7159 to 7216 a BP (KIA 686) confirming a Holocene age of ca. 6450 a BP as previously mentioned by Schmincke, 1998.

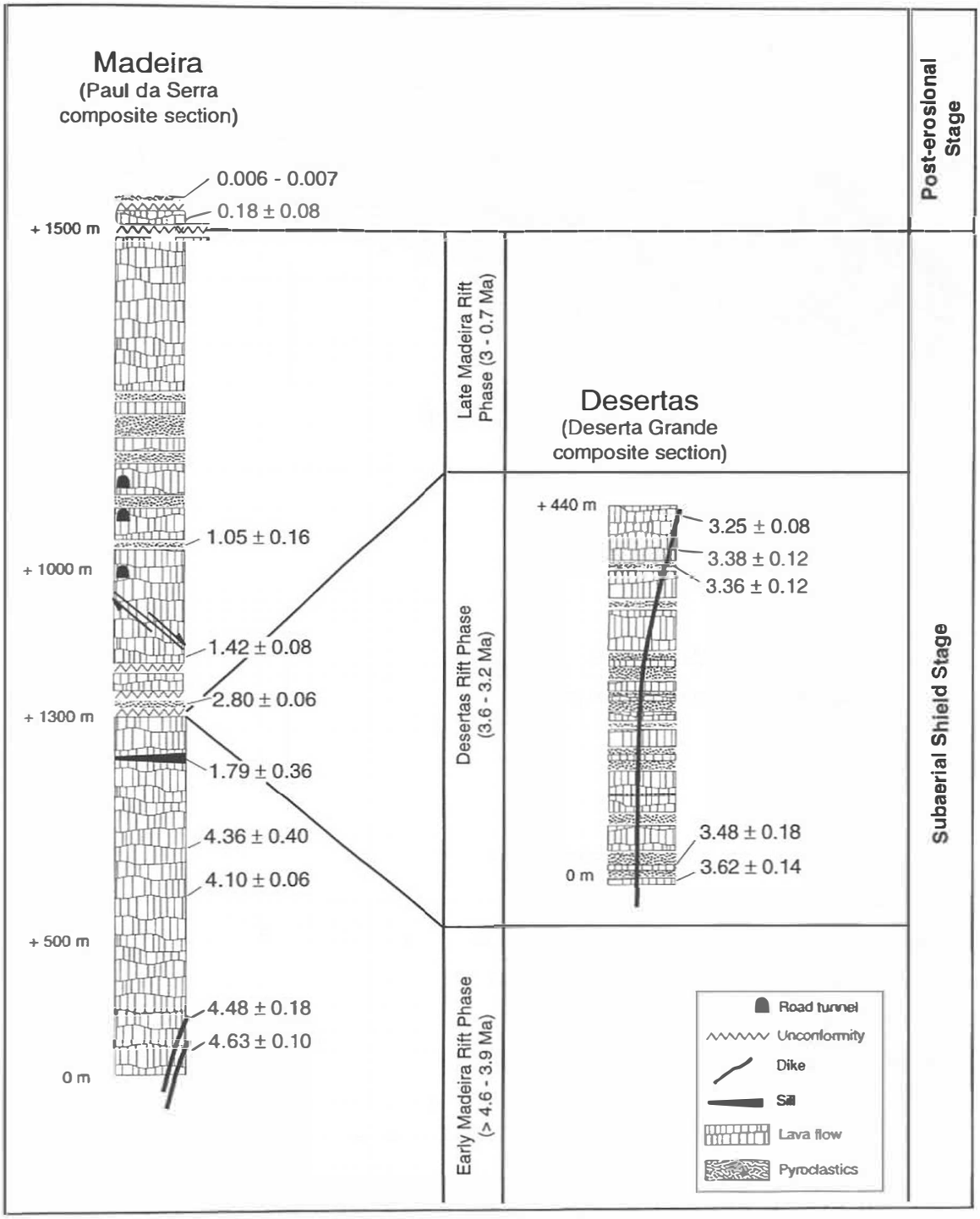

Figure 3.4:

Stratigraphic sections are shown for Paul da Serra on Madeira (left) and Deserta Grande (right) summarizing the subaerial evolution of the Madeira/Desertas volcanic system. Elevations are given in meter above sea level (note that Paul da Serra profile is a composite section). All ages in million years with 2 σ errors. ^{14}C radiocarbon ages calibrated to B.P.

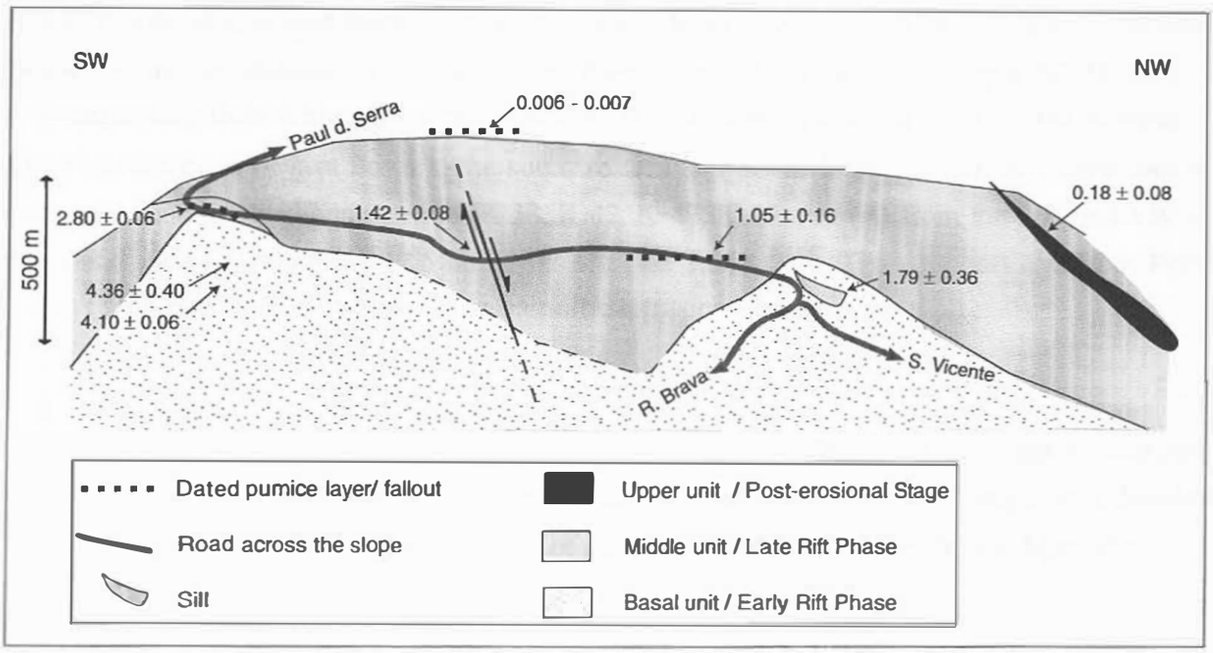

Figure 3.5:
Schematic outcrop sketch of Paul da Serra profile (eastern slope) in central Madeira. Encumeada pass is at the road junction in right part of the figure. All ages in million years.

Desertas Islands (Ilhéu Chão - Deserta Grande - Ilhéu do Bugio)

All nine rocks dated from the Desertas Islands fall within a narrow range of 3.2 and 3.6 Ma (Figure 3.3). A profile through the entire stratigraphic column exposed on Deserta Grande is shown in Figure 4. The oldest ages come from the lava flows at the base of the lava succession on Deserta Grande and Ilhéu Chão with 3.62± 0.14 (K 31), 3.48± 0.18 Ma (DGR 2) and 3.62± 0.24 (K 22) respectively. Samples from a lava flow (DGR 47) and from an amphibole megacryst in a scoria cone from the top of Deserta Grande yielded identical ages within error of 3.38± 0.12 and 3.36± 0.12 respectively. A young dike (DGR 9) that cuts the entire lava pile gives a similar age of 3.25± 0.08 Ma. A basaltic beach cobble from the western shore of Ilhéu do Bugio produced an age of 3.35±0.06 Ma (K 11); dikes from the same island which cut the entire lava sequence give ages of 3.35± 0.06 and 3.36± 0.2 Ma (K5, K15), within error of the youngest units from Deserta Grande.

Porto Santo

Samples from Porto Santo have older ages (11.1-14.3 Ma) than found on Madeira or the Desertas Islands (Table 3.1, Figure 3.3). The investigated samples cover the entire stratigraphic succession of the island: clastic seamount stage in the NE, alkali basaltic lava sequence in the SW, and dikes and minor trachytic and basaltic intrusions which cut both units. The oldest age

(14.31± 0.22 Ma) comes from a benmoreitic dike (K 49) associated with a trachytic intrusion belonging to the seamount stage in the northwest part of the island. Sample K 55 from a submarine lava flow with an age of 13.85± 0.34 Ma comes from the base of the basaltic to hawaiitic sequence of lava flows at the southwestern end of the island. Dikes and intrusions of both mafic and evolved composition (K 38, K 42, K 47, K 67a, K 68) from the NE and SW of the island yield ages between 12.5 and 13.2 Ma (see Table. 3.1). The youngest age from Porto Santo (11.07± 0.10 Ma) comes from a basanitic intrusion (K 43).

Ampére Seamount

A rounded beach cobble of hawaiitic composition (DS 797-1) from Ampére Seamount gives the oldest age (31.2± 0.2 Ma) of the samples dated in this study. This sample was dredged from the eastern part of the summit plateau of Ampére in 160 m water depth (see Appendix).

3.5 Discussion

Geochronological evolution of Madeira and the Desertas Islands

Considering the new $^{40}Ar/^{39}Ar$ age determinations and field observations, the old stratigraphic division based on the lithological mapping by Zbyszewski et al. (1973, 1975) has to be partly revised. We propose the following evolution for Madeira:

1) Shield Stage (> 4.6-0.7 Ma)

A) Early Madeira Rift Phase (> 4.6-3.9 Ma)

This volcanic phase includes the oldest subaerial exposed rocks of Madeira (basal unit). A concentration of volcanic vents and east-west oriented dike swarms in the center of the eastern half of the island suggest that volcanism during the Early Madeira Rift Phase primarily originated from an E-W orientated rift system. The oldest radiometric ages (4.63± 0.10 Ma) from Madeira come from an east-west oriented tholeiitic dike swarm at Porta da Cruz. Rift zones are a common feature of oceanic volcanic islands (e.g. Carracedo, 1994). In the ideal case, triple-armed rift zones with regular geometry at 120° to one another occur as a result of least-effort fracturing produced by magma-induced vertical upward loading (Luongo et al., 1991). As is the case with many Hawaiian volcanoes (e.g. Kilauea), a third rift zone on Madeira with an angle at about 120° to both other arms could probably not develop to the NE, because of the buttressing effect of the large submarine cone of Porto Santo Island (Figure 3.2).

B) Desertas Rift Phase (3.6-3.2 Ma)

The subaerial part of the Desertas Ridge formed between 3.2-3.6 Ma during which time Madeira was almost completely inactive. At the Paul da Serra profile in central Madeira, an unconformity marks this time interval (Figure 3.4). In eastern Madeira north of Funchal, an

unconformity also occurs separating the Early and Late Madeira Rift Phases. The lowermost flow of the Late Rift Phase, just above the unconformity, was dated at 3.05 Ma (Watkins and Abdel-Monem, 1971). No age data is available from rocks beneath the unconformity. A lava flow just above a prominent unconformity with the Early Madeira Rift Phase (basal unit) in Curral das Freiras produced an age of 2.97 Ma (Mata et al., 1995). The youngest age from below the unconformity is 3.91± 0.08 Ma (MA 227). These observations suggest that most of the magma supply shifted to the Desertas Rift arm between 3.0-3.9 Ma. Although speculative, one possible cause for the shift in magma supply between 3.9 and 3.6 Ma to the Desertas Rift Arm may have been collapse of the NE sector of the Madeira Rift Arm (see Figure 3.2). The bathymetry north of Porto da Cruz is very irregular at depths between 1000-2000 m, possibly reflecting the presence of landslide deposits. More detailed bathymetry, however, is necessary to test this hypothesis. A similar scenario has been proposed for the shift of volcanic activity on La Palma (Canary Islands) to the N-S oriented La Cumbre Vieja Rift from the Taburiente shield volcano 700,000 years ago (Ancochea et al., 1994; Klügel et al., in press). At around 3 Ma, volcanism along the Desertas Rift arm ceased, possibly reflecting a shift in the magma supply further to the SW as a result of NE directed plate motion.

C) Late Madeira Rift Phase (3-0.7 Ma)

Beginning at ca. 3 Ma, volcanic activity shifted back to Madeira. As noted above, at Paul da Serra, Curral das Freiras and Ribeiro Frio, the oldest flows overlying major unconformities separating the Early and Late Madeira Rift Phase yielded ages between 2.8-3.0 Ma (Watkins and Abdel-Monem, 1971; Mata et al., 1995; this study). Field observations and age dates from thick lava sequences that cover most of the island show that the late Madeira Rift Phase continued without a significant pause until 0.7 Ma. Although previously mapped as belonging to the basal unit (β1 of Zbyszewski et al., 1975), scoria cone complexes such as Pico Ruivo (2.6 Ma), the highest peak on Madeira, and those near the São Lorenço Peninsula (1.6-1.9 Ma; Mata et al.,1995) yield ages within the range for the Late Rift Stage. These eruption centers are located along the axis of the Late Madeira Rift and are cut by dense dike swarms oriented in the E-W direction. Four of these dikes near Pico Ruivo yield ages between 1-1.8 Ma (Feraud et al., 1981), showing that they are contemporaneous with the thick lava sequences dipping gently to the north and south and thus probably represent feeder dikes for the late Madeira Rift Phase lava sequences.

2) Post-erosional Stage (< 0.7 Ma)

Because of the uncertainties in radiometric age dating of young magmatic rocks, the exact gap between the end of the Madeira Rift Phase and the Post-erosional Stage is uncertain. The two deposits from this stage that have been dated thus far yield ages of ca. 0.2 Ma (MA 85) and 6200-7200 years before present (KIA 685 and KIA 686). It is conspicuous that the youngest activity (e.g. cinder cones in upper São Vicente valley, intra-canyon flows at Porto do

Moniz, Seixal, SãoVicente and the tephra layer on top of Paul da Serra) are located in the western part of Madeira, whereas the oldest rocks are found in the eastern part and the center of the island. The generally westward migration of volcanism on Madeira could potentially reflect NE motion of the African plate.

Eruption rates

Estimating the subaerial volume of Madeira (ca. 430 km^3) and the Desertas Islands (ca. 7 km^3) and considering the oldest available radiometric age (4.63 Ma), an average magma eruption rate of about 95 km^3/Ma can be calculated for the subearial part of the Shield Stage. Upon closer examination of eruption rates for the different units, distinct differences become apparent. Whereas the Early Madeira Rift Phase shows relatively high rates of 150 km^3/Ma, magma eruption decreased during the Desertas Rift Phase to 20 km^3/Ma and increased again to 100 km^3/Ma during the Late Madeira Rift Phase. Although erosion may have removed a considerable volume from the Desertas, it is unlikely that eruption rates during the subaerial Desertas Rift Phase approached those of the Madeira Rift Phases. As has been suggested to explain the shift of activity to the Desertas Rift, the decrease in eruption rates between ca. 3.0-3.9 Ma could also result from blocking of the magma plumbing system due to sector collapse. This may have caused an increase in intrusion relative to extrusion during the Desertas Rift Phase. The eruption rate during the Post-erosional Stage of ca. 2 km^3/Ma is negligible.

The hotspots with the lowest estimated eruption rates occur in the Atlantic Ocean. These include St. Helena (24 km^3/Ma), Bouvet (40 km^3/Ma), Cape Verdes (40 km^3/Ma), Ascension (60 km^3/Ma), and Gough (110 km^3/Ma) (Gerlach, 1990; see also Crisp, 1984 and Bohrson et al., 1996). The eruption rates reported for these islands fall within the range determined for Madeira 20-150 km^3/Ma. It should be noted, however, that it is difficult to directly compare eruption rates for individual islands, since these estimates are often averages for the entire island and often it has not been determined which evolutionary stage(s) the island was in during its subaerial history. Eruption rates for Madeira, on the other hand, are considerably lower than those estimated for the Canary Islands (e.g. 2000-10,000 km^3/Ma for the subaerial Miocene Shield Stage and up to 500 km^3/Ma for the Post-erosional Stage on Gran Canaria; Bogaard et al., 1988; Hoernle and Schmincke, 1993a; Schmincke and Sumita 1998;). Madeira also shows low (subaerial) eruption rates when compared to ocean islands in the Indian and Pacific Oceans, e.g Reunion (2400 km^3/Ma) or Mangaia (100-1000 km^3/Ma) (Gerlach, 1990).

The submarine base of the Madeira/Desertas group makes up about 98% of the volcanic complex having a volume of ~ 26,800 km^3. The submarine volumes were estimated based on the break in bathymetry between the volcanic edifice and the gentle seafloor. Calculating an eruption rate for the submarine base is difficult due to lack of age data and speculative assessment of the intrusive to extrusive ratio. We realize that the volume of the edifice hidden in the clastic apron

may be 2 to 3 times more than the estimate based on the bathymetry alone as seen e.g. for Gran Canaria (Schmincke and Sumita, 1998). Assuming that the Madeira/Desertas complex began forming about 9.5 Ma ago (an age intermediate between the oldest ages obtained from Madeira and Porto Santo), then the average rate of growth during the submarine stage was ~ 5500 km^3/Ma or ca. 36 times as high as during the early subaerial rift stage on Madeira. However, in comparison to other ocean island volcanoes, Madeira has a relatively low average submarine growth rate. Production rates of more than 20,000 km^3/Ma have been estimated for the nearby Canary Islands (Schmincke and Sumita, 1998), whereas a rate of 90,000 km^3/Ma was calculated for the Kilauea volcano on Hawaii (Dzurisin et al., 1984).

Geochronological evolution of Porto Santo (11.1-14.3 Ma)

The $^{40}Ar/^{39}Ar$ age data (Samples K 49 and K 46) from the trachytic to basaltic submarine sequence in the northeast is in good agreement with paleontological data from intercalated shallow water limestones (Cachao et al., 1998). Both types of data yield an age of ca. 14 Ma for the end of the seamount stage in NE Porto Santo. An alkali basaltic lava flow (K 55) overlying pillow basalts but underlying a conglomerate consisting of beach cobbles and boulders, produced a similar age, indicating that the transition from seamount to ocean island in the SW also occurred at ≈14 Ma. Seven samples from basaltic and trachytic dikes and intrusions ranged in age from 11.07-13.17 Ma, probably reflecting the time span of active volcanism on Porto Santo. Most of this subaerial history, however, has been eroded away.

Seine, Ampère (31 Ma) and Coral Patch Seamount

Bathymetric data show that Seine and Ampère Seamounts have flat summit plateaus between 60-200 m below sea level and steep flanks. The morphology of both seamounts and the occurrence of well-rounded beach cobbles among dredged samples from Ampère Seamount indicate that both were probably islands formerly. A highly vesicular scoria sample, dredged from the 1000 m deep summit of nearby Coral Patch Seamount, also points to a shallow water or possible subaerial origin. Ocean island volcanoes that form above a hotspot are generally drowned as the volcano moves away from the hotspot as a result of 1) cessation of magma supply, 2) erosion and 3) cooling and subsidence of the underlying lithosphere (e.g. Werner et al., 1999). The E-W elongated shape of the Ampère/Coral Patch structure may be related to old fracture zones in the oceanic crust which were used by the rising magma.

The Madeira Hotspot track

Considering the assumed NE directed African plate motion (e.g. Duncan, 1981; Morgan, 1983) and the available geochemical (Geldmacher and Hoernle, in prep.), age and bathymetric data for the entire region, a specific Madeira hotspot track can be proposed (Figure 3.1). The hotspot track includes the Madeira/Desertas volcanic complex, Porto Santo Island, Seine Seamount, possibly Unicorn Seamount, Ampère Seamount, Coral Patch Seamount and the upper

alkaline summit of Ormonde Seamount. The presence of alkaline rocks on Ormonde Seamount is consistent with a hotspot origin. $^{40}Ar/^{39}Ar$ age dating of these rocks (65-67 Ma, Feraud et al., 1982; Feraud et al., 1986) further show that they are significantly younger than the underlying early Cretaceous oceanic lithosphere. For these reasons, we believe that the alkaline top of Ormond Seamount could be part of the Madeira hotspot track.

As the distance from Madeira/Desertas (0->4.6 Ma) increases, the age of volcanic and plutonic rocks becomes systematically older: Porto Santo (11-14.3 Ma), Ampère (31 Ma), Ormonde (65-67 Ma). A small seamount off the SW coast of Madeira (Figure 3.2) extending from about 4000 m water depths up to 500 m below sea level is assumed to mark the present center/surface expression of the Madeira hotspot.

In order to determine the rate of plate motion for the underlying plate from a hotspot track, the oldest ages from each volcano are generally used, assuming that they are similar to the ages of the main stage of volcanism when the volcano lay over the center of the hotspot. We note, however, that on a slow plate, such as the NW part of the African Plate, there may be several million years difference in the oldest age obtained from samples on the top and on the flanks of an island/seamount and the main growth stage, resulting in larger errors for the plate motion. On Madeira, for example, fossils from reef debris of "Vindobonian" age, which corresponds to an age between 5.2 and 6 Ma (Carvalho and Brandão, 1991; Schmincke, 1998), occur in uplifted parts of the submarine base of the island.

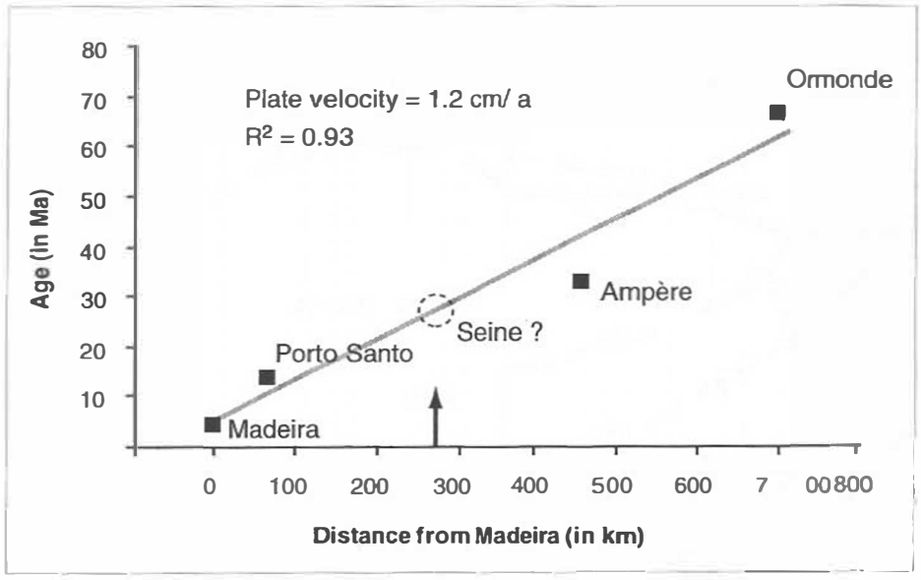

Figure 3.6:

Age (oldest available from each volcano, see text for details) versus distance from Madeira (midpoint of each volcano). From Seine Seamount no age data are available, but considering the distance from Madeira an age of 25-30 Ma is predicted.

As illustrated on Figure 3.6, age relationship of the volcanoes (using the oldest available radiometric ages from each volcano) against distance from Madeira shows a linear correlation. The slope of the correlation line yields a calculated absolute plate velocity of 1.2 cm/a above the Madeira hotspot (with the condition that the hotspot is fixed in respect to the over-riding plate). From Seine Seamount, located midway between Porto Santo and Ampère Seamount, no age data are available, but regarding the position on the correlation line in Figure 6 an age of 25-30 Ma is predicted.

The Madeira hotspot track can be traced beyond Ormonde Seamount to the other side of the Azores-Gibraltar fracture zone as proposed by Morgan (1983). Taking right lateral strike-slip motion between 60 and 72 Ma along the Azores-Gibraltar fracture zone into consideration (Purdy, 1975), the 70-72 Ma old (McIntyre and Berger, 1982) alkaline Serra de Monchique complex in southern Portugal could represent the continuation of the Madeira hotspot track on the Eurasian plate (Figure 3.1). The lateral distance between Ormonde Seamount and Serra de Monchique of ca. 270 km agree well with the ca. 200 km wide offset of the magnetic anomalies 31-34 across the Azores-Gibraltar fracture zone (Cande and Kristoffersen, 1977). The close relationship is also supported by the proposed geochemical similarities between the Serra de Monchique and Ormond magmatic rocks (Bernard-Griffiths et al., 1997).

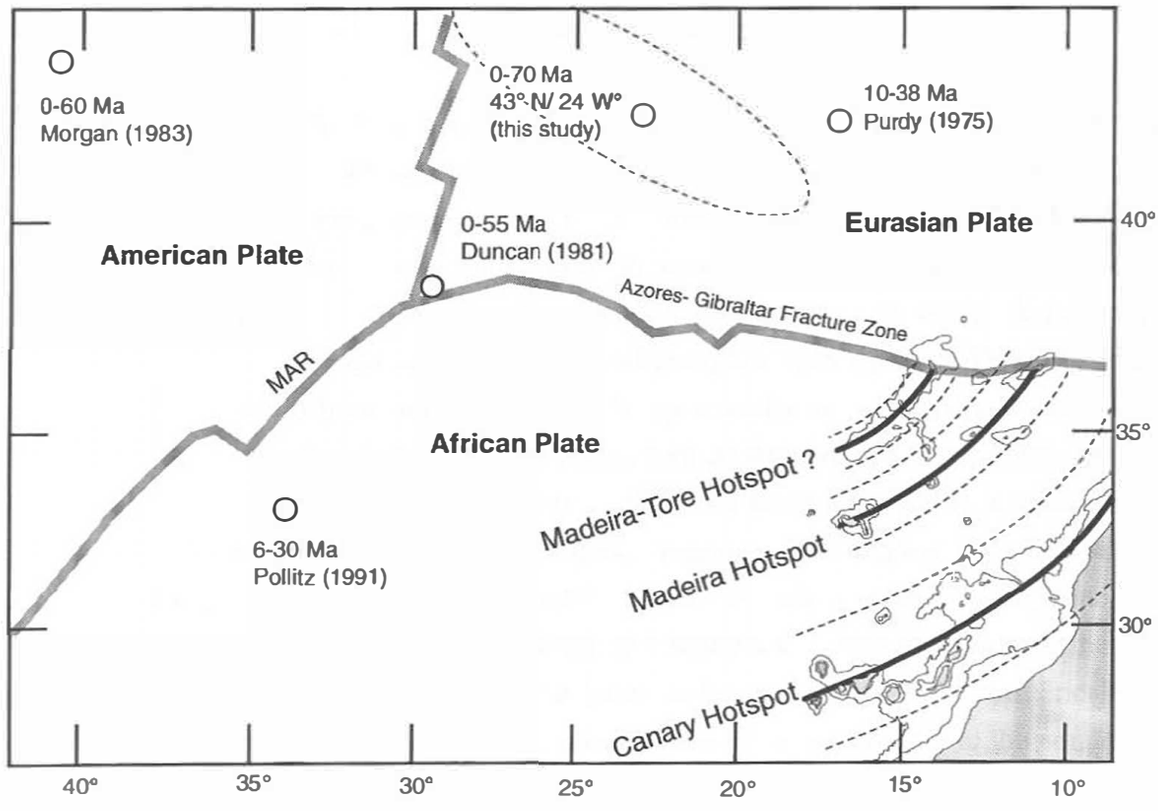

Figure 3.7:

Location of rotation pole for the African Plate (valid for the time period 0-70 Ma) based on the proposed Madeira hotspot track. The African plate motion is a counter-clockwise rotation

about a pole at 43° N/ 24° W. An error ellipse was calculated for this pole by calculating the intersections of big circles placed orthogonal to the outer limits of the track. For comparison rotation poles of Purdy (1975), Duncan (1981), Morgan (1983) and Pollitz (1991) for the periods of 10-38 Ma, 0-55 Ma, 0-60 Ma and 6-30 Ma respectively are also shown. Possible hotspot tracks are also indicated for the Canary Islands and the Madeira-Tore Rise.

Based on the curvature of the proposed Madeira hotspot track, the rotation pole for the African plate has been modeled by calculating the intersections of big circles placed orthogonal to the track (Figure 3.7). Assuming an ideal case, the center of Madeira (32°45'/ 17°00'), Porto Santo (33°03'/ 16°20), Ampère Seamount (35°04/ 12° 56') and Ormonde Seamount (36°42/ 11°08'9) were selected as fixed points for the track. The calculated pole at 43°36'N / 24°33'W correlates well with the rotation pole calculated by Duncan (1981) at 38°N/ 30°W for the time period of 0-55 Ma (Figure 3.7), using the South Atlantic hotspot tracks. Pollitz (1991) propose a change in the location of the pole at around 6 Ma to a position at 18.5°N/ 15.8°W and therefore only the rotation pole for the 6-30 Ma time interval is shown. The 6-30 Ma pole does not fit the proposed Madeira hotspot track and also can not explain the spatial distribution of the Canary Islands. The postulated pole change at 6 Ma is not evident in the Madeira hotspot system because it would require a shift in the volcanic age progression to the east (which would probably have resulted in reactivation of Porto Santo volcano).

Based on the position of islands and seamounts an angular velocity of 0.47°/Ma can be calculated which converts into an absolute plate motion of 1.2± 0.7 cm/a above the Madeira hotspot. The large error range results from 1) the short overall length of the Madeira hotspot track due to the proximity to the rotation pole, 2) uncertainty in integrating over a long time period in which possible variations in plate velocity or pole position are averaged. For example, O'Conner et al. (1999) proposed a decrease in African plate velocity since 19 to 30 Ma. The Madeira hotspot track differs from most other hotspot tracks in two important ways: 1) The track is irregularly distributed (e.g. elongated alignment of Ampère and Coral Patch Seamounts (EW) and possibly Seine and Unicorn (N-S)). 2) There are large and varying distances between individual volcanic complexes. Both of these features, in addition to the very low eruption/production rates, could be explained by a weak, pulsating or blob-type plume, as has been proposed for the Canary Islands (Hoernle and Schmincke, 1993b). Assuming that mantle upwelling is in the form of discrete spherical blobs, as has been observed in numerical models for plume initiation (e.g., Keken, 1997), their ascent rate will be proportional to the square of the radius of the blob (Stokes law). This means that small blobs rise very slowly and are more susceptible to displacement during ascent due to the horizontal asthenospheric mantle flow than larger ones which have a higher ascent rate resulting in irregularly distributed volcanoes at the surface. The large age differences and distances between large volcanoes and volcanic complexes

along the hotspot track suggest that intervals of up to 10-25 Ma may separate individual pulses (or blobs) of upwelling plume mantle.

The elongation of the Madeira-Tore Rise (Figure 3.1) does not point to Madeira but rather to the west of Madeira. Based on gravimetric data, it has been proposed that the Madeira-Tore Rise was formed at the Mid Atlantic Ridge (Peirce and Barton, 1991). However, samples from the top of Josephine Seamount, at the NE end of the Madeira-Tore Rise, have alkali basaltic compositions and Miocene ages (Eckhardt et al., 1975; Wendt et al., 1976; Matveyenkov et al., 1994). This could be explained by production of minor volcanism associated with the movement along the Azores-Gibraltar fracture zone. Wendt et al. (1976) note the coincidence of eruption age and intensive convergence tectonics and uplift along this boundary. Alternatively, the Madeira-Tore Rise could be interpreted as a separate hotspot track, formed by a separate small hotspot north or west of Madeira (see Figure 3.7). This would be consistent with the available geochemical data from Josephine Seamount. Additional age and geochemical data from seamounts forming the Madeira-Tore Rise, however, are necessary to test this hypothesis.

Using the calculated Euler Pole for the proposed Madeira hotspot track, the Selvagen Islands and the seamounts southeast of Madeira and northeast of the Canary Islands could belong to the earlier part of the nearby Canary Island hotspot track (Figure 3.7). This has also been proposed based on geophysical (Holik and Rabinowitz, 1991), geochemical and geochronological (Geldmacher et al., in prep.) studies. If these seamounts, the Selvagen and Canary Islands result from a single hotspot, this plume must be considerably wider (ca. 400 km) than the proposed Madeira or possible Madeira-Tore Rise Plumes (ca. 150- 200 km).

3.6 Conclusions

Madeira and the Desertas Islands form a single volcanic system consisting of the E-W oriented Madeira Rift Arm and the NNW-SSE Desertas Rift Arm. The two rift arms join at the eastern end of Madeira and northern end of the 60 km long, primarily submarine Desertas Ridge at an angle of 110°. The subaerial evolution of the Madeira/Desertas volcanic system can be divided into a voluminous (99.5 % of the subaerial volume) Shield Stage (> 4.6-0.7 Ma) and a low-volume (0.5 %) Post-erosional Stage (< 0.7 Ma). During the Shield Stage, volcanism occurred on Madeira almost exclusively from 3.9-4.6 Ma (Early Madeira Rift Phase) and from 0.7-3.0 Ma (Late Madeira Rift Phase). The Desertas Islands formed in a short interval between 3.2-3.6 Ma, during which time the Madeira Rift was almost completely inactive, possibly reflecting blockage of the central and western parts of the Madeira Rift Arm due collapse of the NE sector of the Madeira Rift. Minor post-erosional volcanism continued into the Holocene with the last eruption on Madeira occurring 6000-7000 years B.P. Average growth rates for the

submarine (5500 km^3/Ma) and subaerial (100-150 km^3/Ma) Shield stages on Madeira are among the lowest found for ocean island volcanoes.

A shallow seamount SW of Madeira probably marks the present location of the > 70 Ma old Madeira hotspot track which includes the Madeira/Desertas volcanic system (0-4.6 Ma), Porto Santo Island (11.1-14.3 Ma), Seine, possibly Unicorn, Ampère (31 Ma), Coral Patch and Ormonde (65-67 Ma) Seamounts, and the Serra de Monchique intrusive complex (70-72 Ma) in southern Portugal. Based on the proposed Madeira hotspot track, we calculate a rotation pole at 43°36' N / 24°33' W and an angular velocity of 0.47°/Ma for the African Plate with a plate motion above the Madeira hotspot of 1.2 cm/a which agrees well with the pole of rotation for the African Plate calculated by Duncan (1981) using the South Atlantic hotspot tracks. The large and varible age gaps between individual volcanoes in the Madeira Hotspot track, in addition to the very low magmatic productivity, can best be explained by a very weak hotspot, which is only intermittently active.

Acknowledgments

We thank Director H. Costa-Neves and the staff from the Parque Natural da Madeira for co-operation and excellent logistical support during field studies on Madeira and especially the Desertas Islands. Captain M. Gross, officers and crew of the F. S. POSEIDON are gratefully acknowledged for their help in obtaining submarine rock samples used in this study. Especial thanks to R. Schmidt and A. Klügel for stimulating discussions in and out of the field. G. Zankl and F. Marks assisted with sample preparation. J. Sticklus provided technical support during $^{40}Ar/^{39}Ar$ laser dating at Geomar. Many thanks also to D. Rodriguez (University of Madeira) and H. Blazy (University Hamburg) for varied help. S. Karstel (Geomar) is thanked for providing bathymetric maps. We thank H. Staudigel, Sinton, M. Reid and W. White for their constructive reviews that have led to significant improvements. This study was supported by Deutsche Forschungsgemeinschaft project Ho 1833/1.

References

Ancochea, A., F. Hernán, A. Cendrero, J. M. Cantagrel, J. M. Fúster, E. Ibarolla, and J. Coello, J., Constructive and destructive episodes in the building of a young Oceanic Island, La Palma, Canary Islands, and genesis of the Caldera de Taburiente, *J. Volcanol. Geotherm. Res., 60,* 243-262, 1994.

Auzende, J. M., J. Olivet, A. Le Lann, X. Le Pichon, J. Monteiro, A. Nicolas, and A. Ribeiro, Sampling and observation of oceanic mantle and crust on Gorringe Bank, *Nature, 273*, 45-49, 1978.

Bernard-Griffiths, J., G. Gruau, G. Cornen, B. Azambre, and Joel Macé, Continental lithospheric contribution to alkaline magmatism: Isotopic (Nd,Sr,Pb) and geochemical (REE) evidence from Serra de Monchique and Mount Ormonde complexes, *J. Petrol., 38-1*, 115-132, 1997.

Bogaard P. v. d., H.-U. Schmincke, and A. Freundt, Eruption Ages and Magma Supply Rates During the Miocene Evolution of Gran Canaria. *Naturwissenschaften. 75*, 616-617, 1988

Bohrson, W. A., M. R. Reid, A. L. Grunder, M. T. Heizler, T. M. Harrison, and J. Lee, Prolonged history of silicic peralkaline volcanism in the eastern Pacific Ocean, J. Geophys. Res., 101-B5, 11,475-11,474, 1996.

Cachao, M., D. Rodrigues, C. M. Silva, and J. Mata, Biostratigrafia (Nanofosseis calcarios) e interpretacao paleoambiental do Neogenico de Porto Santo (Madeira), V Congresso Nacional de Geologia, *Comun. Inst. Geologico Mineiro Llisboa, 84 (1),* A91-A94, 1998.

Cande, S. C., and Y. Kristoffersen, Late Cretaceous magnetic anomalies in the North Atlantic, *Earth Planet. Sci. Lett., 35*, 215-224, 1977.

Carracedo, J. C., The Canary Islands: an example of structural control on the growth of large ocean-island volcanoes, *J. Volcanol. Geotherm. Res., 60*, 225-241, 1994.

Carvalho, G. d., and J. M. Brandão, *Geologia do Arquipelago da Madeira*, Mus. Nac. d. Hist. Nat., Lisbon, 1991.

Cornen, G., Petrology of the alkaline volcanism of Gorringe Bank (southwest Portugal), *Mar. Geol., 47*,101-130, 1982.

Crisp, J. A. Rates of magma emplacement and volcanic output, *J. Volcanol. Geotherm. Res., 20*, 177-221, 1984.

Cyagor II Group, Intraoceanic tectonism on the Gorringe Bank: observations by submersible, in *Ophiolites and oceanic lithosphere,* edited by G. Gass, S. J. Lippard, and A. W. Shelton, pp. 113-120, Geological Society of London, London, 1984.

Dalrymple, G. B., and W. A. Duffield, High precision $^{40}Ar^{39}Ar$ dating of Oligocene tephra from the Mogollon-Datil volcanic field using a continuos laser system, *Geophys. Res. Lett., 15*, 463-466, 1988.

Duffield, W. A., and G. B. Dalrymple, The Taylor Creek Rhyolite of New Mexico: a rapidly emplaced field of domes and lava flows, *Bull. Volcanol., 52*, 475-478, 1990.

Duncan, R. A., Hotspots in the southern oceans-an absolute frame of reference for motion of the Gondwana continents, *Tectonophys., 74*, 29-42, 1981.

Dzurisin, D., R. Y. Koyanagi, and T. T. English, Magma supply and storage at Kilauea volcano, Hawaii, J. *Volcanol. Geotherm. Res., 21*, 177-206, 1984.

Eckhardt, F. J., P. Müller, and H. Raschka, Geochemische und petrologische Untersuchungen an Basalten der Meteor-Kuppenfahrt (Mittlerer Atlantik) (abstract), *Fortschritte in der Mineralogie, 53*, Tagung der Sektion Geochemie der Deutschen Mineralogischen Gesellschaft, Karlsruhe, 1975.

Féraud, G., H.-U. Schmincke, J. Lietz, J. Gastaud, G. Pritchard, and U. Bleil, New K-Ar ages, chemical analyses and magnetic data of rocks from the island of Santa Maria (Azores), Porto Santo and Madeira (Madeira Archipelago) and Gran Canaria (Canary Islands), *Bull. Volcanol., 44-3*, 359-375, 1981.

Féraud, G., J. Gastaud, J.-M. Auzende, J.-L. Olivet, and G. Cornen, $^{40}Ar/^{39}Ar$ ages for alkaline volcanism and the basement of Gorringe Bank, North Atlantic Ocean, Earth Planet. *Sci. Lett., 57*, 211-226, 1982.

Féraud, G., D. York, C. Mével, G. Cornen, C. M. Hall, and J.-M. Auzende, Additional $^{40}Ar^{39}Ar$ dating of the basement and the alkaline volcanism of Gorringe Bank (Atlantic Ocean), *Earth Planet. Sci. Lett., 79*, 255-269, 1986.

Ferreira, M. P., R. Macedo, V. Costa, and J. H. Reynolds, Rare-Gas Dating, II. Atempted Uranium-Helium dating of young volcanic rocks from the Madeira Archipelago, *Earth Planet. Sci. Lett., 25*, 142-150, 1975.

Ferreira, M. P., and J. Cotelo Neiva, Carta Geologica de Portugal, Folha da Ilha de Porto Santo, *Instituto Geologico e Minereiro*, Lisbon, 1997.

Geldmacher, J., K. Hoernle, 72 Ma Geochemical evolution of the Madeira hotspot (eastern North Atlantic): Recycling of Palaeozoic Oceanic Crust (≤ 500 Ma), *in prep.*

Geldmacher, J., K. Hoernle, P. v. d. Bogaard, G. Zankl and D. Garbe-Schönberg, New $^{40}Ar/^{39}Ar$ dating and geochemical evolution of the Selvagen Archipelago and neighboring seamounts in the eastern North Atlantic: Evidence for the passing of the ancient Canary Plume ?, *in prep.*

Gerlach , D. C., Eruption rates and isotopic systematics of ocean islands: Further evidence for small-scale heterogeneity in the upper mantle, *Tectonophysics , 172*, 273-289, 1990.

Hoernle, K., G. Tilton and H.-U. Schmincke, Sr-Nd-Pb isotopic evolution of Gran Canaria: evidence for shallow enriched mantle beneath the Canary Islands, *Earth Planet. Sci. Lett., 106*, 44-63, 1991.

Hoernle, K., and H.-U. Schmincke, The petrology of the tholeiites through melilite nephelinites on Gran Canaria, Canary Islands: crystal fractionation, accumulation and depths of melting, *J. Petrol., 34*, 573-597, 1993a.

Hoernle, K., and H.-U. Schmincke, The role of partial melting in the 15 Ma geochemical evolution of Gran Canaria: a blob model for the Canary hotspot, *J. Petrol., 34*, 599-626, 1993b.

Hoernle, K., Y.-S. Zhang, and D. Graham, Seismic and geochemical evidence for largescale mantle upwelling beneath the eastern Atlantic and western and central Europe, *Nature, 374*, 34-39, 1995.

Holik, J. S., and P. D. Rabinowitz, Effects of the Canary hotspot volcanism on structure of oceanic crust off Morocco, *J. Geophys. Res., 96*, 12039-12067, 1991.

Hughes, D. J., and G. C. Brown, Basalts from Madeira: A petrochemical contribution to the genesis of oceanic alkali rock series, *Contrib. Mineral. Petrol., 37*, 91-109, 1972.

Keken, P. v., Evolution of starting mantle plumes: a comparison between numerical and laboratory models, *Earths Planet. Sci. Lett., 148*, 1-11, 1997

Klügel, A., K. Hoernle, H.-U. Schmincke, and J. D. L. White, The chemically zoned 1949 eruption on La Palma (Canary Islands): Petrologic evolution and magma supply dynamics of a rift-zone eruption, *J. Geophys. Res.*, in press.

Litvin, V. M., V. V. Matveyenkov, E. L. Onishchenko, M. V. Rudenko, and A. M. Sagalevich, New data on the Structure of Ampère Seamount, *Oceanology, 22-1*, 62-64, 1982.

Luongo, G., E. Cubellis, F. Obrizzo, and S. M. Petrazzuoli, A physical model for the origin of volcanism of the Tyrrhenian margin: the case of the Neapolitan area, *J. Volcanol. Geotherm. Res., 48*, 173-185, 1991.

Marova, N. A., and Y. D. Yevsyukov, The geomorphology of the Ampère submarine seamount (in the Atlantic Ocean), *Oceanology, 27-4*, 452-455, 1987.

Mata, J., T. Boski, A. Boven, and J. Munhá, Geochronologia das Lavas da Madeira: Novas Dataçoes K.-Ar, *Gaia, 11*, 53-56, 1995.

Matveyenkov, V. V., S. G. Poyarkov, O. V. Dmitriyenko, A. I. Al´Mukhamedov, G. R. Gamsakhurdia, and O. L. Kuznetsov, Geological particularities of the Seamount Structure in the Azoro-Gibraltar Zone, *Oceanology, 33-5*, 664-673, 1994.

McIntyre, R. M., and G. W. Berger, A note on the geochronology of the Iberian Alkaline Province, *Lithos 15*, 133-136, 1982.

Mitchel-Thomé, R. C., *Geology of the middle Atlantic Islands*, Borntraeger, Berlin, 1976.

Morgan, W. J., Plate motions and deep mantle convection, *Geol. Soc. Am. Mem., 132*, 7-22, 1972.

Morgan, W. J., Hotspot tracks and the opening of the Atlantic and Indian Oceans, in *The Sea; Oceanic Lithosphere*, vol. 7, edited by C. Emiliani, C., pp. 443-487, Wiley & Sons, New York, 1981.

Morgan, W. J., Hotspot tracks and the early rifting of the Atlantic, *Tectonophys., 94*, 123-139, 1983.

O'Conner, J. M., P. Stoffers, P. v. d. Bogaard and M. McWilliams, First seamount age evidence for significantly slower African plate motion since 19 to 30 Ma, *Earth Planet. Sci. Lett., 171*, 575-589, 1999.

Peirce, C., and P. J. Barton, Crustal structure of the Madeira-Tore Rise, eastern North Atlantic – results of a DOBS wide-angle and normal incidence seismic experiment in the Josephine Seamount region, *Geophys. J. Int., 106*, 357-378, 1991.

Pitman, W., and M. Talwani, Sea floor spreading in the North Atlantic, *Geol. Soc. Am. Bull., 83-3*, 619-646, 1972.

Pollitz, F. F., Two-stage model of African absolute motion during the last 30 million years: *Tectonophys., 194*, 91-106, 1991.

Schmidt, R., H.-U. Schmincke, J. McPhie, and P. v. d. Bogaard, Volcanology, geochemistry and age evolution of a shoaling to emerged seamount, Porto Santo (Central East Atlantic), *in prep.*

Schmincke, H.-U., and H. Staudigel, Pillow lavas on central and eastern Atlantic Islands (La Palma, Gran Canaria, Porto Santo, Santo Maria) (Preliminary report), *Bull. Soc. Géol. France, 7-4*, 871-883, 1976.

Schmincke H.-U. and M. Sumita, Volcanic evolution of Gran Canaria reconstracted from apron sediments: Synthesis of VICAP project drilling, Proceedings of the Ocean Drilling Program, Scientific Results, 157, 443-469, 1998.

Schmincke, H.-U., Volcanic and chemical evolution of the Canary Islands, in *Geology of the Northwest African margin* edited by E. Seibold, pp. 273-306, Springer-Verlag, New York, 1982.

Schmincke, H.-U., Zeitliche, strukturelle und vulkanische Entwicklung der Kanarischen Inseln, der Selvagens Inseln und des Madeira-Archipels, in *Handbuch der Reptilien und Amphibien Europas* edited by W. Bischoff, pp. 27-69, Aula Verlag, Wiesbaden, 1998.

Smith, W. H. F., and D. T. Sandwell, Global seafloor topography from satellite altimetry and ship depth soundings, *Science, 277*, 1956-1962, 1997.

Stuiver, M., and P. Reimer, Extendet ^{14}C Data base and revise calib 3.0 ^{14}C programm: *Radiocarbon, 35*, 215-230, 1993.

Verhbitsky, E. V., and V. G. Zolotarev, Heat flow and the Eurasian-African plate boundary in the eastern part of the Azores-Gibraltar fracture zone, *J. Geodynam., 11*, 267-273, 1989.

Walker, G. P. L., The dike complex of Koolau volcano, Oahu: Internal structure of a Hawaiian rift zone, in *Volcanism in Hawaii, vol. 1350*, edited by R. W. Decker, T. W. Wright, and P. H. Stauffer, pp. 961-993, US Geol. Surv. Prof. Paper, 1987.

Watkins, N. D., and A. Abdel-Monem, Detection of the Gilsa Geomagnetic Polarity Event on the Island of Madeira, *Geol. Soc. Am. Bull., 82*, 191-198, 1971.

Wendt, I., P. Kreuzer, and P. Müller, K-Ar age of basalts from Great Meteor and Josephine seamounts (Eastern North Atlantic), *Deep-Sea Res., 23-9*, 849-862, 1976.

Wendt, I., and C. Carl, The statistical distribution of the mean squares weighted deviation: *Chem. Geol., 86*, 275-285, 1991.

Werner, R., K. Hoernle, P. v. d. Bogaard, C. Ranero, R. v. Huene, and D. Korich, A drowned 14 Ma old Galápagos Archipelago off the coast of Costa Rica: Implications for evolutionary and tectonic models, *Geology, 27*, 499-502, 1999.

York, D., Least squares fitting of a straight line with correlated errors, *Earth Planet. Sci. Lett., 5*, 320-324, 1969.

Young, H. D., Statistical Treatment of Experimental Data, *88, McGraw-Hill*, New York, 5101-5112, 1962.

Zbyszewski, G., A. Candido de Medeiros, O. d. Veiga Ferreira, and C. Torre de Assunçao, *Carta Geologica de Portugal 1/50,000, Noticia Explicativa da Folha Ilhas Desertas*, Servicos Geologicos de Portugal, Lisbon, 1973.

Zbyszewski, G., O. d. Veiga Ferreira, A. Candido de Medeiros, L. Aires-Barros, L. C. Silva, J. M. Munha, and F. Barriga, *Carta Geologica de Portugal 1/50,000, Noticia Explicativa das Folhas A e B da Ilha da Madeira*, Servicos Geologicos de Portugal, Lisbon, 1975.

Zhang Y-S., and T. Tanimoto, Ridges, hotspots and their interaction as observed in seismic velocity maps, *Nature 355*, 45-49,1992.

Chapter 4

The geochemical evolution of the Madeira hotspot

This chapter consists of an individual paper that is submitted to Earth and Planetary Sciences Letters. The large data set presented in the Appendix of the original paper is given in the Appendix of this thesis.

The 72 Ma Geochemical Evolution of the Madeira Hotspot (eastern North Atlantic): Recycling of Palaeozoic (≤ 500 Ma) Basaltic and Gabbroic Oceanic Crust

Jörg Geldmacher and Kaj Hoernle,

GEOMAR Research Center, Wischhofstrasse 1-3, D-24148 Kiel, Germany

corresponding author: jgeldmac@geomar.de (Fax: ++49 431 600 2978)

Key words: Madeira, hotspot, Sr-Nd-Pb isotope geochemistry, recycling age, oceanic crust

Abstract

Major element, trace element and Sr-Nd-Pb isotopic data of volcanic rocks from the Madeira Archipelago (eastern North Atlantic) and seamounts of the Madeira hotspot track (Ampère Coral Patch and Ormonde) are presented in this study. Although the Sr and Nd isotopic ratios are similar to those in normal mid-ocean-ridge basalt (N-MORB), the incompatible element signatures and Pb isotopic compositions ($^{206}Pb/^{204}Pb$= 18.7-19.8) show similarities to the HIMU (high time-integrated $^{238}U/^{204}Pb$) mantle component. On the $^{206}Pb/^{204}Pb$ versus $^{207}Pb/^{204}Pb$ isotope correlation diagram, all samples plot below the Northem Hemisphere Reference Line (NHRL; Δ 7/4 = -1.0 to -7.2) and form a 400 Ma isochron. These data are consistent with the presence of recycled Paleozoic oceanic crust in the Madeira source. Variations in major element and isotope geochemistry (e.g. positive correlation between SiO_2 and FeO^T with Pb isotope ratios in primitive samples) point to a heterogeneous plume source containing both upper (primarily altered basaltic) and lower (primarily unaltered gabbroic) ocean crust. The more fertile basaltic crustal component is preferentially sampled during the shield stage of volcanism, whereas the gabbroic crustal component is primarily sampled during the post-erosional stage. We propose that plume material becomes progressively depleted through melt extraction as it is sheared by lithospheric drag. Systematic decrease in $^{143}Nd/^{144}Nd$ and increase in $^{207}Pb/^{204}Pb$ isotopic ratios along the hotspot track with increasing age and proximity to Iberia are attributed to increased contamination by continental lithosphere.

4.1 Introduction

It is widely accepted that oceanic crust can be recycled through the mantle as a result of subduction to a thermal boundary layer (such as the upper-lower mantle boundary or core-mantle boundary) and then subsequent return to the surface by mantle plumes which form ocean islands volcanoes [1, 2]. Based on the radioactive decay of unstable isotopes, ages of 1-2.5 Ga are commonly proposed for the recycling of oceanic crust (see Zindler and Hart [3] for summary). Several recent studies, however, provide evidence that recycling times can be significantly shorter. Hanan and Graham [4] show evidence that MORB contains a ubiquitous component, which they interprete to reflect ≥ 300 Ma old oceanic crust. Thirlwall [5] argues that OIB with intermediate $^{206}Pb/^{204}Pb$ and low Δ 7/4 represents recycled oceanic crust with ages between 400 and 1400 Ma. Samples from altered Jurassic ocean crust from the Atlantic can have trace element and Sr-Nd-Pb isotope characteristics similar to basalts from the island of St. Helena [6], the Atlantic type locality for the HIMU mantle endmember which is commonly believed to require ~ 2 Ga recycling times [e.g. 3, 7]. Finally, a study of the Carribean Large Igneous Province (CLIP) proposed that large volumes of oceanic lithosphere can be recycled on time scales of 300-500 Ma in starting plume heads [8].

The geochemical evidence for recycling of oceanic crust largely comes from ocean island basalt (OIB) with elevated $^{206}Pb/^{204}Pb$ isotope ratios, reflecting high time-integrated $^{238}U/^{204}Pb$ ratios ("high μ "=HIMU). The HIMU component is also characterized by a particular trace element pattern with enrichment in highly incompatible elements, in particular Nb and Ta, relative to other incompatible elements [e.g. 9]. Enrichment of U and Th relative to Pb can either be produced by hydrothermal alteration of the former oceanic crust shortly after creation near the ancient ridge axis [e.g. 10, 6] or by fluid mobilization during subduction [e.g. 11, 12]. The elevated U/ Pb ratios lead to radiogenic Pb isotope ratios relative to MORB as the oceanic crust ages. Most ocean-island volcanic rocks form an array on the $^{206}Pb/^{204}Pb$ versus $^{207}Pb/^{204}Pb$ isotope correlation diagram clustering around the Northern Hemisphere Reference Line (NHRL), in particular when islands showing enriched Sr and Nd isotope ratios (i. g. Dupal signatures) are excluded [13]. The slope of the NHRL correlates to an age of 1.8 Ga, which has generally been interpreted to reflect the average recycling age of oceanic crust. Because of its shorter half life, ^{235}U ($t_{1/2}$ = 0.7 Ga) is in a more advanced state of decay relative to ^{238}U ($t_{1/2}$ = 4.47 Ga), such that the present $^{238}U/^{235}U$ ratio is 137.88. Therefore young recycled oceanic crust with elevated U/Pb ratios will have low $^{207}Pb/^{204}Pb$ and intermediate $^{206}Pb/^{204}Pb$ ratios relative to endmember HIMU from St. Helena, Tubuaii and Mangaia with $^{206}Pb/^{204}Pb > 20.5$ and $^{207}Pb/^{204}Pb > 15.7$ [7].

In this paper we present petrological and geochemical data (including major and trace element compositions and Sr, Nd and Pb isotope ratios) from the Madeira Archipelago and from Ampère, Coral Patch and Ormonde Seamounts. Evidence for recycling of upper and lower oceanic crust over short time scales will be presented. We will also evaluate the 72 Ma evolution of the Madeira hotspot.

4.2 Geological Background and Review of Previous Studies

The Madeira archipelago is located in the eastern North Atlantic at the end of a slightly curved northeast-southwest oriented chain of islands and seamounts (Fig. 4.1a). Spatial distribution and systematic increase in the age of volcanoes from southwest to northeast indicate that Madeira Island (i. e., the small seamount southwest of Madeira represents the present location of a > 70 Ma old hotspot which also formed the Desertas and Porto Santo Islands; Seine, possibly Unicorn, Ampère, Coral Patch and Ormonde Seamounts; and the alkaline Serra de Monchique complex in SW Portugal [14]. A low-velocity anomaly, observed in seismic tomography models, extending to depths of at least 1200 km beneath the region also support a hotspot related origin for this volcanic province [15, 16]. Seamounts north of the Madeira archipelago form the elongated Madeira Tore Rise that extends to within 150 km of Madeira Island. It is unclear if these seamounts belong to the Madeira hotspot track.

The Madeira Archipelago consists of five principal islands (Fig. 4.1b). The largest island of Madeira, Porto Santo Island ~ 45 km to the northeast of Madeira and the three narrow Desertas Islands (Ilhéu Chão, Deserta Grande and Bugio), situated on a submarine ridge extending more than 60 km SSE of the eastern tip of Madeira. The archipelago is located on 140 Ma old oceanic crust [17] and ascends from more than 4000 m water depths to an elevation of 1862 m above sea level (Pico Ruivo on Madeira Island).

The oldest rocks in the archipelago occur on Porto Santo Island (11-14 Ma, see summary in Geldmacher et al., [14]). Recent geological mapping [18], age determinations [14] and a detailed volcanological and geochronological study [19] show that the Island has a complex structure with simultaneous occurrence of primitive and evolved rocks throughout its eruptive history. Volcanic rocks range from alkali basalt to rhyolite [20]. In contrast to Porto Santo, Madeira and the Desertas Islands form a single volcanic system consisting of two rift arms: the E-W oriented Madeira Rift Arm and the NNW-SSE oriented Desertas Rift Arm. Based on geological mapping [21, 22], recent age determinations and field observations [14, 23], the

subaerial evolution of Madeira/Desertas can be divided into two stages: 1) Shield Stage (> 4.6-0.7 Ma) which can be subdivided in to an Early Madeira Rift Phase (> 4.6-3.9 Ma), a Desertas Rift Phase (3.6-3.2 Ma) and a subsequent Late Madeira Rift Phase (3-0.7 Ma), and 2) Post-Erosional Stage (< 0.7 Ma) (Fig. 4.1b).

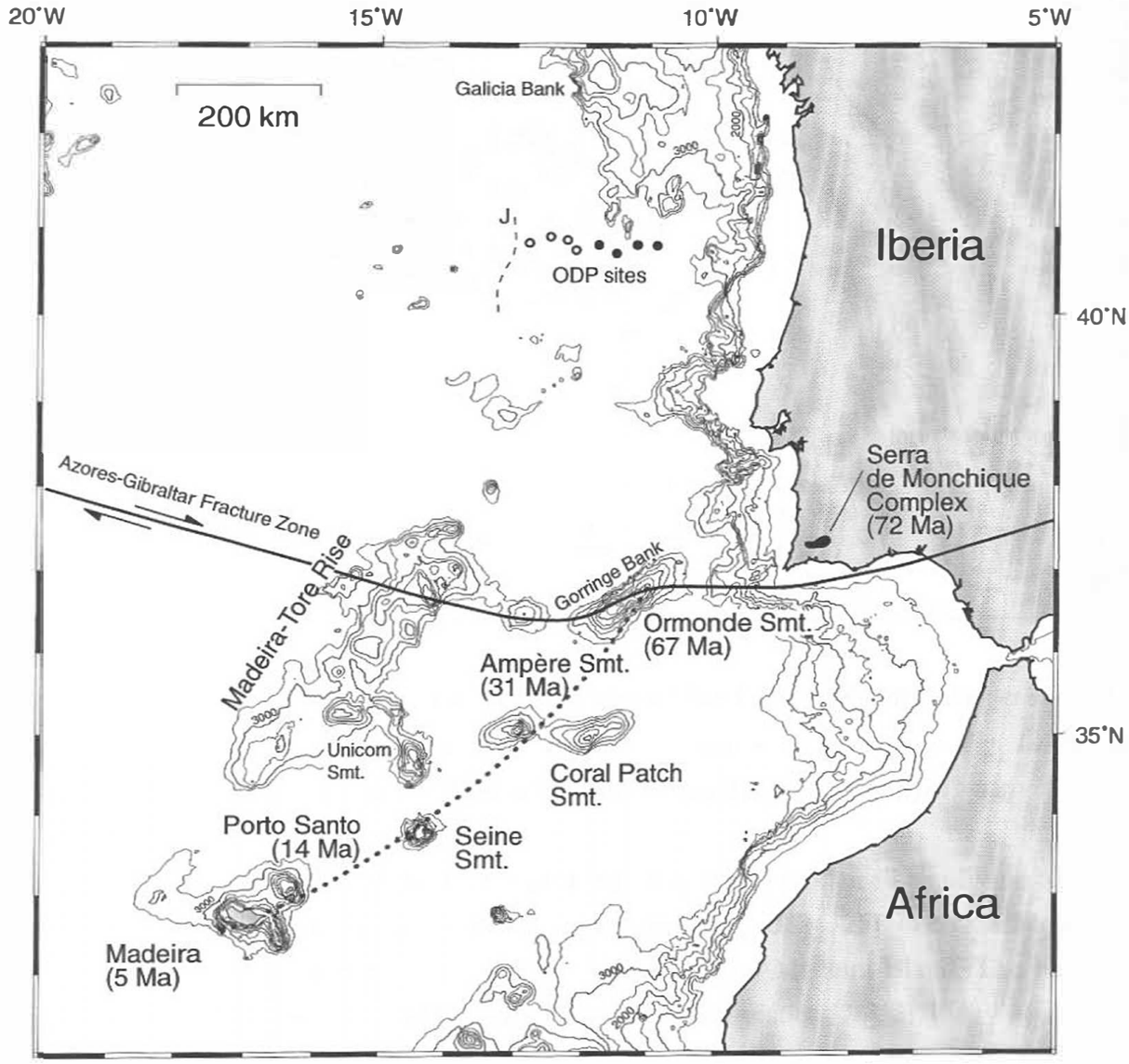

Fig. 4.1a:

Bathymetric map of seamounts and islands in the eastern North Atlantic. Source: TOPEX [60]. Azores-Gibraltar Fracture Zone after Verhbitsky and Zolotarev [61]. Proposed Madeira hotspot track (shown as thin dotted line) and oldest available age data for each island or seamount (see [14] and references therein). Also shown are ODP sites (from west to east: 1070, 897, 899, 898, 1069, 900, 1065, 901) and the crest of the J anomaly marking the oldest seafloor magnetic anomalies [59]. Sites where blocks of continental crust have been drilled are marked with closed circles.

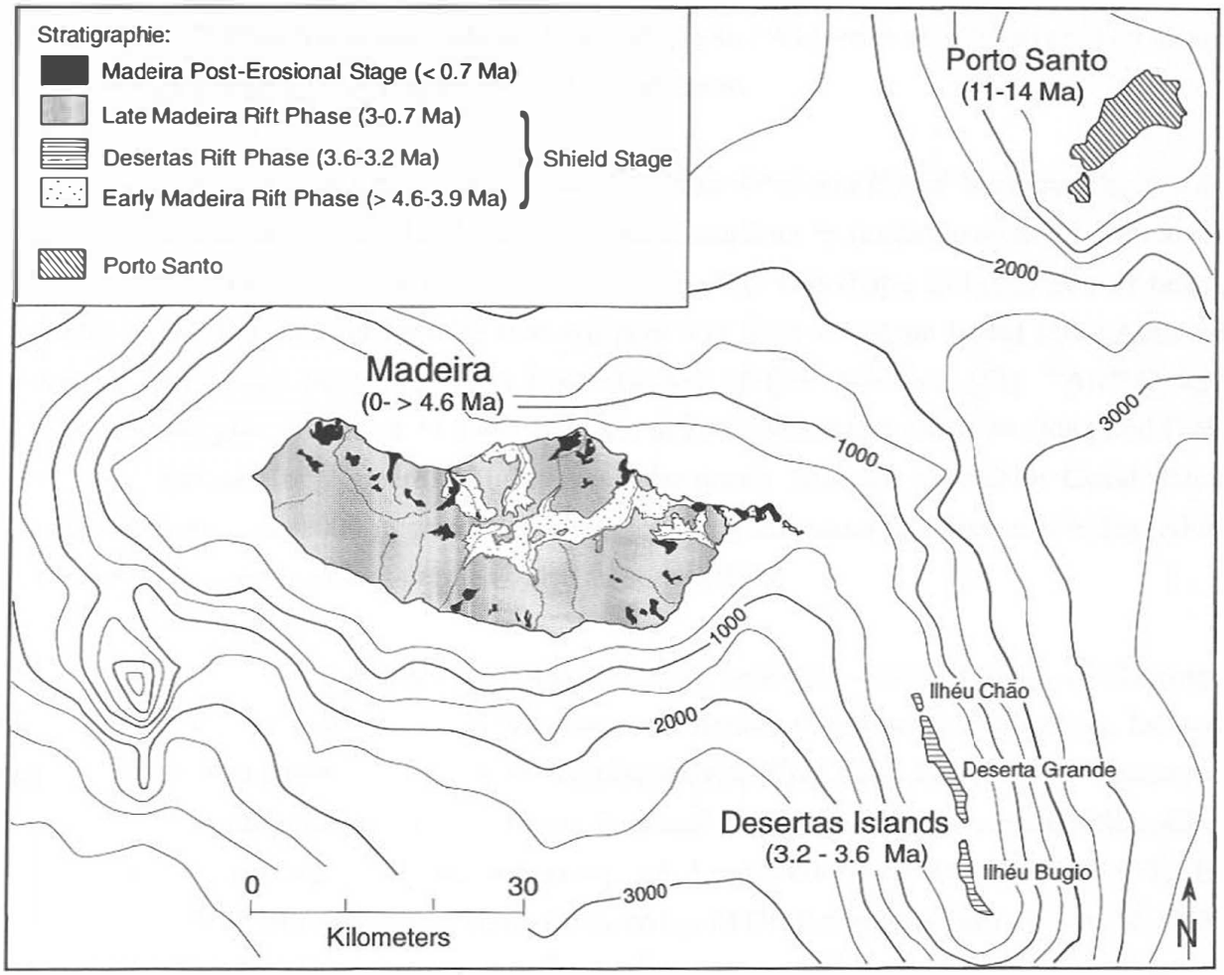

Fig. 4. Ib:

Map of the Madeira Archipelago. Geology of Madeira Island after Geldmacher et al. [14] based on Zbyszewski et al. [21]. Source of bathymetric data is the same as in Fig. 1a. Small seamount southwest of Madeira could mark the present location of the Madeira hotspot.

Previous studies of Madeira show that it consists primarily of an alkali olivine basaltic suite ranging from basanites through hawaiite and mugeartite [20, 24, 25]. In contrast to Porto Santo, evolved rocks (trachytes, rhyolites) are very minor on Madeira Island. The basaltic rocks of the Archipelago show HIMU trace element characteristics [26]. Halliday et al. [27, 28] first recognized MORB-like Sr- and Nd- isotope compositions but low $^{207}Pb/^{204}Pb$ ratios lying below the Northern Hemisphere Reference Line (negative Δ 7/4) in the volcanic rocks from Madeira Island. They proposed that enrichment of the oceanic lithosphere by carbonate or subsolidus fluid phases with extreme U/Pb ratio could produce the low Δ 7/4 signature within 200 Ma, which would not significantly affect the Sr and Nd isotopic systems due to the long half lives of ^{87}Rb (48 Ga) and ^{147}Sm (106 Ga). Hoernle et al. [29] argued for interaction of an HIMU-type plume with N-MORB-like asthenosphere and lithosphere to explain the Madeira Sr-Nd-Pb isotopic composition. Mata et al. [26] expanded this model and proposed that a mixed HIMU and enriched mantel (EM I) plume was diluted by depleted MORB source

mantle (DMM) from the asthenosphere. Thirlwall [5] and Widom et al. [30] favored an origin of the Madeira source from young recycled oceanic crust.

Ampère and Coral Patch Seamounts are located 460 km NE of Madeira (Fig. 4.1a). Bathymetric data shows that the shape of Ampère Seamount is similar to a Guyot with a flat summit that extends to 59 m below sea level [31, 32]. The shape and presence of beach cobbles on its flat summit indicate that Ampère was once an ocean island [14]. Alkaline basaltic rocks have been described from the top of the seamount [33]. $^{39}Ar/^{40}Ar$ age determinations give an age of 31.2 Ma [14]. Coral Patch Seamount forms an elongated E-W oriented ridge east of Ampère. Highly vesicular scoria near the summit of Coral Patch located at more than 1000 m water depth suggests that this seamount formerly extended to much shallower depths or possibly was also an ocean island.

Further to the northeast, Ormonde Seamount forms the eastern summit of Gorringe Bank, a 250 km long submarine ridge along the Azores-Gibraltar fracture zone, located approximately 100 km west of the Iberian continental rise (Fig. 4.1a). Except for the Ormonde summit, the remainder of Gorringe Bank is considered to be a fragment of oceanic lithosphere of early Cretaceous age [34] uplifted along the Azores-Gibraltar fracture zone [35]. In contrast, the 65-67 Ma [34, 36] volcanic rocks on top of Ormonde Seamount consist of alkali basalts and nephelinites to phonolites [37]. Taking right lateral strike-slip motion along the Azores-Gibraltar fracture zone into account [38], the Ormonde Seamount alkaline magmatism must have formed at or near the base of the Iberian continental rise. It is postulated that the 70-72 Ma old [39] alkaline magmatism at Serra de Monchique in southern Portugal also represents early activity of the Madeira hotspot [14]. The subvolcanic complex of mainly nepheline syenite bodies and low-silica lamprophyric dikes (representing the type locality for monchiquites) has been displaced eastwards from the hotspot track by right lateral strike-slip motion of ca. 200 km along the Azores-Gibralter fracture zone shortly after emplacement [38, 40].

4.3. Sampling and Petrography

An extensive sample suite has been collected from all five islands of the Madeira Archipelago (coordinates of sampling sites are given in Table A in the Appendix). The sampling sites cover all stratigraphic units of the Madeira/Desertas volcanic rift system: Early Madeira Rift Phase (EMRP), the Desertas Rift Phase (DRP) and the Late Madeira Rift Phase (LMRP) of the Shield Stage, as well as the Post-Erosional Stage (PE). Additional samples

were dredged from Ampère and Coral Patch Seamounts during the RV Poseidon 235 cruise and from Ormonde Seamount during RV Victor Hensen 97 cruise.

The major phenocryst phases in the basaltic rocks are olivine and Ti-augite. Plagioclase and Fe/Ti oxide phenocrysts are also present in some basaltic samples. The groundmass consists primarily of plagioclase needles, Ti-augite, Fe/Ti oxides, rare olivine and sometimes glass. The rare evolved rocks (benmoreites, trachytes) are dominated by plagioclase both as phenocrysts and in the groundmass. Minor phases include Fe/Ti oxide and biotite.

Samples from Ormonde Seamount include an altered phonolite (VH-97-77) with sanidine phenocrysts in a matrix dominated by anorthoclase and pseudomorphs of foids and a gneiss (VH-97-76) with alkali feldspar, quartz and biotite.

4.4 Analytical techniques

Whole rock major element compositions of all samples were determined by X-ray fluorescence (XRF) on glass pellets except for 6 glass samples measured by electron microprobe (EMP). After evaluation of thin sections and XRF data, 64 samples were selected for trace element analyses by inductively coupled plasma mass spectrometry (ICP-MS) and 58 of these for Sr, Nd, and Pb isotope ratio determinations on thermal ionization mass spectrometers (TIMS). A description of analytical methods and estimates of accuracy and precision are found in the Appendix at EPSL Online.

4.5 Results

Major and trace element composition

Major and trace element data for whole rock and glass samples from the Madeira hotspot track are presented in Tables A, B and C (in Appendix at EPSL Online). According to the classification of Le Maitre [41], basaltic samples from Madeira/Desertas range from transitional-tholeiites to basanites, whereas more evolved samples range from hawaiites to trachytes (Fig. 4.2). Only the oldest samples from Madeira (Early Rift Phase) extend to transitional tholeiites. Fresh glass from dike margins of this unit also have tholeiitic compositions (Table B). Subsequent stratigraphic units (Desertas Rift Phase and Late Madeira Rift Phase) overlap extensively, containing basanites, alkali basalts, hawaiites and rare

mugearites and benmorites. Samples of the Post-Erosional Stage fall almost exclusively within the basanite field. Despite considerable overlap, a general tendency towards greater silica-undersaturation with decreasing age can be discerned. Samples from Porto Santo and Ampère Seamount fall completely within the alkali basaltic suite and overlap primarily with late Shield Stage samples from Madeira and the Desertas.

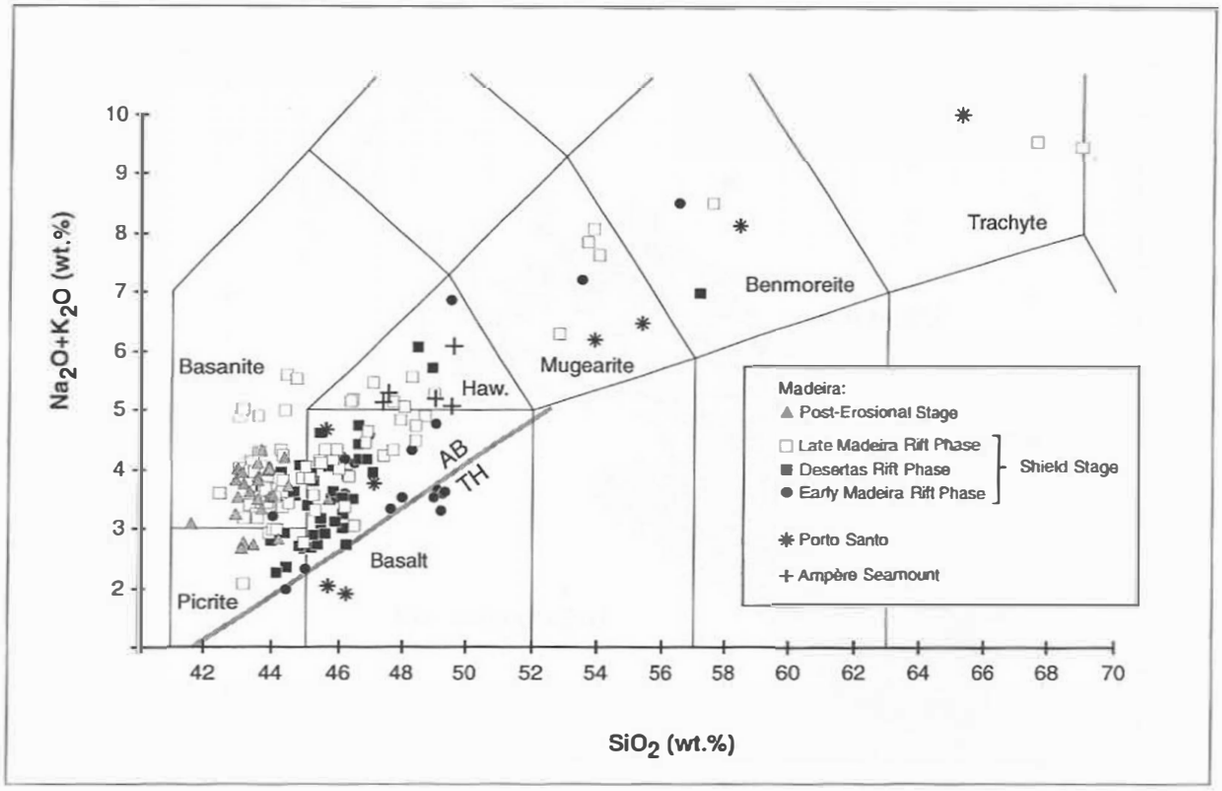

Fig. 4.2:

Total-alkalis versus SiO_2 diagram (TAS) after Le Maitre [41] with boundary between alkaline (AB) and tholeiitic (TH) basalts after Macdonald and Katsura [62]. Samples normalized to 100% on a volatile free basis. Madeira/Desertas units show a slight decrease in silica saturation with decreasing age. Only samples with less than 2.5 wt.% H_2O are shown.

The CaO/Al_2O_3 ratio, Co and Ni decrease with decreasing MgO, reflecting fractionation of olivine and clinopyroxene. FeO^T and TiO_2 show little variation until 6 wt.% MgO and then decrease consistent with late-stage fractionation of Fe/Ti oxides. P_2O_5, Sr and Zr increase until 3-4 wt.% MgO and then decrease as a result of apatite and plagioclase crystallization. SiO_2, K_2O, Na_2O, Ba, and Rb increase with decreasing MgO, illustrating that these elements behave incompatibly until advanced stages of differentiation.

Even though all stratigraphic units of the Madeira and Desertas Islands show considerable overlap, there is a general tendency to lower SiO_2 and FeO^T (Fig. 4.3) and slightly higher contents of incompatible elements and oxides, such as Na_2O, K_2O, P_2O5, Sr, Ba, Rb, Zr (in samples with > 5 wt.% MgO) with decreasing age of the units.

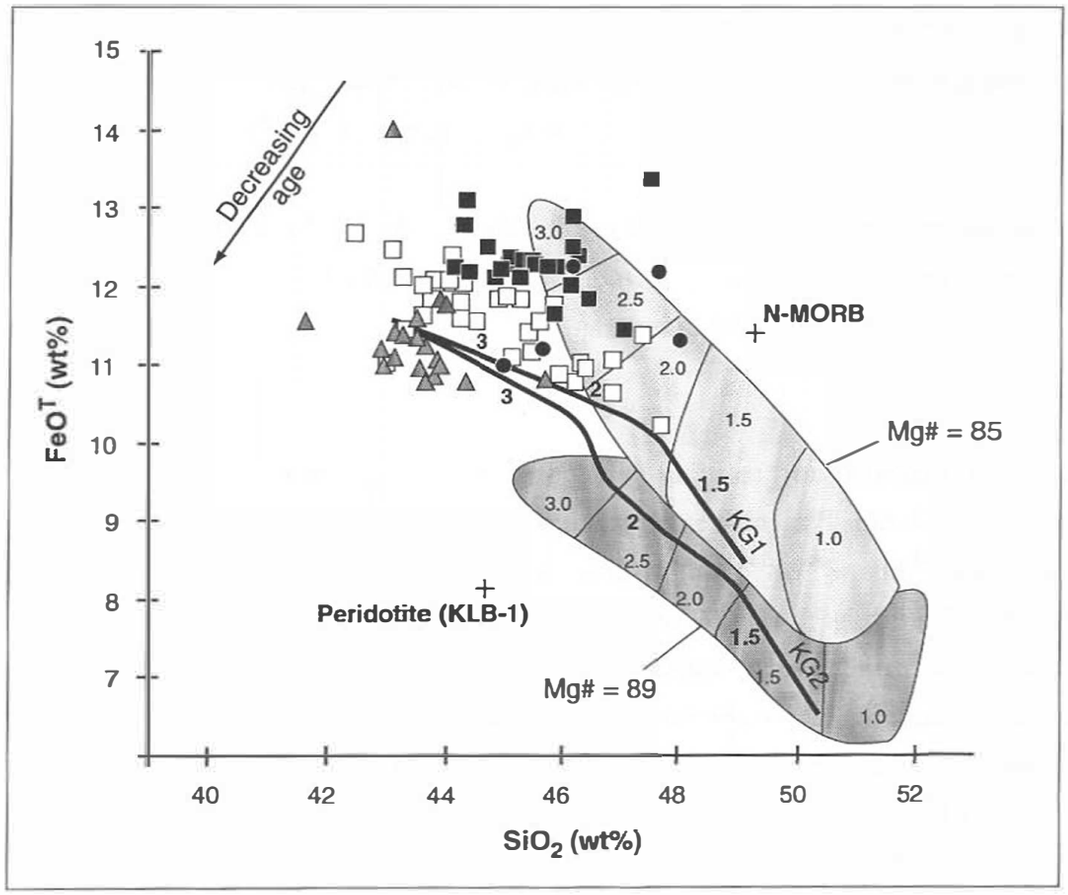

Fig. 4.3:

At a given SiO_2 content, FeO^T decreases systematically with decreasing age from the two oldest units Early Madeira Rift Phase (filled circles) and Desertas Rift Phase (filled squares) to the Late Madeira Rift Phase (open squares) to the Post-Erosional Stage lavas (shaded triangles). Also shown are the results of high pressure melting experiments: 1) fields for partial melts formed by melting peridotites KLB-1 (with Mg# = 89) and HK 66 (with Mg# = 85) at various pressures (numbers in GPa) after Hirose and Kushiro [43], and 2) curves showing melt composition for melts of a homogeneous mixtures of natural peridotite (KLB-1) and average MORB at ratios of 1:1 (KG 1) and 2:1 (KG 2) at different pressures (simplified after Kogiso et al. [44]). All numbers in GPa. Only primitive samples which have fractionated less than 10 % olivine, based on the relationship between MgO and Ni after Hart and Davis [63], are plotted.

On an incompatible element diagram (Fig. 4.4), primitive samples from all Madeira/Desertas units, Porto Santo and Ampère exhibit enriched OIB-like trace element patterns with strong enrichments in the light rare earth elements (LREE) as is illustrated by $(La/Yb)_N$ of 7-18. In particular, the rocks from the Madeira hotspot show features characteristic of the HIMU ocean islands [26], such as St. Helena, Mangaia and Tubuaii. These features include enrichment in Nb and Ta and relative depletion in K and Pb, as well as high Ce/Pb (26-59) and Nd/Pb (8-31) but relatively low K/Nb (81-188), Ba/Nb (3.3-6.8) and La/Nb (0.4-1.2) (e.g. [9, 42]. The heavy (H) REE for all samples form steep inverse trends (Fig. 4.4) and have high $(Sm/Yb)_N$ ratios of 2.4-6.1.

The gneiss sample VH-97-76 (not shown in Fig. 4.4), dredged at Ormond Seamount, clearly has continental crustal trace element compositions (characterized by large relative enrichments in Rb, Ba and Pb and large relative depletion in Nb).

Sr-Nd-Pb Isotopes

Sr-, Nd- and Pb isotope ratios of representative samples from Madeira, the Desertas, Porto Santo, Ampère, Coral Patch and Ormond are presented in Table 4.1. Although all samples have enriched HIMU-like trace element patterns, their $^{87}Sr/^{86}Sr$ and $^{143}Nd/^{144}Nd$ ratios show considerable overlap with the field for Atlantic N-MORB (Fig. 4.5). The Sr and Nd isotope data for the Madeira/Desertas volcanic rift system form a linear array and show systematic variation with age. The oldest units (Early Madeira Rift Phase and Desertas Rift Phase) have the most enriched compositions (most radiogenic Sr and least radiogenic Nd), whereas the youngest Post-Erosional Stage samples have the most depleted compositions (least radiogenic Sr and most radiogenic Nd) while Late Madeira Rift Phase samples have intermediate compositions. Porto Santo, Ampère and Coral Patch have similar compositions to the Madeira/Desertas shield stage samples. The $^{206}Pb/^{204}Pb$ ratio correlates positively with the $^{207}Pb/^{204}Pb$ and $^{208}Pb/^{204}Pb$ ratios (Fig. 4.6a,b). All Pb isotope ratios become less radiogenic with decreasing age. Porto Santo samples fall on the Madeira/Desertas trend, overlapping with fields for the Late Madeira Rift Phase and the Post-Erosional Stage. The chemical composition (in particular the major elements and Pb isotope ratios) suggests that the subaerially exposed portion of Porto Santo represents the Late Shield Stage on this island. On the $^{206}Pb/^{204}Pb$ verses $^{207}Pb/^{204}Pb$ diagram, all volcanics from the Madeira Archipelago plot beneath the NHRL, forming a positive correlation (R^2= 0.90) characterized by Δ 7/4 as low as -7.2 in the most radiogenic samples. Although Ampère and Coral Patch volcanics plot above the Madeira array, they still fall below the NHRL.

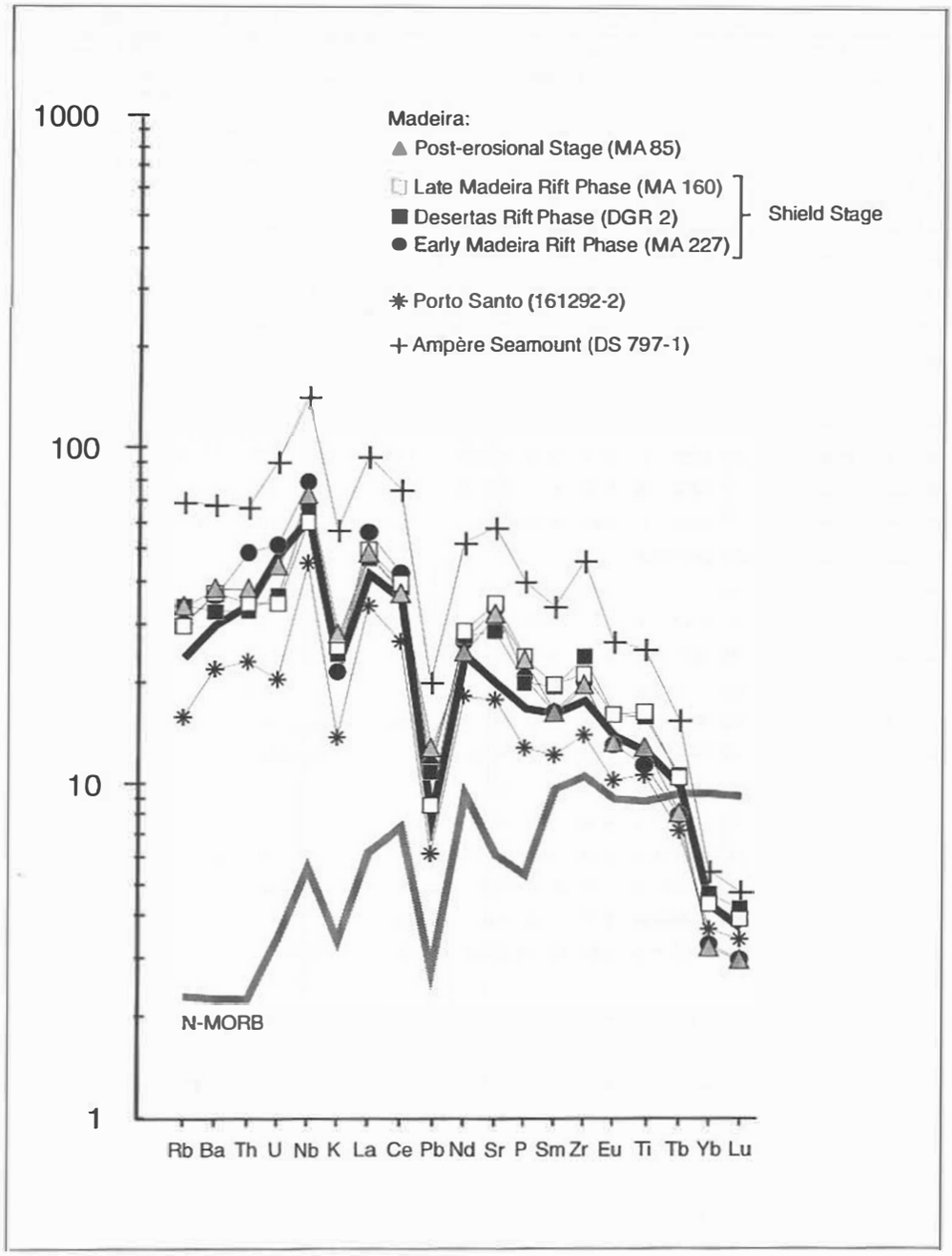

Fig. 4.4:

Multi-element diagram of representative primitive samples of each unit from Madeira/Desertas normalized to primitive mantle after Hofmann [64]. Also shown are the patterns of a representative tholeiite from Porto Santo and an alkali basalt from Ampère Seamount. As illustrated, all volcanics from the Madeira Archipelago and Ampère Seamount have similar incompatible element characteristics to HIMU basanites from St. Helena (thick black line) (sample 68 from Chaffey et al. [65]). Average N-MORB (gray line) is from Hofmann [64].

Table 4.1a: Sr and Nd isotope data from the Madeira Islands and hotspot track

Sample	Rock typ	Age	Rb** (ppm)	Sr** (ppm)	$^{87}Sr/^{86}Sr_m$	$^{87}Rb/^{86}Sr$	$^{87}Sr/^{86}Sr_{in}$	Sm** (ppm)	Nd** (ppm)	$^{143}Nd/^{144}Nd_m$	$^{147}Sm/^{144}Nd$	$^{143}Nd/^{144}Nd_{in}$	$\varepsilon Nd_{(0)}$
Madeira: Post-Erosional Stage													
MA 218a	AB	0.0	25.42	716	0.702757 (6)	0.10	0.702757	7.66	38.6	0.513120(10)	0.12	0.513120	9.41
Md191292-5*	B	0.2	23.41	707	0.702723(15)	0.10	0.702723	7.42	37.4	0.513138 (9)	0.12	0.513138	9.76
Md191292-6*	B	0.2	24.51	659	0.702666(11)	0.11	0.702666	6.92	33.6	0.513151 (7)	0.12	0.513151	10.01
Md191292-8*	B	0.2	17.20	600	0.702654(10)	0.08	0.702654	6.34	30.7	0.513189 (8)	0.12	0.513189	10.75
Md 33*	B	0.2	16.38	575	0.702648(12)	0.08	0.702648	6.03	29.0	0.513159 (7)	0.12	0.513159	10.16
MA 85	B	0.2	18.29	588	0.702658 (9)	0.09	0.702658	6.38	29.9	0.513178(10)	0.13	0.513178	10.54
MA 87	B	0.2	25.25	633	0.702706 (8)	0.11	0.702706	7.67	37.3	0.513146 (6)	0.12	0.513146	9.91
MA 88	B	0.2	18.59	543	0.702696 (9)	0.10	0.702695	6.96	33.3	0.513123 (9)	0.13	0.513123	9.46
Madeira: Late Rift Phase													
MA 115	B	0.7	32.53	1156	0.702887 (5)	0.08	0.702886	12.69	70.0	0.513004 (8)	0.11	0.513003	7.15
MA 16	H	1	32.37	642	0.702950(12)	0.15	0.702948	9.88	51.5	0.513042 (5)	0.11	0.513042	7.90
MA 17	AB	1	23.24	547	0.702841 (9)	0.12	0.702840	7.71	36.3	0.513055 (6)	0.13	0.513054	8.15
MA 23	AB	1	20.51	575	0.702914 (8)	0.10	0.702912	8.06	39.3	0.513025 (9)	0.12	0.513024	7.56
MA 53	B	1	20.22	798	0.702945(14)	0.07	0.702944	10.04	51.7	0.513040 (4)	0.12	0.513040	7.86
MA 66	B	1	18.50	703	0.702854 (9)	0.08	0.702853	9.32	46.3	0.513072 (4)	0.12	0.513071	8.47
MA 142	P	1.3	15.99	595	0.702747 (5)	0.08	0.702745	8.39	37.9	0.513115 (5)	0.13	0.513114	9.31
MA 137	B	1.5	18.95	495	0.702771 (5)	0.11	0.702769	7.00	32.2	0.513101 (8)	0.13	0.513099	9.04
MA 160	B	1.5	15.92	637	0.702783(10)	0.07	0.702782	7.66	34.4	0.513112 (8)	0.13	0.513110	9.25
MA 162	B	1.5	16.16	606	0.702819 (6)	0.08	0.702818	8.12	36.9	0.513068 (8)	0.13	0.513067	8.40
MA 75b	AB	1.8	23.24	644	0.702890 (6)	0.10	0.702887	8.38	39.7	0.513028 (6)	0.13	0.513026	7.62
Md1*	H	2	27.72	1413	0.702904(16)	0.06	0.702903	11.72	63.8	0.513065 (9)	0.11	0.513064	8.35
Md3*	B	2	23.78	670	0.702896(16)	0.10	0.702894	7.03	34.8	0.513065 (8)	0.12	0.513063	8.35
Md5*	B	2	24.49	903	0.702879(15)	0.08	0.702877	9.05	45.9	0.513048 (9)	0.12	0.513046	8.02
Md9*	M	2	42.83	1376	0.702824(14)	0.09	0.702821	13.33	72.9	0.513047 (7)	0.11	0.513046	8.00
Md12*	B	2	23.36	758	0.702863(11)	0.09	0.702860	7.74	37.5	0.513049 (7)	0.12	0.513047	8.04
Md21*	B	2	24.07	1110	0.702876(14)	0.06	0.702874	11.03	56.0	0.513055 (9)	0.12	0.513053	8.15
Madeira Early Rift Phase													
MA 227	TB	3.9	16.17	608	0.702822(10)	0.08	0.702818	6.36	31.8	0.513063 (6)	0.12	0.513060	8.33
MA 208	AB	4.1	20.15	876	0.702860 (6)	0.07	0.702857	9.72	47.5	0.513047 (8)	0.12	0.513043	8.01
MA 215	TB	4.5	11.64	427	0.702872 (5)	0.08	0.702867	6.11	25.9	0.513016 (7)	0.14	0.513012	7.41
MA 120	Th	4.7	0.59	358	0.702946(10)	0.01	0.702946	6.54	27.6	0.513018 (7)	0.14	0.513013	7.44
MA 123	Th	4.7	1.75	590	0.702876(15)	0.01	0.702875	10.86	53.9	0.513035 (8)	0.12	0.513031	7.78
MA 127	TB	4.7	12.17	728	0.702843 (8)	0.05	0.702840	9.55	44.1	0.513029 (6)	0.13	0.513025	7.68
Md13796-1	TB	4.5	14.53	479	0.702841 (6)	0.09	0.702835	6.92	29.8	0.513026 (7)	0.14	0.513022	7.59
Desertas Rift Phase													
DGR 14 (G)	P	3.3	14.20	462	0.702920 (8)	0.09	0.702915	6.07	26.9	0.513024 (9)	0.14	0.513021	7.56
K 11 (B)	TB	3.3	14.50	486	0.702918 (7)	0.09	0.702914	6.90	30.6	0.513033 (6)	0.14	0.513030	7.73
DGR 47 (G)	B	3.4	23.31	716	0.702979 (7)	0.09	0.702975	11.37	53.3	0.513007 (4)	0.13	0.513004	7.23
DGR 2 (G)	AB	3.4	18.24	526	0.702890 (6)	0.06	0.702885	7.52	33.2	0.513046 (4)	0.12	0.513043	7.99
K 18 (C)	P	3.5	15.25	737	0.702967 (7)	0.04	0.702964	13.85	67.4	0.513010 (5)	0.12	0.513007	7.29
K 22 (C)	AB	3.6	7.71	509	0.702984(10)	0.10	0.702982	6.31	31.5	0.513001 (9)	0.14	0.512998	7.12
K 26 (G)	P	3.6	17.84	624	0.702990 (6)	0.08	0.702986	9.21	41.5	0.513009(10)	0.13	0.513005	7.26
Porto Santo													
K 43	B	11	21.81	845	0.702843 (5)	0.07	0.702831	12.21	59.2	0.513059 (9)	0.12	0.513050	8.30
K 45	B	11.5	n.d.	n.d.	0.702923 (7)	n.d.	n.d.	n.d.	n.d.	0.513065 (6)	n.d.	n.d.	n.d.
K 67	AB	11	14.77	788	0.702921 (6)	0.05	0.702912	9.70	47.0	0.513031(10)	0.12	0.513022	7.77
PS161292-2*	Th	12	8.44	329	0.702830(11)	0.07	0.702818	4.76	21.9	0.513085 (9)	0.13	0.513075	8.82
PS 2*	Be	12	42.40	1178	0.702960 (9)	0.10	0.702942	13.96	81.1	0.513044 (7)	0.10	0.513036	8.06
PS 3*	AB	12	18.33	1266	0.703039(16)	0.04	0.703032	12.21	64.3	0.512979 (8)	0.11	0.512970	6.15
PS 4*	B	12	9.71	847	0.702938(14)	0.03	0.702932	8.11	40.9	0.513019 (8)	0.12	0.513010	7.55

Sample	Rock typ	Age	Rb** (ppm)	Sr** (ppm)	$^{87}Sr/^{86}Sr_m$	$^{87}Rb/^{86}Sr$	$^{87}Sr/^{86}Sr_{in}$	Sm** (ppm)	Nd** (ppm)	$^{143}Nd/^{144}Nd_m$	$^{147}Sm/^{144}Nd$	$^{143}Nd/^{144}Nd_{in}$	$\varepsilon Nd_{(t)}$
PS 36*	AB	12	16.22	611	0.702869(17)	0.08	0.702856	7.49	37.8	0.513086 (6)	0.12	0.513077	8.86
PS 37.1*	T	12	49.82	829	0.702951(12)	0.17	0.702921	13.10	79.0	0.513007(12)	0.10	0.512999	7.35
PS 41*	M	12	33.78	1032	0.702840(12)	0.09	0.702823	11.65	63.7	0.513074 (9)	0.11	0.513065	8.64
PS 53*	M	13	23.79	1149	0.702841(12)	0.06	0.702830	12.28	66.5	0.513084 (8)	0.11	0.513075	8.84
K 55	AB	13.8	17.59	651	0.702882 (6)	0.08	0.702866	10.31	51.1	0.513036 (9)	0.12	0.513025	7.90
Coral Patch Seamount													
DS 790-1	H	31	6.67	411	0.702948 (7)	0.048	0.702927	9.29	43.9	0.512980(10)	0.13	0.512954	6.95
Ampère Seamount													
DS797-1b	H	31	37.25	1063	0.703005(10)	0.10	0.702961	13.12	62.9	0.512969 (5)	0.13	0.512944	6.74
DS-797-2	H	31	25.23	878	0.702990 (6)	0.08	0.702953	13.84	63.7	0.512957 (5)	0.13	0.512930	6.48
DS-797-7	H	31	38.98	992	0.702984 (7)	0.11	0.702934	13.24	63.8	0.512972 (6)	0.12	0.512946	6.79
VH-97-103	H	31	52.43	926	0.702972 (7)	0.16	0.702899	11.17	53.6	0.512991(10)	0.12	0.512965	7.16
Ormonde Seamount													
VH-97-77	Ph	66	53.29	209	0.708498 (6)	0.88	0.707808	4.40	15.3	0.512936(55)	0.07	0.512861	6.00
VH-97-76	Gn	?	95.32	315	0.726341 (6)	0.74		0.99	8.4	0.510860 (6)	0.17		

* = Analyses at UCSB; ** = ICP-MS data; Rock type: AB= alkali basalt, B= basaite, H= hawaiite, P=picrite, M= mugeratite, TB= transitional basalt, Th= tholeiite, Be= benmoreite, Ph= phonolite, Gn= gneiss, Age data from Geldmacher et al. (2000); Deserta Rift Phase samples from: G = Deserta Grande, B = Deserta Bugio, C = Ilhéo Chão

Table 4.1b: Pb isotope data from the Madeira Islands and hotspot track

Sample	Rock typ	Age	U** (ppm)	Th** (ppm)	Pb** (ppm)	$^{206}Pb/^{204}Pb_m$	$^{207}Pb/^{204}Pb_m$	$^{208}Pb/^{204}Pb_m$	μ	κ	$^{206}Pb/^{204}Pb_{in}$	$^{207}Pb/^{204}Pb_{in}$	$^{208}Pb/^{204}Pb_{in}$	Δ7/4
Madeira: Post-Erosional Stage														
MA 218a	AB	0.0	1.51	5.56	3.01	18.967 (3)	15.515 (3)	38.595 (8)	32.17	3.80	18.967	15.515	38.595	-3.2
Md191292-5*	B	0.2	1.17	4.38	2.94	18.885 (5)	15.517 (4)	38.543(10)	25.43	3.87	18.884	15.517	38.542	-2.1
Md191292-6*	B	0.2	0.91	3.40	2.05	18.840 (9)	15.523 (7)	38.468(17)	28.44	3.85	18.839	15.523	38.467	-1.0
Md191292-8*	B	0.2	0.71	2.64	1.42	18.796(15)	15.514(11)	38.394(29)	31.87	3.82	18.795	15.514	38.393	-1.4
Md 33*	B	0.2	0.72	2.57	1.45	18.779 (3)	15.505 (3)	38.375 (9)	31.31	3.71	18.778	15.505	38.374	-2.2
MA 85	B	0.2	0.91	3.14	2.27	18.731 (2)	15.502 (2)	38.327 (5)	25.46	3.56	18.731	15.502	38.326	-2.0
MA 87	B	0.2	1.31	4.58	2.22	18.881 (3)	15.505 (2)	38.458 (7)	37.79	3.61	18.880	15.505	38.456	-3.3
MA 88	B	0.2	1.05	3.84	1.91	18.876 (2)	15.505 (2)	38.467 (4)	35.03	3.78	18.875	15.505	38.465	-3.2
Madeira: Late Rift Phase														
MA 115	B	0.74	2.47	9.30	2.91	19.787 (2)	15.564 (2)	39.447 (4)	55.65	3.89	19.781	15.564	39.439	-7.2
MA 16	H	1	1.60	7.61	3.47	19.441 (1)	15.558 (1)	39.134 (3)	29.93	4.92	19.436	15.558	39.127	-4.0
MA 17	AB	1	1.24	4.39	2.25	19.304 (2)	15.543 (1)	38.970 (3)	35.69	3.65	19.298	15.543	38.963	-4.0
MA 23	AB	1	1.43	5.32	2.53	19.407 (2)	15.548 (1)	39.077 (3)	36.63	3.85	19.401	15.548	39.070	-4.7
MA 53	B	1	1.88	6.79	2.79	19.304 (1)	15.544 (1)	38.997 (2)	43.55	3.74	19.298	15.544	38.989	-3.9
MA 66	B	1	1.38	5.46	2.24	19.092 (2)	15.536 (1)	38.780 (3)	39.56	4.09	19.086	15.535	38.772	-2.5
MA 142	P	1.3	0.93	3.38	1.82	18.935 (3)	15.512 (3)	38.543 (7)	32.66	3.76	18.928	15.511	38.535	-3.2
MA 137	B	1.5	0.83	3.01	1.56	18.920 (3)	15.513 (2)	38.534 (6)	33.87	3.75	18.912	15.512	38.524	-2.9
MA 160	B	1.5	0.71	2.81	1.52	18.996 (3)	15.524 (2)	38.631 (6)	29.90	4.09	18.989	15.524	38.622	-2.6
MA 162	B	1.5	0.92	3.53	1.83	19.133 (3)	15.520 (2)	38.756 (6)	32.21	3.97	19.125	15.520	38.747	-4.5
MA 75b	AB	1.8	1.19	4.06	2.13	19.600 (2)	15.560 (1)	39.277 (4)	36.48	3.51	19.590	15.560	39.266	-5.5
Md1*	H	2	1.30	6.92	3.56	19.263 (2)	15.535 (2)	38.927 (5)	23.54	5.51	19.255	15.535	38.914	-4.4
Md3*	B	2	1.00	3.87	2.49	19.420 (1)	15.542 (1)	39.072 (3)	25.92	4.01	19.412	15.542	39.062	-5.4
Md5*	B	2	0.88	3.98	2.34	19.032 (3)	15.533 (2)	38.730 (6)	24.14	4.68	19.025	15.533	38.719	-2.1
Md9*	M	2	1.71	6.53	4.08	19.400 (2)	15.543 (2)	39.051 (4)	27.18	3.94	19.391	15.543	39.041	-5.1
Md12*	B	2	0.80	3.25	4.44	19.347 (4)	15.541 (4)	39.011(12)	11.62	4.21	19.343	15.541	39.006	-4.7
Md21*	B	2	1.09	4.65	3.50	19.334 (2)	15.546 (1)	39.010 (4)	20.10	4.42	19.328	15.546	39.001	-4.1

Sample	Rock typ	Age	U** (ppm)	Th** (ppm)	Pb** (ppm)	$^{206}Pb/^{204}Pb_m$		$^{207}Pb/^{204}Pb_m$		$^{208}Pb/^{204}Pb_m$		μ	κ	$^{206}Pb/^{204}Pb_o$	$^{207}Pb/^{204}Pb_o$	$^{208}Pb/^{204}Pb_o$	Δ 7/4
Madeira Early Rift Phase																	
MA 227	TB	3.9	1.05	4.03	2.00	19.059	(1)	15.528	(1)	38.773	(3)	33.95	3.95	19.039	15.527	38.747	-2.9
MA 208	AB	4.1	1.27	5.45	2.44	19.170	(3)	15.524	(2)	38.840	(6)	33.50	4.43	19.149	15.523	38.810	-4.5
MA 215	TB	4.5	0.53	1.96	1.18	19.789	(3)	15.576	(3)	39.471	(7)	29.41	3.82	19.768	15.575	39.446	-6.0
MA 120	Th	4.7	1.17	3.27	1.29	19.468	(2)	15.556	(2)	39.123	(4)	59.28	2.88	19.425	15.554	39.083	-4.5
MA 123	Th	4.7	0.78	3.00	1.61	19.515	(2)	15.563	(1)	39.187	(3)	31.36	3.99	19.493	15.562	39.158	-4.4
MA 127	TB	4.7	0.63	2.33	1.48	19.524	(2)	15.567	(2)	39.201	(4)	27.43	3.85	19.504	15.566	39.176	-4.1
Md13796-1	TB	4.5	0.72	2.45	1.75	19.570	(2)	15.567	(2)	39.238	(6)	26.99	3.50	19.551	15.567	39.217	-4.5
Desertas Rift Phase																	
DGR 14 (G)	P	3.3	0.67	2.31	1.34	19.620	(3)	15.556	(2)	39.278	(6)	32.76	3.55	19.603	15.555	39.259	-6.2
K 11 (B)	TB	3.3	0.64	2.27	1.50	19.533	(2)	15.549	(2)	39.176	(5)	27.55	3.69	19.519	15.549	39.160	-5.9
DGR 47 (G)	B	3.4	1.07	3.91	2.09	19.680	(2)	15.566	(1)	39.388	(3)	33.54	3.76	19.662	15.565	39.366	-5.8
DGR 2 (G)	AB	3.4	0.74	2.70	1.89	19.521	(2)	15.561	(2)	39.206	(6)	37.45	3.96	19.508	15.560	39.190	-3.7
K 18 (C)	P	3.5	1.36	5.22	2.35	19.348	(2)	15.551	(2)	39.082	(4)	41.92	4.06	19.328	15.551	39.056	-2.9
K 22 (C)	AB	3.6	1.03	4.04	1.59	19.353	(2)	15.560	(1)	39.134	(3)	25.41	3.77	19.330	15.559	39.103	-4.6
K 26 (G)	P	3.6	0.88	3.23	1.69	19.651	(2)	15.570	(2)	39.358	(4)	34.27	3.77	19.632	15.569	39.335	-5.1
Porto Santo																	
K 43	B	11	1.53	5.65	2.63	19.099	(4)	15.528	(3)	38.766	(8)	37.28	3.83	19.036	15.525	38.688	-3.3
K 45	B	11.5	n.d.	n.d.	n.d.	19.065	(5)	15.538	(4)	38.723	(10)	n.d.	n.d.	n.d.	n.d.	n.d.	-2.0
K 67	AB	11	1.26	5.30	2.53	18.957	(2)	15.523	(2)	38.658	(4)	31.84	4.36	18.902	15.521	38.582	-2.3
PS161292-2*	Th	12	0.42	1.90	1.10	19.261	(1)	15.552	(1)	38.908	(2)	24.50	4.72	19.215	15.549	38.839	-2.7
PS 2*	Be	12	1.90	8.99	4.73	18.939	(1)	15.512	(1)	38.610	(3)	25.67	4.90	18.891	15.510	38.536	-3.2
PS 3*	AB	12	1.46	6.77	2.45	19.241	(3)	15.538	(2)	38.960	(6)	38.56	4.79	19.169	15.535	38.850	-3.9
PS 4*	B	12	1.09	4.72	1.80	19.316	(3)	15.547	(3)	39.030	(7)	39.25	4.48	19.243	15.544	38.926	-3.8
PS 36*	AB	12	0.95	3.85	2.21	19.296	(2)	15.542	(2)	38.930	(5)	27.88	4.17	19.244	15.539	38.861	-4.1
PS 37.1*	Th	12	2.23	14.26	6.86	19.330	(2)	15.546	(1)	39.010	(3)	21.06	6.60	19.290	15.544	38.928	-4.0
PS 41*	M	12	1.64	6.00	3.55	18.878	(2)	15.508	(2)	38.487	(5)	29.57	3.77	18.820	15.505	38.487	-3.0
PS 53*	M	13	1.40	6.77	3.98	18.851	(2)	15.508	(2)	38.478	(4)	22.46	4.99	18.806	15.506	38.478	-2.7
K 55	AB	13.8	1.43	5.47	2.45	19.282	(2)	15.541	(2)	38.926	(4)	37.62	3.95	19.201	15.537	38.825	-4.0
Coral Patch Seamount																	
DS 790-1	H	31	1.81	3.11	1.38	19.478	(3)	15.577	(3)	39.119	(6)	84.86	1.78	19.069	15.558	38.887	-2.5
Ampère Seamount																	
DS797-1b	H	31	1.87	5.51	3.57	19.655	(2)	15.590	(2)	39.397	(4)	34.24	3.05	19.490	15.583	39.237	-3.1
DS-797-2	H	31	2.40	4.86	2.61	19.763	(3)	15.593	(3)	39.433	(7)	60.20	2.09	19.473	15.580	39.240	-4.0
DS-797-7	H	31	2.48	6.42	2.59	19.637	(3)	15.599	(2)	39.414	(5)	62.60	2.68	19.336	15.585	39.157	-2.0
VH-97-103	H	31	2.16	5.29	2.10	19.614	(6)	15.601	(5)	39.419	(12)	67.32	2.53	19.290	15.586	39.158	-1.6
Ormonde Seamount																	
VH-97-77	Ph	66	2.70	0.37	2.62	19.415	(2)	15.619	(2)	38.253	(4)	0.52	5.18	18.733	15.586	38.223	12.9
VH-97-76	Gn	?	0.13	0.67	14.92	15.749	(4)	15.327	(4)	35.535	(10)	66.29	0.14				2.3

* = Analyses at UCSB; ** = ICP-MS data; Rock type: AB= alkali basalt, B= basaite, H= hawaiite, P=picrite, M= mugeratite, TB= transitional basalt, Th= tholeiite, Be= benmoreite, Ph= phonolite, Gn= gneiss. Age data from Geldmacher et al. (2000); Desertas Rift Phase samples from: G = Deserta Grande, B = Deserta Bugio, C = Ilhéo Chão

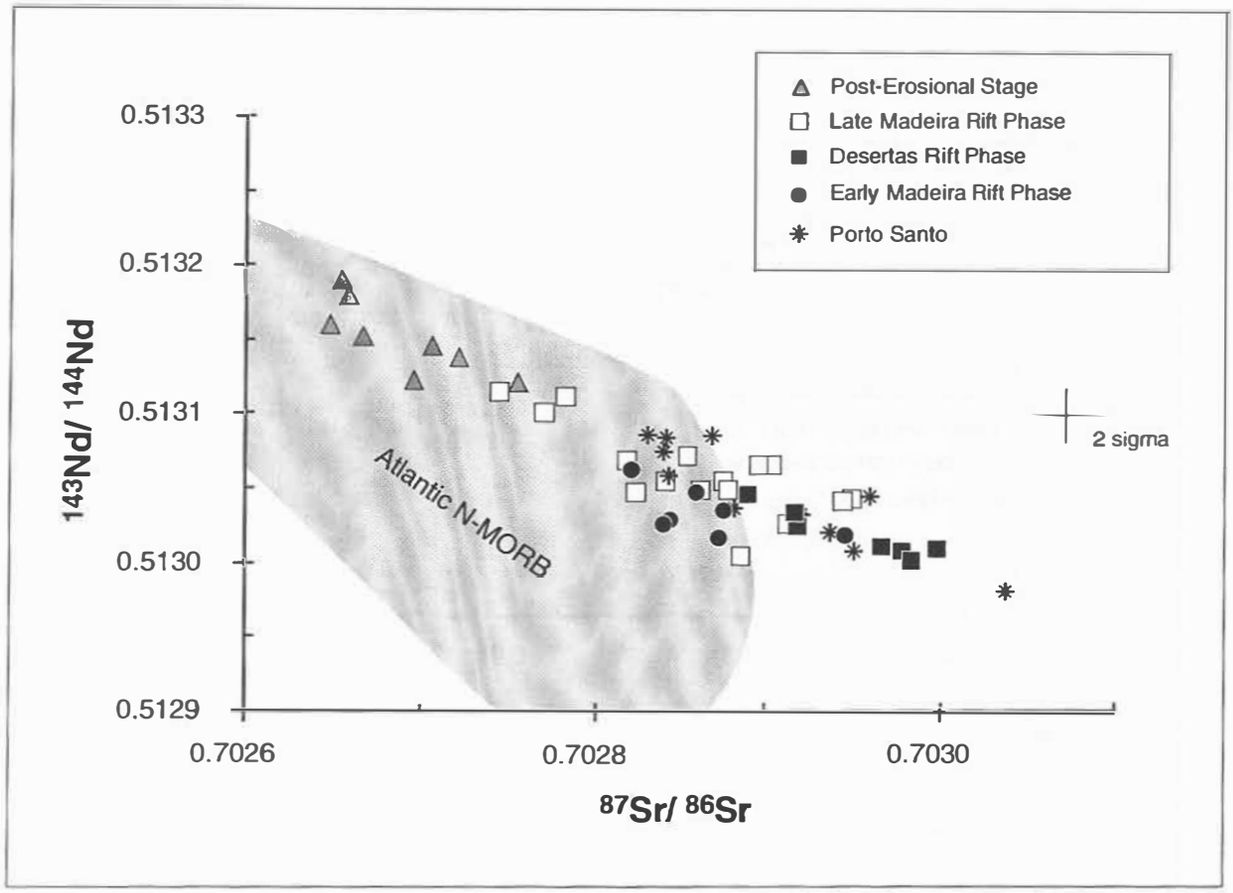

Fig. 4.5:
$^{87}Sr/^{86}Sr$ versus $^{143}Nd/^{144}Nd$ isotope correlation diagram for volcanics from the Madeira Archipelago. Samples show considerable overlap with the field for Atlantic N-MORB. The early Shield Stage samples on Madeira (Early Madeira Rift Phase, Desertas Rift Phase) have the most enriched composition (most radiogenic Sr and least radiogenic Nd) whereas the Post-Erosional Stage volcanics have the most depleted composition (least radiogeneic Sr but most radiogenic Nd). Data for Atlantic N-MORB between 10°N and 30°N are from [66-68].

4.6 Discussion

Origin of geochemical variations in the Madeira/Desertas magma source

High pressure melt experiments show that variations in SiO_2 and FeO^T in primitive rocks are likely to reflect differences in depths of melting and source composition [43, 44]. The addition of MORB to peridotitic source material results in elevated FeO^T contents of partial melts at all pressures [44]. This relationship is clearly seen on a plot of SiO_2 verses FeO^T (Fig. 4.3). The compositional fields of partial melts from a pure mantle peridotite with Mg# = 89.6 (KLB-1) form an inverse array between SiO_2 and FeO^T at various pressures. Melt

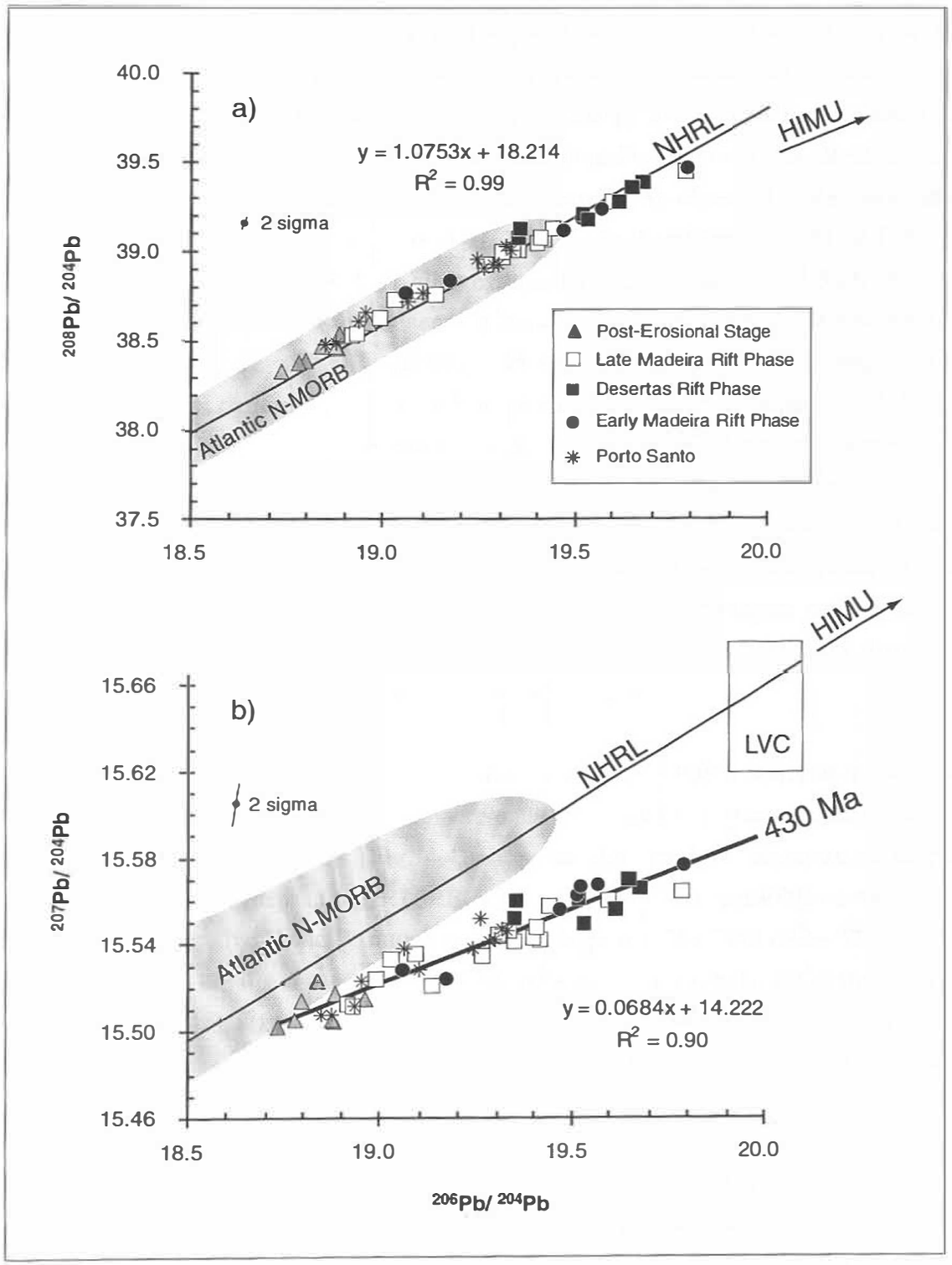

Fig. 4.6:

Pb isotope ratios for Madeira Archipelago samples. In the $^{206}Pb/^{204}Pb$ versus $^{207}Pb/^{204}Pb$ diagram, the samples form a linear array below the Northern Hemisphere Reference Line (NHRL). The positive correlation formed by the data (R^2=0.90) cannot be explained by mixing depleted MORB-source mantle (DMM) with HIMU-mantle, since the basalts with the most radiogenic Pb have Δ7/4 (deviation from the NHRL) as low as – 7.2. For data sources for Atlantic N-MORB see Fig. 5. Field for LVC from [51].

compositions of a more fertile peridotite with Mg#= 85 (HK-66) also form an inverse array but yield higher FeO^T contents at all pressures for a given SiO_2 content [43]. A similar effect is reported for homogeneous mixtures of peridotite (KLB-1) and N-MORB (1:1 (KG 1) and 2:1 (KG 2) mixtures of KLB-1 to N-MORB are shown in Fig. 4.3) [44]. In all experiments, SiO_2 decreases and FeO^T increases with increasing pressure. As observed in the experiments of Hirose and Kushiro [43] and Kogiso et al. [44], melts from more fertile or FeO^T-rich peridotite have slightly higher FeO^T at all pressures for a given amount of SiO_2. Primitive volcanic rocks from the Madeira and Desertas Islands have SiO_2 and FeO^T contents consistent with formation at pressures ≥ 2 GPa (depths ≥ 65 km) to pressures > 3 GPa (depths > 100 km). The steep HREE patterns (Fig. 4.4) indicate melt generation at pressures ≥ 1.3-1.7 GPa (depths ≥ 40-50 km) if pyroxenite was present in the source [45]. Different stratigraphic units on Madeira and the Desertas form inverse arrays which show decreasing FeO^T and SiO_2 with decreasing age, consistent with decreasing fertility of the source beneath Madeira over the last ~ 5 Ma. In conclusion, the major element variations of the primitive samples appear to reflect the presence of an Fe-rich, most likely MORB component, in the magma source that may represent recycled upper (basaltic) oceanic crust. The role of this component diminished during the evolution of the Madeira/Desertas magmatic system.

Incompatible trace element data also supports recycled MORB material in the source of Madeira/Desertas (and Porto Santo, Ampère and Coral Patch) magmas. Primitive mantle-normalized trace element patterns (Fig. 4.4) show the characteristic signature of recycled oceanic crust, i. e. enrichment in light (L)REE and other highly incompatible elements, peak at Nb and Ta, and negative K and Pb anomalies [7, 9]. High μ ($^{238}U/^{204}Pb$) ratios (20-43) of the Madeira archipelago basalts also point toward the presence of recycled crust in the source. It is unlikely that these high μ ratios, especially in large-degree tholeiitic melts, can be generated through melting processes alone and therefore are likely to at least in part reflect high source ratios.

If radiogenic Pb isotope ratios and enrichment in FeO^T and SiO_2 content indicate recycled oceanic crust in the magma source, then these parameters should correlate positively. To assess the relative FeO^T enrichment, we have calculated an "Fe-Si enrichment index" based on the vertical deviation for each sample from the KG1 curve (1:1 KLB-1/ N-MORB mixture) determined in the melting experiments of Kogiso et al. [44] shown in Fig. 4.3. This index plotted against $^{206}Pb/^{204}Pb$ (Fig. 4.7) shows a remarkably good positive correlation providing additional strong evidence for recycled MORB material in the magma source of the Madeira and Desertas Islands. Furthermore, it can be seen that with decreasing age of the stratigraphic units, the volcanic rocks become less radiogenic in Pb (Fig. 4.6) and less

enriched in FeO^T (Fig. 4.3 and 4.7), presumably reflecting progressive depletion of recycled altered oceanic crust in the magma source with decreasing age.

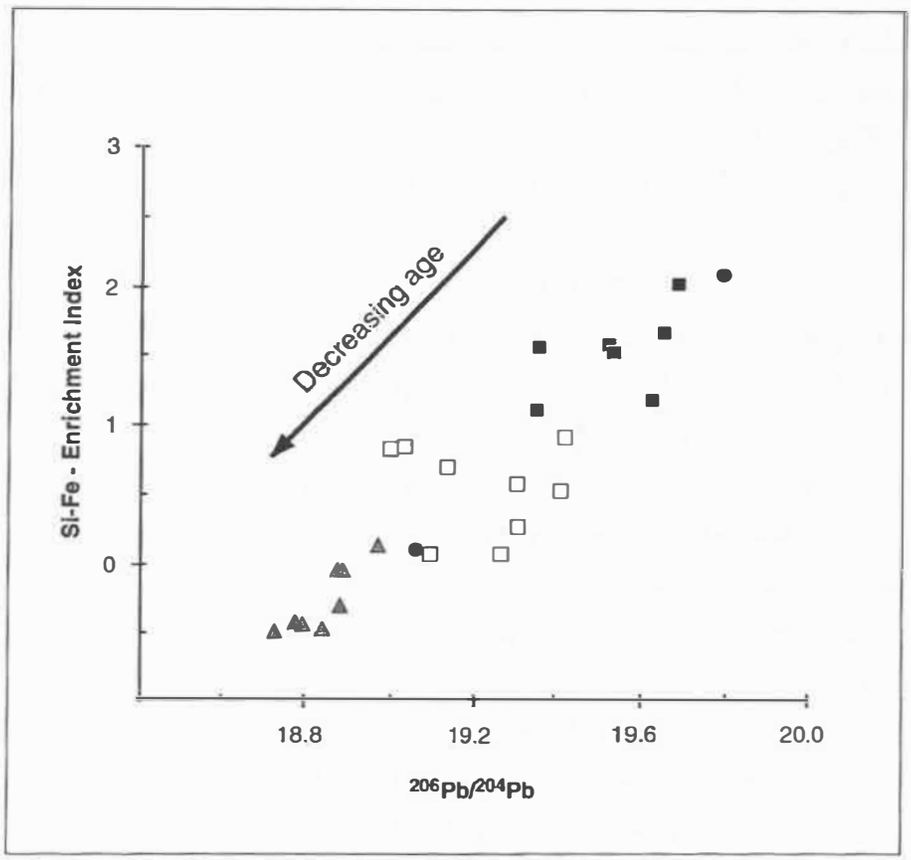

Fig. 4.7:
Si-Fe-Enrichment Index (vertical deviation of each sample from the KG 1 melt composition line shown in Fig. 4) and $^{206}Pb/^{204}Pb$ isotope ratio correlate positively and both decrease with decreasing age of the units. Symbols as in Fig. 7.

Evidence for Paleozoic (≤ 0.5 Ga) recycled oceanic crust in the Madeira source

Lead isotope ratios between N-MORB and endmember HIMU could reflect either mixing between MORB and HIMU or younger recycling ages. On both Pb isotope correlation diagrams (Fig. 4.6), the Madeira archipelago rocks form excellent positive linear correlations indicative of two component mixing. Atlantic N-MORB could serve as the less radiogenic component; however, endmember HIMU ocean islands do not lie on the extensions of the Madeira trends on either Pb isotope diagram, ruling out mixing of N-MORB and endmember HIMU to explain the Madeira Pb isotope data.

The low $^{207}Pb/^{204}Pb$ ratios at a given $^{206}Pb/^{204}Pb$ ratio relative to the NHRL (e.g. Δ 7/4 as low as – 7.2) and Atlantic N-MORB suggest relatively recent increase in μ of the Madeira

source [27, 28]. The slope of the correlation ($y = 0.0684\ x + 14.222$, $r^2 = 0.90$) on the $^{206}Pb/^{204}Pb$ verses $^{207}Pb/^{204}Pb$ isotope diagram correlates with an age of 430 Ma, which serves as a minimum age for the ancient oceanic crust. This age possibly reflects the age of hydrothermal activity (i.e. increase in μ) near the ancient mid ocean ridge at which the crust was formed. Assuming that the MORB source has evolved with a μ of 9 over the last 430 Ma, then the Madeira array could have been generated from MORB crust with initial $^{206}Pb/^{204}Pb$ = 17.68 and $^{207}Pb/^{204}Pb$ = 15.44 and μ's ranging from 15 in the post-erosional basanite source to 32 in the early shield transitional tholeiite source. The presence of young recycled oceanic crust in the Madeira magma source is also consistent with the Sr and Nd isotopic composition (Fig. 4.5) which only varies slightly from N-MORB. This reflects the larger half-lives of ^{87}Rb (48 Ga) and ^{147}Sm (106 Ga) compared to those of U (^{238}U = 4.47 Ga, ^{235}U = 0.71 Ga) and Th (^{232}Th = 14 Ga). The well-correlated isotopic arrays of the Madeira volcanic rocks on $^{87}Sr/^{86}Sr$ vs. $^{143}Nd/^{144}Nd$ (Fig. 4.5) and the $^{206}Pb/^{204}Pb$ vs. $^{208}Pb/^{204}Pb$ (Fig. 4.6), $^{143}Nd/^{144}Nd$ (Fig. 4.8) and $^{87}Sr/^{86}Sr$ (not shown) diagrams, however, require either 1) coupled fractionation of parent/daughter ratios for the different systems, or 2) mixing of at least two components. Since the parent/daughter ratios have been fractionated during melting to form the large range in mafic Madeira rock types, it is difficult to assess directly the parent/daughter ratios in the source. Although sea floor alteration/metamorphism are likely to affect the $^{87}Sr/^{86}Sr$, Rb/Sr, U/Pb and Th/Pb ratios [e.g. 6], it is unlikely that alteration/metamorphism or processes acting during subduction will affect the Sm/Nd and $^{143}Nd/^{144}Nd$ ratios. Therefore, it is difficult to explain the correlations between $^{87}Sr/^{86}Sr$ and $^{143}Nd/^{144}Nd$ (Fig. 4.5) and $^{206}Pb/^{204}Pb$ vs. $^{143}Nd/^{144}Nd$ (Fig. 4.8) as a result of correlated parent/daughter ratios in a source which originally had uniform isotope ratios.

Below we present two possible scenarios for generating the Madeira Archipelago arrays by two component mixing of 1) a shield-type component with radiogenic Pb and Sr but unradiogenic Nd, very low Δ 7/4 ($\leq$ -7.2) and enriched FeO^T and SiO_2 with 2) a post-erosional component having unradiogenic Pb and Sr but radiogenic Nd, Δ 7/4 $\geq$ 0 and relative depletion of FeO^T. In both scenarios, the shield endmember most likely reflects altered recycled oceanic crust which due to its very low Δ 7/4 must be young ($\leq$ 500 Ma; e. g., Thirlwall [5]). The post-erosional endmember could either reflect 1) lower, less-altered portions of the oceanic crust, for example gabbro or ultramafic cumulates [8], or 2) depleted MORB-source mantle (DMM) in the asthenosphere or lithosphere.

The OIB incompatible element characteristics (in particular HIMU-type) of the post-erosional basanites, which overlap with those of the Early Shield Stage basalts, however, are not consistent with this endmember being DMM. In addition, three samples from the Post-

Erosional Stage have $^{187}Os/^{188}Os$ (0.139- 0.144) considerably higher than N-MORB (< 0.125) and are interpreted to reflect the presence of Paleozoic oceanic crust in the source of these post-erosional volcanic rocks [30]. Therefore, the post-erosional endmember also appears to represent young recycled oceanic crust and not DMM.

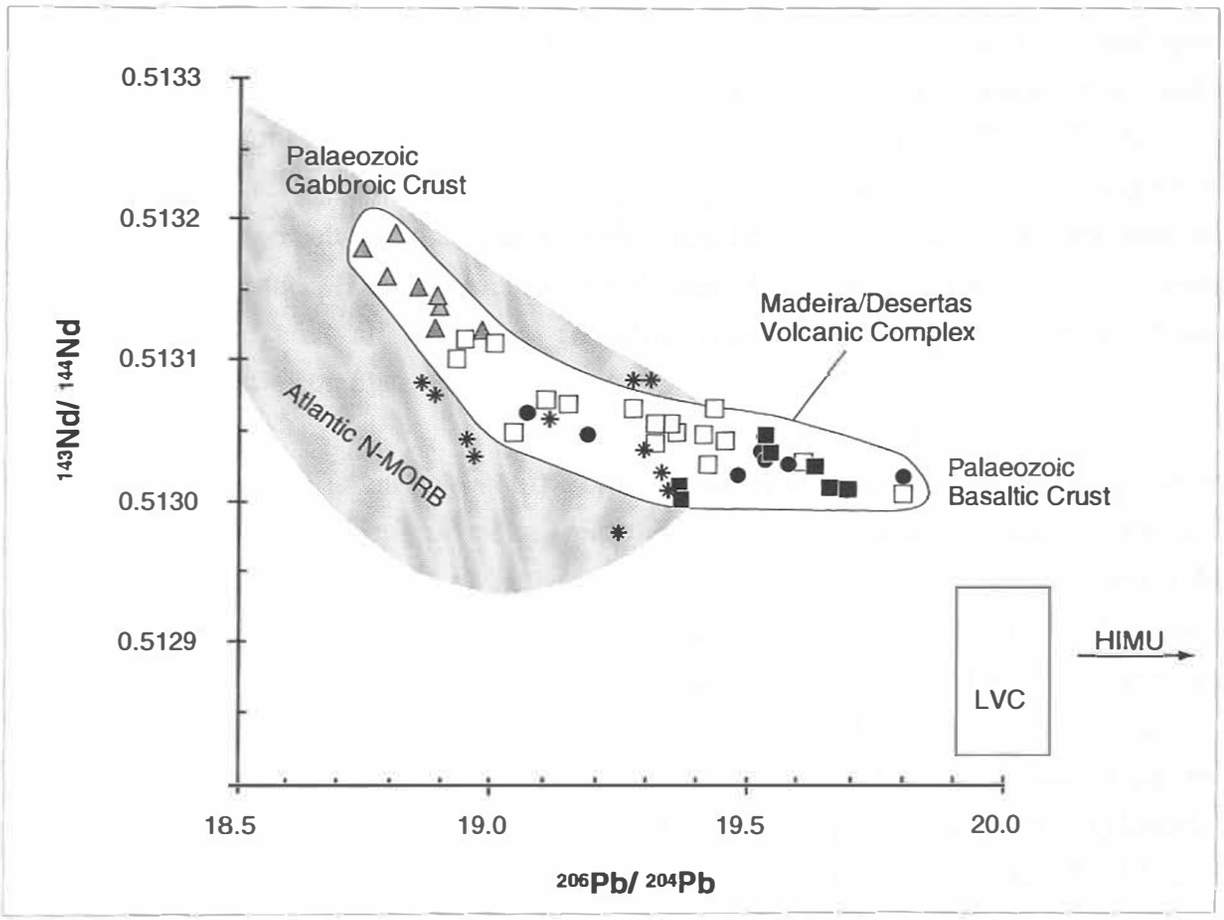

Fig. 4.8:

$^{206}Pb/^{204}Pb$ versus $^{143}Nd/^{144}Nd$ isotope ratios for samples from the Madeira Archipelago, in particular the Madeira/Desertas volcanic complex, correlate negatively forming a concave up hyperbola. The correlation could reflect mixing of melts from 1) Paleozoic basaltic ocean crust (with radiogenic Pb but unradiogenic Nd) and 2) Paleozoic gabbroic ocean crust (with unradiogenic Pb but radiogenic Nd, similar to N-MORB in composition). Symbols as in Fig. 3. Field for LVC from [51].

The difference in Fe-enrichment and Sr-Nd-Pb isotopic composition between the two Madeira archipelago endmembers are consistent with the Early Shield Stage endmember being primarily altered basaltic upper crust and the Post-Erosional Stage endmember being less altered, lower oceanic crust consisting primarily of gabbro and possibly some ultramafic cummulates. In a study of basaltic and gabbroic ocean crust beneath the neighboring Canary Islands, the basaltic upper crust (pillow basalts and dikes/sills) has higher FeO^T (average of

10.8 wt.% at average SiO_2 of 50.3 wt.%), $^{87}Sr/^{86}Sr$ (0.7038), $^{206}Pb/^{204}Pb$ (18.9) and μ (41) and lower $^{147}Sm/^{144}Nd$ (0.17) and $^{143}Nd/^{144}Nd$ (0.51297) than the gabbroic lower crust with FeO^T (8.5 wt.% at similar SiO_2 of 50.8 wt.%), $^{87}Sr/^{86}Sr$ (0.7034) $^{206}Pb/^{204}Pb$ (18.6), μ (5), $^{147}Sm/^{144}Nd$ (0.21) and $^{143}Nd/^{144}Nd$ (0.51301) ([6] and unpublished data). The relative differences between the Early Madeira Shield and Post-Erosional endmembers are the same as observed between the upper and lower Jurassic ocean crust beneath the Canaries, suggesting a recycled upper (altered basaltic) oceanic crustal source for the Early Shield Stage volcanic rocks and a recycled lower (gabbroic) crustal source for the Post-Erosional rocks. The differences in absolute values for Sr, Nd and Pb isotopic ratios may reflect differences in degree of alteration and/or age between the Jurassic ocean crust beneath the Canaries and the recycled Paleozoic crust in the Madeira source. In conclusion, the Madeira plume is heterogeneous consisting of recycled altered upper (basaltic) oceanic crust and less-altered lower (gabbroic±ultramafic cumulates) crust.

Although the different levels of the crust are likely to have evolved separately during the recycling process, mixing of melts from the two sources could produce the observed binary mixing arrays (Fig. 4.5, 4.6). If the upper and lower oceanic crust were formed at the same time, then the array on the uranogenic Pb isotope diagram will still have age significance, representing a two point isochron with an age of ~ 430 Ma. The Nd isotope data is also consistent with a Paleozoic age for the oceanic crust. Taking the average Nd isotope composition for the Early Shield (0.51303) and the Post-Erosional (0.51315) Stages and the average $^{147}Sm/^{144}Nd$ for the upper (0.17) and lower (0.21) Jurassic crust beneath the Canaries, we generate a two point Sm-Nd isochron with an age of ~ 460 Ma and initial $^{143}Nd/^{144}Nd$ of 0.51252. Finally, even if both Madeira endmembers reflect unrelated batches of recycled ocean crust, the negative Δ 7/4 combined with intermediate $^{206}Pb/^{204}Pb$ of both endmembers reflect young (<500 Ma) recycling ages [5]. Interestingly, plate tectonic reconstructions [46] show that the ancient Ural ocean closed above the region where Madeira is located today 300-400 Ma ago, reflecting the possible source of recycled oceanic crust.

The young recycling age, postulated above, implies that the entire process, from hydrothermal alteration to subduction into the mantle, storage and return of the former oceanic crust to the surface in a mantle plume occurred within the last 500 Ma. Recent seismic tomographic data from Southeast Siberia suggest that a detached subducting slap can sink into the mantle at a rate of ca. 10 km/Ma after it becomes detached [47]. In an earlier study, slightly higher velocities of 10-20 km/Ma were calculated for slab descent in an active subduction zone [48]. In accordance with these rates, it would take 150-300 Ma for a slab to sink to the core-mantle boundary layer. Ascent times for mantle plumes from the core-mantle

boundary to the base of the lithosphere determined by numerical modeling range from 50 to 100 Ma [49]. Consequently, the recycling of a portion of subducted material through the entire mantle would require 200-400 Ma. This is fully consistent with the ≤ 500 Ma recycling ages derived from Pb and Nd isotope systematics of volcanic rocks from the Madeira Archipelago even if additional time elapsed at the Earth's surface between creation and subduction.

Far less recycling time would be required if the subducting slabs became inhibited and stored at the endothermic upper-lower mantle transition zone (660 km discontinuity) as seen for some slabs in the Northwest Pacific [50]. If mantle plumes originate at this boundary, the required overall recycling time would dramatically decrease to 44-90 Ma (neglecting the time for storage and heating which is unknown both scenarios). We can estimate the storage time at a thermal boundary layer for oceanic crust recycled by the Madeira plume. No high ^{3}He signatures which would point to a contribution of lower mantle material have been found in the Madeira/Desertas samples so far (Graham pers. com.). Assuming an origin at the upper/lower mantle boundary at ca. 660 km, the residence time can be constrained to be < 400 Ma. Assuming a plume origin from the core-mantle thermal boundary, the residence time would be significantly shorter (< 300 Ma).

Using Pb, Sr and Nd isotope data Hoernle et al. [51] have shown that volcanic rocks from the Canaries, western and central Europe and the western Mediterranean converge on a restricted composition ($^{206}Pb/^{204}Pb \approx 19.9$-$20.1$, $^{207}Pb/^{204}Pb \approx 15.62$-$15.68$, $^{87}Sr/^{86}Sr \approx 0.7030$-$0.7034$ and $^{143}Nd/^{144}Nd \approx 0.51282$-$0.51294$) which is thought to reflect a common isotopic endmember, referred to as the Low Velocity Component (LVC). In contrast to the nearby Canary and Selvagen Islands (located 500 and 300 km southeast of Madeira) as well as the belt of seamounts northeast of the Canaries, the radiogenic Madeira endmember has higher $^{143}Nd/^{144}Nd$ and lower $^{207}Pb/^{204}Pb$ than the LVC (see Fig. 4.6 and 4.8) (Geldmacher at al., in prep.). This suggests deviation of the Madeira plume from a distinct source from other intraplate volcanism in the eastern North Atlantic, western Mediterranean and western central Europe.

Dynamic model for the geochemical evolution of the Madeira/Desertas volcanic complex

The island of Madeira (or a small seamount SW of Madeira) represents the present location of the ≥ 72 Ma old Madeira hotspot [14]. The irregular distribution of islands and seamounts along the Madeira hotspot track, the large age intervals between individual volcanic complexes (Fig. 4.1) and the very low eruption/growth rates of the Madeira/Desertas volcanic complex imply that the Madeira hotspot is a weak, pulsating (or blob-type) plume.

Each volcanic complex may therefore represent a separate plume pulse [14]. Considering the low growth rates and low buoyancy flux [52], Madeira could serve as a low productivity endmember for hotspot systems.

A model for explaining the origin and evolution of volcanic complexes in the Madeira hotspot system must be able to explain several features of the Madeira/Desertas volcanic complex. 1) Estimated eruption rates decrease from 5,500 km^3/Ma during the submarine Shield Stage to 20-150 km^3/Ma during the subacrial part of the Shield Stage (Early Madeira Rift Stage, Desertas Rift Stage, Late Madeira Rift Stage) to ≈ 2 km^3/Ma during the Post-Erosional Stage, inferred to reflect decreasing magma production rates with decreasing age [14]. 2) FeO^T and SiO_2 content decrease with decreasing age (Figure 3), which correlates with decreasing Pb and Sr and increasing Nd isotope ratios (e. g. Fig. 4.5, 4.7). These variations are interpreted to result from an increasing contribution of lower (less-altered gabbroic) recycled crust relative to upper (more-altered basaltic) ocean crust to the melts. 3) The La/Yb and La/Sm ratios and some incompatible element ratios (e.g. Nb/Yb, Th/Sm, Th/Lu) show a general increase with decreasing age. Since FeO^T, SiO_2 and Sr-Nd-Pb isotope ratios indicate that the source becomes less fertile and more depleted with age, these variations suggest decreasing degrees of melting with decreasing age, consistent with the inferred decrease in magma production rates.

Taking the above constraints into consideration, we propose the following model to explain the formation of the Madeira/Desertas volcanic complex. During the late Miocene, a pulse of plume material containing recycled oceanic crust ascended through the upper mantle. In the shallow asthenosphere, the solidus for the altered, basaltic upper crust was crossed first, followed by the solidus for the gabbroic lower crust (Fig. 4.9). Melts from the lower and upper crust mixed at the top of the melt column forming the voluminous early Shield Stage magmas. At this time eastern Madeira lay above the center of the plume and magma was provided to both the Madeira and Desertas Rifts.

As the plate moved northeastward, eruption rates decreased on Madeira and the Desertas during the Pliocene reflecting decreased magma production rates above the downstream portion of the plume pulse. The lithosphere dragged residual plume material at its base to the northeast (hatched region of plume in Fig. 4.9), whereas movement of the upper asthenosphere in the direction of plate motion caused plume material, only depleted in its basaltic component, to spread beneath the residual plume material. In the Quaternary plume material was depleted in its basaltic component beneath the seamount to the southwest of Madeira (Fig. 4.1b), which extends to depths shallower than 500 m and is believed to be the

present location of the center of the Madeira hotspot. Minor melting occurred beneath Madeira in a secondary melting zone located further downstream in the plume pulse. This is a

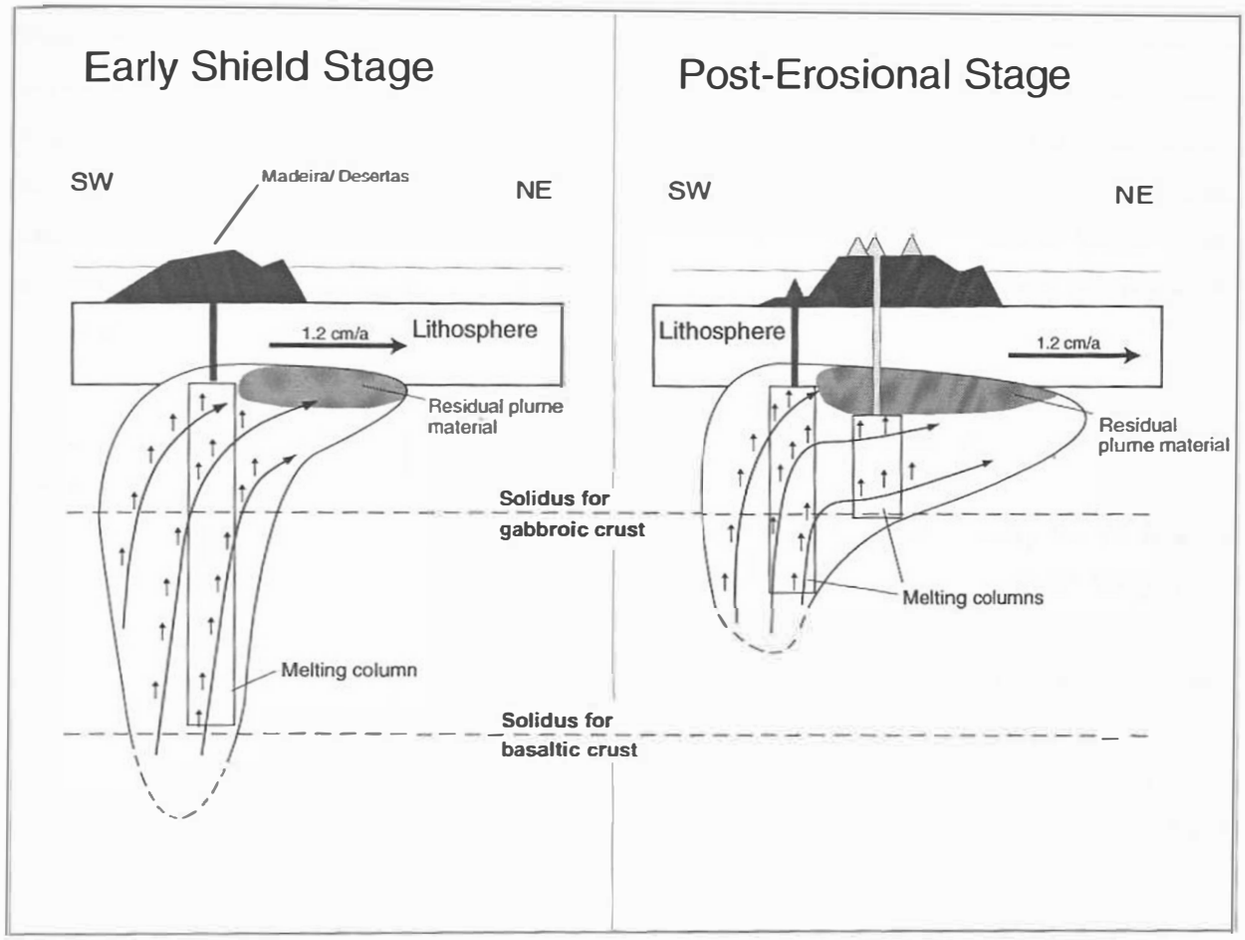

Fig. 4.9:

Simplified cartoon of a dynamic model for the geochemical evolution of Madeira/Desertas volcanic complex. A pulse of plume material, containing recycled oceanic crust, rises through the upper mantle and begins to melt upon crossing the solidus for altered basaltic crust. As the plume pulse continues to upwell, the solidus for the lower gabbroic portion of the crust is also crossed. During the Shield Stage, the volcano is over the center of the plume pulse. Erupted melts represent an average of melts from the upper and lower portions of the recycled oceanic crust. During the Post-Erosional Stage, the volcano is situated above the downstream edge of the upwelling pulse of plume material, as a result of plate motion to the northeast. Since the melts from the basaltic portion of the recycled crust have already been extracted beneath the seamount volcano SW of Madeira, melts forming the post-erosional lavas primarily come from the lower gabbroic portion of the crust. The hatched area represents residual plume material pooled at the base of the lithosphere.

result of further adiabatic decompression due to ongoing ascent of plume material when the plume pulse flattened and spread out beneath the residual plume material at the base of the lithosphere. A similar process has recently been proposed to explain rejuvenated volcanism on the Hawaiian Islands and has been successfully modeled for the Hawaiian plume [53]. Post-Erosional melts formed beneath Madeira are enriched in the gabbroic component from the recycled oceanic crust, since melt extraction at deeper depths removed most of the basaltic component beneath the seamount to the SW. Lower volumes of melt were produced during the Post-Erosional stage due to the shorter melting column beneath Madeira at this time. Although more-depleted source material was melted during the Post-Erosional Stage, lower degrees of melting led to a slight increase in La/Yb and La/Sm and in some incompatible element concentations.

Isotopic variation in the Madeira Hotspot track: Source variation or shallow level contamination ?

Variations in initial $^{206}Pb/^{204}Pb$, $^{207}Pb/^{204}Pb$ and $^{143}Nd/^{144}Nd$ ratios along the 72 Ma old Madeira hotspot track are shown in Fig. 4.10a,b. Only samples from the Shield Stage from each volcano are included for the sake of comparison. Although the initial $^{206}Pb/^{204}Pb$ ratio shows no systematic variation along the hotspot track, initial $^{87}Sr/^{86}Sr$, $^{207}Pb/^{204}Pb$, and $^{208}Pb/^{204}Pb$ ratios increase and $^{143}Nd/^{144}Nd$ ratios decrease with increasing age of the volcanoes or with decreasing distance to the continental shelf (e.g. Fig. 4.11). These variations could reflect either 1) temporal variation in the composition of the plume source or 2) lithospheric contamination of plume melts.

1) Source variation

a) Evolving plume source

Isotopic variations in volcanic rocks of a hotspot track can reflect an 'evolving plume source', as has been proposed for the Kerguelen hotspot by Class et al. [54]. It has recently been shown that this model is also consistent with the ~ 90 Ma evolution of the Galápagos hotspot [8, 55, 56]. Assuming that the plume source is homogeneous and does not receive input of new material, the isotopic composition of the plume source will evolve solely by in situ radioactive decay and therefore the initial isotopic composition of the erupted primitive

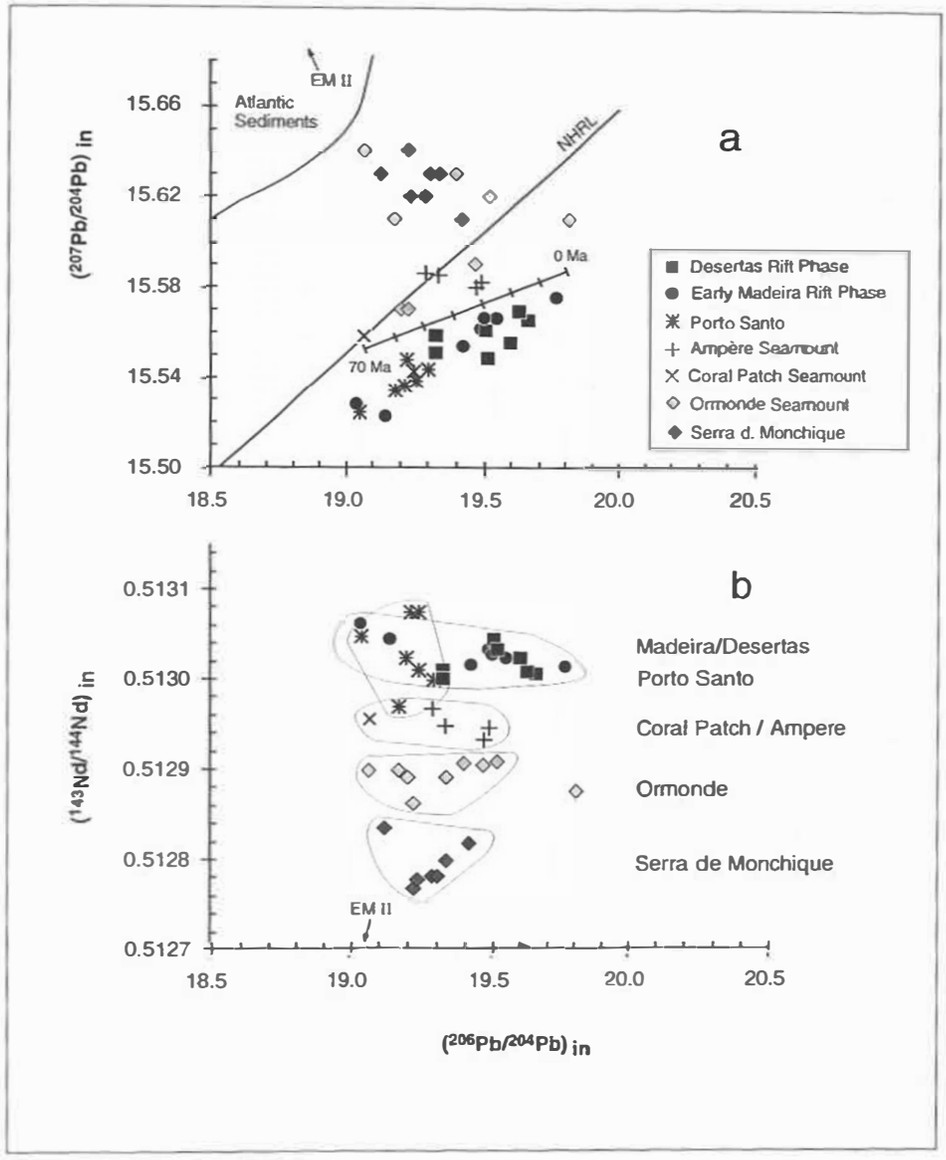

Fig.4.10:

Initial Pb and Nd isotope ratios for Shield Stage samples of the 72 Ma old Madeira hotspot track, which includes data from Ormonde Seamount and the Serra de Monchique alkaline complex from Bernard-Griffiths et al. [57]. From Porto Santo only the most enriched group of samples is shown which are believed to represent the Early Shield Stage magmas on this island. a) Initial Pb isotope ratios show constant $^{206}Pb/^{204}Pb$ ratios over the entire hotspot track but increasing $^{207}Pb/^{204}Pb$ ratios with increasing age of the volcano. The Northern Hemisphere Reference Line (NHRL) is shown for reference. Also shown is the field for Atlantic sediments from Hoernle et al. [58] and Ben Othman et al. [69]. A possible Pb evolution curve is modeled for a $\mu = 70$. Marks show intervals of 10 Ma before present assuming a homogeneous "evolving" magma source. b) Initial $^{143}Nd/^{144}Nd$ ratio (plotted against $^{206}Pb/^{204}Pb$) decrease systematically with increasing age along the hotspot track. In both diagrams, a mixture of an EM II-like component or Atlantic sediments with the Madeira plume lavas could generate the observed variations.

volcanic rocks should reflect this. If the plume products are relatively young (e.g. < 100 Ma), isotopes which have small parent/daughter ratios (e.g. $^{207}Pb/^{204}Pb$ and $^{87}Sr/^{86}Sr$) will not show significant variation. Isotope ratios which are associated with relatively large parent/daughter ratios (e.g. $^{206}Pb/^{204}Pb$, $^{208}Pb/^{204}Pb$ and $^{143}Nd/^{144}Nd$) will increase with decreasing age of the hotspot volcanoes. Although it has been shown that the Madeira source is heterogeneous consisting of altered basaltic upper crust and gabbroic lower crust, mixtures of melts from these two sources produced during the Shield Stage of volcanism could approximate the evolution of a homogeneous source, if melting conditions were similar beneath each volcanic complex. Nevertheless, the "evolving plume source model" cannot adequately explain the large relative variation in $(^{207}Pb/^{204}Pb)_{in}$ as compared to $(^{206}Pb/^{204}Pb)_{in}$ (see the calculated evolution curve in Fig. 4.10a). We also note that an extremely high μ of ~ 70 is required in the source to generate the range in $(^{206}Pb/^{204}Pb)_{in}$ within 70 Ma.

b) Variable contribution of a third plume component

An alternative explanation for the temporal variation in the isotope ratios of the Madeira hotspot track is a decreasing contribution of EM II-type material or recycled oceanic sediments to the source of the Shield Stage melts with decreasing age (Fig. 4.10 and 4.11). Although this possibility cannot be ruled out, there is no obvious explanation why the amount of this enriched (EM-type) component decrease systematically with decreasing age.

2) Shallow level lithospheric contamination

Decreasing interaction of plume melts with enriched (EM-type) lithospheric mantle, continental crust or oceanic sediments with increasing distance from the continental margin could also generate the variations observed along the Madeira hotspot track. The Serra de Monchique alkaline magmas, located in southern Portugal, have been interpreted to show continental lithospheric mantle contamination (Bernard-Griffiths et al., [57]). These authors also found evidence for a continental component in a clinopyroxene separated from Ormonde Seamount which had very low $^{143}Nd/^{144}Nd$ of 0.512626, even though the whole rock sample with $^{143}Nd/^{144}Nd$ of 0.512943 showed no evidence of this component. They proposed that the clinopyroxene was contaminated within the mantle in a wedge of continental lithosphere beneath the seamounts, detached during passive continental rifting. Evidence for increasing contamination by enriched lithospheric mantle with decreasing distance from the African continental margin also comes from primitive volcanic rocks from the Canary and Cape Verde Islands [6, 30, 58]. These authors interpret the presence of enriched lithospheric mantle beneath oceanic crust to have occurred during the rifting of Pangaea.

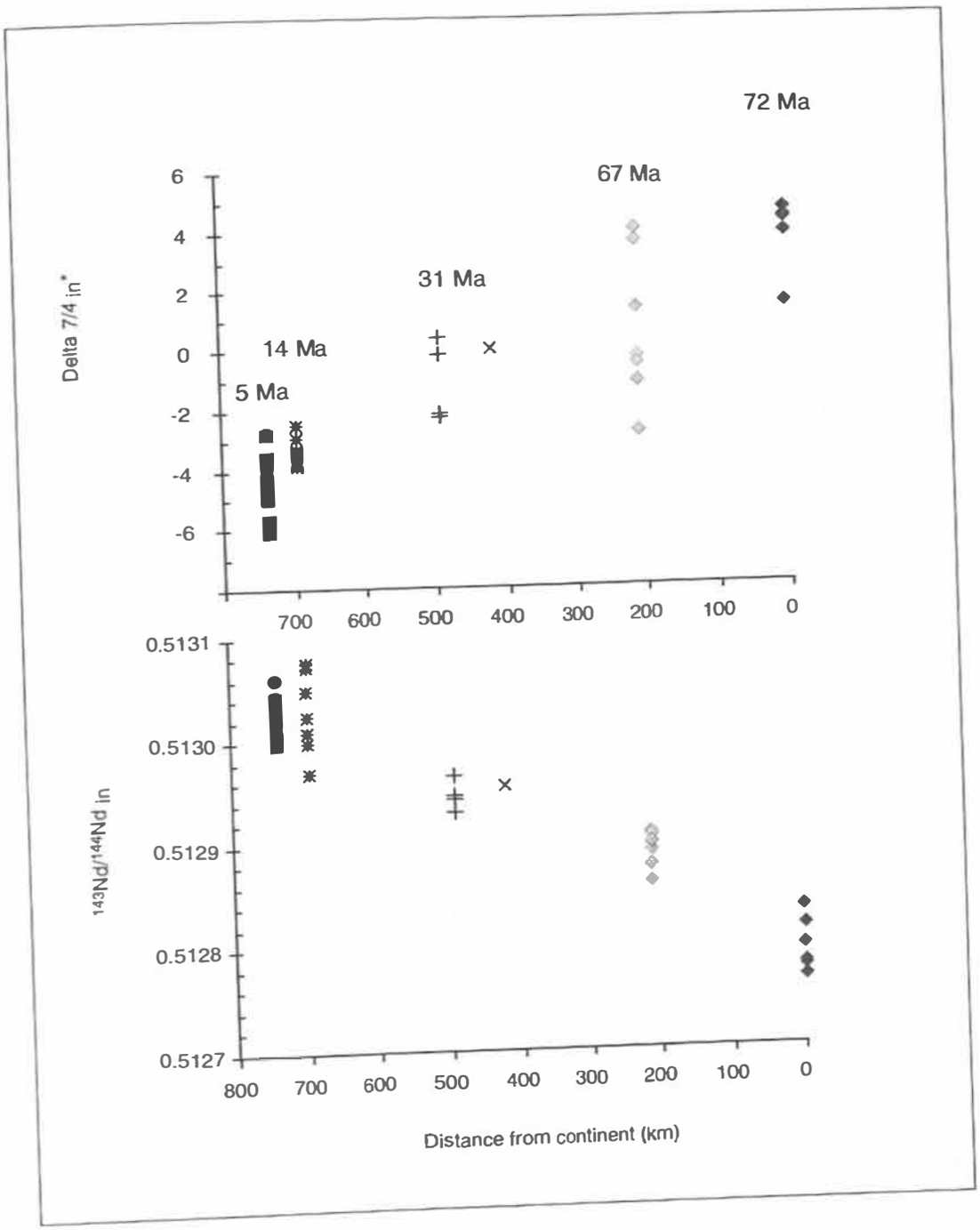

Fig. 4.11:
Observed variations in initial $^{207}Pb/^{204}Pb$ (expressed as Δ 7/4) and initial $^{143}Nd/^{144}Nd$ ratios for Shield Stage samples of the Madeira hotspot track (see Fig. 10) plotted against minimum distance of individual volcanoes from the African or European continents. Good correlations support shallow level contamination with continental-type lithosphere. Maximum age data are from [14, 34, 39]. Symbols as in Fig. 10.

Finally, it has been shown that fault blocks of continental crust (formed during continental break-up) can extend well into ocean basins. Blocks of continental crust (containing tonalitic gneiss, meta-anorthosite and shallow water carbonates) have been drilled to the north of Madeira in the basement of the Iberian Abyssal Plain during ODP Leg 173 (see Fig. 4.1). These blocks have been found up to 200 km away from the Iberian continental rise [59]. Continental metamorphic and plutonic igneous rocks also outcrop on the nearby Galicia Bank. The continental gneiss (VH-97-76) dredged at Ormonde Seamount may also represent a piece of continental crust in the basement of Goringe Bank, uplifted as a result of movements along the Azores-Gibraltar fracture zone; however, a drop-stone origin cannot be ruled out for this sample. Although the gneiss has low $^{143}Nd/^{144}Nd$ (0.5109) and high $^{87}Sr/^{86}Sr$ (0.7263), the $^{206}Pb/^{204}Pb$ (15.75) and $^{207}Pb/^{204}Pb$ (15.33) are to low to serve as a possible contaminant for the oldest Madeira hotspot track volcanoes. We note, however, that the dredged gneiss sample does have the appropriate composition to serve as the EM I-type endmember observed in the Canary Islands volcanic rocks [6, 30, 58]. In light of the evidence for transitional continental to oceanic lithosphere occurring in a several hundred kilometer belt along continental margins, we believe plume-lithosphere interaction to be the most likely explanation for the compositional variations along the Madeira hotspot track.

4.7 Conclusions

Major element, trace element, and radiogenic isotope characteristics of the volcanic rocks from the Madeira Archipelago can be explained by the presence of recycled oceanic crust in the Madeira hotspot source. Variation in FeO^T, SiO_2 and Sr, Nd and Pb isotope ratios points to a heterogeneous source containing two endmembers. One endmember, sampled predominately during the early Shield Stage, is characterized by high FeO^T and SiO_2 and enriched Pb, Sr and Nd isotope ratios. We interpret this endmember to reflect upper (altered basaltic) oceanic crust. The other endmember, characterized by lower FeO^T and SiO_2 and more depleted Sr, Nd and Pb isotope ratios, sampled primarily during the Post-Erosional Stage most likely represents the lower (gabbroic) oceanic crust. Low Δ 7/4 ratios (up to – 7.2), moderately enriched $^{206}Pb/^{204}Pb$, and Sr and Nd isotopic ratios similar to N-MORB point to a young (Palaeozoic) recycling age ($\leq$ 500 Ma) of the recycled crust, as do Sm-Nd and Pb-Pb isotope systematics. The continuous decrease of the isotopically enriched component in the Madeira magma source with decreasing age can be explained by progressive melting and exhaustion of recycled altered basaltic ocean crust in a discrete pulse of plume material as it upwells and spreads out at the base of the lithosphere. Low volumes of volcanism and lower degrees of melting during the Post-Erosional Stage can be explained by a secondary melting

zone located downstream of the plume (pulse) stem where the plume material is depleted in its basaltic component. Other volcanic islands and seamounts of the >70 Ma old Madeira hotspot track are also attributed to discrete blobs or pulses of upwelling plume material. Systematic decrease in $(^{143}Nd/^{144}Nd)_{in}$ and increase in $(^{207}Pb/^{204}Pb)_{in}$ ratios of the Shield Stage magmas of the Madeira hotspot track with decreasing distance from the continental margin is interpreted to reflect increasing interaction of plume melts with continental lithosphere.

Acknowledgements

We are particularly indebted to H.-U. Schmincke for his support in initiating this study and for providing samples to KH for preliminary analyses. We gratefully acknowledge Director H. Costa-Neves and the staff from the Parque Natural da Madeira (in particular H. P. Fernandes and F. R. Vieira) for their excellent logistical support during our field studies on the Desertas Islands without which the study of these islands would not have been possible. Captain M. Gross, officers and crew of the F.S. POSEIDON are thanked for their help in obtaining submarine rock samples used in this study and A. Freiwald and P. Halbach are thanked for placing additional submarine samples from cruise VICTOR HENSEN-97 and SONNE 83 at our disposal. D. Garbe-Schönberg and T. Arpe (ICP-MS laboratory, University Kiel), O. Schneider, K. Wolff, D. Rau (EMS and XRF laboratories, GEOMAR) and E. Zuleger, S. Vetter and particularly F. Hauff (TIMS laboratory, GEOMAR) are thanked for their analytical support. G. Zankl, F. Marks and S. Duggen assisted with sample preparation and analyses. D. Rodrigues , M. Hort, R. Schmidt and F. Hauff are thanked for fruitful discussions. This study was supported by the Deutsche Forschungsgemeinschaft (DFG project HO1833/1).

References

1 C.G. Chase, Oceanic island Pb: Two-stage histories and mantle evolution, Earth Planet. Sci. Lett. 52, 277-284, 1981.

2 A.W. Hofmann and W.M. White, Mantle plumes from ancient oceanic crust, Earth Planet. Sci. Lett. 57, 421-436, 1982.

3 A. Zindler and S.R. Hart, Chemical geodynamics, Ann. Rev. Earth Planet. Sci. 14, 493-571, 1986.

4 B.B. Hanan and D.W. Graham, Lead and helium isotope evidence from oceanic basalts for a common deep source of mantle plumes, Science 272, 991-995, 1996.

5 M.F. Thirlwall, Pb isotopic and elemental evidence for OIB derivation from young HIMU mantle, Chemical Geology 139, 51-74, 1997.

6 K. Hoernle, Geochemistry of Jurassic oceanic crust beneath Gran Canaria (Canary Islands): Implications for crustal recycling and assimilation, J. Petrol. 39-5, 859-880, 1998.

7 C. Chauvel, A.W. Hofmann and P. Vidal, HIMU-EM: The French Polynesian connection, Earth Planet. Sci. Lett. 110, 99-119, 1992.

8 F. Hauff, K. Hoernle, G. Tilton, D.W. Graham and A.C. Kerr, Large volume recycling of oceanic lithosphere over short time scales: Geochemical constraints from the Caribbean Large Igneous Province, Earth and Planet. Sci. Lett. 174, 247-263, 2000.

9 B.L. Weaver, The origin of ocean island basalt end-member compositions: trace element and isotopic constraints, Earth Planet. Sci. Lett. 104, 381-397, 1991.

10 H. Staudigel, G.R. Davis, S.R. Hart, K.M. Marchant and B.M. Smith, Large scale isotopic Sr, Nd and O isotopic anatomy of altered oceanic crust: DSDP/ODP sites 417/418, Earth and Planet. Sci. Lett. 130, 169-185, 1995.

11 S.R. Hart and H. Staudigel, Isotopic characterization and identification of recycled components, in: Crust/mantle recycling at convergence zones, S.R. Hart, and Gülen, L., ed., pp. 15-28, Kluwer Acad. Publ., 1989.

12 T. Kogiso, T. Yoshiyuki and S. Nakano, Trace element transport during dehydration processes in the subducted oceanic crust: Experiments and implications for the origin of ocean island basalts, Earth and Planet. Sci. Lett. 148, 193-205, 1997.

13 S.R. Hart, A large-scale isotope anomaly in the Southern Hemisphere mantle, Nature 309, 753-757, 1984.

14 J. Geldmacher, P.v.d. Bogaard, K. Hoernle and H.-U. Schmincke, $^{40}Ar/^{39}Ar$ Age Dating of the Madeira Archipelago and hotspot track (eastern North Atlantic), Geochemistry, Geophysics, Geosystems 1, 2000.

15 Y.-S. Zhang and T. Tanimoto, Ridges, hotspots and their interaction as observed in seismic velocity maps, Nature 355, 45-49, 1992.

16 H. Bijwaard, W. Spakman and E. Engdahl, Closing the gab between regional and global time tomography, J. of Geophys. Res. 103, B 12, 30.055-30.078, 1998.

17 W. Pitman and M. Talwani, Sea floor spreading in the North Atlantic, Geol. Soc. Am. Bull. 83-3, 619-646, 1972.

18 M.P. Ferreira and J. Cotelo Neiva, Carta Geologica de Portugal, Folha da Ilha de Porto Santo, Instituto Geologico e Minereiro, 1997.

19 R. Schmidt, H.-U. Schmincke, J. McPhie and P.v.d. Bogaard, Volcanology, geochemistry and age evolution of a shoaling to emergent seamount, Porto Santo (Central East Atlantic), in prep.

20 H.-U. Schmincke and M. Weibel, Chemical study of rocks from Madeira, Porto Santo, and Sao Miguel, Terceira (Azores), Neues Jahrb. Min. Abhandl. 117-3, 253-281, 1972.

21 G. Zbyszewski, O. Da Veiga Ferreira, A. Candido de Medeiros, L. Aires-Barros, L.C. Silva, J.M. Munhá and F. Barriga, Noticia Explicativa das Folhas A e B da Ilha da Madeira, Serviços Geológicos de Portugal, Lisbon, 1975.

22 G. Zbyszewski, A. Candido de Medeiros, O. Da Veiga Ferreira and C. Torre de Assunção, Noticia Explicativa da Folha Ilhas Desertas, Serviços Geológicos de Portugal, Lisbon, 1973.

23 J. Mata, T. Boski, A. Boven and J. Munhá, Geochronologia das Lavas da Madeira: Novas Datações K.-Ar, Gaia 11, 53-56, 1995.

24 D.J. Hughes and G.C. Brown, Basalts from Madeira: A petrochemical contribution to the genesis of oceanic alkali rock series, Contrib. Mineral. Petrol. 37, 91-109, 1972.

25 L. Aires-Barros, M. Matias and A. Miranda, Preliminary note on the petrology of Madeira Island, Bol. Mus. Lab. Min. Geol. Fac. Chien. de Lisboa 14-1, 5-28, 1974.

26 J. Mata, R. Kerrich, N.D. MacRae and T.-W. Wu, Elemental and isotopic (Sr, Nd, and Pb) characteristics of Madeira Island basalts: evidence for a composite HIMU-EM I plume fertilizing lithosphere, Can. J. Earth Sci. 35, 980-997, 1998.

27 A.N. Halliday, G.R. Davies, D.-C. Lee, S. Tommasini, C.R. Paslick, J.G. Fitton and D.E. James, Lead isotope evidence for young trace element enrichment in the oceanic upper mantle, Nature 359, 623-627, 1992.

28 A.N. Halliday, G.R. Davies, D.-C. Lee, S. Tommasini, C.R. Paslick, J.G. Fitton and D.E. James, Correction to "Lead isotope evidence for young trace element enrichment in the oceanic upper mantle", Nature 362, 184, 1993.

29 K. Hoernle, J. Gill and H.-U. Schmincke, Extreme fractionation of (Nb, K, Th)/ U ratios during metasomatism of Jurassic oceanic lithospheric mantle, in: AGU 1993 fall meeting, Eos, Trans. 74;43, pp. 633, American Geophysical Union, San Francisco, 1993.

30 E. Widom, K.A. Hoernle, S.B. Shirey and H.-U. Schmincke, Os isotope systematics in the Canary Islands and Madeira: Lithospheric contamination and mantle plume signature, J. Petrol. 40/2, 279-296, 1999.

31 V.M. Litvin, V.V. Matveyenkov, E.L. Onishchenko, M.V. Rudenko and A.M. Sagalevich, New data on the structure of Ampère Seamount, Oceanology 22-1, 62-64, 1982.

32 N.A. Marova and Y.D. Yevsyukov, The geomorphology of the Ampère submarine Seamount (in the Atlantic Ocean), Oceanology 27-4, 452-455, 1987.

33 V.V. Matveyenkov, S.G. Poyarkov, O.V. Dmitriyenko, A.I. Al´Mukhamedov, G.R. Gamsakhurdia and O.L. Kuznetsov, Geological particularities of the seamount structure in the Azores-Gibraltar Zone, Oceanology 33-5, 664-673, 1994.

34 G. Féraud, D. York, C. Mével, G. Cornen, C.M. Hall and J.-M. Auzende, Additional ^{40}Ar-^{39}Ar dating of the basement and the alkaline volcanism of Gorringe Bank (Atlantic Ocean), Earth Planet. Sci. Lett. 79, 255-269, 1986.

35 J.M. Auzende, J. Olivet, A. Le Lann, X. Le Pichon, J. Monteiro, A. Nicolas and A. Ribeiro, Sampling and observation of oceanic mantle and crust on Gorringe Bank, Nature 273, 45-49, 1978.

36 G. Feraud, J. Gastaud, J.-M. Auzende, J.-L. Olivet and G. Cornen, $^{40}Ar/^{39}Ar$ ages for alkaline volcanism and the basement of Gorringe Bank, North Atlantic Ocean, Earth Planet. Sci. Lett. 57, 211-226, 1982.

37 G. Cornen, Petrology of the alkaline volcanism of Gorringe Bank (southwest Portugal), Mar. Geol. 47, 101-130, 1982.

38 G.M. Purdy, The eastern end of the Azores-Gibraltar plate boundary, Geophys. J. Royal Astron. Soc. 43, 973-1000, 1975.

39 R.M. McIntyre and G.W. Berger, A note on the geochronology of the Iberian Alkaline Province, Lithos 15, 133-136, 1982.

40 S.C. Cande and Y. Kristoffersen, Late Cretaceous magnetic anomalies in the North Atlantic, Earth Planet. Sci. Lett. 35, 215-224, 1977.

41 R.W. Le Maitre, P. Bateman, A. Dudek, J. Keller, M. J. Lameyre Le Bas, P.A. Sabine, R. Schmidt, H. Sorensen, A. Streckeisen, A.R. Woolley and B. Zanettin, A classification of igneous rocks and glossary of terms: Recommendations of the International Union of Geological Sciences Subcommision on the systematics of igneous rocks, Blackwell, Oxford,1989.

42 B.L. Weaver, D.A. Wood, J. Tarney and J.L. Joron, Geochemistry of ocean island basalts from the South Atlantic: Ascension, Bouvet, St. Helena, Gough and Tristan da Cunha, in: Alkaline Igneous Rocks, J.G. Fitton and B.G. Upton, ed.,pp.253-267, Geol. Soc. Spec. Publ. 30, 1987

43 K. Hirose and I. Kushiro, Partial melting of dry peridotites at high pressures: Determination of compositions of melts segreated from peridotite using aggregates of diamond, Earth Planet. Sci. Lett. 114, 477-489, 1993.

44 T. Kogiso, K. Hirose and E. Takahashi, Melting experiments on homogeneous mixtures of peridotite and basalt: application to the genesis of ocean island basalts, Earth Planet. Sci. Lett. 162, 45-61, 1998.

45 M.M. Hirschmann and E.M. Stolper, A possible role for garnet pyroxenite in the origin of the "garnet signature" in MORB, Contrib. Min. Pet. 124, 185-208, 1996.

46 C.R. Scotese, Continental Drift, Paleaomap Project 6, Arlington,1994.

47 M.A. Richards, Prospecteing for Jurassic slabs, Nature 397, 203-204, 1999.

48 S.P. Grand, Mantle shear structure beneath the Americas and surrounding oceans, J. Geophys. Res. 99/B6, 11,591-11,661, 1994.

49 P.F. Thompson and P.J. Tackley, Generation of mega-plumes from the core-mantle boundary in a compressible mantle with temperature-dependent viscosity, Geophys. Res. Lett., 1998.

50 H.-W. Zhou and R.W. Clayton, P and S wave travel time inversions for subducting slab under the Island arcs of the Northwest Pacific, J. Geophys. Res. 95, 6829-6851, 1990.

51 K. Hoernle, Y.-S. Zhang and D. Graham, Seismic and geochemical evidence for large-scale mantle upwelling beneath the eastern Atlantic and western and central Europe, Nature 374, 34-39, 1995.

52 N.H. Sleep, Hotspots and mantle plumes: some phenomenology, J. Geophys. Res. 95, 6715-6736, 1990.

53 N.M. Ribe and U.R. Christensen, The dynamical origin of Hawaiian volcanism, Earth Planet. Sci. Lett. 171, 517-531, 1999.

54 C. Class, S.L. Goldstein, S.J.G. Galer and D. Weis, Young formation age of a mantle plume source, Nature 362, 715-721, 1993.

55 F. Hauff, K. Hoernle, P.v.d. Boogard, G.E. Alvarado and D. Garbe-Schönberg, Age and geochemistry of basaltic complexes in western Costa Rica: Contributions to the geotectonic evolution of Central America, Geochemistry Geophysics Geosystems, in press.

56 K. Hoernle, P.v.d. Bogaard, R. Werner, F. Hauff, G. Alvarado and D. Garbe-Schönberg, The missing links in the 90 Ma history of the Galapagos hotspot: Implications for the tectonic and biological evolution of the Americas, Nature submitted.

57 J. Bernard-Griffiths, G. Gruau, G. Cornen, B. Azambre and J. Macé, Continental lithospheric contribution to alkaline magmatism: Isotopic (Nd, Sr, Pb) and geochemical (REE) evidence from Serra de Monchique and Mount Ormonde complexes, J. Petrol. 38-1, 115-132, 1997.

58 K. Hoernle, G. Tilton and H.-U. Schmincke, Sr-Nd-Pb isotopic evolution of Gran Canaria: evidence for shallow enriched mantle beneath the Canary Islands, Earth Planet. Sci. Lett.106, 44-63, 1991.

59 R.B. Whitmarsh and ODP Leg 173 shipboard scientific party, Drilling reveals transition from continental breakup to early magmatic crust, EOS Trans. Am. Geophys. Union 79-14, 173-181, 1998.

60 W.H.F. Smith and D.T. Sandwell, Global seafloor topography from satellite altimetry and ship depth soundings, Science 277, 1956-1962, 1997.

61 E.V. Verhbitsky and V.G. Zolotarev, Heat flow and the Eurasian-African plate boundary in the eastern part of the Azores-Gibraltar fracture zone, J. Geodyn. 11, 267-273, 1989.

62 G.A. MacDonald and T. Katsura, Chemical composition of Hawaiian lavas, J. Petrol. 5, 82-133, 1964.

63 S.R. Hart, and K.E. Davis, Nickel partitioning between olivine and silicate melt, Earth Planet. Sci. Lett. 40, 203-219, 1978.

64 A.W. Hofmann, Chemical differentiation of the Earth: the relationship between mantle, continental crust, and oceanic crust, Earth Planet. Sci. Lett. 90, 297-314, 1988.

65 D.J. Chaffey, R.A. Cliff and B.M. Wilson, Characterization of the St Helena source, in: Magmatism in the Ocean Basins, A.D. Saunders and M.J. Norry, eds., pp. 257-276, Geol. Soc. Spec. Pub. 42, 1989.

66 B. Dupré and C.J. Allègre, Pb-Sr-Nd isotopic correlation and the chemistry of the North Atlantic mantle, Nature 286, 17-21, 1980.

67 E. Ito, W.M. White and C. Göpel, The O, Sr, Nd and Pb isotope geochemistry of MORB, Chem. Geol. 62, 157-176, 1987.

68 R.S. Cohen and R.K. O'Nions, The lead, neodymium and strontium isotopic structure of oceanic ridge basalts, J. Petrol. 23, 299-324, 1982.

69 D. Ben Othman, W.M. White and J. Patchett, The geochemistry of marine sediments, island arc magma genesis, and crust-mantle recycling, Earth Planet. Sci. Lett. 94, 1-21, 1989.

Chapter 5

Evolution of the Selvagen archipelago and neighboring seamounts

This chapter consists of an individual paper that is in preparation for submission.

Temporal and geochemical evolution of the Selvagen archipelago and neighboring seamounts in the eastern North Atlantic: Earlier history of the ≥70 Ma old Canary Hotspot

Jörg Geldmacher[1]*, Kaj Hoernle[1], Paul van den Bogaard[1] Goor Zankl[1] and Dieter Garbe-Schönberg[2]

[1] GEOMAR Research Center, Wischhofstrasse 1-3, 42148 Kiel, Germany

[2] Institut für Geowissenschaften, Universität Kiel, Ohlshausenstr. 40, 24118 Kiel, Germany

* Corresponding author: jgeldmac@geomar.de

Abstract

Major elements, trace elements, Sr-Nd-Pb isotopes, and $^{40}Ar/^{39}Ar$ age determinations of volcanic rocks from the Selvagen Islands and neighboring seamounts in the eastern North Atlantic are presented. The evolution of the archipelago can be divided into an Oligocene (24-30 Ma) basanitic to phonolitic shield stage, an ~ 12 Ma volcanic hiatus accompanied by extensive erosion and sedimentation of marine carbonates and two rejuvenated or post-erosional stages (ca. 8-12 Ma and at 3.4 Ma) consisting of alkali basalt and basanitic dikes, lava flows and pyroclastic deposites with rare phonolitic tuff. Samples from associated seamounts yield ages of 9 Ma (Dacia), 17 Ma (Conception Bank) and 68 Ma (Lars). The volcanic rocks from the seamounts range from alkali basalts and basanites to phonolites. Trace element and Sr-Nd-Pb isotopic composition of the Selvagen Islands and neighboring seamounts are consistent with derivation from the Canary plume. A crude southwest to northeast increasing age progression for the > 800 km long and 450 km wide belt of islands and seamounts is also consistent with a plume-type model, yielding an absolute plate velocity of ~ 12 mm/a. Either a continuous plume (300-400 km in diameter) sheared by lithospheric drag and/or asthenospheric wind or interaction of a lower mantle plume with the 660 km discontinuity resulting in formation of individual diapirs could explain the poorly-defined, broad hotspot track.

5.1 Introduction

Striking features of the worlds ocean basins are the linear chains of volcanic islands and seamounts, which are in general attributed to hotspot volcanism that is explained by narrow, stationary upwelling of hot mantle material (plumes). To explain many broader, more complex areas of oceanic intra plate volcanism, however, the classical hotspot theory appears to be inadequate (e.g. Vogt, 1991; Mc Nut et al., 1997).

In this and two comparison studies (Geldmacher et al., 2000; Geldmacher and Hoernle subm.) we evaluate the origin of the eastern North Atlantic volcanic province, which extends ~ 1800 km from the Sahara seamounts in the south to the Azores-Gibraltar Fracture zone in the north with a width of ~ 700 km. This volcanic province contains three volcanic island groups (Canary, Selvagen and Madeira) and more than 20 large volcanic seamounts (Fig. 5.1a). In this study, we concentrate on the temporal and spatial evolution of the central part of the eastern North Atlantic volcanic province (Fig. 5.1b). Here we present comprehensive geochemical and Ar/Ar age data sets for the evolution of the Oligocene-Pliocene Selvagen Volcano and reconnaissance geochemical and age data from five large seamounts to the east of the Selvagen Islands. The volcanoes in the eastern North Atlantic province are situated on three distinct bathymetric anomalies oriented NE to SW: 1) the Madeira Islands, Madeira Tore Rise and several additional large seamounts (including Seine, Ampère, Ormonde) in the north, 2) the Canary and Selvagen Islands and several large seamounts to the northeast, 3) the Sahara Seamounts in the south. Regional models for this volcanism range from volcanism along a suture zone running along the Atlantic margin of NW Africa (Schmincke, 1982) to multiple small (100-200 km) hotspots (Morgan, 1972), to large-scale upwelling beneath the entire region (Hoernle et al., 1995).

A wide variety of models have been proposed to explain the age sequence and spatial distribution of the Canary Island group and the northeasterly seamounts. They include volcanism resulting from decompression melting 1) beneath rising lithospheric blocks due to tectonic shortening (Arana and Ortiz, 1991), 2) along an extension of the South Atlas fault system (Anguita and Hernan, 1975), or 3) a mantle plume (e.g. Morgan, 1972; Holik and Rabinowitz, 1991; Hoernle et al., 1991; Hoernle and Schmincke, 1993a; Hoernle and Schmincke, 1993b).

Recent studies of the geochronological and geochemical evolution of the Madeira archipelago and seamounts to the northeast of Madeira provide strong evidence for a plate motion induced age progression from SW to NE (Madeira hotspot track) (Morgan, 1983; Geldmacher et al., 2000; Geldmacher and Hoernle, subm.).

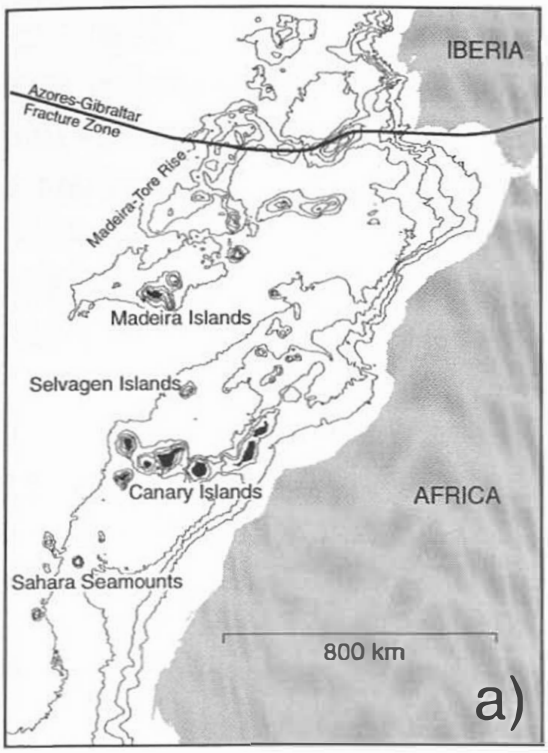

Fig. 5.1:

*Island groups and seamounts in the eastern North Atlantic. Source: TOPEX (Smith and Sandwell, 1997). a) Schematic overview map b) Bathymetric map. * Asterisks mark our working names given to unnamed seamounts. Oldest available ages in parenthesis (in Ma) except for Madeira Islands where complete age range is given. Data for the Canary Islands from Abdel-Monem et al. (1971, 1972), Schmincke (1977), Cantagrel et al. (1984), Le Bas et al. (1986), Bogaard et al. (1988), Ancochea et al. (1990, 1994), Coello et al. (1992), Bogaard and Schmincke (1998), and Bogaard, unpublished data. Madeira Island ages from Geldmacher et al. (2000) and from Selvagen Islands and seamounts from this study. Shaded field shows the extent of a seismic chaotic facies (UCF), interpreted to be of volcanic origin (Holik and Rabinowitz, 1991). The layer is time transgressive, starting at the Creataceous/Tertiary boundary in the north and becoming younger to the south.*

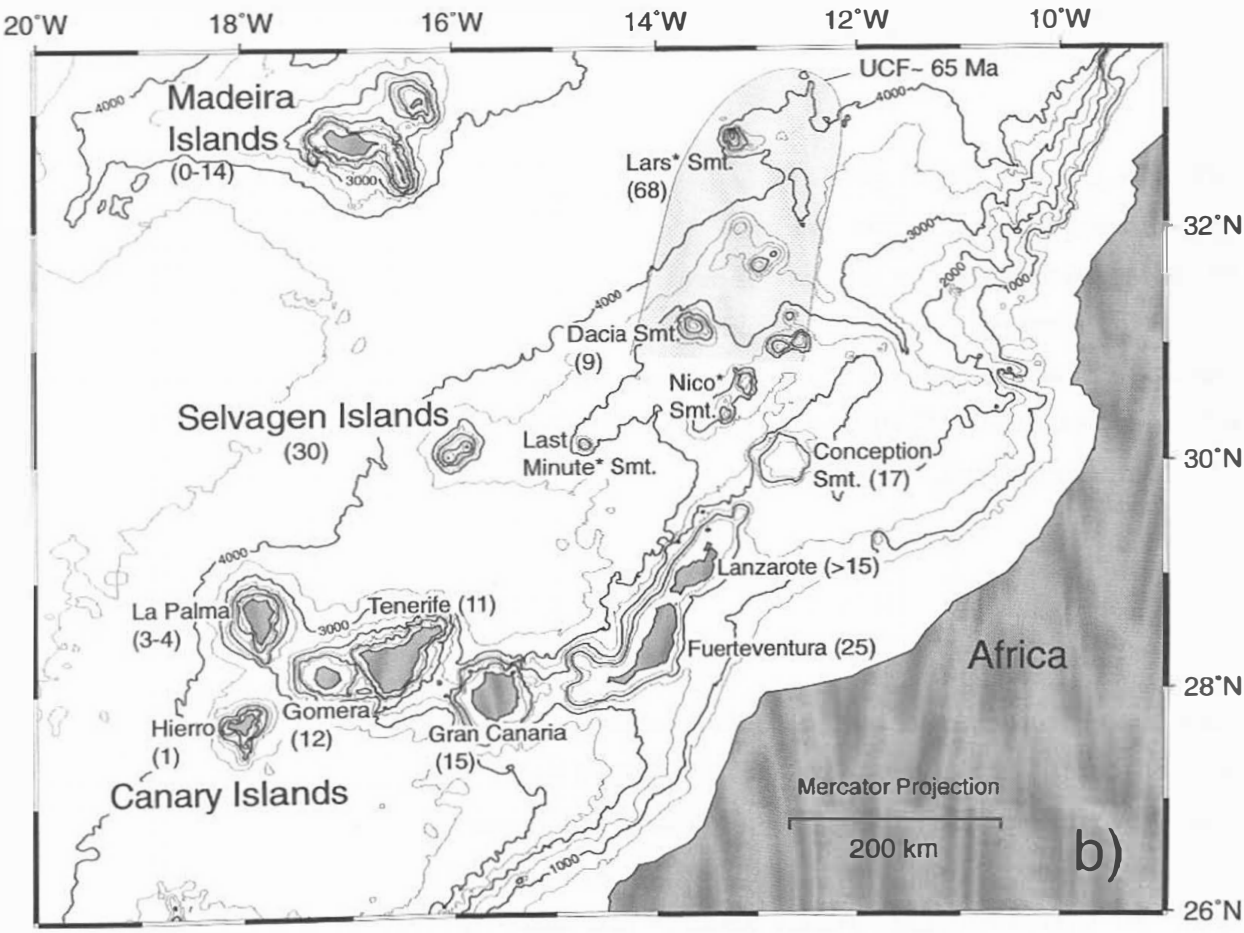

In this study, we present volcanological, petrological and geochemical data (including major and trace elements and Sr, Nd, Pb isotopes) as well as $^{40}Ar/^{39}Ar$ age determinations from volcanic rocks from the Selvagen Islands and seamounts to the NE and E of the archipelago. Our data suggest that these volcanic structures formed the earlier (Oligocene to late Cretaceous) Canary hotspot track. The data further imply that the Canary hotspot track is ~ 450 km wide and ~ 800 km long and that general but diffuse age progression exists from older in the NE (68 Ma) to younger in the SW (1 Ma).

5.2 General Geology

Selvagen archipelago

The Selvagen Islands lie 270 km south of Madeira Island in the eastern North Atlantic (Fig. 5.1b). The island group is located on the edge of a positive bathymetric anomaly hosting seven large seamounts to the east and northeast of the Selvagens and the Canary Islands 160 km to the south. The archipelago consists of the main island Selvagem Grande (2.4 km^2, highest altitude: 163 m a.s.l.) and a group of small islands, the largest being Selvagem Pequena (0.2 km^2, highest altitude: 49 m a.s.l.), 18 km to the SW of Selvagem Grande (Fig. 5.2). The Selvagen Island group forms the two summits of a SW-NE elongated cone that ascends from more than 3000 m water depth.

a) Selvagem Grande

This table-topped island has steep cliffs crowned by a plateau at ~ 100 m a. s. l.. The subaerially exposed portion of the island can be divided into five main stratigraphic units which are in order of increasing stratigraphic position: I) basanitic to phonolitic basement, II) abrasion platform covered by Oligocene/Miocene carbonate sediments, III) mafic dikes, IV) epiclastic conglomerates, and V) primarily basanitic/alkali basaltic volcanic sequence (summarized in part by Honnorez, 1966 and geological mapping by Zbyszewski et al., 1979) (Fig. 5.3). A composite profile summarizing the stratigraphy of Selvagem Grande and Selvagem Pequena is shown in Fig. 5.4.

I) Basement

The basement unit consists primarily of greenish phonolitic intrusions (dikes and sills) (Honnorez, 1966). Sanidine (5-30 %), nepheline (≤ 15 %) and amphibole (≤ 10) are the most abundant phenocrysts in the phonolites. Clinopyroxene and magnetite dominate the very fine-grained matrix. Accessory minerals are sphene, sodalite, apatite and zircon. Locally, the phonolites are intruded into layers containing volcanic bombs (Samples J 33, J 34). The

bombs contain 1-3 % amphibole, 1 % orthopyroxene and less than 1 % magnetite as phenocryst phases. K-Ar ages of 24-27 Ma have been reported from phonolites from these units (Portugal Ferreira et al., 1988).

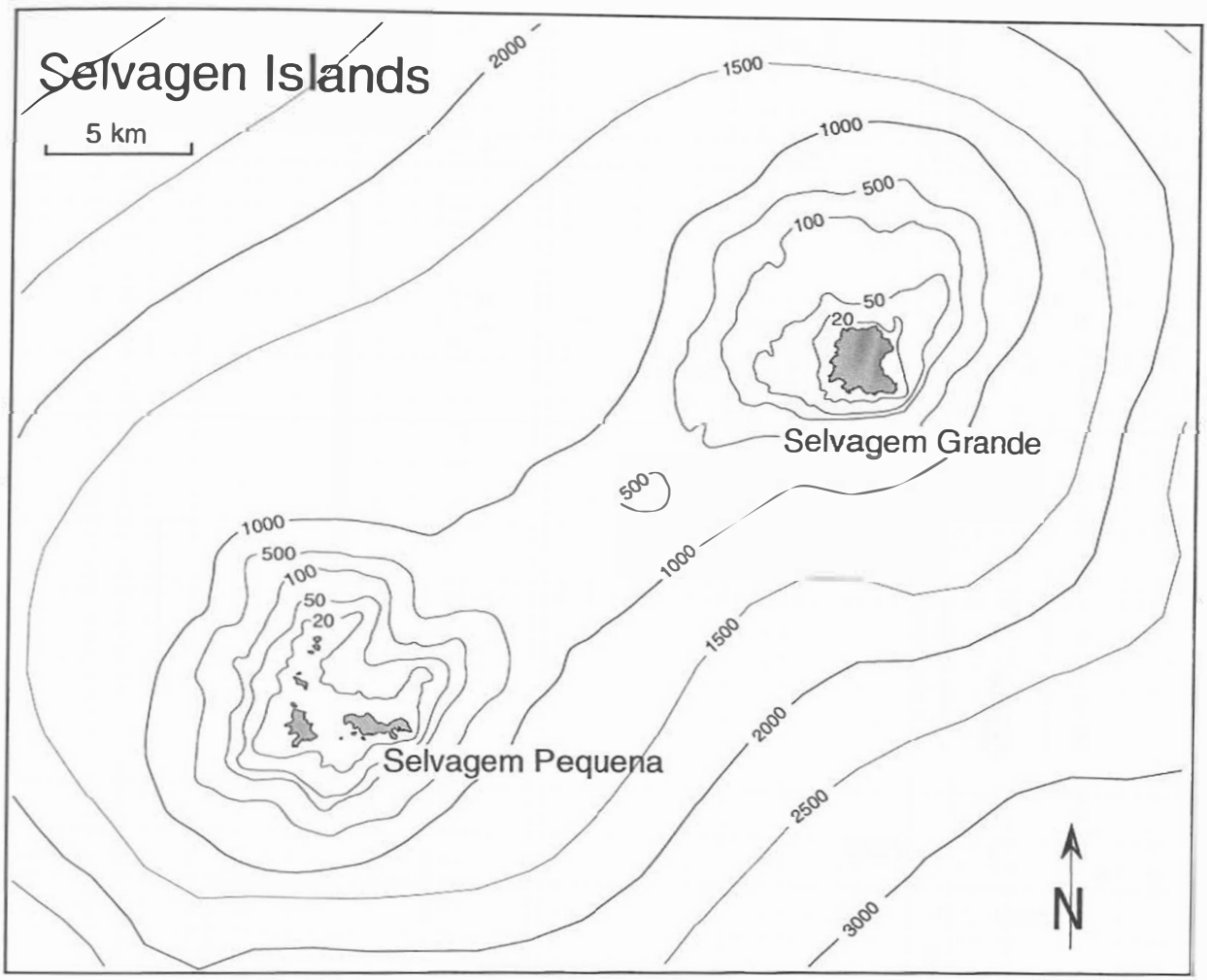

Fig. 5.2:

Selvagen archipelago bathymetry. Source: TOPEX (Smith and Sandwell, 1997). Shallow bathymetry above 1500 m after Carvalho and Brandão (1991).

II) Abrasion platform and overlying carbonate bank

At ~ 80 m above sea level, the basement complex is truncated by an abrasion platform that is overlain by organogenic calcareous sediments (2-5 m thick) containing Oligocene and Miocene shallow-water marine fossils (see Mitchel-Thomé, 1976 and references therein and H. Zankl, pers. com.). A distinctive feature of Selvagem Grande is the occurrence of carbonate dikes infilling fractures probably caused by volcanic stress (Mitchel-Thomé, 1976). These fractures cut the phonolitic basement and have subsequently been filled by infiltrated calcareous sands from the overlying carbonate platform (Morais, 1940), thus forming carbonate dikes with vertical layering that is often symmetrical to dike axis.

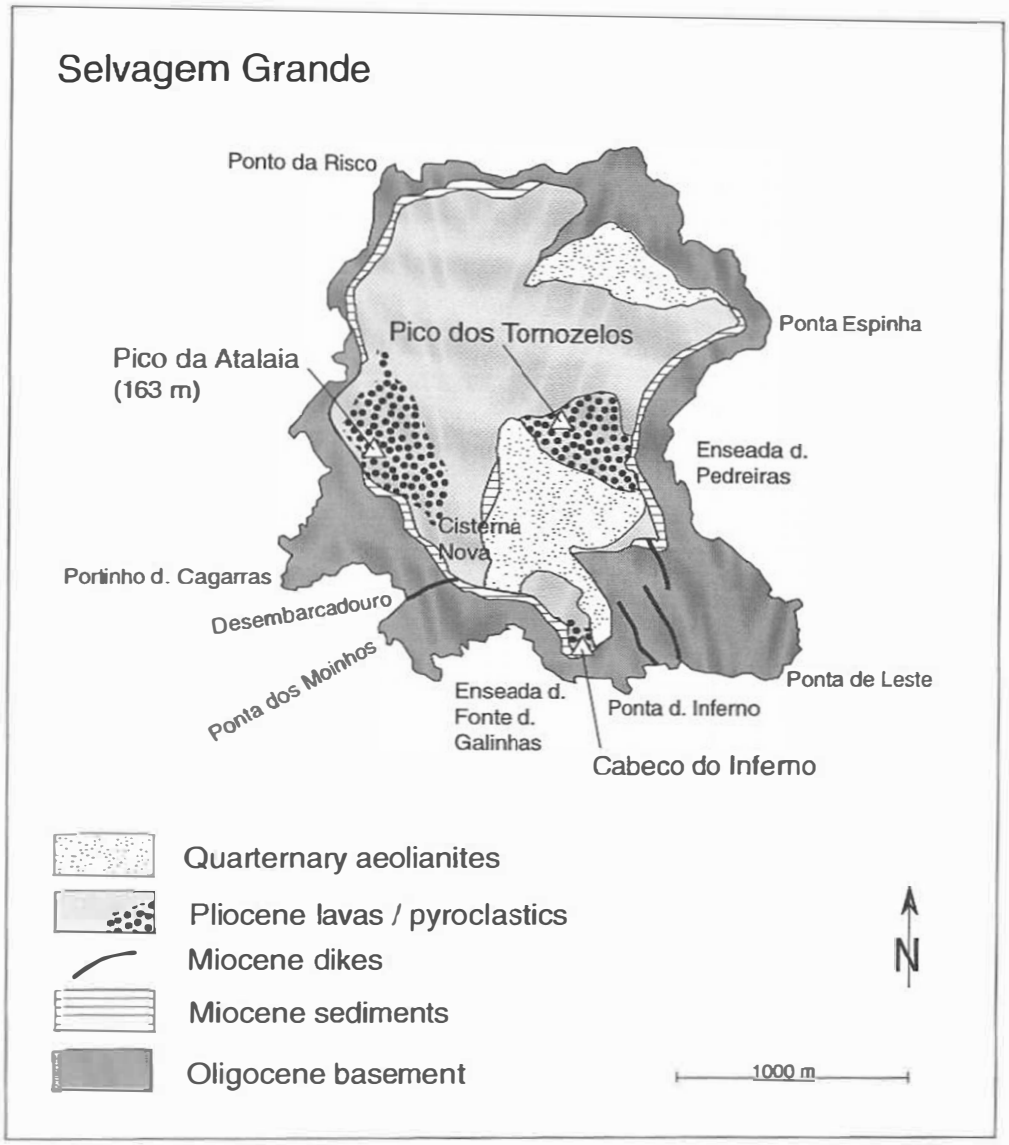

Fig. 5.3:
Geological map of Selvagem Grande. Modified from Zbyszewski et al. (1979).

III) Mafic dikes in southeast Selvagem Grande

The tephritic to phonolitic basement and the calcareous sediments are cut by mafic olivine-bearing (≤ 5 %) dikes in the southeastern part of the island.

IV) Epi-clastic conglomerate

The carbonate sediments are overlain by 3-4 m, greenish, fine-grained clastic sediments in the southwestern part of the island. The conglomerate is epi-clastic and contains 1) carbonate (Miocene algae, snails, echinodermata and mostly micritic pellets) and 2) lithic particles (amphibole and pyroxene crystals, minor tachylitic glass particles and coarse clasts of mafic through phonolitic volcanic rocks, as well as amphibole cummulates). All particles

are rounded, including the carbonates, indicating that the underlying Miocene carbonates have been reworked and re-sedimented.

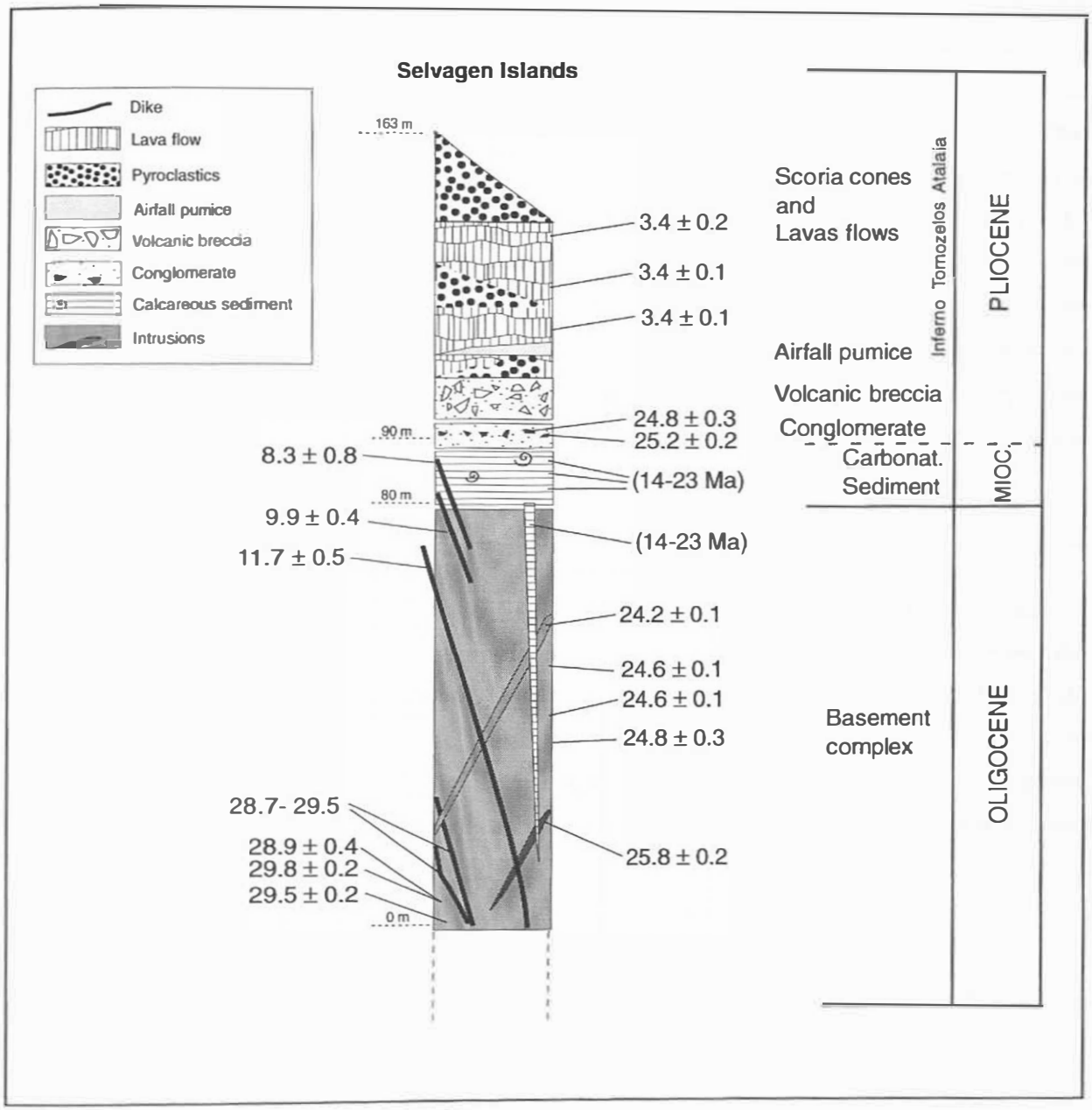

Fig. 5.4:

Composite sections for Selvagem Grande and Selvagem Pequena summarizing the stratigraphic sequence of the archipelago. Radiometric age data in Ma (with 2 σ error). Ages in parenthesize for carbonate sediments are derived from $^{87}Sr/^{86}Sr$ analyzes (see text for details).

V) Young volcanic unit

The base of this unit in the southern and eastern Selvagem Grande consists of a coarse, orange volcanic breccia (≤ 8 m). The dense volcanic clasts of the breccia (up to several centimeters in diameter) are oxidized and appear to have been deposited under subaerial conditions in contrast to the underlying epi-clastic conglomerates. Overlying the breccia in the southern part of the island is a sequence of bomb layers, scoria and lava flows that thickens towards the Inferno volcanic center in southern Selvagem Grande (see Fig. 5.3). This sequence is overlain by a phonolitic airfall pumice. The pumice is non-stratified, can be 1-3 m thick and is whitish to light beige. The Tornozelos cinder cone (eastern Selvagem Grande) overlies this pumice and is in turn overlain by the plateau-forming mafic lava flows from the Atalaia cinder cone in the western part of the island. Lavas from the young volcanic unit yielded K-Ar ages of 4 -11.5 Ma (Portugal Ferreira et al., 1988). The lavas contain up to 10-15 % olivine, 3-5 % clinopyroxene (Ti-augite) and occasionally less than 1 % nepheline phenocrysts in a groundmass composed primarily of olivine, clinopyroxene, plagioclase and magnetite.

b) Selvagem Pequena

This small, highly-eroded island (~ 0.5 km^2, highest altitude 49 m) is formed by pyroclastic agglomerates of reddish vesicular lapilli that are highly dissected by nephelinitic and phonolitic dikes (Honnorez, 1966). The numerous other small islands (e.g. Ilhéus do Norte, Ilhéu de Fora) located on the same shallow (< 20 m below sea level) submarine platform as Selvagem Pequena (Fig. 5.2) show the same general geology as Pequena (Zbyszewski et al., 1979). No age data have been published from the western islands including Selvagem Pequena.

Seamounts to the East and Northeast of the Selvagen Islands

The seamounts to the E and NE of the Selvagen Islands form a scattered group of volcanoes located between 90 km and 420 km north of the easternmost Canary Islands (Fig. 5.1). No geochemical or age data have been published from these seamounts. Only the larger volcanic complexes have been named on bathymetric maps. To avoid confusion, the unnamed seamounts, which we dredged during the Poseidon 235 cruise, have been given working names marked by an * on Figure 5.1. All of the seamounts except Conception Bank, rise from depths of more than 3000 m. Guyot-shaped or table-topped structures were dredged. Elevation of summit plateaus decrease from south to north: beginning in the south, the large Guyot-shaped Conception Bank Seamount, situated on a NE extension of a ridge formed by the eastern Canary islands of Lanzarote and Fuerteventura has a wide, flat plateau that reaches up to 250 m below sea level. Approximately 80 km NW of Conception Bank the NE-SW

elongated Nico Seamount with two summits rises to water depths of less than 300 and 400 m. Dacia Seamount is located to the NE and forms a plateau at 400 m water depth. At the northeastern end of the belt, Lars Seamount forms a top plateau at around 900 m water depth. An exception is the cone-shaped Last Minute Seamount, located halfway between Nico Seamount and Selvagem Grande, which reaches a minimum water depth of 1100 m.

All dredged samples were basaltic except for one sample from Last Minute Seamount, which was phonolitic. Dacia and Conception Bank Seamounts contain olivine (ol) and variable amounts of clinopyroxene (cpx) and plagioclase (plg) phenocryst phases (see sample list in the Appendix). The samples from Nico, Last Minute and Lars Seamount are aphyric. The groundmass of basaltic samples consists primarily of plg needles, cpx and variable amounts of tachylite. Beach cobbles and boulders were dredged from Conception Bank and Nico Seamount. Samples from Conception Bank Seamount were often highly vesicular.

5.3 Preparation and analytical techniques

Most submarine samples were encrusted by carbonate or covered with manganese crusts and are in part strongly altered. After cutting the freshest parts from each sample, they were crushed, washed in distilled water in an ultrasonic bath, hand-picked (under a binocular microscope) and subsequently powdered in an agate mill. Rock powders were dried in a furnace to drive off moisture. H_2O and CO_2 were analyzed with an infrared photometer (Rosemount CSA 5003). Whole rock major element data and trace elements Ni, Co, Cr, Ga, V, Zn, Rb, Sr, Zr, Nb, Ce, Y and Ba were determined by X-ray fluorescence spectrometry (XRF) on fused glass beads using a Phillips X'Unique PW1480 X-ray flourescence spectrometer at GEOMAR and calibrated with international standards. Additional trace elements (Cs, Hf, W, Tl, Y, Rb, Ba, Th, Nb, Ta, U, Pb, Zr and all REE) were determined from mixed acid (HF-aqua regia-$HClO_4$) pressure digests using a VG Plasmaquad PQ1 inductively coupled plasma-mass spectrometer (ICP-MS) at the Department of Geology, University of Kiel. Details of the analytical methods have been described by Garbe-Schönberg (1993). The accuracy of standard material BHVO-1, BE-N and Ja 2, analyzed along with the samples, is better than 10% for Pr, Hf, Rb, Ba, Th, Nb, U, La, Ce, Nd, Sr, Sm, Zr, Eu, Tb, Dy, Ho, Er, Tm, Yb and Lu, up to 15 % for Ta, Pb and Y and generally better than 4 % for all REE in respect to the reference values. Duplicate digests of samples yield a precision better than 3%. Mean and standard deviation for international reference material analyzed along with the samples are given in Table 5.2 and 5.3.

Sr, Nd and Pb isotopic ratios were measured at GEOMAR on a Finnigan MAT 262 thermal ionization mass spectrometer (TIMS) in static mode. Samples were leached in 6N HCL for 1 h at 120°C. A subset of submarine samples was leached for 3.5 h in a mix of 6N HCL and 8 N HNO_3 for Sr analyses. The chemical separation techniques have been described in Hoernle and Tilton (1991). $^{87}Sr/^{86}Sr$ was fractionation-corrected within-run to $^{86}Sr/^{88}Sr$ of 0.1194 and the precision of the standard runs for NBS987 was 0.710254±11 (n=7), $^{143}Nd/^{144}Nd$ was normalized within-run to $^{146}Nd/^{144}Nd$= 0.7219 and La Jolla yielded an average ratio of $^{143}Nd/^{144}Nd$ = 0.511844± 9 (n=9). NBS981 (n=19) gave $^{206}Pb/^{204}Pb$= 16.893± 4, $^{207}Pb/^{204}Pb$= 15.433± 5 and $^{208}Pb/^{204}Pb$= 36.513± 16. All Pb isotope analyses were corrected for fractionation to the values given in Todt et al. (1996). The total chemistry blanks were < 200 pg and are thus negligible. Replicate analyses of standards give an external reproducibility better than 0.025% per amu for Pb and better than 0.000015 for $^{143}Nd/^{144}Nd$ and $^{87}Sr/^{86}Sr$. Replicate analyses of samples were within analytical uncertainty.

The ages of 24 samples (including 4 seamount samples) were determined by $^{40}Ar/^{39}Ar$ laser total fusion analyses at the GEOMAR Geochronology Laboratory using a 25 W Spectra Physics argon ion laser connected to a MAP 216 series mass spectrometer fitted with a Baur-Signer ion source and a Johnson electron multiplier. Between 8-11 (except sample DS 822-2) single grains (rock/glass fragments or plagioclase crystals) of each sample were completely fused and analyzed (see Table 5.1 for number of single particles analyzed).

Details of preparation, analytical methods and experiment parameters are given in Geldmacher et al. (2000). Age uncertainties were calculated by partial differentiation of the age equation (Dalrymple and Duffield, 1988) and include uncertainties in the determination of the flux monitor (J), the blank determination, the regression of the intensities of the individual isotopes, and the mass discrimination correction (1.0083 per AMU). Ages and error estimates were calculated as mean apparent age of each set of particles (rock chips, crystals) fused using the method of Young (1962) (single fusion ages weighted by the inverse of their variance), assuming an initial 'atmospheric' $^{40}Ar/^{39}Ar$ ratio of 295.5. Isochrons have been calculated as inverse isochrons using York's least squares fit that accommodates errors in both ratios and correlation of errors (York, 1969). In order to estimate the scatter of the single fusion data from each set, mean squared weighted deviates (MSWD) were calculated for the mean apparent ages and isochron ages (Wendt and Carl, 1991). If the scatter was greater than predicted from the analytical uncertainties (MSWD > 1), the analytical error was expanded by multiplying by the square root of the MSWD (York, 1969).

Due to the reasonably good control of the initial $^{40}Ar/^{36}Ar$ ratios in isotope correlation diagrams (see Appendix), inherited or excess ^{40}Ar can be ruled out for samples within 2σ error from the accepted initial value of 295.5 or lower. Therefore, except for sample J 9 and J 35g, the mean apparent age, instead of the isochron age, is preferred to represent the age of crystallization. Because the mean squared weighted deviates (MSWD) for the mean apparent ages of samples J 9 and J 35g show a large scatter (MSWD > 3), the isochron age (with MSWD of 1.85 and 2.24) is accepted for these samples instead of the apparent age. However, there are no significant differences between isochron and mean apparent age for these samples. In general, all samples presented in this study have similar isochron and mean apparent ages within 2σ error of each other. Accepted ages are presented in Table 5.1. All errors are quoted at the 2σ level. Mean apparent ages, isochron ages and mean square weighted deviates (MSWD) are presented in the Appendix.

5.4 Results

Results of the age determinations and their stratigraphic relationship are shown in the composite profiles of Fig. 5.4.

a) Selvagen archipelago

$^{40}Ar/^{39}Ar$ age determinations

Unit I: Basement

K-feldspar and amphibole crystals from basement phonolitic samples (J2, J9, J23, J32) yielded a very restricted age range of 24.2 - 24.8 Ma (Table 5.1), which agrees well with K-Ar age determinations of 24 to 27 Ma for phonolitic samples (Portugal Ferreira et al., 1988). A mafic intrusion yielded an age of 25.8± 0.2 Ma (J 41), slightly older than the phonolites. Amphibole crystals from two mafic clasts from the epi-clastic conglomerate overlying the carbonate platform yielded ages of 24.8± 0.3 Ma (J 35g) and 25.2± 0.2 Ma (J 35f) within the age range observed in the basement samples.

Unit III: Mafic Dikes

Three samples from mafic dikes that cut the basement and the carbonates give mid Miocene ages of 8.3± 0.8 Ma (J 43), 9.9± 0.4 Ma (J 36), and 11.7± 0.5 Ma (J 42).

Unit V: Young Volcanic Unit

Samples from lava flows from each eruptive center yielded identical ages within the analytical uncertainty of 3.4± 0.1 Ma (J 49, Tornozelos), 3.4± 0.1 (J 30, Inferno) and 3.4± 0.2 Ma (J 8, Atalaia).

Table 5.1:

Sample	Type	N	Age (Ma)
Selvagem Grande			
Pliocene lavas			
J 49 Basanitic flow, Tornozelous complex	wr	11	**3.4 ± 0.1**
J 30 Alkali basaltic flow, Inferno complex	wr	11	**3.4 ± 0.1**
J 8a Alkali basaltic flow, Atalaia complex	wr	8	**3.4 ± 0.2**
Miocene dikes			
J 43 Basanitic dike	wr	14	**8.3 ± 0.8**
J 36 Basanitic dike	wr	14	**9.9 ± 0.4**
J 42 Basanitic dike	wr	12	**11.7 ± 0.5**
Oligocene basement			
J 32 Phonolitic intrusion	kfsp	10	**24.2 ± 0.1**
J 9 Phonolitic boulder	kfsp	11	**24.6 ± 0.1**
J 23 Phonolitic intrusion	kfsp	9	**24.6 ± 0.1**
J 2 Ponolitic clast in breccia	kfsp	15	**24.8 ± 0.3**
J 35f Phonotephr. clast in Unit III	amph	10	**25.2 ± 0.2**
J 35g Tephritic clast in Unit III	amph	9	**24.8 ± 0.3**
J 41a Phonotephritic intrusion	amph	10	**25.8 ± 0.2**
Selvagem Pequena			
SP 2 Tephriphonolitic dike	wr	14	**28.7 ± 0.4**
J 54 Tephritic boulder	amph		**28.9 ± 0.4**
J 54 Tephritic boulder	kfsp		**29.8 ± 0.2**
J 56B Tephritic dike	amph		**28.9 ± 0.2**
J 56A Tephritic dike	amph		**29.2 ± 0.3**
J 50 Breccia	amph		**29.5 ± 1.6**
J 55 Phonolitic dike	amph		**29.5 ± 0.2**

Table 5.1 (continued):

Sample	Type	N	Age (Ma)
Dacia Seamount			
DS 809-1 Basanitic clast	wr	11	**9.2 ± 0.3**
Conception Seamount			
DS 822-4 Alkali basaltic pebble	wr	9	**16.6 ± 0.2**
DS 822-2 Alkali basaltic boulder	wr	3	**17.5 ± 0.6**
Lars Seamounmt			
DS 832-2 Tephritic clast	wr	10	**67.7 ± 0.2**

Table 5.1:

Radiometric ages calculated from $^{40}Ar/^{39}Ar$ isotope composition of whole rocks (wr), alkali feldspar and amphibole phenocrysts (kfsp, amph). N = Number of single crystals / whole rock particles analyzed. Errors are quoted at the 2 σ-level. Accepted ages are listed, based on the criteria discussed in the Analytical Techniques chapter (see Appendix for analytical details).

Selvagem Pequena

Seven samples from Selvagem Pequena covering the entire geochemical range gave nearly identical ages around 29 Ma. Ages of amphibole separates from the agglomeratic breccia yielded an age of 29.5± 1.6 Ma (J 50). Dikes that cut the agglomerates yielded ages of 28.7± 0.4 Ma (SP 2), 28.9± 0.2 Ma (J 56B), 29.2± 0.3 Ma (J 56A) and 29.5± 0.2 Ma (J 55). Mineral separates from a beach boulder (J 54) gave ages of 28.9± 0.4 Ma for amphiboles and 29.8± 0.2 for alkali feldspar (Table 5.1). Therefore, the age of Selvagem Pequena is slightly older than the Basement Unit on Selvagem Grande (24.2 - 25.8 Ma).

Major and trace elements

Major and trace element data for all samples are given in Table 5.2 and 5.3. According to the classification of Le Maitre (1989) (see Fig. 5.5), Selvagem Pequena (29-30 Ma) ranges in composition from basanite through phonolite. Samples from the Basement Unit I (24-26 Ma) on Selvagem Grande are compositionally very similar to those from Selvagem Pequena, ranging for the most part from tephrite to phonolite (Fig. 5.5, 5.6). Although no difference in age is apparent between mafic and evolved samples from Selvagem Pequena, the tephrites and phonotephrites (24.8-25.8) from Selvagem Grande yield slightly older ages than the tephriphonolites and phonolites (24.2-24.8 Ma).

The Oligocene rocks on both Selvagem Pequena and Selvagem Grande show increasing SiO_2, Al_2O_3 and alkalis and decreasing FeO^T, CaO, CaO/Al_2O_3, TiO_2 and P_2O_5 with decreasing MgO (e.g., Fig. 5.6). The tephriphonolites and phonolites on Selvagem Pequena are slightly more undersaturated in SiO_2 than those on Selvagem Grande (Fig. 5.6, 5.6).

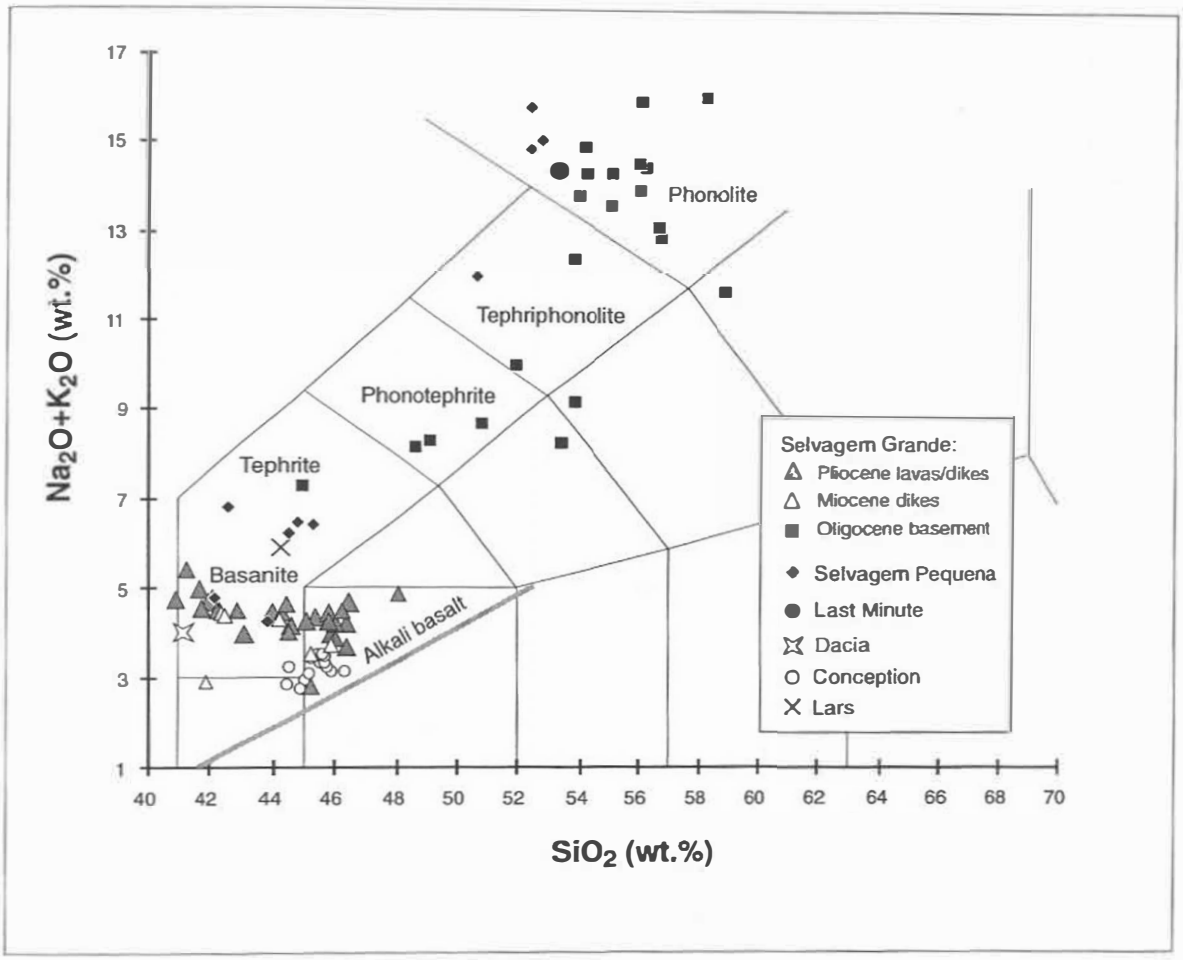

Fig. 5.5:
Total-alkalis versus SiO_2 diagram (TAS) after Le Bas et al. (1986) for volcanic units of the Selvagen Islands and sampled seamounts. Boundary of alkali basalts from McDonald and Katsura (1964). Samples are normalized to 100% on a volatile free basis.

On multi element diagrams (Fig. 5.7), tephritic to phonolitic samples from the Oligocene Basement Unit from Selvagem Grande and samples from Selvagem Pequena form enriched patterns with strong depletions in P and Ti and peaks at Sr and Zr. In general, the groups form similar patterns except for the depletion in mobile elements Rb and K in the tephritic sample from Selvagem Pequena, which most likely reflects alteration.

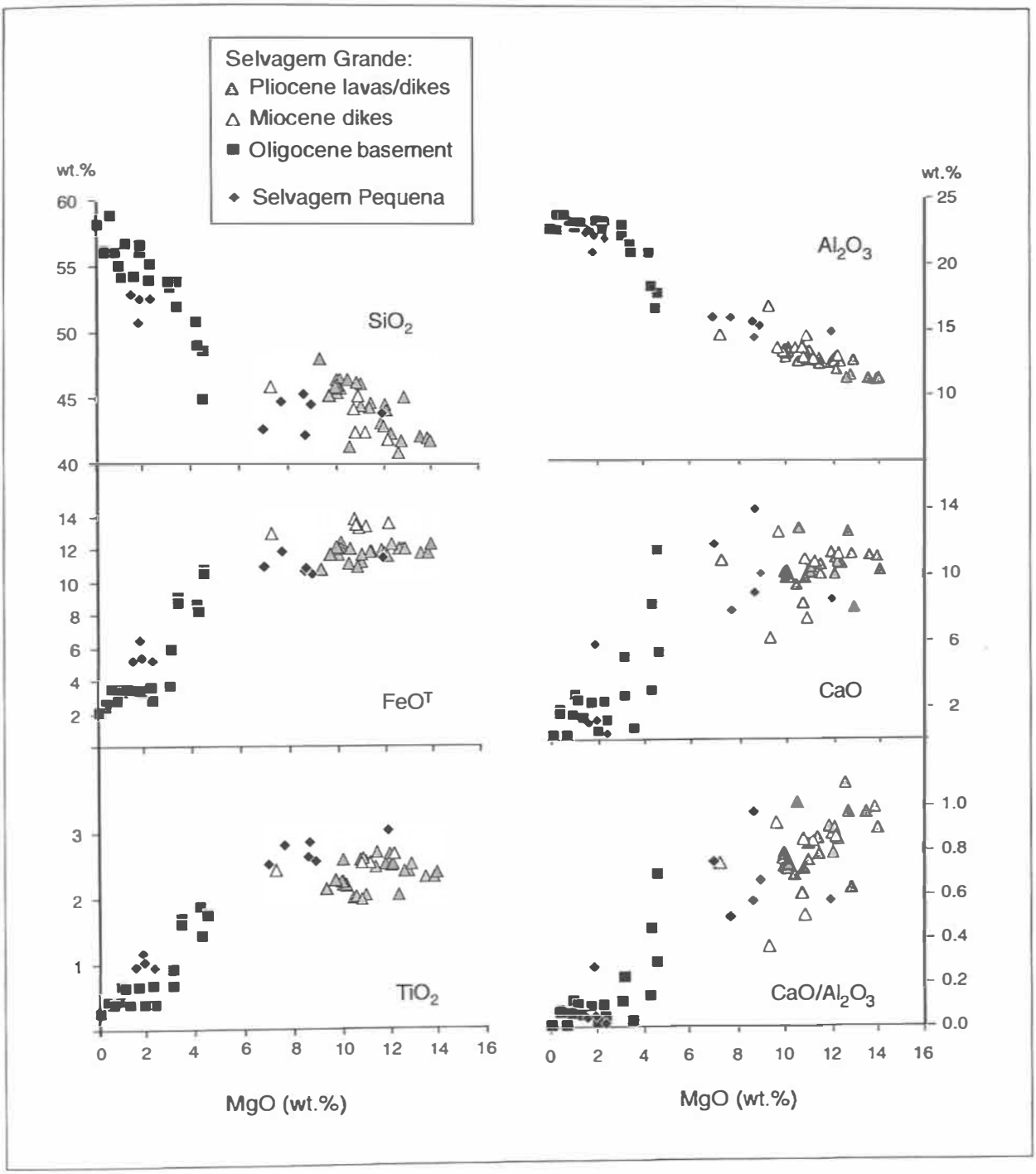

Fig. 5.6:

Selected major element variations verses MgO for samples from Selvagem Grande and Selvagem Pequena. Samples are normalized to 100% on a volatile free basis.

The Unit III Miocene dikes (8-12 Ma) on Selvagem Grande range from alkali basalt to basanite (Fig. 5.5) and completely overlap the Pliocene (3.4 Ma) mafic volcanic rocks of Unit IV in major element composition, except for slightly higher FeO^T (Fig. 5.6) and lower Na_2O. Both Pliocene volcanics and Miocene dikes have similar major element and compatible trace element correlations: SiO_2 and Al_2O_3 increase and P_2O_5, CaO, CaO/Al_2O_3 ratio, Ni and Cr

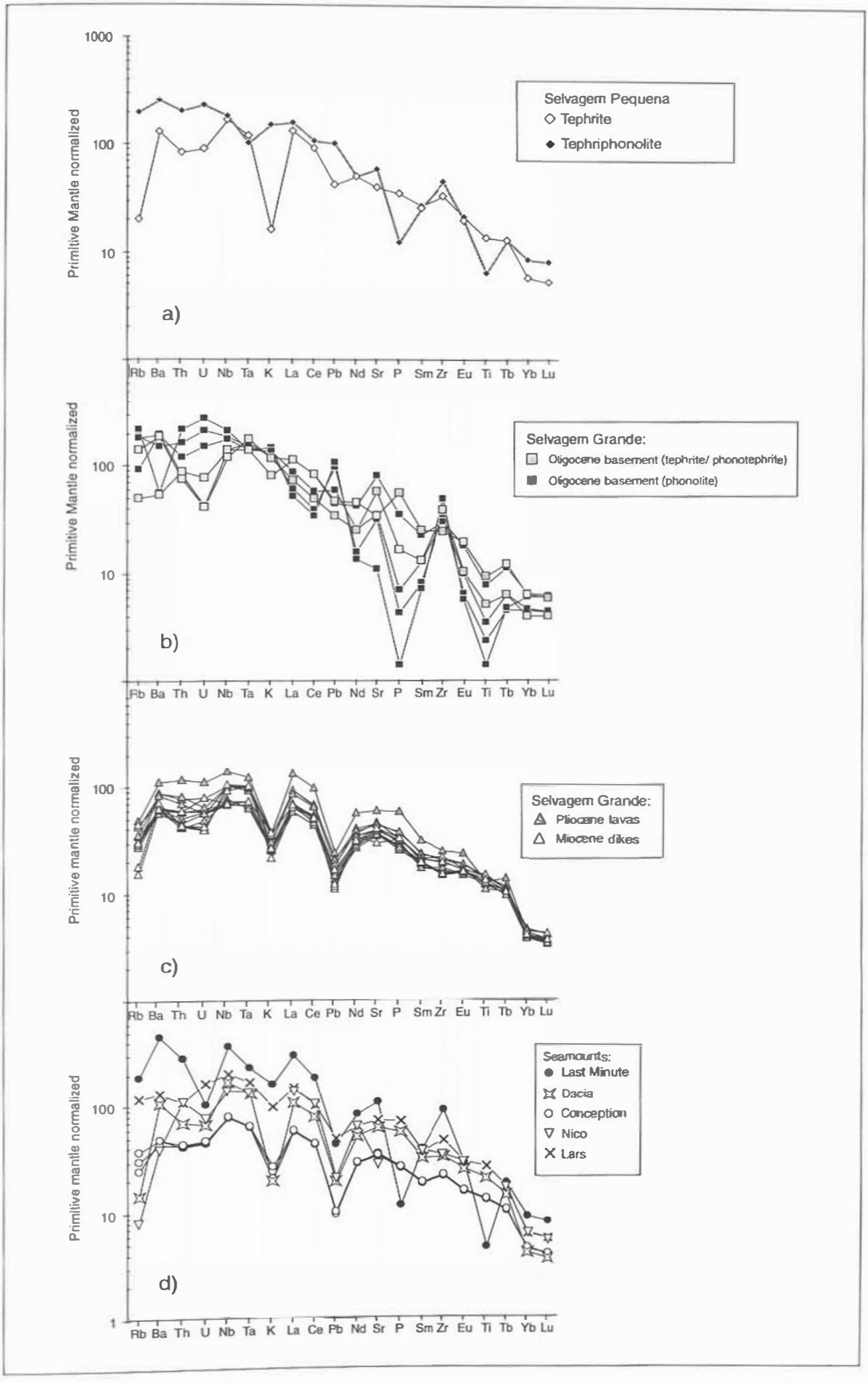
Primitive Mantle normalized
1000
100
10
Rb Ba Th U Nb Ta K La Ce Pb Nd Sr P Sm Zr Eu Ti Tb Yb Lu
Selvagem Pequena
◇ Tephrite
◆ Tephriphonolite
a)
Selvagem Grande:
Oligocene basement (tephrite/ phonotephrite)
Oligocene basement (phonolite)
b)
Primitive mantle normalized
Selvagem Grande:
Pliocene lavas
Miocene dikes
c)
Seamounts:
Last Minute
Dacia
Conception
Nico
Lars
d)
1

Fig. 5.7 (previous page): *Multi-element diagram of Oligocene basement from Selvagem Pequena (a) Selvagem Grande (b), Miocene alkali basaltic/basanitic dikes and Pliocene lavas from Selvagem Grande (c) and sampled seamounts (d). Normalized to primitive mantle after Hofmann (1988).*

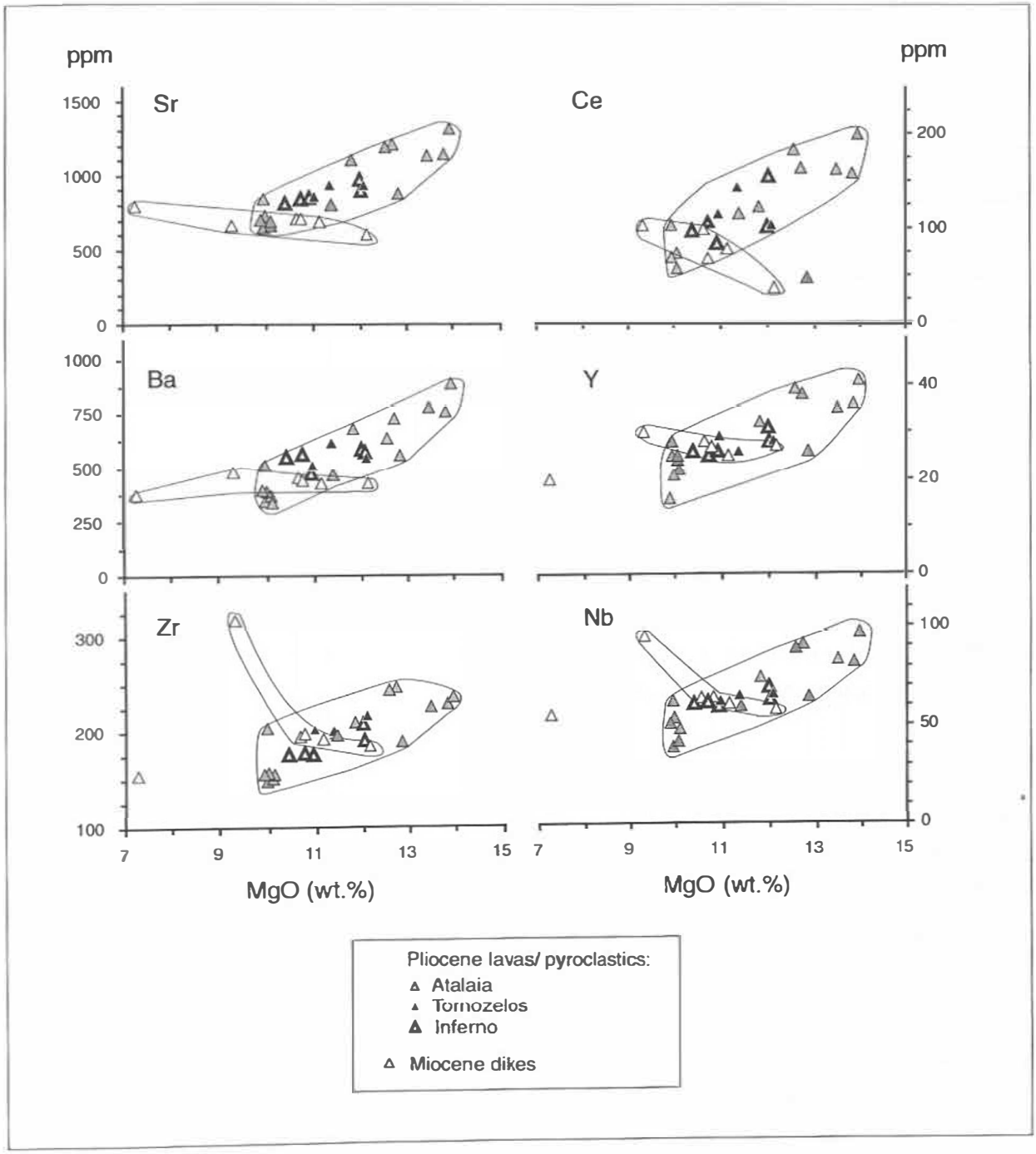

Fig. 5.8:
Trace element contents of alkali basaltic to basanitic Miocene dikes and Pliocene lavas on Selvagem Grande in respect to MgO. The Miocene basalts form an inverse correlation with MgO, whereas the Pliocene basalts form a positive correlation.

decrease with decreasing MgO, whereas Fe_2O_3 , K_2O, Na_2O and TiO_2 show no distinct trends. However, the Miocene dikes and the Pliocene volcanic rocks differ in their incompatible trace element correlations with MgO. Whereas the Miocene dikes show a general increase in incompatible element content with decreasing MgO, the Pliocene volcanic rocks show decreasing incompatible trace element concentrations (e.g. Sr, Ba, Nb, La, Ce, Nd, Sr, Sm, Eu) with decreasing MgO (Fig. 5.8).

On the multi-element diagram (Fig. 5.7), samples from both units exhibit enrichment in highly and moderately incompatible elements and depletion in the Heavy Rare Earth Elements (HREE) relative to the Light Rare Earth Elements (LREE) (e.g. $(La/Yb)_n$ = 15-18, $(Sm/Yb)_n$ = 4.5-7.3) similar to patterns for Ocean Island Basalts (OIB). The patterns show characteristic enrichment of Nb and Ta, as well as depletion in K and Pb and Ba/Nb < 9 and Ba/La < 10 and thus resemble the trace element characteristics of HIMU basalts (generally believed to represent recycled oceanic crust with high time integrated $^{238}U/^{204}Pb$ isotope ratios = "high μ") (e.g. Weaver, 1991).

Sr-, Nd,- and Pb isotopes

Sr-, Nd-, and Pb isotope ratios of representative samples from the Selvagen archipelago and neighboring seamounts are listed in Table 5.4. Oligocene, Miocene and Pliocene volcanic rocks from the Selvagen Islands have similar $^{143}Nd/^{144}Nd$ (0.51289 – 0.51292). The $^{87}Sr/^{86}Sr$ isotopic ratios (0.702999-0.703484) show relatively greater variation. The generally higher $^{87}Sr/^{86}Sr$ of the Oligocene and Miocene volcanic rocks most likely reflect greater seawater alteration of these older samples that were submarine during part of their history.

On plots of $^{206}Pb/^{204}Pb$ vs. $^{207}Pb/^{204}Pb$ and $^{208}Pb/^{204}Pb$ (Fig. 5.9), Oligocene Basement Unit and Miocene/Pliocene volcanic rocks define two distinct groups, with the Oligocene rocks having more radiogenic Pb isotopic compositions (Oligocene rocks: $^{206}Pb/^{204}Pb$= 19.65–19.90, $^{207}Pb/^{204}Pb$= 15.52–15.61, $^{208}Pb/^{204}Pb$= 39.47–41.15; Miocene/Pliocene rocks: $^{206}Pb/^{204}Pb$= 19.33–19.40, $^{207}Pb/^{204}Pb$= 15.55 – 15.58, $^{208}Pb/^{204}Pb$= 39.14 – 39.23). The volcanic rocks from Selvagem Grande and Selvagem Pequena overlap completely in their Nd and Pb isotopic composition with mafic alkaline volcanic rocks from the Canary Islands but have distinct Nd and Pb isotopic compositions from Madeira archipelago volcanic rocks.

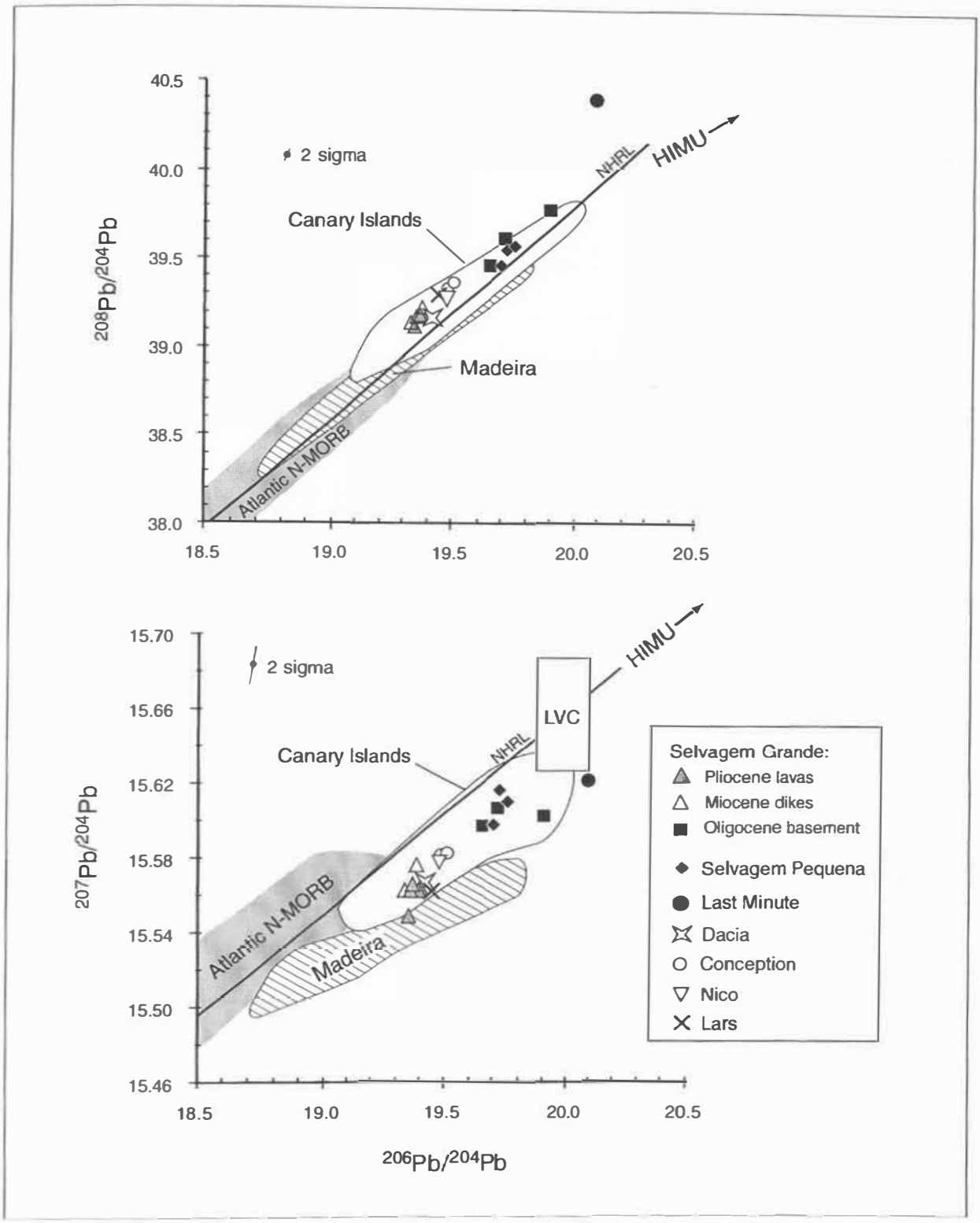

Fig. 5.9:

$^{206}Pb/^{204}Pb$ vs. $^{208}Pb/^{204}Pb$ and $^{207}Pb/^{204}Pb$ for samples from Selvagen archipelago and the seamounts analyzed in this study. Pb isotopic ratios largely overlap with the field for the Canary Islands forming a positively correlating trend below the Northern Hemisphere Reference Line (NHRL) in the $^{206}Pb/^{204}Pb$ vs. $^{207}Pb/^{204}Pb$ diagram. Data sources for Atlantic N-MORB between 10°N and 30°N from Dupré and Allègre (1980); Cohen and O'Nions (1982); Ito et al. (1987), Madeira data from Geldmacher and Hoernle (submitted), Canary

Islands from Hoernle et al. (1991) and Hoernle (unpublished data). Only data from Miocene to recent mafic alkaline volcanic rocks, which do not show evidence of lithospheric contamination (Hoernle, 1998), are shown. The Low Velocity Component (LVC) is a common plume component found throughout western and central Europe and the western Mediterranean (Hoernle et al., 1995). We assume that the parent/daughter ratios of the seamounts and Selvagen archipelago volcanics were not significantly modified by partial melting and fractionation processes. Therefore the measured isotopic compositions are believed to represent the composition of the sources at the present.

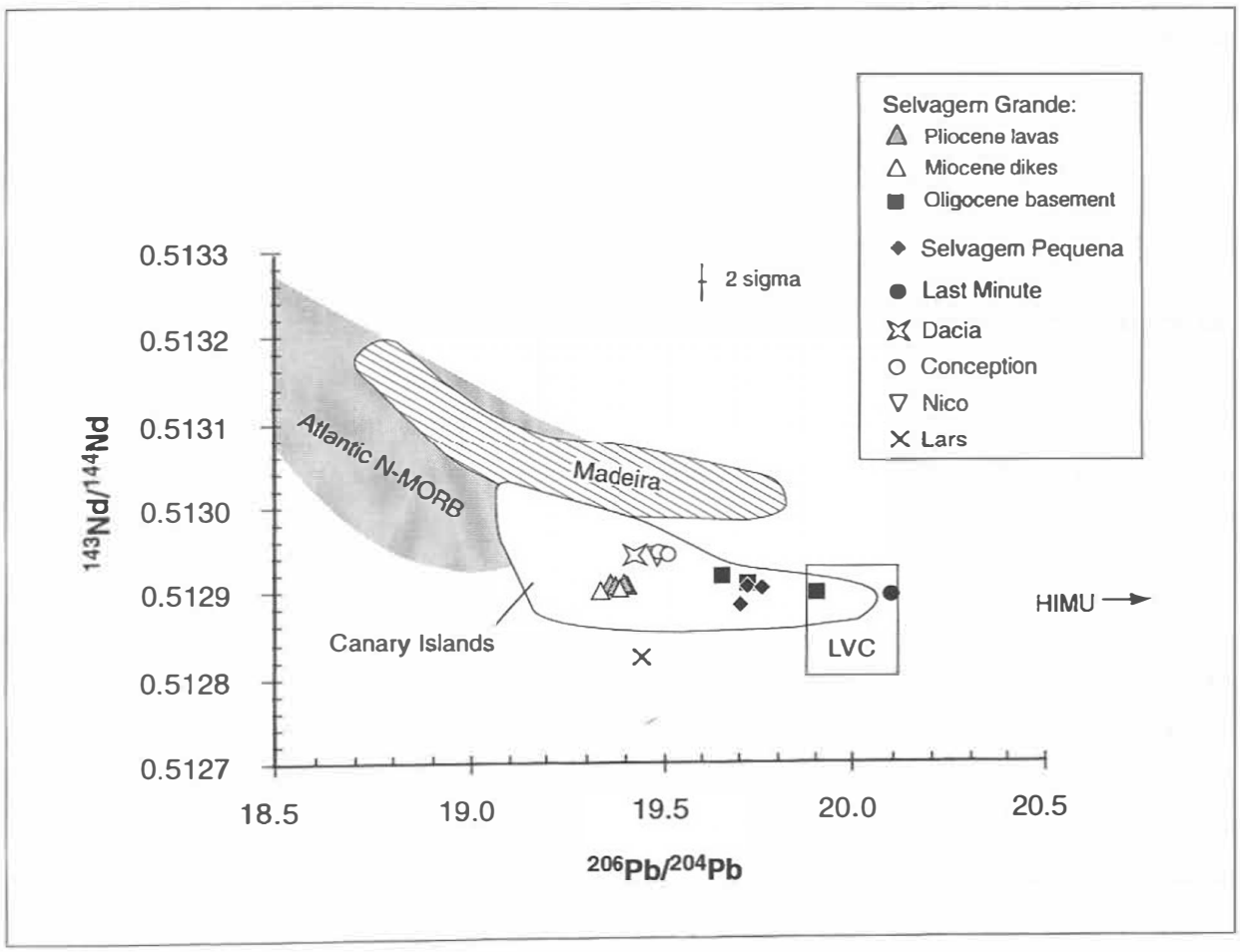

Fig. 5.10:
$^{206}Pb/^{204}Pb$ vs. $^{143}Nd/^{144}Nd$ diagram. Samples from the Selvagen archipelago and the seamounts analyzed in this study do not show any influence of the Madeira hotspot but overlap with the field for Canary Island data. Data sources as for Fig. 5.8.

Additionally, one calcareous dike (J 21) and three samples from the base, middle and top of the carbonate sediments (J 59 a,b,c), covering the abrasion platform above the Oligocene basement on Selvagem Grande, were analyzed for their $^{87}Sr/^{86}Sr$ ratio in order to

date the carbonates through correlation with the Sr-seawater evolution curve of Paytan et al. (1993). The $^{87}Sr/^{86}Sr$ ratios of carbonate sediments and dikes range between 0.7083 and 0.7088, which correspond with ages of 14 - 24 Ma. An Oligocene to Miocene age for the carbonates has also been proposed based on palaeontological data (see Mitchel-Thomé, 1976). Interestingly, there is no correlation between stratigraphic position and seawater evolution, reflecting re-deposition of the largely unconsolidated carbonate particles in a high energetic, shallow marine environment or secondary changes of the $^{87}Sr/^{86}Sr$ ratio. The lowest ratio (≈ 24 Ma) could reflect possible gain or exchange of Sr with coexisting magmatic rocks that would lower the $^{87}Sr/^{86}Sr$ ratio (Gieskes et al., 1986). However, since later diagenetic modification, e.g. due to interaction with more recent seawater, will increase the $^{87}Sr/^{86}Sr$ ratio of Cenozoic carbonate rocks, the highest ratio (≈ 14 Ma) is taken as the minimum age for the carbonate rocks.

b) Seamounts

$^{40}Ar/^{39}Ar$ age determinations

The oldest age of 67.7 ±0.2 Ma (DS 832-2) was determined on a sample from the northern summit of Lars Seamount. Two samples from the upper southern slope of Conception Bank Seamount yielded ages of 16.6 ±0.3 (DS 822-4) and 17.5 ± 0.6 Ma (DS 822-2). An age of 9.2 ±0.3 Ma was determined for a sample from the top of Dacia Seamount (DS 809-1).

Major and trace elements

Major and trace element compositions show that all samples from the Dacia, Conception, Lars and Nico Seamounts have primitive alkali basalt to basanitic compositions with enriched HIMU-like OIB trace element signatures (Fig. 5.7). The anomalously low Rb and K contents for the Nico and Lars Seamount samples, as well as the low Ba and Sr for Nico Seamount, most likely reflect alteration of these samples. The sample from Last Minute Seamount has a phonolitic composition, which has similar major and trace element characteristics to the Oligocene samples from the Selvagen Islands.

Sr, Nd, and Pb isotopes

The Sr, Nd, and Pb isotopic ratios of selected samples from Dacia, Nico, Conception Bank and Lars Seamounts are similar to those from the Miocene and Pliocene volcanic rocks from Selvagem Grande (Fig. 5.9, 5.10). Sample DS 832-2 from Lars Seamount has slightly lower $^{143}Nd/^{144}Nd$ ratios (see Fig. 5.10) than Selvagen and other seamount samples. The phonolite sample from Last Minute Seamount (DS 836-2) has radiogenic Pb (e.g. $^{206}Pb/^{204}Pb$

ratio of 20.1) and has a similar composition to Oligocene samples from the Selvagen (Fig. 5.9, 5.10).

Table 5.2: XRF data

Sample	J-1	J-4	J-6	J-7	J-8a	J-10	J-12	J-13	J-14	J-15	J-16
Unit	PL/At.	PL/At.	PL/At.	PL/At.	PL/At.	PL/At.	PL/At.	PL/At.	PL/At.	PL/At.	PL/At.
Rock type	AB flow	B bomb	B bomb	AB flow	AB flow	B block	AB flow	B bomb	B bomb	AB flow	B flow
SiO_2	44.23	39.92	42.12	44.33	45.73	41.03	46.03	40.44	39.83	43.62	43.95
TiO_2	2.54	2.21	2.47	2.16	2.18	2.27	2.19	2.34	2.35	2.44	2.67
Al_2O_3	12.56	10.81	12.2	12.89	13.28	10.95	13.48	11.18	11.09	12.24	12.64
Fe_2O_3 [T]	11.89	11.22	11.72	12.00	11.56	11.53	11.99	11.70	11.80	11.71	11.71
MnO	0.17	0.19	0.18	0.20	0.19	0.20	0.19	0.20	0.20	0.18	0.17
MgO	9.71	12.78	11.53	9.76	9.81	13.53	10.00	12.34	12.24	12.43	11.23
CaO	10.23	12.61	11.28	10.76	9.78	11.29	9.80	12.48	12.46	9.78	10.02
Na_2O	3.10	3.36	2.65	3.03	3.32	3.39	2.96	3.80	3.59	3.07	3.11
K_2O	1.13	1.10	1.22	0.79	0.80	1.17	0.68	1.02	0.99	1.03	0.97
P_2O_5	0.78	1.27	1.04	0.56	0.62	1.32	0.52	1.53	1.60	0.84	0.78
CO_2	0.2	1.56	0.12	0.96	0.06	0.28	0.05	1.17	0.11	1.58	0.07
H_2O	1.95	1.04	2.37	1.08	0.65	1.01	1.12	0.23	1.19	0.04	1.25
Total	99.83	99.33	100.22	99.87	99.28	99.27	100.36	99.74	98.77	100.28	99.88
V	241	215	239	226	230	211	237	226	226	234	243
Cr	495	536	422	394	421	635	435	505	504	592	442
Co	64	65	59	65	58	65	61	64	66	60	58
Ni	550	465	369	370	264	534	350	434	484	429	343
Zn	138	121	124	122	128	120	131	128	126	122	120
Rb	26	29	25	18	19	31	16	25	17	29	19
Sr	836	1125	1097	669	645	1139	660	1204	1186	876	797
Y	28	35	32	24	25	36	25	38	39	26	26
Zr	205	227	211	153	148	229	151	247	244	189	199
Nb	62	83	74	43	39	82	42	91	89	64	59
Ba	512	779	682	371	340	759	372	724	631	559	469
Ce	103	162	122	73	69	158	57	163	183	47	115
Ga	19	16	16	17	18	18	18	14	16	19	19

Table 5.2
(continuation)

Sample	J-18	SG-10	SG-12	SG-13	J-26	J-27	J-28	J-29	J-30	J-45	J-46
Unit	PL/At.	PL/At.	PL/At.	PL/At.	PL/Inf.	PL/Inf.	PL/Inf.	PL/Inf.	PL/Inf.	PL/Inf.	PL/Inf.
Rock type	B flow	B flow	AB dike	AB block	AB bomb	AB flow	B bomb	B bomb	AB flow	B flow	B bomb
SiO_2	39.70	45.79	44.99	45.07	45.27	45.25	40.40	40.75	45.23	43.03	41.96
TiO_2	2.28	2.22	2.22	2.22	2.04	1.96	2.01	1.99	1.96	2.42	2.62
AL_2O_3	10.83	13.27	12.89	13.04	13.14	13.29	12.33	12.14	13.29	12.35	12.26
Fe_2O_3 T	11.71	12.08	11.77	11.97	11.11	10.92	11.79	11.92	10.74	11.29	11.53
MnO	0.20	0.19	0.26	0.22	0.19	0.20	0.25	0.21	0.18	0.19	0.18
MgO	13.27	10.11	9.77	9.73	10.76	10.14	10.28	11.85	10.53	11.62	11.72
CaO	12.52	9.85	9.93	10.03	10.13	10.43	12.73	12.60	9.67	10.46	11.47
Na_2O	3.42	3.61	3.22	3.34	2.99	3.50	4.17	3.45	3.41	2.81	3.41
K_2O	0.90	0.82	0.88	0.82	0.80	1.03	1.11	0.88	0.96	1.06	0.98
P_2O_5	1.59	0.66	0.60	0.60	0.76	0.67	1.55	1.40	0.71	0.81	0.97
CO_2	2.12	0.03	0.06	0.03	0.12	0.95	0.11	1.77	0.06	0.53	0.51
H_2O	0.07	0.55	0.94	0.70	1.84	0.55	0.98	0.05	1.33	2.17	0.92
Total	99.92	100.54	98.85	99.10	100.4	100.12	99.03	100.35	99.28	100.01	99.83
V	228	230	225	224	211	208	209	220	199	227	250
Cr	470	363	361	375	449	454	348	347	459	457	406
Co	66	60	71	63	58	53	66	66	55	59	61
Ni	470	332	468	314	456	435	377	351	360	360	342
Zn	128	135	129	125	121	131	152	135	114	123	121
Pb	12	19	19	20	19	24	28	24	20	25	25
Sr	1307	657	723	701	836	813	1516	1310	839	894	972
Y	41	22	21	16	26	26	44	42	25	28	31
Zr	237	156	158	156	176	177	253	221	178	191	209
Nb	97	48	54	51	59	61	107	93	63	63	69
Ba	887	334	390	393	471	549	1035	829	564	560	585
Ce	199	n.d.	n.d.	n.d.	84	97	205	157	106	154	102
Ga	16	20	16	17	18	18	15	17	17	17	17

Table 5.2
(continuation)

Sample	J-47b	J-48	J-49	J-19A	J-38	J-36	J-37	J-39	J-42	J-43	SG-1b
Unit	PL/Tom.	PL/Tom.	PL/Tom.	PL	PL	MD	MD	MD	MD	MD	MD
Rock type	B flow	B flow	B flow	AB dike	AB dike	B dike	B dike	AB dike	B dike	B dike	AB dike
SiO_2	43.25	43.91	44.19	41.20	43.66	41.86	42.08	41.70	42.00	39.54	41.71
TiO_2	2.48	2.46	2.57	2.09	1.95	2.52	2.48	2.42	2.53	2.53	2.22
Al_2O_3	11.78	12.31	12.56	12.40	15.14	12.63	12.95	13.41	12.75	12.27	13.19
$Fe_2O_3{}^T$	11.38	11.78	11.69	10.65	9.84	13.26	13.19	12.26	13.35	12.78	11.74
MnO	0.18	0.25	0.20	0.20	0.17	0.21	0.19	0.20	0.20	0.19	0.17
MgO	11.88	11.26	10.90	8.80	8.47	11.00	10.16	9.99	10.62	11.47	6.60
CaO	10.7	10.6	10.58	14.90	10.45	10.82	10.97	11.44	10.90	11.43	13.44
Na_2O	3.57	3.30	3.48	2.00	2.21	3.52	2.87	2.17	3.14	2.06	2.27
K_2O	0.78	1.08	1.12	0.52	2.22	0.84	1.19	1.08	1.17	0.66	1.08
P_2O_5	0.94	0.85	0.87	0.56	0.55	0.69	0.68	0.72	0.71	0.70	0.66
CO_2	0.04	0.04	0.09	2.67	3.84	0.13	2.42	3.66	0.03	0.60	2.79
H_2O	1.38	0.60	0.76	3.82	1.19	1.41	0.17	0.67	1.26	4.33	2.62
Total	99.64	99.76	100.32	101.01	100.80	100.38	100.83	101.10	100.16	99.99	99.81
V	256	237	246	224	203	271	263	251	255	268	230
Cr	516	526	480	284	252	401	370	302	391	339	358
Co	61	64	59	60	43	69	66	62	67	70	57
Ni	468	447	424	307	122	239	236	204	233	220	248
Zn	120	153	122	125	119	121	121	126	122	115	118
Rb	9	28	29	10	42	10	28	22	28	10	21
Sr	936	929	851	699	657	690	708	753	706	602	794
Y	28	26	29	22	30	25	28	27	26	27	20
Zr	217	202	203	162	317	193	196	202	198	185	155
Nb	66	65	62	42	95	61	63	67	63	58	55
Ba	545	615	511	376	481	425	455	558	443	425	377
Ce	103	142	114	78	103	78	98	97	67	37	n.d.
Ga	16	17	19	19	18	16	14	21	19	17	18

Table 5.2
(continuation)

Sample	J-25	J-33	J-34	J-35B	J-35F	J-35G	J-2	J-3	J-9	J-11	J-23
Unit	OB (?)	OB	OB	OB	OB	OB	OB	OB	OB	OB	OB
Rock type	M clast	B bomb	Tp bomb	Pt clast	Pt clast	T clast	P breccia	P breccia	P breccia	P block	Tp intrus.
SiO_2	50.26	46.16	45.5	44.75	42.89	42.35	52.38	51.58	52.57	56.21	49.36
TiO_2	0.88	1.46	1.42	1.67	1.56	1.65	0.38	0.38	0.41	0.25	0.63
AL_2O_3	20.70	18.35	18.14	18.31	15.65	15.58	21.97	21.61	21.02	21.79	20.90
$Fe_2O_3{}^T$	5.59	7.86	7.66	7.63	9.57	9.93	2.32	2.64	2.48	2.04	3.38
MnO	0.12	0.24	0.21	0.23	0.22	0.23	0.19	0.20	0.14	0.16	0.15
MgO	2.95	2.99	3.06	3.76	4.05	4.31	0.34	2.20	0.35	0.03	2.84
CaO	4.93	6.64	7.10	9.50	11.49	11.44	1.99	1.32	1.57	0.43	2.64
Na_2O	4.19	6.88	7.65	5.05	4.77	4.42	10.01	9.60	11.04	10.88	6.64
K_2O	3.58	0.96	1.08	2.59	2.41	2.45	3.44	3.75	3.83	4.53	4.68
P_2O_5	0.36	0.98	1.25	0.46	1.21	1.22	0.10	0.10	0.09	0.03	0.15
CO_2	0.10	6.08	5.11	5.38	5.30	0.45	0.21	0.16	0.05	0.06	0.12
H_2O	5.46	0.09	0.06	0.62	0.83	4.74	5.03	4.80	4.57	3.03	6.34
Total	99.75	99.57	99.10	100.81	101.02	99.89	98.62	98.64	98.40	99.67	98.21
V	104	193	190	226	227	229	43	37	55	25	66
Cr	<18	38	55	<18	30	34	<18	<18	32	39	<18
Co	20	36	36	31	42	44	12	11	12	8	13
Ni	30	53	71	38	41	46	5	25	11	5	15
Zn	74	114	130	110	116	124	124	109	88	94	86
Pb	85	29	31	31	33	29	94	124	111	135	82
Sr	1107	935	1053	799	620	615	692	1936	574	207	1531
Y	23	35	38	27	36	37	18	18	14	14	17
Zr	387	325	319	236	245	255	529	508	373	517	305
Nb	84	88	92	83	74	78	197	220	133	153	116
Ba	1190	1102	1049	1053	660	374	1041	1037	885	335	1135
Ce	85	139	171	75	130	129	79	90	<10	56	20
Ga	21	19	18	13	19	15	28	29	34	34	22

Table 5.2
(continuation)

Sample	J-24	J-31	J-32	J-41a	SG-3	SG-4	SG-5	SG-6	SG-7	SG-8	SP-1
Unit	OB	OB	OB	OB	OB	OB	OB	OB	OB	OB	SP
Rock type	P intrus.	P dike	P intrus.	P intrus.	P breccia	P breccia	P breccia	S breccia	P intrus.	P intrus.	T boulder
SiO_2	51.55	51.38	52.38	46.94	52.78	52.77	52.97	55.22	53.63	51.58	37.81
TiO_2	0.65	0.64	0.64	1.37	0.42	0.37	0.37	0.38	0.37	0.68	2.24
AL_2O_3	21.06	21.35	21.84	17.44	21.69	21.63	21.65	22.12	21.82	21.51	14.03
Fe_2O_3 T	3.32	3.29	3.29	7.85	2.70	3.21	3.27	3.30	3.34	3.47	9.75
MnO	0.16	0.15	0.16	0.24	0.16	0.16	0.16	0.15	0.18	0.15	0.23
MgO	0.90	1.60	1.08	4.16	0.83	1.83	1.81	0.60	1.23	2.17	6.17
CaO	2.75	2.22	2.45	8.01	2.46	1.44	1.75	0.47	1.40	2.50	10.97
Na_2O	8.66	9.57	10.09	4.22	9.76	7.60	7.72	5.50	6.61	9.36	5.55
K_2O	4.03	3.96	4.25	3.72	3.89	5.49	4.49	5.41	5.53	3.80	0.48
P_2O_5	0.15	0.15	0.15	0.77	0.11	0.08	0.08	0.37	0.08	0.152	0.68
CO_2	0.09	0.06	0.06	0.07	0.76	0.67	0.96	0.15	0.07	0.20	0.32
H_2O	5.99	3.99	2.19	4.87	2.90	5.58	5.91	6.43	6.08	4.44	5.15
Total	99.68	98.73	98.95	100.54	98.76	101.19	101.51	100.47	100.72	100.38	94.48
V	76	61	65	169	34	44	43	54	54	61	270
Cr	<18	<18	<18	51	<18	<18	<18	<18	<18	<18	38
Co	13	14	12	27	<4	<4	5	<4	<4	4	37
Ni	13	25	14	47	<2	<2	<2	3	<2	<2	25
Zn	83	84	86	110	92	128	147	88	138	87	121
Rb	75	85	104	58	100	115	107	141	130	86	10
Sr	742	413	634	1522	648	1053	563	1498	1932	550	664
Y	17	19	17	30	19	18	19	<2	5	17	34
Zr	334	331	330	319	346	467	498	470	489	306	303
Nb	119	120	124	84	96	140	144	147	145	108	96
Ba	1179	1113	1172	1252	1065	961	944	1154	1084	1130	737
Ce	56	95	64	107	n.d.	n.d.	n.d.	n.d.	n.d.	n.d.	n.d.
Ga	21	23	24	17	23	32	29	23	27	21	20

Table 5.2
(continuation)

Sample	J-51	J-54	J-56	J-57	J-58	SP-2	J-52	J-53	J-55	DS809-1	DS822-1
Unit	SP	SP	SP	SP	SP	SP	SP	SP	SP	Dacia	Concept.
Rock type	B dike	T boulder	T dike	T dike	B dike	Tp dike	P boulder	P boulder	P dike	B clast	AB boulder
SiO_2	39.93	40.06	41.76	42.26	37.05	47.54	49.39	49.25	47.63	39.39	43.53
TiO_2	2.77	2.53	2.41	2.46	2.52	1.10	0.92	0.97	0.87	3.54	2.27
AL_2O_3	13.51	14.18	14.27	14.50	12.61	19.44	20.74	20.63	19.82	11.98	13.58
Fe_2O_3 *	10.49	10.65	9.91	10.02	9.60	6.05	4.89	5.07	4.73	13.91	12.53
MnO	0.17	0.22	0.18	0.18	0.18	0.22	0.18	0.19	0.19	0.18	0.14
MgO	10.85	6.85	8.36	8.03	7.62	1.72	1.44	1.79	2.14	11.00	10.91
CaO	12.67	12.17	12.45	11.87	16.72	5.83	4.33	4.39	4.11	11.10	10.67
Na_2O	3.00	4.91	3.84	4.19	3.52	6.70	9.24	9.14	9.40	3.24	2.02
K_2O	0.85	0.85	2.00	1.77	0.64	4.49	4.78	4.74	4.85	0.60	0.62
P_2O_5	0.54	0.87	0.43	0.45	0.52	0.25	0.21	0.21	0.21	1.17	0.59
CO_2	3.86	4.02	2.32	2.78	3.44	0.27	2.60	2.54	2.95	0.30	0.08
H_2O	0.75	1.50	1.25	0.64	4.71	4.86	0.28	0.15	0.17	2.70	2.93
Total	100.57	100.01	100.29	100.27	100.21	99.15	99.55	99.64	97.60	99.11	99.87
V	356	300	307	313	323	152	120	131	119	293	261
Cr	332	125	256	272	504	32	<18	<18	<18<	354	470
Co	55	53	45	47	59	9	16	16	17	43	50
Ni	124	71	106	103	168	18	16	23	18	159	337
Zn	88	117	89	95	88	96	131	136	133	123	105
Rb	13	21	37	31	12	122	143	142	150	10	11
Sr	596	751	698	634	421	1148	1563	1533	1455	1032	587
Y	23	29	26	23	23	32	31	33	29	29	26
Zr	186	304	221	216	214	465	532	519	504	308	194
Nb	52	79	63	56	58	117	148	144	139	87	43
Ba	534	839	664	660	422	1491	1544	1545	1486	639	322
Ce	60	136	56	51	55	n.d.	122	137	113	80	112
Ga	16	17	19	15	18	26	33	31	31	18	20

Table 5.2
(continuation)

Sample	DS822-2	DS822-3	DS822-4	DS822-5	DS822-6	DS822-7	DS822-8	DS822-9	DS822-11	DS822-12
Unit	Concept.	Concept.	Concept.	Concept.	Concept.	Concept.	Concept.	Concept.	Concept.	Concept.
Rock type	AB boulder	AB pebble	AB pebble	AB pebble	AB pebble	AB pebble	AB pebble	AB pebble	AB pebble	B pebble
SiO_2	44.82	44.07	44.94	43.55	44.77	44.66	44.26	45.12	44.63	42.57
TiO_2	2.31	2.26	2.30	2.24	2.32	2.37	2.32	2.33	2.33	2.35
AL_2O_3	13.65	13.54	13.54	13.21	13.99	14.23	13.59	13.79	13.87	13.55
Fe_2O_3 T	12.56	12.69	12.77	12.69	12.74	11.86	12.70	12.80	12.73	12.46
MnO	0.17	0.16	0.17	0.16	0.17	0.16	0.17	0.18	0.17	0.14
MgO	10.01	9.89	10.45	10.82	9.50	8.69	10.23	10.00	9.92	9.84
CaO	10.78	10.94	10.5	11.13	10.73	11.03	10.92	10.58	10.59	11.49
Na_2O	2.43	2.39	2.40	2.16	2.53	2.46	2.51	2.58	2.63	1.93
K_2O	0.64	0.80	0.75	0.69	0.74	0.57	0.82	0.84	0.83	0.69
P_2O_5	0.57	0.58	0.56	0.61	0.60	0.58	0.67	0.57	0.59	0.58
CO_2	0.28	0.43	0.12	0.47	0.11	0.13	0.26	0.07	0.11	0.58
H_2O	2.23	2.05	1.95	2.56	1.94	2.93	2.14	1.59	1.81	3.53
Total	100.45	99.80	100.45	100.29	100.14	99.67	100.59	100.45	100.21	99.71
V	268	260	256	268	258	275	256	262	260	284
Cr	413	395	414	435	374	405	431	409	402	455
Co	52	49	51	51	50	43	47	55	47	46
Ni	222	205	224	261	185	183	199	214	259	234
Zn	105	103	100	104	101	103	105	106	102	100
Rb	14	19	18	18	15	12	20	22	21	17
Sr	580	570	551	589	575	589	626	562	571	590
Y	27	27	27	27	26	26	29	24	26	26
Zr	196	194	196	195	199	208	209	198	202	202
Nb	43	42	45	41	44	43	45	44	46	43
Ba	288	271	246	308	260	237	332	300	305	296
Ce	86	108	88	92	96	107	95	94	97	105
Ga	22	16	19	16	19	21	20	19	22	22

Table 5.2
(continuation)

Sample	DS822-13	DS822-15	DS822-28	DS822-30	DS832-2	DS836-2	BM ± 2σ
Unit	Concepl.	Concepl.	Concepl.	Concepl.	Lars	Last Minu.	Standard
Rock type	AB pebble	B pebble	AB pebble	B clast	T clast	P fragm.	
SiO_2	45.05	42.56	42.29	43.08	42.37	49.00	49.69 ± 0.33
TiO_2	2.32	2.27	2.29	2.24	4.65	0.84	1.14 ± 0.02
AL_2O_3	13.72	13.44	13.59	13.30	14.40	18.50	16.09 ± 0.44
Fe_2O_3 T	12.82	12.51	12.29	12.93	13.54	5.27	9.61 ± 0.07
MnO	0.18	0.16	0.16	0.17	0.16	0.26	0.15 ± 0.00
MgO	10.18	10.21	9.01	1093	4.93	1.81	7.47 ± 0.34
CaO	10.46	12.49	12.56	10.76	9.12	3.06	6.35 ± 0.02
Na_2O	2.62	2.13	2.26	2.33	2.69	7.98	4.96 ± 0.31
K_2O	0.85	0.59	0.64	0.78	2.98	5.20	0.17 ± 0.00
P_2O_5	0.57	0.63	0.63	0.62	1.50	0.25	0.12 ± 0.01
CO_2	0.06	1.04	1.65	0.26	0.49	0.25	n.d.
H_2O	1.72	1.87	2.61	1.86	2.06	5.19	n.d.
Total	100.55	99.90	99.98	99.26	98.89	9761	
V	254	271	260	264	343	61	205 ± 7
Cr	411	429	350	418	111	<18	133 ± 6
Co	52	45	44	52	18	14	42 ± 5
Ni	205	211	166	282	47	7	61 ± 4
Zn	104	101	103	101	229	173	119 ± 3
Rb	21	12	13	17	65	119	7 ± 3
Sr	559	666	593	589	1178	2014	225 ± 3
Y	26	29	29	27	42	40	30 ± 3
Zr	197	202	202	194	511	954	101 ± 3
Nb	44	43	44	43	93	268	9 ± 1
Ba	308	307	269	283	722	2921	251 ± 17
Ce	96	91	98	94	9	310	n.d.
Ga	20	18	22	16	23	28	19 ± 7

Table 5.2:

Major elements (in wt. %) and trace elements (in ppm) determined by XRF. Units: PL = Pliocene (At. = Atalaia, Inf. = Inferno, Torn. = Tornozelos), MD = Miocene Dikes, OB = Oligocene Basement, SP = Selvagem Pequena. Rock types: B = basanites, AB = alkali basalts, T = tephrite, Pt = phonotephrite, Tp = tephriphonolite, P = phonolite, M = mugearite, B = benmorite. BM standard is the average of n=7 which run with the samples

Table 5.3: Trace element data in ppm (ICP-MS)

Sample	J 7	J 8a	J 10	SG 10	SG 12	SG 13	J 30	J 45	J 49	J 36	J 42	J 43	SG 1b
Unit	PL	Pt.	Pt.	PL	PL	PL	PL	PL	PL	MD	MD	MD	MD
Type	AB	AB	B	B	AB	AB	AB	B	B	B	B	B	AB
Pr	8.93	8.53	18.7	8.67	9.80	9.49	12.4	13.1	12.5	10.9	10.8	10.5	9.57
Hf	3.95	4.04	5.42	3.78	4.22	4.02	4.37	4.73	4.98	5.12	5.12	5.09	4.24
Y	20.1	20.7	25.9	22.7	20.3	19.8	21.7	22.4	22.7	24.3	24.1	21.6	19.8
Rb	16.3	16.6	26.8	19.0	17.0	15.1	15.7	19.4	23.7	9.80	24.4	8.60	16.7
Ba	378	350	699	381	406	381	547	551	517	447	445	387	395
Th	4.22	3.90	9.82	3.47	4.98	4.87	6.50	6.76	5.84	3.66	3.57	3.69	4.96
Nb	44.0	43.7	89.9	49.1	46.6	44.8	65.8	66.5	65.5	67.2	67.0	59.6	44.8
Ta	2.42	2.47	4.43	2.27	2.65	2.66	3.37	3.57	3.56	3.73	3.68	3.68	2.63
U	1.22	1.19	2.34	1.01	1.21	1.32	1.66	1.33	1.19	0.85	0.83	0.88	1.65
La	40.9	37.1	85.4	41.6	44.0	43.1	58.9	58.9	54.2	43.2	42.7	40.7	43.3
Ce	77.5	71.9	161	76.4	85.6	82.9	109	113	105	88.8	87.2	84.4	84.1
Pb	2.65	2.45	4.36	2.28	2.82	2.66	3.83	3.71	3.30	1.98	2.06	2.22	2.96
Nd	34.2	32.9	68.8	34.0	38.6	37.2	44.8	49.3	46.8	42.5	42.1	41.3	37.7
Sr	669	654	1106	752	688	673	858	850	829	724	730	555	763
Sm	7.27	6.85	12.2	6.79	7.82	7.58	8.29	9.27	9.04	8.39	8.36	8.23	7.72
Zr	153	162	249	170	152	147	192	201	209	217	217	196	149
Eu	2.29	2.18	3.47	2.18	2.42	2.33	2.49	2.78	2.75	2.52	2.50	2.46	2.38
Tb	0.90	0.90	1.32	0.90	0.99	1.00	0.98	1.10	1.09	1.03	1.03	1.02	0.99
Gd	6.51	6.34	9.89	6.58	6.78	6.62	7.10	8.02	8.00	7.40	7.22	7.16	6.72
Tb	0.90	0.90	1.32	0.90	0.99	1.00	0.98	1.10	1.09	1.03	1.03	1.02	0.99
Dy	4.89	4.79	6.36	4.74	5.14	5.12	5.01	5.50	5.44	5.40	5.36	5.31	5.15
Ho	0.86	0.87	1.07	0.83	0.90	0.91	0.89	0.95	0.95	0.98	0.98	0.95	0.92
Er	2.05	2.08	2.53	2.12	2.30	2.29	2.16	2.28	2.24	2.42	2.40	2.37	2.35
Tm	0.27	0.26	0.30	0.26	0.28	0.28	0.27	0.28	0.27	0.31	0.30	0.30	0.27
Yb	1.57	1.62	1.80	1.57	1.64	1.65	1.66	1.65	1.65	1.93	1.88	1.85	1.67
Lu	0.21	0.22	0.24	0.21	0.23	0.23	0.22	0.22	0.22	0.26	0.27	0.26	0.23

Sample	J 25	J 35g	J 9	J 11	J 32	J 41a	SP 1	SP 2	DS 809-1	DS 822-2	DS 822-4	DS 822-9	DS 830-2
Unit	OB (?)	OB	OB	OB	OB	OB	Pequ.	Pequ.	Dacia	Concept.	Concept.	Concept.	Nico
Type	M	T	P	P	P	Pt	T	Tp	B	AB	AB	AB	AB
Pr	8.79	15.9	6.28	5.44	9.82	15.1	16.4	17.5	16.3	8.88	8.74	8.90	20.3
Hf	7.31	5.21	6.41	8.50	5.32	6.07	6.11	8.53	6.56	4.44	4.35	4.50	7.74
Y	16.7	30.7	15.0	17.8	18.6	27.9	31.8	32.2	28.2	25.3	25.0	25.6	33.4
Rb	76.8	27.5	105	121	100	50.9	10.8	106	7.95	13.6	16.9	20.4	4.50
Ba	1173	335	939	351	1204	1219	802	1558	654	298	271	302	251
Th	6.30	7.43	13.8	18.5	10.1	6.78	6.78	16.4	5.90	3.47	3.57	3.65	9.43
Nb	77.0	90.4	119	138	113	89.6	104	112	107	49.9	49.4	50.4	90.1
Ta	6.46	5.07	5.47	5.13	5.05	6.04	4.20	3.66	4.89	2.29	2.30	2.36	4.97
U	0.87	1.62	4.47	5.82	3.20	0.88	1.83	4.74	1.37	0.94	0.97	0.98	1.63
La	46.3	72.3	39.0	33.1	55.3	73.1	81.9	99.4	66.7	36.7	36.2	37.1	90.3
Ce	81.5	138	64.7	56.4	95.6	137	150	174	132	72.2	70.9	72.4	173
Pb	6.27	8.51	17.8	19.8	10.9	8.07	7.49	18.3	3.45	1.68	1.77	1.76	3.70
Nd	30.6	57.0	19.4	16.5	32.0	52.6	61.1	60.6	63.2	34.6	34.0	35.1	78.2
Sr	1088	642	594	208	656	1523	740	1096	1157	644	611	625	531
Sm	5.24	10.1	3.26	2.90	5.17	9.05	10.7	10.0	12.5	7.36	7.17	7.40	14.8
Zr	392	245	376	501	328	302	329	450	320	210	210	214	334
Eu	1.58	2.94	0.97	0.86	1.49	2.69	3.12	2.89	3.70	2.29	2.24	2.31	4.27
Tb	0.61	1.19	0.44	0.46	0.62	1.08	1.23	1.25	1.35	0.97	0.96	0.98	1.58
Gd	4.27	8.57	2.75	2.57	4.25	7.65	9.36	8.29	10.4	6.85	6.66	6.90	11.7
Tb	0.61	1.19	0.44	0.46	0.62	1.08	1.23	1.25	1.35	0.97	0.96	0.98	1.58
Dy	3.45	6.34	2.69	2.99	3.53	5.94	6.28	6.92	6.52	5.26	5.14	5.29	8.21
Ho	0.65	1.22	0.56	0.65	0.70	1.13	1.13	1.35	1.05	0.93	0.91	0.93	1.40
Er	1.79	3.13	1.67	2.12	1.99	3.00	3.06	3.86	2.52	2.40	2.36	2.44	3.45
Tm	0.26	0.42	0.27	0.35	0.29	0.42	0.39	0.56	0.30	0.31	0.30	0.31	0.45
Yb	1.69	2.72	1.91	2.58	1.98	2.80	2.44	3.62	1.68	1.85	1.82	1.86	2.62
Lu	0.26	0.38	0.28	0.39	0.29	0.41	0.34	0.52	0.23	0.26	0.25	0.26	0.36

Table 5.3 (continued)

Sample	DS 832-2	DS 836-2	Average	Standdev.
Unit	Lars	L. Minute	BHVO	2 σ
Type	T	P		
Pr	20.4	31.1	5.33	0.08
Hf	9.98	15.2	4.42	0.03
Y	43.0	41.5	24.2	1.93
Rb	64.1	105	9.47	0.95
Ba	806	2858	137	4.83
Th	8.99	24.1	1.19	0.16
Nb	129	237	18.1	0.70
Ta	6.05	8.31	1.06	0.06
U	3.41	2.18	0.42	0.08
La	95.0	190	15.9	0.67
Ce	167	301	37.6	1.27
Pb	8.79	7.77	2.08	0.30
Nd	76.9	98.7	24.0	0.15
Sr	1357	1968	419	35.2
Sm	14.5	15.2	6.04	0.11
Zr	461	890	170	12.9
Eu	4.31	4.25	2.00	0.01
Tb	1.59	1.76	0.92	0.01
Gd	12.3	12.3	6.12	0.05
Tb	1.59	1.76	0.92	0.01
Dy	8.07	9.19	5.18	0.06
Ho	1.40	1.69	0.95	0.01
Er	3.54	4.41	2.50	0.00
Tm	0.43	0.58	0.32	0.00
Yb	2.56	3.65	1.96	0.00
Lu	0.36	0.51	0.27	0.00

For abbreviations see Table 5.2

5.5 Discussion

Evolution of Selvagen archipelago

The subaerially-exposed history of the Selvagen Islands can be subdivided into six evolutionary stages of which three are magmatic: 1) Oligocene (24-30 Ma) shield stage, 2) a magmatic hiatus (14-23 Ma) accompanied by subaerial erosion to sea level and the subsequent formation of a carbonate bank on the eroded basement beneath sea level, 3) a mid Miocene (~ 8-12 Ma) rejuvenated stage, 4) a second magmatic hiatus accompanied by subaerial erosion and formation of submarine conglomerates, 5) a Pliocene (3.4 Ma) rejuvenated stage, and 6) a third magmatic hiatus (0-3.4 Ma).

1) Oligocene Shield Stage

The similarity in age and composition (in particular Nd-Pb isotopic composition) of the Basement Unit on Selvagem Grande (24-26 Ma) and Selvagem Pequena (29-30 Ma) suggest that both may be from the shield stage of a single, large Selvagen Volcano (Fig. 5.2).

The Pb isotopic composition of eastern North Atlantic volcanoes is particularly diagnostic in distinguishing the shield stage from post-erosional or rejuvenated volcanism. Detailed studies of Gran Canaria and Fuerteventura, Canary Islands (Hoernle et al., 1991; Hoernle and Tilton, 1991) and the Madeira/Desertas volcanic complex (Geldmacher and Hoernle, subm.) show that the shield stage of volcanism is characterized by more radiogenic Pb isotopes (e.g. $^{206}Pb/^{204}Pb \approx 19.5$-$20.0$) than the later rejuvenated stages (e.g. $^{206}Pb/^{204}Pb \approx 18.8$-$19.5$). This distinction holds up well in the Selvagen Islands where the Oligocene volcanic rocks have $^{206}Pb/^{204}Pb = 19.7$-19.9 in contrast to the Miocene and Pliocene rocks with $^{206}Pb/^{204}Pb = 19.3$-19.4 (Fig. 5.9, 5.10, Table 5.4).

In contrast to other eastern North Atlantic ocean islands, no tholeiitic or alkali basaltic rocks have been discovered during the shield stage on the Selvagens. These rocks, however, may form part of the submarine base of the volcano. Basanitic to phonolitic rocks occur during the later part of the shield stage on other North Atlantic ocean island volcanoes. For example, on Gran Canaria, transitional tholeiitic lavas were erupted between 14-15 Ma, alkali basalts to peralkaline rhyolites and trachytes from ~ 13.5-14 Ma and basanites and phonolites were erupted or intruded from ~13-7 Ma (Schirnick et al., 1999).

Selvagem Grande and Selvagem Pequena form two separate summits of a single, larger volcanic complex and join at depths of less than 1000 m (Fig. 5.2). The flat (< 20 m depth) plateau where Selvagem Pequena and the numerous small surrounding islands and rock peaks are located, obviously represents the remains of a former continuous, larger island.

The similar immobile isotope ratios of Nd and Pb support derivation of the evolved Oligocene Selvagen samples (phonotephrite through phonolite) from the associated mafic (basanite and tephrite) volcanic rocks through fractional crystallization of the observed phenocryst and groundmass phases. The major and trace element compositions of the evolved Oligocene rocks (Fig. 5.6, 5.7) can be explained by combined fractionation of phenocryst phase amphibole and microphenocryst phases apatite and sphene and accumulation of phenocryst phase sanidine and microphenocryst phase zircon. Amphibole fractionation beginning at 5 wt.% MgO results in a steep decrease of the K/Rb. The characteristic trace element signatures of amphibole fractionation (e.g. troughs in Ba, K, Sm, Ti on multi-element diagrams) are partly masked by accumulation of sanidine (that occurs as a phenocryst up to 30 modal percent) and results in high Ba, K and Sr concentrations. Increase of the Nb and Ta ratio with decreasing MgO points to sphene fractionation (Green and Pearson, 1986). Steep depletion of P with decreasing MgO results from apatite fractionation.

Table 5.4a: Sr and Nd isotope data from the Selvagen Islands and neighboring seamounts

Sample	RT	Age	Rb* (ppm)	Sr* (ppm)	$^{87}Sr/^{86}Sr$ m.	$^{87}Sr/^{86}Sr_m$ (strong leach)	$^{87}Rb/^{86}Sr$	$^{87}Sr/^{86}Sr$ initial	Sm* (ppm)	Nd* (ppm)	$^{147}Sm/^{144}Nd$	$^{143}Nd/^{144}Nd$ m.	$^{143}Nd/^{144}Nd$ initial
Selvagem Grande													
J 8a	AB	3.4	16.62	654	0.703040(6)		0.07	0.703036	6.85	32.85	0.13	0.512908(7)	0.512906
SG 10	B	(3.4)	18.99	752	0.703041(6)		0.07	0.703038	6.79	34.02	0.12	0.512914(6)	0.512911
J 30	AB	3.4	15.68	858	0.703152(8)		0.05	0.703150	8.29	44.82	0.11	0.512906(10)	0.512904
J 45	B	(3.4)	19.36	850	0.703105(7)		0.07	0.703101	9.27	49.30	0.11	0.512912(6)	0.512910
J 45 Dupl.					0.703108(7)							0.512904(6)	
J 49	B	3.4	23.70	829	0.703076(6)		0.08	0.703072	9.04	46.77	0.12	0.512910(6)	0.512907
J 36 (MD)	B	9.9	9.80	724	0.703154(6)		0.04	0.703148	8.39	42.47	0.12	0.512906(9)	0.512898
J 42 (MD)	B	11.7	24.45	730	0.703168(8)		0.10	0.703153	8.36	42.13	0.12	0.512904(6)	0.512896
J 35g(MC)	T	24.8	27.48	642	0.703074(7)		0.12	0.703031	10.12	56.99	0.11	0.512912(6)	0.512895
J 9	Ph	24.6	104.64	594	0.703663(6)	0.703874(7)	0.51	0.703484	3.26	19.38	0.10	0.512911(7)	0.512895
J 32	Ph	24.2	100.30	656	0.703151(5)		0.44	0.702999	5.17	32.02	0.10	0.512902(6)	0.512887
J 41a	T	25.8	50.95	1523	0.703384(7)	0.703291(7)	0.10	0.703256	9.05	52.58	0.10	0.512922(6)	0.512904
Selvagem Pequena													
SP 1	T	(29)	10.80	740	0.703101(7)		0.04	0.703084	10.69	61.06	0.11	0.512906(5)	0.512886
J 56	B	29			0.703252(9)							0.512888(8)	
SP 2	Tp	29.7	106.01	1096	0.703188(6)		0.28	0.703073	10.01	60.58	0.10	0.512906(5)	0.512887
Dacia Seamount													
DS 809-1	B	9.2	7.95	1157	0.703062(5)		0.02	0.703059	12.53	63.16	0.12	0.512946(4)	0.512939
Conception Seamount													
DS 822-4	AB	16.6	16.90	611	0.703044(6)		0.08	0.703025	7.17	34.05	0.13	0.512949(5)	0.512936
DS 822-9	AB	(17)	20.36	625	0.703043(7)		0.09	0.703026	7.40	35.07	0.13	0.512947(7)	0.512933
Nico Seamount													
DS 830-2a	AB		4.50	531	0.703199(7)		0.02		14.78	78.24	0.11	0.512949(7)	
Lars Seamount													
DS 832-2	T	67.7	64.08	1357	0.703459(6)	0.703502(9)	0.14	0.703327	14.55	76.92	0.11	0.512827(10)	0.512777
Last Minute Seamount													
DS 836-2	Ph		104.61	1968	0.703492(7)	0.703369(9)	0.15		15.24	98.71	0.09	0.512897(9)	

Table 5.4a: *Ages in parenthesis are supposed by stratigraphic relationship. * Trace elements given in ppm are determined by ICP-MS. For abbrevitions see Table 5.4b.*

2) Magmatic Hiatus

The formation of the Oligocene shield was followed by a 12 m.y. pause of volcanism in which extensive subaerial erosion led to truncation of the basement at sea level. Marine carbonate sediments covering the basement on Selvagem Grande, provide proof for a shallow submarine setting during the early to mid Miocene.

3) Mid Miocene rejuvenated stage

The rejuvenated magmatic activity initiated in the mid Miocene (8-12 Ma) by intrusion of alkali basaltic and basanitic dikes on Selvagem Grande. Their Pb-isotopic ratios ($^{206}Pb/^{204}Pb$ = 19.33 – 19.38) clearly classify them as a rejuvenated or post-erosional stage. It is likely that the dikes were associated with subaerial extrusive activity.

Table 5.4b: Pb isotope data from the Selvagen Islands and neighboring seamounts

Sample	RT	Age	Pb* (ppm)	U* (ppm)	Th* (ppm)	$^{206}Pb/^{204}Pb$ m.	$^{207}Pb/^{204}Pb$ m.	$^{208}Pb/^{204}Pb$ m.	μ	κ	$^{206}Pb/^{204}Pb$ initial	$^{207}Pb/^{204}Pb$ initial	$^{208}Pb/^{204}Pb$ initial
Selvagem Grande													
J 8a	AB	3.4	2.451	1.186	3.896	19.399 (4)	15.564 (3)	39.177 (9)	31.40	3.40	19.383	15.564	39.159
SG 10	B	(3.4)	2.279	1.005	3.466	19.395 (2)	15.563 (2)	39.172 (4)	28.63	3.56	19.380	15.562	39.154
J 30	AB	3.4	3.829	1.656	6.505	19.351 (4)	15.550 (3)	39.117 (7)	28.04	4.06	19.336	15.549	39.097
J 45	B	(3.4)	3.711	1.334	6.758	19.359 (1)	15.563 (1)	39.172 (3)	23.32	5.24	19.347	15.562	39.151
J 49	B	3.4	3.302	1.186	5.837	19.370 (3)	15.566 (2)	39.190 (6)	23.32	5.08	19.358	15.566	39.170
J 36 (MD)	B	9.9	1.981	0.854	3.661	19.383 (6)	15.577 (4)	39.229(11)	28.02	4.43	19.335	15.575	39.162
J 42 (MD)	B	11.7	2.057	0.831	3.566	19.334 (5)	15.564 (4)	39.136 (9)	26.18	4.44	19.289	15.561	39.073
J 35g(MC)	T	24.8	8.509	1.615	7.431	19.860 (5)	15.517 (4)	41.155 (9)	12.72	4.75	19.811	15.514	41.081
J 9	Ph	24.6	17.824	4.467	13.820	19.716 (3)	15.607 (3)	39.623 (7)	16.45	3.20	19.653	15.604	39.558
J 32	Ph	24.2	10.852	3.202	10.067	19.903 (3)	15.603 (2)	39.786 (6)	19.45	3.25	19.830	15.599	39.710
J 41a	T	25.8	8.067	0.882	6.780	19.650 (1)	15.598 (1)	39.470 (3)	7.15	7.95	19.621	15.596	39.398
Selvagem Pequena													
SP 1	T	(29)	7.487	1.830	6.782	19.722 (4)	15.617 (3)	39.557 (3)	16.03	3.83	19.650	15.614	39.469
J 56	B	29				19.697 (3)	15.598 (3)	39.467 (7)					
SP 2	Tp	28.7	18.330	4.739	16.422	19.756 (2)	15.611 (2)	39.574 (5)	16.97	3.58	19.679	15.607	39.487
Dacia Seamount													
DS 809-1	B	9.2	3.448	1.373	5.901	19.420 (4)	15.567 (4)	39.175 (9)	25.86	4.44	19.383	15.566	39.122
Conception Seamount													
DS 822-4	AB	16.6	1.768	0.970	3.568	19.487 (4)	15.582 (4)	39.333 (9)	35.72	3.80	19.395	15.578	39.221
DS 822-9	AB	(17)	1.763	0.978	3.655	19.509 (3)	15.583 (2)	39.369 (5)	36.19	3.86	19.413	15.579	39.252
Nico Seamount													
DS 830-2a	AB		3.701	1.628	9.432	19.476 (4)	15.580 (3)	39.295 (8)	28.64	5.99			
Lars Seamount													
DS 832-2	T	67.7	8.792	3.412	8.988	19.441 (2)	15.564 (2)	39.300 (5)	25.26	2.72	19.175	15.551	39.069
Last Minute Seamount													
DS 836-2	Ph		7.766	2.184	24.079	20.092 (8)	15.622 (3)	40.408 (4)	18.74	11.39			

Table 5.4: *RT= Rock type: AB = alkali basalts, B = basanites, T = tephrites, Tp = tephriphonolites, Ph = phonolites; Ages in parenthesis are supposed by stratigraphic relationship. * Trace elements given in ppm are determined by ICP-MS. MD= Miocene dikes, MC= Miocene clasts.*

4) Second Magmatic Hiatus

Between 8 and 3.4 Ma, a second magmatic hiatus occurred on Selvagem Grande. The submarine deposited epi-clastic conglomerate indicates a submarine setting for at least the southwestern part of the island. It is likely that the eastern part of the island was subaerial at this time, resulting in erosion of possible Miocene effusive rocks, marine carbonates and some parts of the Oligocene basement (e.g. samples J 35 b,c,f,g). The intensive reworking of carbonate shells and subangular clasts from the Oligocene basement points to a shallow, high-energy environment.

5) Pliocene Rejuvenated Stage

The Pliocene volcanic rocks, including the Inferno, Tornozelos and Atalaia cinder cones, were clearly erupted under subaerial conditions. The phonolitic airfall pumice most

likely originated from a nearby vent to the south of Selvagem Grande, since the pumice rapidly pinches out to the north on Selvagen Grande. This suggests that Selvagem Grande may have been considerably larger in the Pliocene or that there were other small islands nearby.

The Miocene and Pliocene rocks range from alkali basalt to basanite. The similar Nd and Pb isotopic composition (the Pliocene volcanic rocks have identical isotopic composition within the analytical uncertainty) indicates derivation from a common source. Therefore the differences in major and trace element composition between alkali basalts (characterized by high SiO_2 and high Al_2O_3) and basanites (characterized by high MgO, CaO, P_2O_5 and incompatible trace element content; Fig. 5.6, 5.7, 5.8) must reflect differing conditions of melting and fractional crystallization. Although the chemistry of the Miocene dikes, which show increasing incompatible element content with decreasing MgO (Fig. 5.8), is consistent with fractional crystallization of ol and cpx, the decrease in incompatible elements with decreasing MgO (Fig. 5.8) in the Pliocene basalts is inconsistent with fractional crystallization.

A possible reason that would explain both major and trace element composition of the Pliocene volcanic rocks is melting in the presence of CO_2. High pressure melting experiments show that low degree silicate partial melts formed from peridotite in the presence of CO_2 are characterized by low SiO_2 and Al_2O_3 and high MgO and CaO contents compared to those of dry partial melts (Hirose, 1997). The low degree of partial melting results in the enrichment of incompatible elements in the basanites relative to the alkali basalts, as well as the higher ratios of more to less incompatible elements (e.g. La/Yb up to 48 in the basanites and down to 23 in the alkali basalts).

The depletion in HREE observed in all mafic samples from the Selvagen Islands and sampled seamounts (Fig. 5.7) can be explained by residual garnet and points melting in the garnet peridotite field at depths ≥ 80 km (Takahashi, 1986) or ≥ 50 km if garnet pyroxenite is involved in the source (Hirschmann and Stolper, 1996), as suggested by the HIMU trace element characteristics.

Sea level changes or vertical tectonics ?

The several submarine-subaerial changes in the evolution of the Selvagen Islands seem to require a complex sequence of uplift and subsidence. Vertical tectonic movements, mostly attributed to subvolcanic intrusions, is a common phenomenon on Atlantic volcanic

ocean islands, e.g. discussed for the submarine parts of La Palma (Staudigel and Schmincke, 1984) and Fuerteventura (Stillman, 1997), Canary Islands and Madeira (Mitchel-Thomé, 1976) and Porto Santo (Schmidt et al., in prep.), Madeira archipelago. The several submarine-subaerial transitions on Selvagem Grande, however, can be explained solely by the Cenozoic sea level changes (Fig. 5.11), which is consistent with the exclusive presence of shallow water marine fossils in the marine sediments and evidence for a high-energy depositional environment.

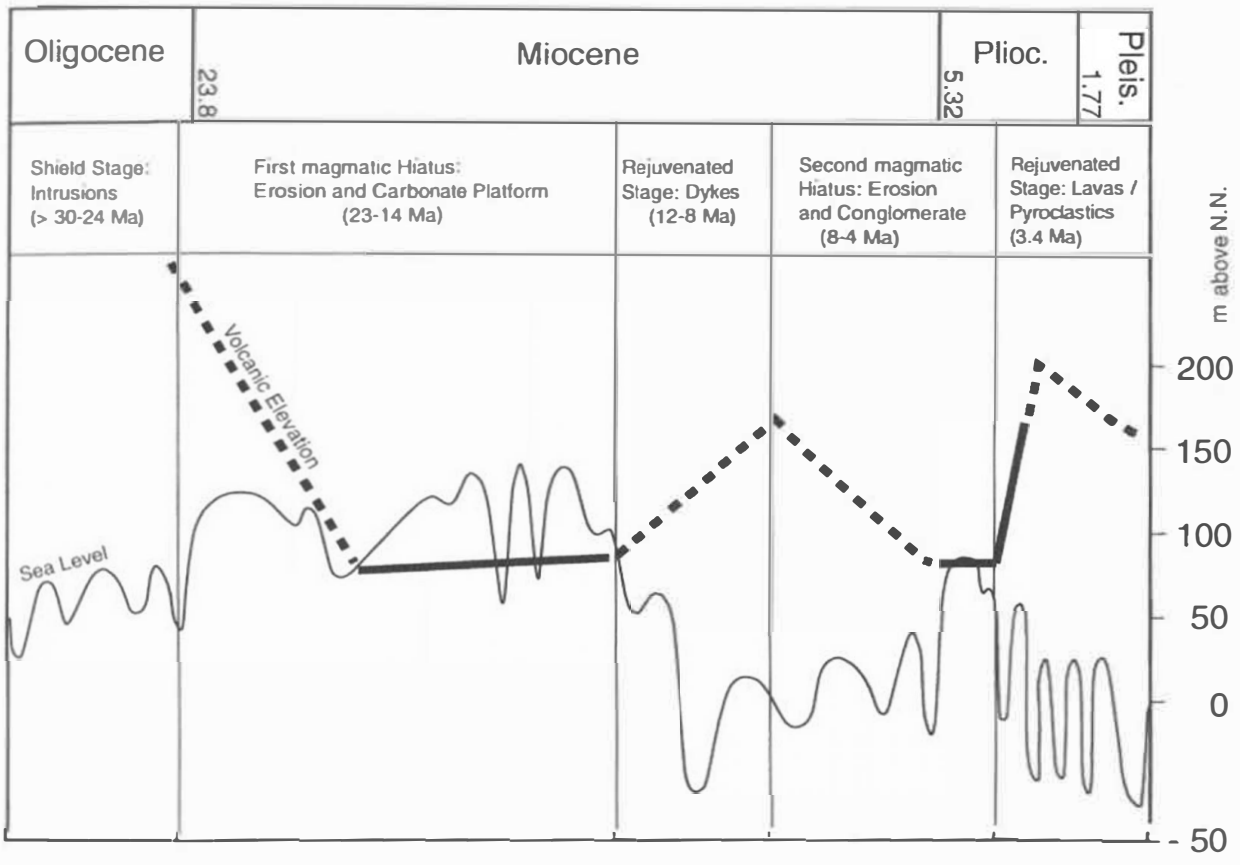

Fig. 5.11:

Comparison between eustatic sea level changes (thin solid line) and elevation of Selvagem Grande (thick line) in meters above sea level. Solid segments of the elevation line mark maximum present-day elevation of the stratigraphic units measured on Selvagem Grande plotted against their age respectively. Broken segments suggest possible elevation of parts that have been already eroded. As can be seen, times of submarine depositions correlate with sea level highs, whereas phases of subaerial erosion (magmatic hiatus) coincides with low sea level. The changes of submarine/subaerial deposition and erosion on Selvagem Grande can therefore be explained solely by eustatic sea level changes without the necessity of additional tectonic uplift or subsidence, although vertical movements of the islands can not be excluded in general. Sea level curve from Hardenbol et al. (1998).

Duration and cause of magmatic gaps

Long-lasting gaps in eruptive activity or at least largely non-volcanic and erosional intervals are a common feature of ocean islands and are also well documented for the Canary Islands, e.g. Gran Canaria (~ 4.7 Ma, Bogaard and Schmincke, 1998) and Fuerteventura (5-7 Ma, Coello et al., 1992) and for the Hawaiian Island chain, e.g. Niihau (2.5 Ma, Clague and Dalrymple, 1989). However, available age data from Selvagem Grande points to a gap of ~ 12 Ma between termination of the Oligocene basement volcanism and emplacement of the Miocene dikes. The age interval between the Oligocene shield and the Pliocene volcanic rocks is ~ 20 Ma. According to Hawaiian terminology (Clague and Dalrymple, 1989), a period of volcanic quiescence separates shield stage volcanism from a volumetrically small post-erosional or rejuvenated stage characterized by silica undersaturated volcanic rock types. Ribe and Christensen (1999) propose that submarine pre-shield stage and shield stage volcanism occurs as the volcano passes over the center of the plume (above the plume stem) and the final post-erosional or rejuvenated stage as it passes over a secondary melting zone located further downstream from the plume center in the direction of plate movement within the flattening plume head. To conserve mass, the layer of buoyant plume material must become thinner when the plume head spreads laterally at the base of the lithosphere, becoming wedge-shaped. This thinning is associated with the further ascent of plume material beneath the spreading plume head resulting in additional minor decompressional melting.

Relationship to the Canary hotspot

Geological, geochemical and age data suggest that the Selvagen archipelago and the belt of seamounts to the east are part of the ancient Canary hotspot track. Nd- and Pb isotopic ratios of samples from the Selvagen archipelago and northeastern seamounts almost completely overlap with the isotopic ratios for the Canary Islands (Fig. 5.9, 5.10) but are distinct from the isotopic signatures of the near-by Madeira Islands, located ~ 300 km NE of the Selvagen archipelago. Using Pb, Sr and Nd isotope data Hoernle et al. (1995) has shown that volcanic rocks from the Canaries, western and central Europe and western Mediterranean converge on a restricted composition at $^{206}Pb/^{204}Pb \cong 19.9\text{-}20.1$, $^{207}Pb/^{204}Pb \cong 15.62\text{-}15.68$, $^{87}Sr/^{86}Sr \cong 0.7030\text{-}0.7034$ and $^{143}Nd/^{144}Nd \cong 0.51282\text{-}0.51294$. Because of the spatial continuity of magmatism and a large low velocity anomaly observed in seismic tomography extending to the core-mantle boundary beneath this region (Ritsema et al., 1999), the isotopic endmember is likely to reflect a common plume source, termed the Low Velocity Component (LVC) by Hoernle et al. (1995). The volcanic rocks from the Selvagen Islands and sampled seamounts of the proposed Canary hotspot track display trends in isotope correlation diagrams (Fig. 5.9, 5.10) that also point to the LVC component. The Madeira Islands represent the purest isotopic endmember of the Madeira hotspot track (Geldmacher and Hoernle, subm.) and form

hyperbolic trends on the $^{206}Pb/^{204}Pb$ versus $^{143}Nd/^{144}Nd$ (Fig. 5.10) and $^{206}Pb/^{204}Pb$ versus $^{87}Sr/^{86}Sr$ (not shown) isotope correlation diagram and a straight linear trend on the $^{206}Pb/^{204}Pb$ versus $^{207}Pb/^{204}Pb$ diagram (Fig. 5.9). In contrast to the volcanic rocks from island groups and seamounts of the proposed Canary hotspot track, the radiogenic Madeira endmember does not point to LVC but to higher (more radiogenic) Nd and lower (unradiogenic) $^{207}Pb/^{204}Pb$. This difference suggests that both volcanic provinces are feed by different sources and thus could represent individual hotspot systems with the Selvagen Islands and the associated seamounts to the east and northeast belonging to the Canary Island hotspot system.

The seamounts often have flattened tops (Conception Bank, Dacia, Nico) and rounded beach cobbles and pebbles were dredged from some of these seamounts (Nico, Conception Bank), both indicating erosion at sea level. In addition, the elevation of summit plateaus decrease from south to north (Conception Bank ≈ 200 m, Nico ≈ 300 m, Dacia ≈ 400 m and Lars Seamount ≈ 900 m) suggesting cooling of the lithosphere and thus transport away from the center of a possible hotspot.

In Fig. 5.12, ages of the seamounts and islands of the proposed Canary hotspot track are plotted against distance from Hiero, the youngest Canary Island, that is generally believed to mark the present location of the Canary hotspot. Beginning in the NE, the oldest age of 68 Ma comes from Lars Seamount. Based on the Pb isotopic composition, however, this sample belongs to the post-erosional stage of the volcano ($^{206}Pb/^{204}Pb$ = 19.44) and therefore represents only a minimum age. Lars Seamount lies at the northern end of an area of anomalously high seismic velocity at the crust-mantle boundary corresponding with a chaotic seismic facies (UCF) (Fig. 5.1). The UFC layer is time transgressive, occurring in sediments marking the Cretaceous/Tertiary boundary in the north near Lars Seamount but becomes younger to the south. Holik and Rabinowitz (1991) propose that this volcanic layer results from the passage of the lithosphere above the ancient Canary Plume. Both the age and spatial distribution of the UFC layer correlate with our age data from Lars Seamount. Isotope data from Dacia (~ 9 Ma), Conception Bank (~ 17 Ma) and Lanzarote (> 15 Ma) indicate that the sampled portions of these volcanoes also belong to the post-erosional or rejuvenated stage (this study; Sun, 1980 and Hoernle, in prep.) and therefore the oldest ages from these volcanic structures represent minimum ages.

Samples from the Selvagen Islands (~ 30 Ma) and Fuerteventura (~ 25 Ma; Le Bas et al., 1986) located in the central portion of the 850 km volcanic belt, also have intermediate ages for their shield stage volcanism, defined on the basis of their radiogenic isotope composition (Hoernle and Tilton, 1991 and this study). Balogh et al. (1999) reported K-Ar

and $^{39}Ar/^{40}Ar$ ages of ~ 64 Ma for syenitic intrusions emplaced within Mesozoic sediments within the uplifted basal complex of Fuerteventura but many of the calculated ages are ambiguous because of evidence for excess Ar and Ar loss. These ages, however, correlate with late Cretaceous fossil ages for sediments intercalated with alkali volcaniclastic rocks (see Le Bas et al., 1986). Nevertheless, the large temporal hiatus of > 40 Ma to the oldest subaerial shield stage samples suggests that the possible magmatism at ~ 64 Ma is unrelated to the formation of Fuerteventura Island and therefore this age will be disregarded in this study.

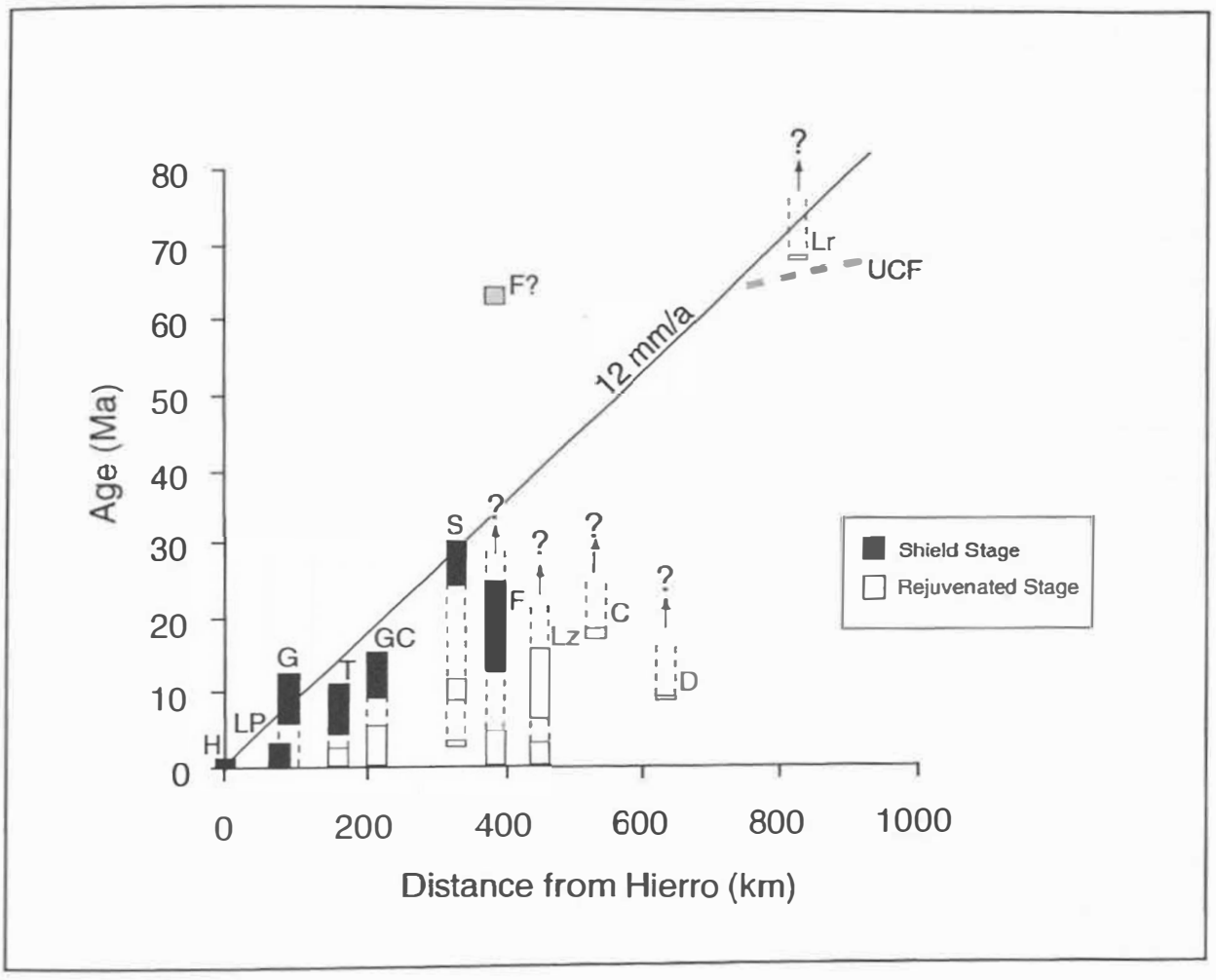

Fig. 5.12:

Radiometric ages of shield stages and rejuvenated or post-erosional stages of islands and seamounts of a possible Canary hotspot track against distance from Hierro. Abbreviations for Islands and Seamounts: H= Hierro, LP= La Palma, G= Gomera, T= Tenerife, GC= Gran Canaria, S= Selvagen Islands, F= Fuerteventura, Lz= Lanzarote, C= Conception Seamount, D= Dacia Seamount and Lr= Lars Seamount (for age references see Fig. 1). Slope of correlation line for the oldest available ages for the shield stage volcanism and a calculated age of about 73 Ma for the shield stage of Lars Seamount (see text for details) correspond with an absolute plate velocity of about 12 mm/a. Also shown is the distribution of the chaotic seismic facies (UCF) from Holik and Rabinowitz (1991) and age range for intrusions within

the sedimentary basal complex of Fuerteventura reported by Balogh et al. (1999). Distance from Hierro measured by projection of volcanoes to the assumed hotspot track of Fig. 5.13.

Radiogenic isotope data from the oldest subaerial volcanic rocks on Gran Canaria (~ 15 Ma), Tenerife (~ 11 Ma) and Gomera (~ 12 Ma) confirm that these rocks belong to the shield stage of these islands (Sun, 1980; Cousens et al., 1990; Hoernle et al., 1991a; Thirlwall, 1997; Hoernle, in prep). The high eruption rates, relatively low degrees of erosion and isotopic compositions of the lavas from the youngest Canary Islands of La Palma (3-4 Ma) and Hierro (~1 Ma) indicate that they are still in their shield stage of evolution (Sun, 1980 and Hoernle, in prep).

The onset of volcanism (shield stage) for the individual Canary Islands show a rough age progression from W to E although duration of volumetrically minor rejuvenated stage magmatism continued on most of the islands until recent times (summarized in McDougal and Schmincke, 1976; Hoernle and Schmincke, 1993b; Schmincke and Sumita, 1998). Regarding the oldest available ages respectively for the shield stage volcanism of the Canary and Selvagen Islands and taking into consideration that the 68 Ma age from Lars Seamount represents a minimum age for this volcano, a crude positive correlation between distance from Hierro and age can be discovered (Fig. 5.12). In conclusion, the isotopic data, degree of erosion of islands and depth of erosional summit plateaus of seamounts and the age progression support an origin of the Selavgen Islands and associated seamounts to the NE from the ancient (early Tertiary-late Creataceous) Canary hotspot.

Plate motion estimate

The estimation of plate velocity is based on the following major assumptions: 1) The oldest available age data (this study and literature data) from the shield stage volcanic rocks represent a date close to the initiation of magmatic activity for the volcanic islands/seamounts respectively, reflecting the arrival of upwelling mantle material at the base of the lithosphere. 2) The growth of the large volcanic cones from the seafloor to sea level where samples were usually collected/dredged is relatively rapid (within several million years) or at least of the same order for the individual islands/seamounts.

Assuming that the minimum age for shield stage volcanism on Lars Seamount is about 5 m.y. older than the 68 m.y. rejuvenated stage sampled in this study (5 m.y. serving as a minimum value for the magmatic hiatus), the correlation on Fig. 5.12 yields a reasonably good correlation coefficient (r^2= 0.94). The slope of the correlation results in an absolute plate

velocity of about 12 mm/a which is slower than the values of 16 and 19 mm/a obtained by Schmincke and Sumita (1998) and Carracedo et al. (1998) respectively, who only used ages from subaerial shield stage volcanism of the Canary archipelago. The value of ~12 mm/a, however, is similar to the absolute plate velocity of 12 mm/a calculated for the nearby Madeira region (Geldmacher et al., 2000).

As noted by Carracedo et al. (1998), perfect age-distance correlations within hotspot-related island/seamount chains can not be expected on slow-moving plates and the lack of such a progression is not an argument against generation of the Canary island/seamount track by a mantle plume. Aside from the general problem of not having age data from the initial (submarine) part of most ocean island volcanoes (see assumptions made above), the main reasons for the discrepancies are: 1) the short over-all length of the track in relation to its proximity to the rotation pole for the African plate (see below), 2) neglect of possible small-scale variations in plate kinematics due to integrating over a long time period, 3) motion of the hotspot center (upwelling mantle plume) that leads to more significant effects on slow moving plates, 4) displacement of ascending plume material due to horizontal asthenospheric mantle flow (mantle wind) and 5) deflection of asthenospheric melts along lithospheric fractures or zones of weakness. The latter is postulated by Carracedo et al. (1998) to explain the origin of the East Canary Ridge extending from Fuerteventura to Lanzarote to Conception Bank Seamount (Fig. 5.1).

A kinematic model for the passage of the eastern North Atlantic over the Canary hotspot proposed by Holik and Rabinowitz (1991) using the plate motion calculations of Morgan (1983) is shown in Fig. 5.13. The hotspot track starts at 60 Ma near Lars Seamount and proceeds southwest to the Canary Island of Hierro (see dotted line). Using the rotation pole calculated for the nearby Madeira hotspot track at ~ 43°N/24°W (Geldmacher et al., 2000), the motion of the lithosphere above the center of the Canary hotspot would describe a less curved track passing through the middle of the belt of seamounts and islands (solid line in Fig. 5.13). In both cases an overall width of 400-450 km for the track is required. For comparison, the proposed Madeira hotspot track (thick broken line after Geldmacher et al., 2000) is also shown in Figure 5.13. Assuming a similarly wide track, the northerly seamounts of the Madeira-Tore Rise could also be attributed to the Madeira hotspot using the rotation poles of Morgan (1983) (dotted line) or Geldmacher et al. (2000) (solid line). Hotspots of similar buoyancy flux (~ 1.0 Mg s^{-1}) to the Canary plume like e.g. the Galapagos hotspot also have a wide track of ~ 400 km width (see Werner et al., 1999; Hoernle et al., 2000). Broad hotspot tracks (~ 500 km width) are also associated to hotspots of even lower buoyancy flux such as St. Helena (O'Conner and le Roex, 1992).

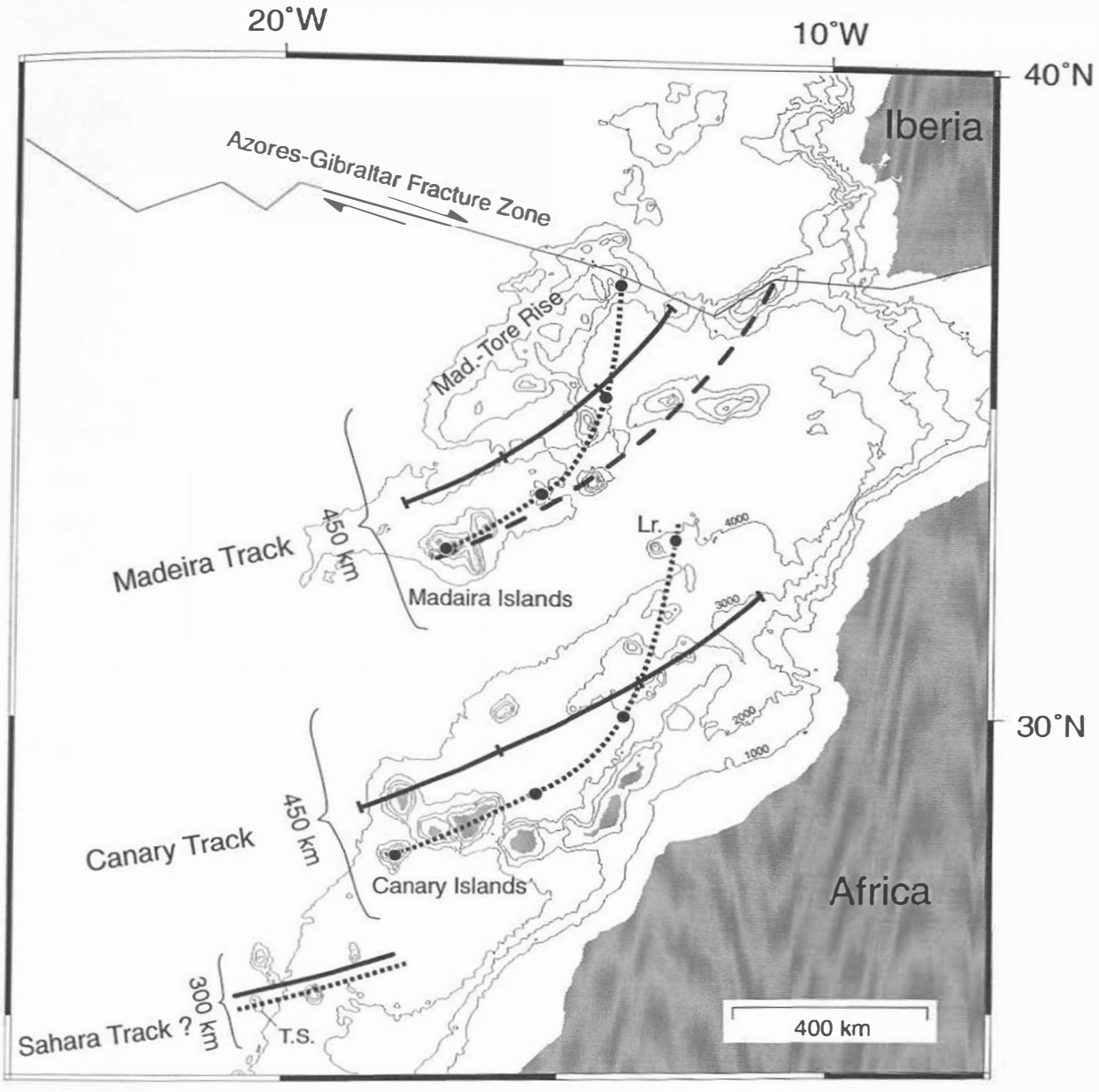

Fig. 5.13:

Possible hotspot tracks in the eastern North Atlantic using the rotation poles for the African plate of Morgan (1983) (doted line) and Geldmacher et al. (2000) (solid line). Seamounts and Islands of the Canary hotspot describe a ~ 450 km wide scattered track. The proposed hotspot tracks for the Madeira hotspot (broken line after Geldmacher et al., 2000) is also shown. Assuming a similarly wide track, the northerly seamounts of the Madeira-Tore Rise could also attributed to the Madeira hotspot using the rotation poles of Morgan (1983) (dotted line) or Geldmacher et al. (2000) (solid line). Small solid circles/ticks mark the position of the hotspot center in distances of 20 m.y. Also shown in Fig. 13 are possible hotspot tracks for the Sahara seamounts. Only age data from Tropic Bank Seamount (T.S.) has been reported thus far from this group (K/Ar ages range from 60-100 Ma; Blum et al., 1996).

An alternative model to explain the unusual width of the Canary hotspot track would be the existence of two close but separate hotspot tracks with widths of ~ 200 km. Experimental data and theoretical calculations show that Rayleigh-Taylor instabilities, responsible for the initiation of starting plumes from a thermal boundary layer, require a distinct distance between neighboring plumes (Whitehead and Luther, 1975). The most conservative estimate based on zero viscosity difference between the upwelling plume and the overlying material, yields a minimum distance that is 4.3 times of the overall thickness of the layer from which the plumes evolves. Seismological observations of the D''- layer at the core mantle boundary from which deep mantle plumes are believed to originate (e.g. Jackson, 1998), suggest a thickness of about 100-400 km that would result in a minimum distances for neighboring plumes of 430–2000 km. Assuming that the plumes originate from a different boundary layer e.g. the 660 km transition zone between upper and lower mantle, the thickness of the thermal boundary layer is limited to a maximum of 50 km if the plumes are within 200 km of each other, which seems unrealistic. Furthermore, two plumes that rise too close to each other will coalesce into a single plume (Kelly and Bercovici, 1997).

Implications for melt generation and plume models

The spatial and temporal irregularities of a possible 400-450 km broad Canary hotspot track seems to be inconsistent with the classical plume model producing relatively narrow linear island/seamount chains with a nearly exact positive age/distance correlation (e.g. Wilson, 1963; Morgan, 1972). Therefore alternative models have to be discussed to explain the volcanism in the East Atlantic. Potential models must regard the following observations: The Selvagen Islands as well as the Canary Islands and the neighboring seamounts (so far as known yet) display melts which show an incompatible element enriched trace element composition (OIB signature) with depletion in HREE as well as an isotopic radiogenic shield stage and an more isotopic depleted post-erosional or rejuvenated evolutionary stage (e.g. Hoernle et al., 1991; Hoernle and Schmincke, 1993a; Hoernle and Schmincke, 1993b and this study). The volcanoes forming a ~ 450 km wide and > 800 km long belt and the beginning of the shield stage show a rough age progression in the direction of plate motion. No major fracture zones or other zones of weakness on which volcanoes are oriented are known in this area (Hinz et al., 1982; Stets and Wurster, 1982), except the ocean-continent boundary below the Fuerteventura-Lanzarote-Conception Bank rise (Carracedo et al., 1998).

Four fundamental different processes for generating non-linear distributed intraplate volcanoes are thinkable; 1) adiabatic decompression melting of the uppermost mantle along tectonic fractures in the lithosphere or intraplate rifting producing "passive" partial melting in the uppermost mantle, 2) adiabatic melting of upwelling mantle due to small-scale convective

instabilities at the edge of the continental lithosphere, 3) dehydration melting due to widespread reducing of the solidus temperature of the upper mantle, and 4) adiabating melting of rising hot mantle material (plume) that is upwelling in a large, sheet-shaped structure or in irregular, pulsating ejected diapirs over an large area.

1) "Passive" adiabatic melting along fracture/faults

Because of the geochemical composition, melt generation in relatively shallow depths (asthenosphere) due to "passive" decompression melting along fractures or rifts is unlikely to explain the isotopic enriched signature of the proposed Canary hotspot track. On the other hand, the upper mantle seems to be heterogeneous (e.g. Zindler and Hart, 1986; Graham et al., 1988) and source material with OIB-like enriched trace element and isotopic compositions could be present below the base of the East Atlantic lithosphere within the depleted upper mantle possible as leftovers of earlier plume upwelling could not be entirely ruled out. As mentioned above, bathymetric structures like rift structures reflecting such shallow processes, however, are absent in the East Atlantic.

2) Convective instabilities at the edge of the continental lithosphere

A possible origin of volcanism and an associated topographic rise subparallel to a near continental lithosphere edge due to small-scale convective upwelling is proposed for the Bermuda Rise in the West Atlantic (Vogt, 1991). The Bermuda Rise is a southwest-northeast elongated swell ~ 1500 km long and 500-1000 km wide crowned by volcanoes of Eocene age. Because of the perpendicular elongation in respect to the northwest directed plate motion and non correlated age progression of the volcanism a non-hotspot process must be considered for the Bermuda rise. Vogt proposed a model of asthenospheric upwelling driven and controlled by the strong thermal contrast across the continental/oceanic lithospheric boundary that is also supported by numerical calculations, showing that thermal instabilities can lead to pulsating convection of the asthenospheric mantle beneath oceanic lithosphere near the continent/ocean boundary (King and Anderson, 1998). Such a process, however, predicts a more or less continues volcanic activity over a large area and not a somehow or even poorly correlation of age progression and seems to be therefore inadequate for the East Atlantic volcanic province.

3) Dehydration melting

Green (1994) has suggested an incipient molten layer in the mantle at depths ≥ 95 km due to dehydration of pargasite amphibole as a result of even small quantities of water supply from rising fluids. Melts generated from this source are low degree melts, with garnet signature (depletion in HREE) and could exist in a widespread layer in the upper mantle. However, to collect and transport this small volume magmas to the surface lithospheric

fractures are necessary which are unknown in this region (see above). Furthermore it is unclear in this model why the volcanism should show an age correlation in the direction of the plate motion.

4) Thermally driven mantle plumes

Magmas generated from a thermally driven plume originating from a thermal boundary layer e.g. at the core/mantle boundary could show the geochemical composition observed in the magmas of the proposed Canary hotspot track. Sketches in Figure 5.14 show two possible models. In the first model, a mantle plume from the core/mantle boundary pierces the 660 km discontinuity and spreads out along the base of the lithosphere and becomes dragged in the direction of plate motion (Fig. 5.14a) as seen in three-dimensional numerical models (Keken van and Gable, 1995). The plume could be heterogeneous, consisting of blobs of enriched recycled plume material (LVC) (dark areas in Figure 5.14a) in a matrix of entrained depleted upper mantle material ("blob model"), as proposed by Hoernle and Schmincke (1993b) for the Canary Islands. Above the center of the conduit, many individual blobs of plume material arrive at the base of the lithosphere. Melting of these plume material results in the shield stage of the volcanism (highest growth rate, most radiogenic isotope composition). Progressive depletion in plume material through melt extraction (Hoernle et al., 2000; Geldmacher and Hoernle, subm.) and increasing entrainment of lower mantle material will lead to a decrease of radiogenic composition during the evolution of an individual volcano Hoernle and Schmincke (1993b). Magmatic hiatuses could reflect intervals when cooler depleted entrained asthenospheric material is in the melting zone beneath an island. With ongoing plate motion the volcanoes move away from the center of the conduit and fewer hot blobs will reach the melting zone beneath the islands.

A second variation of this model is proposed for the Madeira plume by Geldmacher and Hoernle (subm.). A heterogeneous plume pulse containing both upper, altered basaltic crust and lower gabbroic portions of the oceanic crust. During the shield stage magmas are preferentially sampled from the altered upper basaltic portion. The magmatic hiatus reflects the presence of residual plume material in the melting zone beneath the volcano. Minor melting of the remaining lower gabbroic portion during the post-erosional stage results from further adiabatic decompression when the plume pulse flattened and spreads out beneath the residual material according to the model of Ribe and Christensen (1999). In contrast to the Canary model (5.14a), the Madeira hotspot track seems to be the result of discrete pulses of a pulsating rather than a continues plume.

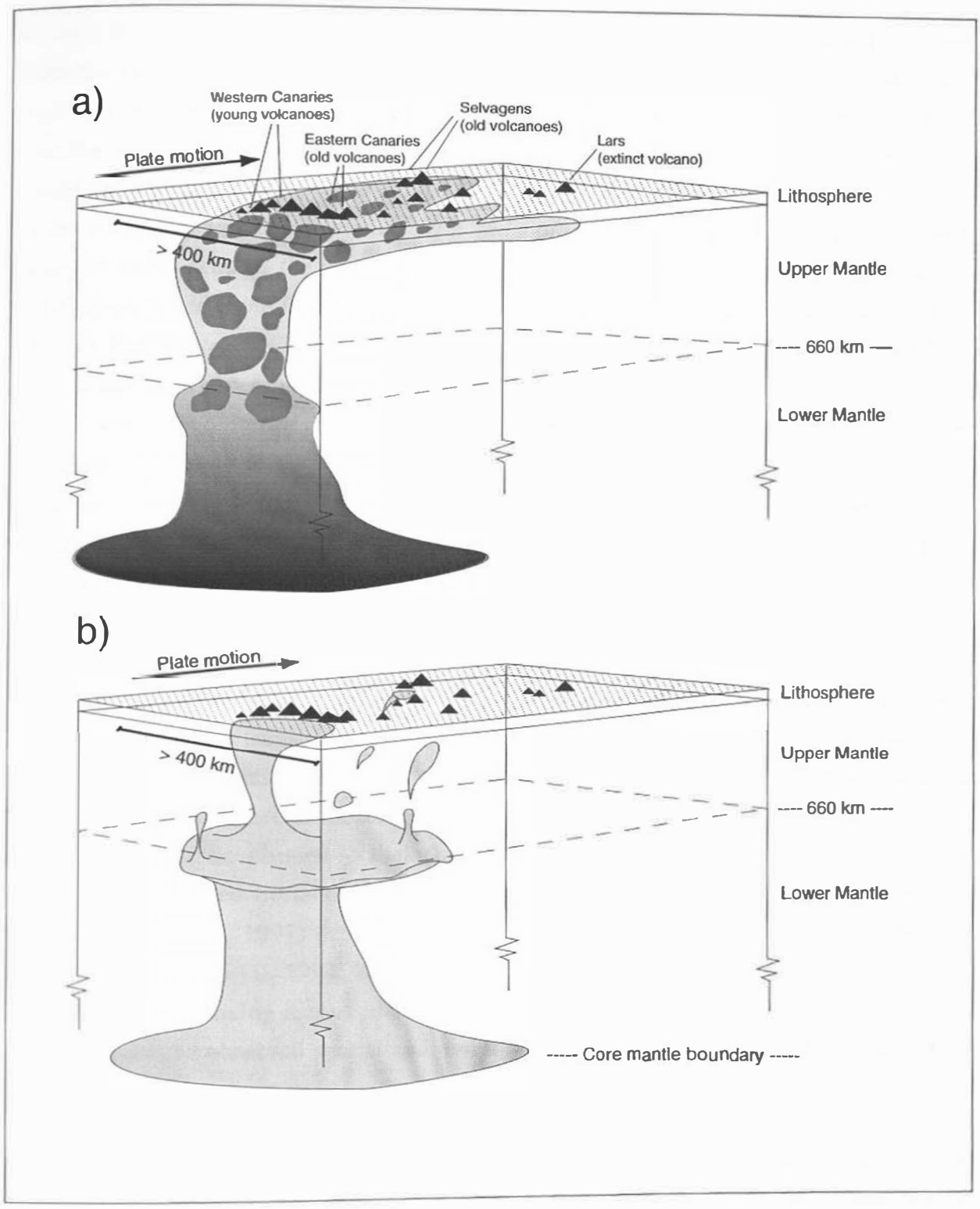

Fig. 5.14:

Simplified model of an upwelling lower mantle plume under the East Atlantic. a:) The upwelling plume containing blobs or zones of enriched mantle material separated by entrained upper mantle material. The plume becomes sheared by lithospheric drag and spreads out over a large area at the base of the lithosphere. Progressive depletion of plume material through melt extraction and increasing entrainment of mantle matrix will lead to a

decrease in the radiogenic composition during the evolution of an individual volcano. Magmatic hiatuses could reflect intervals when surrounding cooler shallow entrained material is in the melting zone beneath an island. With on-going plate motion, the volcanoes move away from the center of the conduit and fewer hot blobs will reach the melting zone beneath the islands.

b:) Interaction of upwelling plumes with the 660 km phase transition lead to a large stationary plume head at the upper/lower mantle boundary that can eject narrower diapirs from different parts of the head causing the observed spatial and temporal distribution of the resulting hotspot track. The diapirs can be heterogeneous, containing enriched plume material that is progressively melted out and exhausted during the shield stage, when the volcano is over the center of the diapir. Due to lithospheric drag, the diapirs spread out at the base of the lithosphere in the direction of plate motion and the volcano is now situated above the downstream edge of the diapir represented by the post-erosional stage. Because enriched recycled material was already largely exhausted at the shield stage, post-erosional magmas show a more depleted composition.

An alternative model is shown in Figure 5.14b. Interaction of upwelling plumes with zones of major phase transitions at 400 km or 660 km associated with major changes of viscosity and other mantle properties could lead to large stationary plume heads at those depths. As seen in numerical models, such lower mantle plumes can trigger much narrower diapiric upper mantle plumes (Nakakuki et al., 1997). The ejecting diapirs can become significantly displaced horizontally before they start to ascend through the upper mantle (Steinbach and Yuen, 1997) or even form a pulsating system of small individual blobs or diapirs (Keken van et al., 1992; Keken van and Gable, 1995). Besides for possible vertical displacement of the rising diapirs in the mantle flow, a wide area of upwelling could also be responsible for the observed spatial and temporal distribution of the resulting hotspot track (see figure).

The diapir can be heterogeneous, containing both isotopic enriched LVC material (veins or blobs of recycled oceanic crust e.g. gt-pyroxenite) and more depleted upper mantle peridotite (mixed into the large plume head at the transition zone, or entrained during ascent of the diapir). Because the solidus of the enriched recycled material will be crossed first during ascent (Hirschmann and Stolper, 1996), first magmas at the shield stage are predominated by more radiogenic ($^{206}Pb/^{204}Pb = > 19.6$) recycled material. During the shield stage, the volcano is over the center of the diapir resulting in the highest growth rate. Due to lithospheric drag, the diapir head spreads out at the base of the lithosphere in the direction of

plate motion. The volcano on the drifting plate will be now situated above the downstream edge of the diapir head that become progressively depleted in enriched recycled material since it was already extracted at the shield stage. Therefore post-erosional magmas show a more depleted isotopic composition resulting from melting of an increasing portion of entrained upper mantle material. Depending from the size of the diapir, this process can be temporal and spatial different for each individual one. For example, new, enriched material is still upwelling in a diapir conduit producing a new shield stage volcano above this place (e.g. shield stage volcanism on the westernmost Canary Islands) while volcanoes above the deflected head of the same diapir (e.g. the eastern Canary Islands) are already in their post-erosional stage (see sketch for the young volcanoes in Fig. 5.14b).

As the lithosphere moves, the diapir will more and more sheared and finally cut off from the lower mantle plume. In numerical models Steinberger and O'Connell (1998) have shown that plume conduits can be strongly distorted by mantle shear flow. If the conduit is tilted by more than about 60° from the vertical, it will become unstable and eventually split up into separate blobs (Whitehead, 1982). Such cut diapirs will flatten and ascent resulting in the re-juvenated (post-erosional) volcanism as described by Ribe and Christensen (1999) because the outwardly spreading mass can not be balanced with steady supply of new plume material. Such a process probably occurred beneath the Selvagen Islands at ~ 3-4 millions years ago resulting in a second short phase of rejuvenated volcanism (Pliocene alkali basaltic to basanitic volcanism at 3.4 Ma). Finally volcanism has ceased on the seamounts in the northern part of the Canary chain.

Bulk earth heat flow calculations (Malamud and Turcotte, 1999) imply the existence of a significant number of small, weak plumes lacking significant surface signature (e.g. linear trends). The resulting seamounts or islands will form segmented tracks instead of long (linear) chains.

A large-scale thermally driven plume model is also consistent with the broad zone of low seismic velocity observed in the seismic tomography beneath the East Atlantic (Zhang and Tanimoto, 1992) that is believed to represent the soure region for LVC (Hoernle et al., 1995). Because of the presently insufficient lateral resolution of seismic tomographic models, no clear distinction can be made between one large zone of upwelling (Fig. 5.14a) or multiple smaller diapirs (Fig. 5.14b). New seismic tomographic models, however, suggest that the low velocity anomaly beneath the East Atlantic is connected to the lower mantle (Goes et al., 1999) or can even be tracked to the core/mantle boundary (Ritsema et al., 1999), as pictured in Fig. 5.14. Although no high ^{3}He signatures, indicating a deep mantle origin, have been

reported from Canary island magmas, $^{3}He/^{4}He$ ratios can be reduced by radiogenic ingrowth due to decay of ^{238}U, ^{235}U and ^{232}Th in the source over long periods of time. Recycled oceanic crust, as is suggested in the source of Canary plume magmas (e.g. Hoernle and Tilton, 1991; Hoernle and Schmincke, 1993b), is relatively enriched in U and Th and is most likely responsible for this process. An alternative explanation would be the re-equilibration of the He isotope ratios as a result of long-term residence of plume material between at the 660 km discontinuity with the overlying upper mantle (Fig. 5.14b).

Interestingly there seems to be no exchange between the Madeira and the Canary hotspots although both are situated less than 500 km away from each other over long periods of time (Fig, 5.13). Geldmacher and Hoernle (subm.) propose that the Madeira source contains young (< 500 Ma) recycled oceanic crust probably situated at the upper-lower mantle transition. It can be speculated that the large upwelling plume head below the upper mantle beneath the Canaries not only eject the narrow diapirs producing the Canary hotspot track but also yield enough conductive heat to initiate the blob-type upwelling (Geldmacher and Hoernle, subm.) of the nearby Madeira plume source.

5.6 Conclusions

In this study, spatial and temporal variations of the Selvagen Islands and associated seamounts to the NE were evaluated. The subaerially-exposed history of the Selvagen Islands can be subdivided into the following evolutionary stages: 1) Oligocene (24-30 Ma) shield stage on Selvagem Grande and Selvagem Pequena with emplacement of tephritic to phonolitic intrusive basement, 2) a magmatic hiatus (12-23 Ma) accompanied by subaerial erosion to sea level and the subsequent deposition of a carbonate bank on the eroded intrusive basement corresponding with a rise in sea level in the early to mid Miocene, 3) a mid Miocene (~ 8-12 Ma) post-erosional stage with alkali basaltic and basanitic dike emplacement on Selvagem Grande, 4) a second magmatic hiatus accompained by subaerial erosion and formation of submarine epiclastic conglomerates, 5) a Pliocene (3.4 Ma) rejuvenated stage consisting of alkali basaltic to basanitic lava flows and pyroclastic rocks and rare evolved tephra, and 6) a third magmatic hiatus (0-3.4 Ma). Samples from the post-erosional or rejuvenated stages show less radiogenic Pb isotope ratios ($^{206}Pb/^{204}Pb$= 19.3-19.4) than shield stage samples ($^{206}Pb/^{204}Pb$= 19.6-19.9). The associated seamounts show decreasing elevation of the summit plateaus from south to north and samples yielded ages of 17 Ma for Conception Bank, 9 Ma for Dacia Seamount and 68 Ma for Lars Seamount. Samples from Dacia, Conception Bank, Lars and Nico Seamounts are alkali basalts and basanites and the sample

from Last Minute Seamount has a phonolitic composition. All samples show enriched trace element signatures. Isotope data from Conception Bank, Nico, Lars and Dacia Seamounts indicate that all sampled portions of this volcanoes belong to their post-erosional or rejuvenated stage ($^{206}Pb/^{207}Pb$= 19.4-19.5) whereas the sample from Last Minute Seamount belong to the radiogenic shield stage ($^{206}Pb/^{207}Pb$= 20.1).

Trace elements and Sr-, Nd- and Pb isotopic ratios of the Selvagen Islands and sampled seamounts are consistent with derivation from a mantle plume source, similar in composition to the nearby Canary Islands (LVC) but distinct from the Madeira mantle source. The geochemical similarity and age progression decreasing from NE to SW for shield stage volcanism on islands and seamounts in the direction of plate motion suggest a common hotspot source for the ~ 800 km long and ~ 450 km wide belt of islands (Canaries and Selvagens) and the seamounts to the northeast (including Lars, Dacia, Conception Bank and Last Minute Seamount). Irregular age sequence and spatial distribution, however, are not consistent with derivation from a classical plume. Two types of endmember models are proposed to explain the wide, diffuse hotspot track: 1) a large (~ 400 km wide) heterogeneous plume containing enriched plume material distributed in zones or blobs within more depleted or residual material. 2) An alternative model is the formation of a large, stationary heterogeneous plume head at the upper-lower mantle transition zone, ejecting individual diapirs from different parts of the head. In both models, the isotopically enriched plume material is progressively consumed during the shield stage of volcanism. During the post-erosional stage, the magmas are therefore predominated by isotopically more depleted source material.

Acknowledgements

We thank captain and crew of FS *Poseidon* for their aid in dredging the seamount volcanoes and in landing on Selvagem Grande during the POS 235 cruise. The Parque Natural da Madeira is thanked for permission to work on the Selvagen Islands. Director H. Costa-Neves and his staff from Parque Natural (in particular M.P.F. De Freitas and R.M. Silva Santos) are gratefully acknowledged for their cooperation and excellent support during three separate trips to the Islands. We further thank the Portuguese Navy for transportation to the Selvagen on two of these trips. V. Cruz is thanked for her invaluable help in administrative communication and for field assistance on Selvagem Grande and M. Hort and H. Zankl for fruitful discussions. F. Marks (sample preparation), D. Rau (XRF laboratory GEOMAR), T. Arpe (ICP-MS laboratory, University Kiel) and in particular S. Vetter (TIMS laboratory,

GEOMAR) are thanked very much for their analytical support. This study was supported by the Deutsche Forschungsgemeinschaft (DFG project HO1833/1). The POSEIDON cruise was funded by the state of Schleswig-Holstein.

References

Abdel Monem A, Watkins ND, and Gast PW (1971) Potassium-argon ages, volcanic stratigraphy and geomagnetic polarity history of the Canary Islands: Lanzarote, Fuerteventura, Gran Canaria, and La Gomera. Am J Sci 271: 490-521

Abdel Monem A, Watkins ND, and Gast PW (1972) Potassium-argon ages, volcanic stratigraphy and geomagnetic polarity history of the Canary Islands: Tenerife, La Palma and Hierro. Am J Sci 272: 805-825

Ancochea E, Fúster JM, Ibarrola E, Cendrero A, Coello J, Hernán F, and Jamond (1990) Volcanic evolution of the island of Tenerife (Canary Islands) in the light of new K-Ar data. J Volcanol Geotherm Res 44: 231-249

Ancochea E, Hernán F, Cendrero A, Cantagrel JM, Fúster JM, Ibarrola E, and Coello J (1994) Constructive and destructive episodes in the building of a young oceanic island, La Palma, Canary Islands, and genesis of the Caldera de Taburiente. J Volcanol Geotherm Res 60: 243-262

Anguita F and Hernan F (1975) A propagating fracture model versus a hotspot origin for the Canary Islands. Earth Planet Sci Lett 27: 11-19

Arana V and Ortiz R (1991) The Canary Islands: Tectonics, magmatism and geodynamic framework. In: Kampuzuna AB and Lubala RT (Eds) Magmatism in extensional structural settings (The Phanerozoic African plate). Springer-Verlag, Barcelona, Spain: 209-563

Balogh K, Ahijado A, Casillas R, and Fernandez C (1999) Contributions to the chronology of the Basal Complex of Fuerteventura, Canary Islands. J Volcanol Geotherm Res 90: 81-101

Blum N, Halbach P, Münch U, and Gerven van M (1996) Pb-Sr-Nd isotopic data of Mesozoic ocean island basalts from the eastern Atlantic ocean continental margin. Chem Erde 56: 193-205

Bogaard Pvd, Schmincke H-U, Freundt A Hall C, and York D (1988) Eruption ages and magma supply rates during the Miocene evolution of Gran Canaria: single $^{40}Ar/^{39}Ar$ laser ages. Naturwissenschaften 75: 616-617

Bogaard Pvd and Schmincke H-U (1998) Chronostratigraphy of Gran Canaria. In: Weaver PPE, Schmincke H-U, Firth JV, and Duffield W (Eds) Proceedings of the Ocean Drilling Program, Scientific Results. 157 127-140

Cantagrel J-M, Cendrero A, Fúster J-M, Ibarrola E, and Jamond C (1984) K-Ar-chronology of the volcanic eruptions in the Canarian Archipelago: Island of La Gomera. Bull Volcanol 47: 597-609

Carracedo JC, Day S, Guillou H, Rodriguez Badiola E, Canas JA, and Perrez Torrado FJ (1998) Hotspot volcanism close to a passive continental margin: the Canary Islands. Geol Mag 135: 591-604

Carvalho Gd and Brandão JM (1991) Geologia do Arquipelago da Madeira. Lisbon, pp 170

Clague DA and Dalrymple GB (1989) The Hawaiian-Emperor Volcanic Chain, Part I. US Geol Survey Professional Paper 1350:

Coello J, Cantagrel J-M, Hernan F, Fuster J-M, Ibarrola E, Ancochea E, Casquet C, Jamond C, Diaz de Teran J-R, and Cendrero A (1992) Evolution of the eastern volcanic ridge of the Canary Islands based on new K-Ar data. J Volcanol Geotherm Res 53: 215-274

Cohen RS and O'Nions RK (1982) The lead, neodymium and strontium isotopic structure of oceanic ridge basalts. J Petrol 23: 299-324

Cousens BL, Spera FJ, and Tilton GR (1990) Isotopic patterns in silicic ignimbrites and lava flows of the Mogan and lower Fataga Formations, Gran Canaria, Canary Islands: temporal changes in mantle source composition. Earth Planet Sci Lett 96: 319-335

Dalrymple GB and Duffield WA (1988) High precision $^{40}Ar/^{39}Ar$ dating of Oligocene tephra from the Mogollon-Datil volcanic field using a continuos laser system. Geophys Res Lett 15: 463-466

Dupré B and Allègre CJ (1980) Pb-Sr-Nd isotopic correlation and the chemistry of the North Atlantic mantle. Nature 286: 17-21

Garbe-Schönberg CD (1993) Simultaneous determination of thirty-seven trace elements in twenty-eight international rock standards by ICP-MS. Geostandard Newsletters 17: 81-97

Geldmacher J, Bogaard Pvd, Hoernle K, and Schmincke H-U (2000) $^{40}Ar/^{39}Ar$ age dating of the Madeira archipelago and hotspot track (eastern North Atlantic). Geochemistry, Geophysics, Geosystems 1

Geldmacher J and Hoernle K (subm.) The 72 Ma geochemical evolution of the Madeira hotspot (eastern North Atlantic): Recycling of Palaeozoic (≤ 500 Ma) oceanic crust.

Gieskes JM, Elderfield H, and Palmer MR (1986) Strontium and its isotope composition in interstitial waters of marine carbonate sediments. Earth Planet Sci Lett 77: 229-235

Goes S, Spakman W, and Bijwaard H (1999) A lower mantle source for Central European volcanism. Science 286: 1928-1931

Graham DW, Zindler A, Kurz MD, Jenkins WJ, Batiza R, and Staudigel H (1988) He, Pb, Sr and Nd isotope constraints on magma genesis and mantle heterogeneity beneath young Pacific seamounts. Contrib Mineral Petrol 99: 446-463

Green DH (1994) Experimental definition of mantle melting and implication for mantle dynamics. Mineral Mag 58: 350-351

Green DH and Fallon TJ (1998) Pyrolite: A Ringwood concept and its current expression. In: Jackson I (Ed) The Earth's mantle. Cambridge University Press, Cambridge: 311-381

Green TH and Pearson NJ (1986) Rare-earth element partitioning between sphene and coexisting silicate liquid at high pressure and temperature. Chem Geol 55: 105-119

Haase KM (1996) The relationship between the age of the lithosphere and the composition of oceanic magmas: Constraints on partial melting, mantle sources and the thermal structure of the plates. Earth Planet Sci Lett 144: 75-92

Hardenbol J, Thierry J, Farley MB, Jaquin T, Graciansky de PC, and Vail PR (1998) Mesozoic and Cenozoic sequence stratigraphy of European basins.

Hinz K, Dostmann H, and Fritsch F (1982) The continental margin off Morocco: seismic sequences, structural elements and geological development. In: von Rad U, Hinz K, Sarnthein M, and Seibold E (Eds) Geology of the Northwest African continental margin. Springer Verlag, Berlin, Heidelberg, New York: 34-60

Hirose K (1997) Partial melt compositios of carbonated peridotite at 3 GPa and role of CO_2 in alkali-basalt magma generation. Geophys Res Lett 24 No. 22: 2837-2840

Hirschmann MM and Stolper EM (1996) A possible role for garnet pyroxenite in the origin of the "garnet signature" in MORB. Contrib Mineral Petrol 124: 185-208

Hoernle K, Werner R, Morgan JP, Garbe-Schönberg D, Bryce J, Mrazek J (in press) Existence of complex zonation in the Galápagos plume for at least 14.5. Ma. Geology

Hoernle K (1998) Geochemistry of Jurassic oceanic crust beneath Gran Canaria (Canary Islands): Implications for crustal recycling and assimilation. J Petrol 39-5: 859-880

Hoernle K and Schmincke H-U (1993a) The petrology of the tholeiites through melilite nephelinites on Gran Canaria, Canary Islands: crystal fractionation, accumulation and depths of melting. J Petrol 34: 573-597

Hoernle K and Schmincke H-U (1993b) The role of partial melting in the 15 Ma geochemical evolution of Gran Canaria: a blob model for the Canary hotspot. J Petrol 34: 599-626

Hoernle K, Tilton G, and Schmincke H.-U (1991) Sr-Nd-Pb isotopic evolution of Gran Canaria: evidence for shallow enriched mantle beneath the Canary Islands. Earth Planet Sci Lett 106: 44-63

Hoernle K and Tilton GR (1991) Sr-Nd-Pb isotope data for Fuerteventura (Canary Islands) basal complex and subaerial volcanics: application to magma genesis and evolution. Schweiz Mineral Petrogr Mitt 71: 5-21

Hoernle K, Zhang Y-S, and Graham D (1995) Seismic and geochemical evidence for large-scale mantle upwelling beneath the eastern Atlantic and western and central Europe. Nature 374: 34-39

Hofmann AW (1988) Chemical differentiation of the Earth: the relationship between mantle, continental crust, and oceanic crust. Earth Planet Sci Lett 90: 297-314

Holik JS and Rabinowitz PD (1991) Effects of the Canary hotspot volcanism on structure of oceanic crust off Morocco. J Geophys Res 96: 12039-12067

Honnorez J (1966) Contribution á l' étude géologique et pétrographique de l' Archipel des Selvagens. Bull Acad roy Sci d' Outre Mer, Classe des Sci Tech N S 16: 1-43

Ito E, White WM, and Göpel C (1987) The O, Sr, Nd and Pb isotope geochemistry of MORB. Chem Geol 62: 157-176

Jackson I (Ed.) (1998) The earth's mantle. Cambridge University Press, Cambridge, pp 566

Keken van PE and Gable CW (1995) The interaction of a plume with a rheological boundary: A comparison between two- and three-dimensional models. J Geophys Res 100: 20,291-20,302

Keken van PE, Yuen DA, and Berg van den A (1992) Pulsating diapiric flows: Consequences of vertical variations in the mantle creep laws. Earth Planet Sci Lett 112: 179-194

Kelly A and Bercovici D (1997) The clustering of rising diapirs and plume heads. Geophys Res Lett 24 No.2: 201-204

King SD and Anderson DL (1998) Edge-driven convection. Earth Planet Sci Lett 160: 289-296

Le Bas MJ, Le Maitre RW, Streckeisen A, and Zanettin B (1986) A chemical classification of volcanic rocks based on the total alkali-silica diagram. J Petrol 27: 745-750

Le Bas MJ, Rex DC, and Stillman CJ (1986) The early magmatic chronology of Fuerteventura, Canary islands. Geol Mag 123: 287-298

Le Maitre RW (1989) A classification of igneous rocks and glossary of terms: Recommendations of the International Union of Geological Sciences Subcommision on the systematics of igneous rocks.

McDonald GA and Katsura T (1964) Chemical composition of Hawaiian lavas. J Petrol 5: 82-133

Malamud BD and Turcotte DL (1999) How many plumes are there? Earth Planet Sci Lett 174: 113-124

McNut MK, Caress DW, Reynolds J, Jordahl KA, and Duncan RA (1997) Failure of plume theory to explain midplate volcanism in the southern Austral islands. Nature 389: 479-482

McDougal I and Schmincke H-U (1976) Geochronology of Gran Canaria, Canary Islands: Age of shield building volcanism and other magmatic phases. Bull Volcanol 40: 1-21

Mitchel-Thomé RC (1976) Geology of the middle Atlantic Islands. Borntraeger, Berlin, pp 382

Morais JC (1940) Archipelago das Selvagens. Mem Not Publ Mus Min Geol Univ Coimbra 2: 1-39

Morgan WJ (1972) Plate motions and deep mantle convection. Geol Soc Am Mem 132: 7-22

Morgan WJ (1983) Hotspot tracks and the early rifting of the Atlantic. Tectonophys 94: 123-139

Nakakuki T, Yuen DA, and Honda S (1997) The interaction of plumes with the transition zone under continents and oceans. Earth Planet Sci Lett 146: 379-391

O'Conner JM and le Roex AP (1992) South Atlantic hot spot-plume systems: 1. Distribution of volcanism in time and space. Earth Planet Sci Lett 113: 343-364

Paytan A, Kastner M, Martin EE, MacDougall JD, and Herbert T (1993) Marine barite as a monitor of seawater strontium isotope composition. Nature 366: 445-449

Portugal Ferreira M, Macedo CR, and Ferreira JF (1988) K-Ar geochronology in the Selvagens, Porto Santo and Madeira Islands (Eastern-Central Atlantic): A 30 m.y. spectrum of submarine and subaerial volcanism. Lunar Planet Inst (abstract) 19: 325-326

Ribe NM and Christensen UR (1999) The dynamical origin of Hawaiian volcanism. Earth Planet Sci Lett 171: 517-531

Ritsema J, Heijst HJv, and Woodhouse JH (1999) Complexe shear wave velocity structure imaged beneath Africa and Iceland. Science 286: 1925-1928

Schirnick C, Bogaard Pvd and Schmincke H-U (1999) Cone sheet formation and intrusive growth of an oceanic island; the Miocene Tejeda Complex on Gran Canaria (Canary Islands). Geology 27: 207-210

Schmidt R, Schmincke H-U, McPhie J, and Bogaard Pvd (in prep.) Volcanology, geochemistry and temporal evolution of a shoaling to emergent seamount, Porto Santo (Central East Atlantic).

Schmincke H-U (1982) Volcanic and chemical evolution of the Canary Islands. In: Seibold E (Ed) Geology of the Northwest African margin. Springer-Verlag, New York: 273-306

Schmincke H-U and Sumita M (1998) Volcanic evolution of Gran Canaria reconstructed from apron sediments: Synthesis of VICAP project drilling. In: Weaver PPE, Schmincke H-U, Firth JV, and Duffield W (Eds) Proceedings of the Ocean Drilling Program, Scientific Results. 157 443-469

Smith WHF and Sandwell DT (1997) Global seafloor topography from satellite altimetry and ship depth soundings. Science 277: 1956-1962

Staudigel H and Schmincke H-U (1984) The Pliocene seamount series of La Palma/Canary Islands. J Geophys Res 89 (13): 11195-11215

Steinbach V and Yuen DA (1997) Dynamical effects of a temperature- and pressure-dependent lower-mantle rheology on the interaction of upwellings with the transition zone. Phys Earth Planet Inter 103: 85-100

Steinberger B and O'Connell RJ (1998) Advection of plumes in mantle flow: implications for hotspot motion, mantle viscosity and plume distribution. Geophys J Int 132: 412-434

Stets J and Wurster P (1982) Atlas and Atlantic - structural relations. In: von Rad U, Hinz K, Sarnthein M, and Seibold E (Eds) Geology of the Northwest African continental margin. Springer Verlag, Berlin, Heidelberg, New York: 69-85

Stillman CJ (1997) The episodic growth and partial destruction of pre-shield-lava Fuerteventura. In: International Workshop, volcanism & volcanic hazards in immature intraplate oceanic islands. La Palma, Canary Islands: abstr 56-58

Sun SS (1980) Lead isotopic study of young volcanic rocks from mid-ocean ridges, ocean islands and island arcs. Phil Trans R Soc London A 197: 409-445

Takahashi E (1986) Melting of dry peridotite KLB-1 up to 14 GPa: implications on the origin of peridotitic upper mantle. J Geophys Res 91: 9367-9380

Thirlwall MF (1997) Pb isotopic and elemental evidence for OIB derivation from young HIMU mantle. Chem Geol 139: 51-74

Todt W, Cliff RA, Hanser A, and Hofmann AW (1996) Evaluation of a ^{202}Pb-^{205}Pb double spike for high precision lead isotope analyses. In: Basu A and Hart S (Eds) Earth Processes: Reading the isotopic code. Geophys Monogr 95 AGU, Washington: 429-437

Vogt PR (1991) Bermuda and Appalachian-Labrador rises: common non-hotspot processes. Geology 19: 41-44

Weaver BL (1991) The origin of ocean island basalt end-member compositions: trace element and isotopic constraints. Earth Planet Sci Lett 104: 381-397

Werner R., Hoernle K, Bogaard Pvd, Ranero C, von Huene R, and Korich D (1999) Crowned 14-m.y.-old Galápagos archipelago off the coast of Costa Rica: Implications for tectonic and evolutionary models. Geology 27: 499-502

Wendt I and Carl C (1991) The statistical distribution of the mean squares weighted deviation. Chem Geol 86: 275-285

Whitehead J and Luther DS (1975) Dynamics of laboratory diapir and plume models. J Geophys Res 80 No 5: 705-717

Whitehead JA (1982) Instabilities of fluid conduits in a flowing earth -are plates lubricated by the asthenosphere? Geophys J R astr Soc 70: 415-433

Wilson JT (1963) Hypothesis of Earth´s behaviour. Nature 198: 925-929

York D (1969) Least squares fitting of a straight line with correlated errors. Earth Planet Sci Lett 5: 320-324

Young HD (1962) Statistical treatment of experimental data. McGraw-Hill 88: 5101-5112

Zbyszewski G, Da Veiga Ferreira O, Aires-Barros L, Matias MJ, Bravo T, and Coello J (1979) Noticia Explicativa da Folha das Ilhas Selvagens. In: Servicos Geologicos de Portugal, Lisbon

Zhang Y-S and Tanimoto T (1992) Ridges, hotspots and their interaction as observed in seismic velocity maps. Nature 355: 45-49

Zhou H-W and Clayton RW (1990) P and S wave travel time inversions for subducting slab under the Island arcs of the Northwest Pacific. J Geophys Res 95: 6829-6851

Zindler A and Hart SR (1986) Chemical geodynamics. Ann Rev Earth Planet Sci 14: 493-571

Chapter 6: Final conclusions

The age and geochemical data presented in this study contribute to the understanding of the magmatic evolution of volcanic ocean islands -especially on slow moving plates. The OIB-like isotope ratios indicate that all islands and seamounts in this region have a mantle plume origin, but establishing the general magmatic and geochronologic evolution of Madeira Island and the Selvagen archipelago shows that these islands bear major differences with the classical evolution of the plume-related Hawaiian Islands. However, on Madeira and Selagem Grande, a more voluminous shield stage and a less voluminous post-erosional or re-juvenated stage can be distinguished by a phase of ceased or at least strongly decreased volcanic activity.

On Madeira, two volcanic rift systems form a single volcanic system which were alternately active during the shield stage. The E-W-oriented Madeira Rift Arm and the NNS-SSE -oriented Desertas Rift Arm join at the eastern end of Madeira and the northern end of the submarine Desertas Ridge at an angle of 110°. During the tholeiitic to basanitic shield stage (> 4.6-0,7 Ma), ca. 99.5 % of the subaerial volume of Madeira (including the Desertas Islands) was erupted, whereas the remaining ca. 0.5 % was erupted during the basanitic post-erosional stage (< 0.7 Ma). The Desertas Islands formed during the shield stage in a short interval between 3.3 and 3.6 Ma. In this period, the Madeira Rift was almost completely inactive. Minor post-erosional volcanism continued into the Holocene with the last eruption on Madeira occuring 6000-7000 years BP. An average growth rate of 5500 km^3/Ma for the submarine and 100-150 km^3/Ma for the subaerial part of the shield stage is estimated based on the available age, bathymetric and topographic data. The low growth rates are a major difference to the Hawaiian system.

The geochemical composition of the Madeira archipelago is explained by the recycling of subducted oceanic crust into the magma source. The idea of relatively young recycled oceanic crust is confirmed by Pb and Nd isotope ratios in the volcanic rocks, indicating an overall age of < 500 Ma for the recycling process. Variations in major elements and radiogenic isotopes point to a heterogeneous plume source containing two endmembers interpreted as altered upper basaltic oceanic crust (high FeO^T and SiO_2 and enriched Pb, Sr and Nd isotope ratios) and lower gabbroic oceanic crust (low FeO^T and SiO_2 and more-depleted Sr, Nd and Pb isotope ratios). The relative proportions of these endmembers in the volcanic rocks on the Madeira/Desertas Islands change with decreasing age of the stratigraphic units. The upper oceanic crust component was predominantly extracted during the early shield stage, whereas the lower oceanic crust component dominates the post-erosional stage. This observation leads to the model of a small, discrete and blob-like plume.

The solidus of the upper basaltic crust components was crossed first in an upwelling discrete plume and therefore adiabatic melts are firstly dominated by this endmember. This process resulted in increasing exhaustion of the altered upper basaltic ocean crust component with progressive melt extraction. When the blob-shaped plume continued spread out, subsequent melts became increasingly depleted in this component and therefore increasingly enriched by melts of the lower oceanic crust endmember. The low-volume, isotopic depleted volcanism at the post-erosional stage and the smaller degree of melting coincide with the proposed model.

Madeira Island is interpreted to represent the present location of a > 70 Ma old hotspot track which includes Porto Santo Island (11.1-14.3 Ma), Seine, possibly Unicorn, Ampère (31 Ma), Coral Patch and Ormonde Seamounts (65-67 Ma), as well as the Serra de Monchique complex in southern Portugal (70-72 Ma). A weak, pulsating plume, forming discrete blobs of upwelling plume material, as proposed for Madeira Island, explains the large and variable age gaps in the Madeira hotspot track. The age relationship of the volcanoes results in a calculated absolute African plate motion of about 1.2 cm/a (in the Madeira region) and a rotation pole at 43°N/ 42°W.

The individual blobs of plume material show increasing contamination of an enriched mantle component, with decreasing distance of the volcanoes to the continental margin reflecting shallow level contamination by displaced portions of continental lithosphere incorporated into the oceanic lithosphere at continental breakup.

Age data from the Selvagen Islands and seamounts to the east and northeast of the archipelago being dated in this study support an origin from a different hotspot system. The basanitic to phonolitic basement is up to 30 Ma old. Extensive erosion has truncated large parts of the basement during a subsequent gap of volcanic activity between about 23 and 12 Ma. At this time marine carbonate sediments were deposited on the basement on Selvagem Grande thus providing proof for a submarine setting. Emplacement of alkali basaltic to basanitic dykes (8-12 Ma), subaerial lava flows and pyroclastics (3.4 Ma) can be attributed to two rejuvenated or post-erosional stages. The Sr-, Nd- and Pb isotopic ratios from all units of the Selvagen Islands, and neighboring seamounts to the east and northeast, show no affinities to the Madeira Islands but almost completely coincide with the isotopic compositions of the Canary Islands, supporting a common plume source.

The geochemical similarity and age progression decreasing from NE to SW for shield stage volcanism on islands and seamounts in the direction of plate motion suggest a common

hotspot origin for the >800 km long and ~450 km wide belt of islands (Canaries and Selvagens) and the seamounts to the northeast (including Lars, Dacia, Conception Bank and Last Minute Seamount). Irregular age relations and spatial distribution, however, are not consistent with the derivation from a classical narrow hotspot. Two types of models are proposed to explain the wide, diffuse track: 1) a large (~ 400 km wide) heterogeneous plume containing enriched plume material distributed in zones or blobs within more depleted or residual material. 2) formation of a large, stationary heterogeneous plume head at the upper-lower mantle transition zone, ejecting individual diapirs from different parts of the head. In both models, the isotopically enriched plume material is progressively consumed during the shield stage of volcanism. During the post-erosional or rejuvenated stage, the magmas are therefore predominated by isotopically more depleted source material.

In summary, the broad belt of volcanic islands and seamounts in the eastern North Atlantic volcanic province between 27° and 37° N can be attributed to mantle plume origin and two separate hotspot systems (the Madeira and Canary hotspot tracks). Both systems differ from classic hotspots like Hawaii in their temporal and spatial distribution. Additional age determinations from undated and unsampled seamounts (in particular from the Madeira-Tore Rise) are needed for further confirmation of this model.

References

Anguita, F., and Hernan, F., 1975, A propagating fracture model versus a hotspot origin for the Canary Islands: Earth Planet. Sci. Lett., v. 27, p. 11-19.

Araña, V., and Ortiz, R., 1991, The Canary Islands: Tectonics, magmatism and geodynamic framework, *in* Kampunzu, A.B., and Lubala, R.T., eds., Magmatism in extensional structural settings (The Phanerozoic African plate): Barcelona, Spain, Springer-Verlag, p. 209-563.

Campbell, I.H., and Griffiths, R.W., 1990, Implications of mantle plume structure for the evolution of flood basalts: Earth Planet. Sci. Lett., v. 99, p. 79-93.

Chase, C.G., 1981, Oceanic island Pb: Two-stage histories and mantle evolution: Earth Planet. Sci. Lett., v. 52, p. 277-284.

Chauvel, C., Hofmann, A.W., and Vidal, P., 1992, HIMU-EM: The French Polynesian connection: Earth Planet. Sci. Lett., v. 110, p. 99-119

Garbe-Schönberg, C.D., 1993, Simultaneous determination of thirty-seven trace elements in twentyeight international rock standards by ICP-MS: Geost. Newslett., v. 17, p. 81-97.

Halliday, A.N., Davies, G.R., Lee, D.-C., Tommasini, S., Paslick, C.R., Fitton, J.G., and James, D.E., 1992, Lead isotope evidence for young trace element enrichment in the oceanic upper mantle: Nature, v. 359, p. 623-627.

Halliday, A.N., Davies, G.R., Lee, D.-C., Tommasini, S., Paslick, C.R., Fitton, J.G., and James, D.E., 1993, Correction to "Lead isotope evidence for young trace element enrichment in the oceanic upper mantle": Nature, v. 362, p. 184.

Hanan, B.B., and Graham, D.W., 1996, Lead and helium isotope evidence from oceanic basalts for a common deep source of mantle plumes.: Science, v. 272, p. 991-995.

Hart, S.R., and Staudigel, H., 1989, Isotopic characterization and identification of recycled components, *in* Hart, S.R., and Gülen, L., ed., Crust/mantle recycling at convergence zones, Kluwer Acad. Publ., p. 15-28.

Hauff, F., Hoernle, K., Tilton, G., Graham, D.W., and Kerr, A.C., 2000, Large volume recycling of oceanic lithosphere over short time scales: Geochemical constraints from the Caribbean Large Igneous Province: Earth Planet. Sci. Lett., v. 174, p. 247-263.

Hoernle, K., 1998, Geochemistry of Jurassic oceanic crust beneath Gran Canaria (Canary Islands): Implications for crustal recycling and assimilation: J. Petrol., v. 39-5, p. 859-880.

Hoernle, K., and Schmincke, H.-U., 1993a, The petrology of the tholeiites through melilite nephelinites on Gran Canaria, Canary Islands: crystal fractionation, accumulation and depths of melting: J. Petrol., v. 34, p. 573-597.

Hoernle, K., and Schmincke, H.-U., 1993b, The role of partial melting in the 15 Ma geochemical evolution of Gran Canaria: a blob model for the Canary hotspot: J. Petrol., v. 34, p. 599-626.

Hoernle, K., and Tilton, G.R., 1991, Sr-Nd-Pb isotope data for Fuerteventura (Canary Islands) basal complex and subaerial volcanics: application to magma genesis and evolution: Schweiz. Mineral. Petrograph. Mitt., v. 71, p. 5-21.

Hoernle, K., Zhang, Y.-S., and Graham, D., 1995, Seismic and geochemical evidence for large-scale mantle upwelling beneath the eastern Atlantic and western and central Europe: Nature, v. 374, p. 34-39.

Hofmann, A.W., and White, W.M., 1982, Mantle plumes from ancient oceanic crust: Earth Planet. Sci. Lett., v. 57, p. 421-436.

Holik, J.S., and Rabinowitz, P.D. 1991, Effects of the Canary hotspot volcanism on structure of oceanic crust off Morocco: J. Geophys. Res., v. 96, p. 12039-12067.

Kogiso, T., Yoshiyuki, T., and Nakano, S., 1997, Trace element transport during dehydration processes in the subducted oceanic crust: Experiments and implications for the origin of ocean island basalts: Earth Planet. Sci. Lett., v. 148, p. 193-205.

Morgan, W.J., 1972, Plate motions and deep mantle convection: Geol. Soc. Am. Mem., v. 132, p. 7-22.

Schmincke, H.-U., 1982, Volcanic and chemical evolution of the Canary Islands, *in* Seibold, E., ed., Geology of the Northwest African margin: New York, Springer-Verlag, p. 273-306.

Staudigel, H., Davis, G.R., Hart, S.R., Marchant, K.M., and Smith, B.M., 1995, Large-scale isotopic Sr, Nd and O isotopic anatomy of altered oceanic crust: DSDP/ODP sites 417/418: Earth Planet. Sci. Lett., v. 130, p. 169-185.

Thirlwall, M.F., 1997, Pb isotopic and elemental evidence for OIB derivation from young HIMU mantle: Chem. Geol., v. 139, p. 51-74.

Todt, W., Cliff, R.A., Hanser, A., and Hofmann, A.W., 1996, Evaluation of a ^{202}Pb-^{205}Pb double spike for high precision lead isotope analyses, *in* Basu, A., and Hart, S., eds., Earth Processes: Reading the isotopic code, Volume 95: Geophys. Monograph: Washington, AGU, p. 429-437.

Weaver, B.L., 1991, The origin of ocean island basalt end-member compositions: trace element and isotopic constraints: Earth Planet. Sci. Lett., v. 104, p. 381-397.

White, R.S., and McKenzie, D., 1989, Magmatism at rift zones: the generation of volcanic continental margins and flood basalts: J. Geophys. Res., v. 94, p. 7685-7729.

Wilson, J.T., 1963, Hypothesis of Earth´s behaviour: Nature, v. 198, p. 925-929.

Zindler, A. and Hart, S.R., 1986, Chemical geodynamics: Ann. Rev. Earth Planet. Sci., v. 14, p. 493-571

Acknowledgements

First, I wish to thank my advisor, Kaj Hoernle, for his encouraging supervision, patience, stimulating discussions and great help during the field work on Madeira, Desertas Islands, Porto Santo and the Selvagen Islands. Many thanks also to Hans-Ulrich Schmincke for his support and in particular for introducing me into the field. I thank both for allowing me to participate in the Madeira project.

I further wish to thank Paul van den Bogaard, Ralf Schmidt, Andreas Klügel and Goor Zankl for their support during several field seasons. I gratefully acknowledge Director Henrique Costa-Neves and his staff from Parque Natural da Madeira (among others Marco P. F. D. Freitas, Rui M. S.antos, Herculano P. Fernandes, Fernando F. da Silva Almoda, Nelson R. dos Santos, Rosa Pires and last but not least Fernando R. Vieira) for cooperation, logistical support and excellent hospitality on Madeira and, in particular, on the Desertas and Selvagen Islands. Without the permission and support of the Parque Natural, large parts of this study would not have been possible. Many thanks also to the Portuguese Navy for providing several lifts to the islands and to Domingos Rodrigues (the "landslide man") from the University of Madeira for his support on Madeira.

Captain M. Gross, officers and crew of the F.S. POSEIDON are gratefully acknowledged for their help in obtaining the submarine rock samples used in this study. All other participants of this cruise (Chief Scientist Kaj Hoernle, Co-Chief Reinhard Werner, Martin Wienecke, Folkmar Hauff, Valentina Cruz, Svend Duggen, Goor Zankl, Susanne Aarburg and Beatrice Neu) are thanked for their help and for a great time at sea. I want to very much thank Colin Devey and Peter Stoffers from the Geological Institute of the University Kiel for the logistical support, without which the POSEIDON cruise would not have been possible. A special thanks goes to Valentina Cruz from the University of Lisbon for her selfless help in communicating with the Portuguese authorities.

I wish to thank Folkmar Zöllmer, Kerstin Wolff and Dagmar Rau (XRF analyses), Otto Schneider (EMS microprobe), Florian Marks, Dagmar Tietgen and, in particular, "magic" Goor Zankl (sample preparation), Jan Sticklus and Paul van den Bogaard (Ar/Ar radiometric dating), Tom Arpe, Heidi Blaschek and Dieter Garbe-Schönberg (ICP-MS lab at Geological Institute/University Kiel) and Silke Vetter and Folkmar Hauff (TIMS laboratory) for help and contribution to the analytical part of this work. Again, I thank Kaj Hoernle for his patience in teaching me all the mysteries of the Sr, Nd and Pb analytics and how to work with the MAT 262 mass spectrometer.

My colleagues and friends at GEOMAR were of great help to me. Special thanks go to the Volcanology and Petrology Department and the Graduate School. Among others, I want to thank Ralf Schmidt, Sebastian Krastel, Mathias Hort, Reinhard Werner, Peter Sachs, Angelika Schmidt, Anne Douglas, Silke Vetter, Nico Urbanski and especially Folkmar Hauff and Paul van den Bogaard for answering my numerous questions and Richard Heath for proofreading of the English in parts of this manuscript. A special thanks goes to Eduard Harms and Svend Duggen, who shared the office with me and made me have a great time (mange tak til Svend for rigelige forsyninger af den "gamle" jule chocolade...). My friend Harald Blazy is thanked very much for writing me a computer program.

Finally I wish to thank my family for their warm-hearted support and confidence. A very special thanks goes to Angie, who shared my dreams and fears throughout.

This work was founded by the Deutsche Forschungsgemeischaft (project HO1833/1).

Appendix to Chapter 3 (Age dating of the Madeira archipelago and hotspot track)

Sample description and sampling sites.

Sample No.	Sample type	Location	Latitude/ Longitude
Madeira			
Ma 85	Basanitic lava flow	Northern Exit of São Vicente village	32°49'08'' 17°02'28''
Ma 19	Plag in pumice layer	Street Encumeada-Paul da Serra, between first and second tunnel	32°44'48'' 17°01'32''
Ma 82c	Plag in trachyte intrusion	Below chapel of São Vicente	32°47'32'' 17°02'00''
Ma 146	Plag in pumice layer	Behind church of São Martinho	32°38'42'' 16°56'25''
Ma 37	Hawaiitic lava flow	Street Encumeada-Paul da Serra, ca. 1 km behind third tunnel	32°44'11'' 17°02'39''
Ma 107	Plag in pumice layer	Lower part of road profile of Porto Novo valley (south side)	32°39'31'' 16°48'30''
Ma 75	Alkali basaltic sill	Quarry near Encumeada pass	32°45'06'' 17°01'07''
Ma 152	Alkali basaltic lava flow	Road cut east of Jardim do Mar (Rib. Funda valley, near road tunnel)	32°43'48'' 17°11'51''
Ma 44	Plag in pumice layer	Street Encumeada-Paul da Serra, 0.5 km south of Casa Lombo do Mouro	32°43'50'' 17°03'00''
Ma 170	Hawaiitic lava flow	Thin flow below lava pile at road cut south part of Machico bay	32°42'32'' 16°45'40''
Ma 227	Transitional basalt boulder	Road cut at Cumeal village (Cural das Freiras valley)	32°43'58'' 16°57'53''
Ma 208	Alkali basaltic lava flow	Lower part of eastern slope of Paul da Serra plateau	32°43'37'' 17°02'43''
Ma 203	Plag in alkali basaltic flow	Lower part of eastern slope of Paul da Serra plateau	32°43'41'' 17°02'47''
13-7-96-1	Transitional basalt dike rim	Cruz da Guarda village (south of Porto da Cruz)	32°44'53'' 16°48'42''
13-7-96-3	Transitional basalt dike rim	Cruz da Guarda village (south of Porto da Cruz)	32°44'53'' 16°48'42''
Desertas Islands			
Ilhéu Chão K 22	Alkali basaltic lava flow	Base of Ilhéu Chão lava flow sequence	32°34'38'' 16°32'27''
Deserta Grande DGR 9	Basanitic dike	Wall behind big land-slide fan near refuge	32°30'35'' 16°30'16''
6302B	Megacryst in scoria cone	Top plateau near southern end of the island	32°29'38'' 16°29'38''
DGR 47	Basanitic lava flow	Pedregal summit	32°32'23'' 16°31'21''
DGR 2	Alkali basaltic lava flow	Base of lava flow sequence (south of refuge)	32°30'30'' 16°30'19''
K 31	Alkali basalti lava flow	Base of lava flow sequence, shore just south of Ponta do Pedregal	32°31'55'' 16°31'23''

Ilhéu do Bugio K 15	Alkali basaltic dyke	Shore near Canto do Furado	32°25'56'' 16°29'17''
K 5	Plag in alkali basaltic dyke	Shore near Ponta da Estância	32°24'24'' 16°28'27''
K 11	Alkali basaltic beach block	Shore near Canto do Furado	32°25'56'' 16°29'17''
Porto Santo K 43	Basanitic intrusion	Near Pico Juliana summit	33°05'23'' 16°19'09''
K 38	Plag in trachytic intrusion	West slope of Pico Castelo (above airport)	33°04'44'' 16°19'51''
K 67a	Alkali basaltic dike	Ridge of Espigao summit	33°02'24'' 16°22'52''
K 48	Alkali basaltic dike	Street between Serra de Dentro and Camacha (below small quarry west of Pico Branco)	33°05'29'' 16°18'36''
K 47	Plag in trachytic intrusion	Street between Serra de Dentro and Camacha (small quarry west of Pico Branco)	33°05'26'' 16°18'23''
K 68	Trachytic intrusion	Near Ana Ferreira summit	33°02'27'' 16°18'51''
K 42	Plag in benmoreitic dike	West slope of Pico Castelo (above airport)	33°04'47'' 16°19'42''
K 46	Plag in basanitic intrusion	Below Pico Juliana summit	33°05'26'' 16°19'02''
K 55	Alkali basaltic lava flow	Lower part of lava flow sequence at Zimbralinho bay (SW part of the island)	33°01'49'' 16°22'57''
K 49	Plag in benmoreitic dike	Street between Serra de Dentro and Camacha (NE of Pico Juliana)	33°05'29'' 16°18'40''
Ampére Seamount DS 797-1	Hawaiitic beach cobble	Eastern part of summit at 35°03' N / 12°54' W (160 m water depth)	35°03'02'' 12°54'0[illegible]''

Appendix to Chapter 3 (Age dating of the Madeira archipelago and hotspot track)

Analytical results

Sample	Mass (mg)	$40^*/39_K$	1s	$^{40}Ar_{atm}$%	Ca/K	1s	Apparent age	1s
MA107	J =0.00221926±0.00000402							
M107 1230.219	2.19E-01	3.806E-01	± 1.01E-01	70.2	3.81	± 0.01	1.52E+06	± 4.0E+05
MA10 62.336	2.34E+00	3.597E-01	± 1.29E-02	74.7	4.66	± 0.00	1.44E+06	± 5.2E+04
MA10 70.622	6.22E-01	3.637E-01	± 3.48E-02	93.7	5.42	± 0.01	1.46E+06	± 1.4E+05
MA10 81.049	1.05E+00	3.440E-01	± 2.16E-02	90.3	4.84	± 0.01	1.38E+06	± 8.7E+04
MA10 90.909	9.09E-01	3.834E-01	± 3.63E-02	80.0	5.74	± 0.01	1.53E+06	± 1.5E+05
MA10 100.575	5.75E-01	3.864E-01	± 6.12E-02	92.2	5.94	± 0.01	1.55E+06	± 2.4E+05
MA10 110.480	4.80E-01	3.810E-01	± 4.43E-02	93.2	4.75	± 0.01	1.52E+06	± 1.8E+05
MA10 120.489	4.89E-01	2.425E-01	± 5.81E-02	95.8	6.28	± 0.01	9.71E+05	± 2.3E+05
M107 471.123	1.12E+00	3.854E-01	± 2.26E-02	63.9	4.19	± 0.01	1.54E+06	± 9.0E+04
M107 480.416	4.16E-01	3.992E-01	± 6.63E-02	79.6	6.45	± 0.02	1.60E+06	± 2.7E+05
M107 490.697	6.97E-01	3.933E-01	± 3.89E-02	80.3	6.41	± 0.01	1.57E+06	± 1.6E+05
M107 500.458	4.58E-01	4.464E-01	± 6.05E-02	74.4	3.50	± 0.01	1.79E+06	± 2.4E+05
M107 510.410	4.10E-01	4.337E-01	± 6.01E-02	81.5	3.58	± 0.01	1.74E+06	± 2.4E+05
MA146	J =0.0021094±0.00000004706							
M14622 520.698	6.98E-01	5.333E-01	± 1.21E-01	73.4	35.47	± 0.07	2.03E+06	± 4.6E+05
M14622 530.266	2.66E-01	6.294E-01	± 2.76E-01	74.4	32.98	± 0.15	2.39E+06	± 1.0E+06
M14622 540.582	5.82E-01	6.081E-01	± 1.57E-01	78.5	33.08	± 0.10	2.31E+06	± 6.0E+05
M14622 550.488	4.88E-01	3.094E-01	± 1.45E-01	92.4	34.29	± 0.07	1.18E+06	± 5.5E+05
M14622 560.526	5.26E-01	4.437E-01	± 1.50E-01	78.5	35.19	± 0.08	1.69E+06	± 5.7E+05
M14622 570.292	2.92E-01	6.358E-01	± 3.31E-01	77.5	35.02	± 0.18	2.42E+06	± 1.3E+06
M14622 581.114	1.11E+00	3.847E-01	± 5.72E-02	76.7	39.41	± 0.07	1.46E+06	± 2.2E+05
M14622 600.276	2.76E-01	5.979E-01	± 2.61E-01	82.6	36.48	± 0.17	2.27E+06	± 9.9E+05
M14622 610.249	2.49E-01	3.410E-01	± 2.52E-01	89.7	34.12	± 0.11	1.30E+06	± 9.6E+05
M14622 620.349	3.49E-01	3.285E-01	± 1.77E-01	84.9	33.09	± 0.12	1.25E+06	± 6.7E+05
MA19	J =0.0021094±0.00000004706							
M19 1180.310	3.10E-01	2.832E-01	± 1.04E-01	86.5	21.96	± 0.07	1.08E+06	± 3.9E+05
M19 FS 61.427	1.43E+00	2.662E-01	± 6.68E-02	40.5	22.11	± 0.03	1.01E+06	± 2.5E+05
M19 FS 30.935	9.35E-01	3.053E-01	± 5.28E-02	52.3	21.05	± 0.05	1.16E+06	± 2.0E+05
M19 FS 40.885	8.85E-01	2.729E-01	± 4.86E-02	42.5	20.78	± 0.05	1.04E+06	± 1.8E+05
M19 FS 10.774	7.74E-01	3.853E-01	± 6.92E-02	27.2	29.01	± 0.08	1.47E+06	± 2.6E+05
M19 FS 20.676	6.76E-01	3.330E-01	± 7.06E-02	36.3	21.07	± 0.06	1.27E+06	± 2.7E+05
M19 FS 50.629	6.29E-01	3.471E-01	± 5.27E-02	25.4	18.05	± 0.04	1.32E+06	± 2.0E+05
M19 FS 90.467	4.67E-01	3.094E-01	± 4.31E-02	44.4	19.80	± 0.05	1.18E+06	± 1.6E+05
M19 FS 80.424	4.24E-01	5.308E-01	± 9.88E-02	2.7	22.59	± 0.06	2.02E+06	± 3.8E+05
M19 FS 70.379	3.79E-01	4.991E-01	± 5.36E-02	5.4	22.48	± 0.07	1.90E+06	± 2.0E+05
M19 FS 100.332	3.32E-01	5.835E-01	± 1.54E-01	6.2	27.26	± 0.08	2.22E+06	± 5.8E+05
MA44	J =0.00221926±0.00000402							
M44 1210.202	2.02E-01	7.907E-01	± 7.72E-02	39.6	1.80	± 0.01	3.16E+06	± 3.1E+05
MA44 10.816	8.16E-01	7.010E-01	± 3.89E-02	77.7	4.30	± 0.01	2.80E+06	± 1.6E+05
MA4420 21.794	1.79E+00	6.927E-01	± 2.54E-02	83.8	1.65	± 0.00	2.77E+06	± 1.0E+05
MA44 31.647	1.65E+00	6.981E-01	± 1.63E-02	84.8	1.82	± 0.00	2.79E+06	± 6.5E+04
MA44 40.826	8.26E-01	6.922E-01	± 3.54E-02	89.3	1.49	± 0.00	2.77E+06	± 1.4E+05

MA44 50.642	6.42E-01	6.816E-01 ± 4.52E-02	89.0	2.01 ± 0.01	2.73E+06 ± 1.8E+05
M44 21 330.974	9.74E-01	7.368E-01 ± 1.46E-02	40.0	2.03 ± 0.00	2.95E+06 ± 5.9E+04
M44 21 341.113	1.11E+00	7.553E-01 ± 1.62E-02	47.4	1.97 ± 0.00	3.02E+06 ± 6.5E+04
M44 21 350.506	5.06E-01	7.790E-01 ± 2.84E-02	71.3	1.91 ± 0.01	3.12E+06 ± 1.1E+05
M44 21 361.470	1.47E+00	7.533E-01 ± 1.64E-02	51.1	3.57 ± 0.01	3.01E+06 ± 6.6E+04
M44 21 370.346	3.46E-01	7.218E-01 ± 3.92E-02	60.8	1.74 ± 0.01	2.89E+06 ± 1.6E+05
MA82c	J =0.0021094±0.000004706				
M82c 1220.254	2.54E-01	3.261E-01 ± 5.53E-02	67.3	3.00 ± 0.01	1.24E+06 ± 2.1E+05
M82C21 380.618	6.18E-01	3.283E-01 ± 2.55E-02	70.7	5.05 ± 0.01	1.25E+06 ± 9.7E+04
M82C21 390.574	5.74E-01	3.444E-01 ± 3.76E-02	72.8	3.58 ± 0.01	1.31E+06 ± 1.4E+05
M82C21 400.814	8.14E-01	3.153E-01 ± 2.20E-02	77.1	4.21 ± 0.01	1.20E+06 ± 8.4E+04
M82C21 410.475	4.75E-01	2.908E-01 ± 5.86E-02	78.4	3.75 ± 0.01	1.11E+06 ± 2.2E+05
M82C 420.494	4.94E-01	3.193E-01 ± 4.67E-02	85.3	5.20 ± 0.01	1.21E+06 ± 1.8E+05
M82C 430.314	3.14E-01	2.677E+00 ± 3.52E+00	94.9	4.57 ± 0.15	1.02E+07 ± 1.3E+07
M82C 440.442	4.42E-01	3.123E-01 ± 8.26E-02	87.9	5.77 ± 0.02	1.19E+06 ± 3.1E+05
M82C 450.202	2.02E-01	1.228E-01 ± 9.97E-02	96.7	5.34 ± 0.03	4.67E+05 ± 3.8E+05
M82C 460.219	2.19E-01	2.394E-01 ± 8.25E-02	88.5	3.31 ± 0.01	9.11E+05 ± 3.1E+05
797-1	J =0.00103666±0.00000268				
797-1 108 276	2.76E-01	1.688E+01 ± 1.59E-01	61.0	5.79 ± 0.02	3.13E+07 ± 3.0E+05
797-1 112 282	2.82E-01	1.688E+01 ± 1.85E-01	57.4	5.14 ± 0.02	3.13E+07 ± 3.5E+05
797-1 1 304	3.04E-01	1.679E+01 ± 1.68E-01	57.5	6.12 ± 0.04	3.11E+07 ± 3.2E+05
797-1 2 388	3.88E-01	1.681E+01 ± 1.28E-01	57.8	5.57 ± 0.03	3.12E+07 ± 2.5E+05
797-1 4 186	1.86E-01	1.718E+01 ± 1.08E-01	51.1	4.62 ± 0.03	3.18E+07 ± 2.1E+05
797-1 5 480	4.80E-01	1.676E+01 ± 8.08E-02	57.6	5.21 ± 0.02	3.11E+07 ± 1.7E+05
797-1 12 231	2.31E-01	1.685E+01 ± 1.47E-01	55.3	4.53 ± 0.22	3.12E+07 ± 2.8E+05
797-1 13 220	2.20E-01	1.659E+01 ± 1.46E-01	64.7	5.13 ± 0.44	3.08E+07 ± 2.8E+05
797-1 15 265	2.65E-01	1.649E+01 ± 3.77E-01	66.3	5.54 ± 0.53	3.06E+07 ± 7.0E+05
797-1 16 201	2.01E-01	1.635E+01 ± 4.43E-01	72.2	3.89 ± 0.70	3.03E+07 ± 8.2E+05
797-1 17 209	2.09E-01	1.691E+01 ± 3.00E-01	64.0	4.79 ± 0.46	3.13E+07 ± 5.6E+05
797-1 18 192	1.92E-01	1.728E+01 ± 3.29E-01	54.3	6.58 ± 0.38	3.20E+07 ± 6.1E+05
797-1 19 194	1.94E-01	1.687E+01 ± 2.31E-01	57.9	4.92 ± 0.32	3.13E+07 ± 4.3E+05
K42	J =0.0010318±0.000002035				
K42 191 355	3.55E-01	7.574E+00 ± 5.69E-01	36.9	30.54 ± 0.17	1.40E+07 ± 1.1E+06
K42 192 580	5.80E-01	7.274E+00 ± 3.62E-01	53.7	30.79 ± 0.09	1.35E+07 ± 6.7E+05
K42 82 200	2.00E-01	7.586E+00 ± 1.19E+00	58.7	55.92 ± 0.54	1.41E+07 ± 2.2E+06
K42 84 160	1.60E-01	7.220E+00 ± 1.97E+00	70.8	71.20 ± 0.72	1.34E+07 ± 3.6E+06
K42 85 316	3.16E-01	7.628E+00 ± 4.65E-01	57.0	29.01 ± 0.12	1.41E+07 ± 8.6E+05
K42 86 261	2.61E-01	6.530E+00 ± 1.11E+00	49.6	72.23 ± 0.38	1.21E+07 ± 2.0E+06
K42 87 358	3.58E-01	7.059E+00 ± 4.96E-01	60.8	31.84 ± 0.19	1.31E+07 ± 9.2E+05
K42 88 378	3.78E-01	6.995E+00 ± 9.03E-01	87.6	60.33 ± 0.36	1.30E+07 ± 1.7E+06
K42 89 858	8.58E-01	7.420E+00 ± 2.29E-01	52.8	26.33 ± 0.12	1.38E+07 ± 4.2E+05
K42 90 991	9.91E-01	7.362E+00 ± 4.08E-01	83.9	35.63 ± 0.11	1.37E+07 ± 7.5E+05
K42 P 128 1108	1.11E+00	6.263E+00 ± 2.58E-01	76.1	50.15 ± 0.20	1.16E+07 ± 4.8E+05
K46	J =0.0010345 1±0.00000196				
K46 157 310	3.10E-01	1.044E+01 ± 2.29E+00	84.7	196.5 ± 1.89	1.94E+07 ± 4.2E+06
K46 158 274	2.74E-01	9.205E+00 ± 1.16E+00	24.5	76.47 ± 0.53	1.71E+07 ± 2.1E+06
K46 66 788	7.88E-01	6.730E+00 ± 3.58E-01	72.0	86.92 ± 0.43	1.25E+07 ± 6.6E+05
K46 67 813	8.13E-01	7.815E+00 ± 3.30E-01	70.0	88.25 ± 0.43	1.45E+07 ± 6.1E+05
K46 68 580	5.80E-01	7.501E+00 ± 3.97E-01	66.7	71.38 ± 0.32	1.39E+07 ± 7.4E+05
K46 69 758	7.58E-01	6.957E+00 ± 3.22E-01	73.8	71.80 ± 0.34	1.29E+07 ± 6.0E+05

K46	70	550	5.50E-01	7.621E+00	± 4.65E-01	22.8	82.84 ± 0.47	1.42E+07 ± 8.6E+05
K46	71	301	3.01E-01	7.310E+00	± 2.42E-01	29.5	12.58 ± 0.09	1.36E+07 ± 4.5E+05
K46	72	350	3.50E-01	6.809E+00	± 7.17E-01	62.6	72.46 ± 0.45	1.27E+07 ± 1.3E+06
K46	73	282	2.82E-01	6.037E+00	± 1.95E+00	84.0	188.6 ± 2.50	1.12E+07 ± 3.6E+06
K49			J =0.0010318±0.000002035					
K49	167	313	3.13E-01	7.966E+00	± 3.06E-01	23.2	8.73 ± 0.04	1.48E+07 ± 5.6E+05
K49	168	405	4.05E-01	7.922E+00	± 6.29E-01	64.6	38.15 ± 0.20	1.47E+07 ± 1.2E+06
K49	41	320	3.20E-01	7.682E+00	± 1.48E-01	24.2	6.14 ± 0.04	1.42E+07 ± 2.8E+05
K49	42	399	3.99E-01	7.958E+00	± 2.36E-01	44.0	14.21 ± 0.07	1.48E+07 ± 4.4E+05
K49	43	299	2.99E-01	6.638E+00	± 5.91E-01	60.5	38.42 ± 0.20	1.23E+07 ± 1.1E+06
K49	44	367	3.67E-01	7.817E+00	± 1.11E-01	19.5	5.77 ± 0.02	1.45E+07 ± 2.1E+05
K49	45	372	3.72E-01	7.222E+00	± 9.73E-01	87.2	43.45 ± 0.21	1.34E+07 ± 1.8E+06
K49	46	531	5.31E-01	7.566E+00	± 4.77E-01	81.9	26.82 ± 0.11	1.40E+07 ± 8.8E+05
K49	47	612	6.12E-01	6.745E+00	± 5.85E-01	88.0	43.44 ± 0.15	1.25E+07 ± 1.1E+06
K49	48	1557	1.56E+00	7.727E+00	± 1.41E-01	68.9	20.41 ± 0.04	1.43E+07 ± 2.6E+05
K49 P	92	1243	1.24E+00	7.595E+00	± 1.27E-01	55.7	18.49 ± 0.05	1.41E+07 ± 2.4E+05
K55			J =0.00103451±0.00000196					
K55	159	204	2.04E-01	6.653E+00	± 2.51E-01	74.2	6.71 ± 0.03	1.24E+07 ± 4.7E+05
K55	160	341	3.41E-01	7.685E+00	± 1.23E-01	76.0	6.74 ± 0.04	1.43E+07 ± 2.3E+05
K55	60	228	2.28E-01	7.503E+00	± 2.45E-01	71.3	6.78 ± 0.04	1.39E+07 ± 4.5E+05
K55	61	235	2.35E-01	7.281E+00	± 2.38E-01	75.9	7.10 ± 0.04	1.35E+07 ± 4.4E+05
K55	63	961	9.61E-01	7.496E+00	± 7.65E-02	74.3	6.64 ± 0.01	1.39E+07 ± 1.4E+05
K55	64	414	4.14E-01	7.195E+00	± 1.53E-01	78.0	7.55 ± 0.03	1.34E+07 ± 2.8E+05
K55	65	470	4.70E-01	7.514E+00	± 1.70E-01	71.6	7.30 ± 0.03	1.40E+07 ± 3.2E+05
K48			J=0.00103451±0.00000196					
K48	163	340	3.40E-01	7.586E+00	± 2.97E-01	70.6	12.49 ± 0.04	1.41E+07 ± 5.5E+05
K48	164	239	2.39E-01	7.498E+00	± 3.15E-01	63.1	12.77 ± 0.05	1.39E+07 ± 5.8E+05
K48	47	823	8.23E-01	9.845E+00	± 1.71E-01	85.9	13.63 ± 0.03	1.83E+07 ± 3.2E+05
K48	49	940	9.40E-01	8.167E+00	± 8.10E-02	78.5	12.69 ± 0.03	1.52E+07 ± 1.5E+05
K48	50	926	9.26E-01	8.565E+00	± 1.35E-01	83.9	13.57 ± 0.03	1.59E+07 ± 2.5E+05
K48	51	908	9.08E-01	7.994E+00	± 8.99E-02	74.5	12.65 ± 0.04	1.49E+07 ± 1.7E+05
K47			J =0.0010318±0.000002035					
K47	163	325	3.25E-01	6.013E+00	± 4.38E-01	30.8	33.53 ± 0.27	1.12E+07 ± 8.1E+05
K47	164	410	4.10E-01	6.664E+00	± 3.13E-01	17.7	25.33 ± 0.12	1.24E+07 ± 5.8E+05
K47	25	240	2.40E-01	7.093E+00	± 5.55E-01	24.9	25.48 ± 0.12	1.32E+07 ± 1.0E+06
K47	26	315	3.15E-01	7.036E+00	± 3.72E-01	26.1	26.42 ± 0.17	1.30E+07 ± 6.9E+05
K47	27	258	2.58E-01	6.420E+00	± 8.73E-01	47.9	22.08 ± 0.23	1.19E+07 ± 1.6E+06
K47	28	718	7.18E-01	6.925E+00	± 1.36E-01	31.1	14.21 ± 0.06	1.28E+07 ± 2.5E+05
K47	29	633	6.33E-01	7.126E+00	± 2.17E-01	17.5	25.75 ± 0.08	1.32E+07 ± 4.0E+05
K47	30	664	6.64E-01	6.730E+00	± 2.19E-01	21.8	22.00 ± 0.10	1.25E+07 ± 4.1E+05
K47	31	656	6.56E-01	6.895E+00	± 2.98E-01	17.2	32.29 ± 0.11	1.28E+07 ± 5.5E+05
K47	32	623	6.23E-01	6.825E+00	± 1.54E-01	47.7	21.97 ± 0.10	1.27E+07 ± 2.9E+05
K47 P	90	1431	1.43E+00	6.927E+00	± 1.58E-01	7.6	29.49 ± 0.11	1.28E+07 ± 2.9E+05
K67a			J =0.0010318±0.000002035					
K67A	157	256	2.56E-01	7.289E+00	± 4.16E-01	36.5	23.77 ± 0.10	1.35E+07 ± 7.7E+05
K67A	159	661	6.61E-01	6.733E+00	± 9.07E-02	29.8	13.43 ± 0.02	1.25E+07 ± 1.7E+05
K67A	160	375	3.75E-01	6.825E+00	± 1.84E-01	35.0	29.60 ± 0.10	1.27E+07 ± 3.4E+05
K67A	161	572	5.72E-01	6.744E+00	± 5.89E-02	48.9	7.85 ± 0.04	1.25E+07 ± 1.1E+05
K67A	162	477	4.77E-01	6.662E+00	± 1.22E-01	44.9	8.85 ± 0.04	1.24E+07 ± 2.3E+05

K67A 163 746	7.46E-01	6.778E+00 ± 4.71E-02	23.9	5.94 ± 0.02	1.26E+07 ± 9.1E+04
K67A 164 913	9.13E-01	6.878E+00 ± 1.26E-01	52.2	19.53 ± 0.05	1.28E+07 ± 2.3E+05
K67A 165 410	4.10E-01	6.972E+00 ± 1.35E-01	46.8	12.92 ± 0.06	1.29E+07 ± 2.5E+05
K68	J =0.00103 18±0.000002035				
K68 158 194	1.94E-01	6.996E+00 ± 7.45E-02	23.6	1.16 ± 0.01	1.30E+07 ± 1.4E+05
K68 166 161	1.61E-01	6.911E+00 ± 9.12E-02	23.4	1.02 ± 0.01	1.28E+07 ± 1.7E+05
K68 167 254	2.54E-01	6.978E+00 ± 7.87E-02	21.9	1.13 ± 0.00	1.29E+07 ± 1.5E+05
K68 168 417	4.17E-01	6.965E+00 ± 4.27E-02	22.6	1.17 ± 0.01	1.29E+07 ± 8.3E+04
K68 169 262	2.62E-01	7.058E+00 ± 6.48E-02	27.2	1.14 ± 0.01	1.31E+07 ± 1.2E+05
K68 170 305	3.05E-01	6.891E+00 ± 5.90E-02	22.9	1.10 ± 0.01	1.28E+07 ± 1.1E+05
K68 171 397	3.97E-01	6.920E+00 ± 4.24E-02	22.5	1.10 ± 0.01	1.28E+07 ± 8.2E+04
137-1	J =0.00103666±0.00000268				
137-1 183 290	2.90E-01	2.443E+00 ± 2.45E-01	76.7	14.52 ± 0.04	4.56E+06 ± 4.6E+05
137-1 184 540	5.40E-01	2.377E+00 ± 1.17E-01	86.2	14.51 ± 0.05	4.44E+06 ± 2.2E+05
137-1 36 1517	1.52E+00	2.325E+00 ± 8.40E-02	87.7	14.58 ± 0.02	4.34E+06 ± 1.6E+05
137-1 37 809	8.09E-01	2.550E+00 ± 9.39E-02	77.4	14.65 ± 0.02	4.76E+06 ± 1.8E+05
137-1 38 695	6.95E-01	2.307E+00 ± 1.03E-01	55.5	14.60 ± 0.05	4.31E+06 ± 1.9E+05
137-1 39 460	4.60E-01	2.345E+00 ± 9.95E-02	83.6	14.68 ± 0.04	4.38E+06 ± 1.9E+05
137-1 34 438	4.38E-01	2.704E+00 ± 1.87E-01	80.0	14.58 ± 0.07	5.05E+06 ± 3.5E+05
137-3	J =0.00103666±0.00000268				
Ma137 77 1552	1.55E+00	2.492E+00 ± 5.46E-02	45.2	14.55 ± 0.02	4.65E+06 ± 1.0E+05
Ma137 78 590	5.90E-01	2.425E+00 ± 9.44E-02	27.8	14.58 ± 0.06	4.53E+06 ± 1.8E+05
Ma137 79 689	6.89E-01	2.604E+00 ± 1.02E-01	15.1	14.72 ± 0.04	4.86E+06 ± 1.9E+05
Ma137 80 702	7.02E-01	2.591E+00 ± 1.06E-01	10.2	14.57 ± 0.04	4.84E+06 ± 2.0E+05
Ma137 81 379	3.79E-01	2.649E+00 ± 1.60E-01	36.0	14.57 ± 0.05	4.95E+06 ± 3.0E+05
137-3 27 1058	1.06E+00	2.433E+00 ± 3.89E-02	30.4	14.66 ± 0.05	4.55E+06 ± 7.3E+04
6302B	J =0.0010318±0.000002035				
6302B 170 354	3.54E-01	1.983E+00 ± 1.16E-01	21.6	10.54 ± 0.04	3.69E+06 ± 2.2E+05
6302B 171 214	2.14E-01	2.012E+00 ± 1.62E-01	10.2	10.59 ± 0.06	3.74E+06 ± 3.0E+05
6302B 107 921	9.21E-01	1.886E+00 ± 5.97E-02	20.2	10.62 ± 0.03	3.51E+06 ± 1.1E+05
6302B 108 890	8.90E-01	1.907E+00 ± 4.81E-02	40.4	10.56 ± 0.03	3.55E+06 ± 9.0E+04
6302B 109 909	9.09E-01	1.829E+00 ± 5.76E-02	28.1	10.60 ± 0.04	3.40E+06 ± 1.1E+05
6302B 110 750	7.50E-01	1.886E+00 ± 6.66E-02	21.1	10.53 ± 0.02	3.51E+06 ± 1.2E+05
6302B 111 392	3.92E-01	1.609E+00 ± 8.36E-02	39.0	10.54 ± 0.04	2.99E+06 ± 1.6E+05
6302B 112 348	3.48E-01	1.561E+00 ± 1.14E-01	44.0	10.50 ± 0.06	2.90E+06 ± 2.1E+05
6302B 113 1545	1.55E+00	1.731E+00 ± 2.66E-02	38.6	10.62 ± 0.02	3.22E+06 ± 5.0E+04
6302B 114 434	4.34E-01	1.502E+00 ± 4.35E-02	41.1	10.59 ± 0.04	2.79E+06 ± 8.1E+04
DGR2	J =0.00103666±0.00000268				
DGR2 192 224	2.24E-01	1.564E+00 ± 3.45E-01	88.9	14.25 ± 0.09	2.92E+06 ± 6.4E+05
DGR2 129 1197	1.20E+00	1.939E+00 ± 5.73E-02	73.5	11.62 ± 0.02	3.62E+06 ± 1.1E+05
DGR2 130 481	4.81E-01	1.778E+00 ± 1.53E-01	90.6	14.46 ± 0.04	3.32E+06 ± 2.9E+05
DGR2 131 308	3.08E-01	1.470E+00 ± 2.16E-01	91.3	14.13 ± 0.05	2.75E+06 ± 4.0E+05
DGR-2 18 673	6.73E-01	1.968E+00 ± 1.37E-01	81.9	13.72 ± 0.05	3.68E+06 ± 2.6E+05
DGR-2 19 901	9.01E-01	1.660E+00 ± 1.91E-01	89.6	16.75 ± 0.04	3.10E+06 ± 3.6E+05
DGR-2 20 1151	1.15E+00	1.782E+00 ± 9.89E-02	85.4	14.34 ± 0.03	3.33E+06 ± 1.8E+05
DGR47	J =0.00103666±0.00000268				
DGR47 191 355	3.55E-01	1.786E+00 ± 1.45E-01	63.3	9.19 ± 0.03	3.34E+06 ± 2.7E+05
DGR47 123 1420	1.42E+00	1.711E+00 ± 6.13E-02	76.2	10.30 ± 0.01	3.20E+06 ± 1.1E+05

DGR47	124	1712	1.71E+00	1.838E+00 ± 6.03E-02	74.8	10.83 ± 0.01	3.43E+06 ± 1.1E+05
DGR47	125	903	9.03E-01	1.846E+00 ± 6.85E-02	73.3	9.49 ± 0.02	3.45E+06 ± 1.3E+05
DGR47	126	499	4.99E-01	1.976E+00 ± 1.43E-01	74.5	11.66 ± 0.03	3.69E+06 ± 2.7E+05
DGR47	127	707	7.07E-01	1.813E+00 ± 8.65E-02	74.3	8.62 ± 0.02	3.39E+06 ± 1.6E+05
DGR9			J =0.00103666±0.00000268				
DGR9	193	655	6.55E-01	1.637E+00 ± 1.18E-01	71.2	19.39 ± 0.04	3.06E+06 ± 2.2E+05
DGR9	72	2212	2.21E+00	1.751E+00 ± 2.03E-02	55.2	6.15 ± 0.01	3.27E+06 ± 3.9E+04
DGR9	73	1550	1.55E+00	1.711E+00 ± 4.91E-02	75.4	10.70 ± 0.02	3.20E+06 ± 9.2E+04
DGR9	74	1040	1.04E+00	1.764E+00 ± 6.10E-02	70.3	12.89 ± 0.02	3.30E+06 ± 1.1E+05
DGR9	75	848	8.48E-01	1.613E+00 ± 6.83E-02	76.0	11.85 ± 0.02	3.01E+06 ± 1.3E+05
DGR9	76	385	3.85E-01	1.923E+00 ± 1.21E-01	66.8	10.09 ± 0.03	3.59E+06 ± 2.3E+05
K11			J =0.00103666±0.00000268				
K11	189	442	4.42E-01	1.889E+00 ± 1.37E-01	50.1	12.52 ± 0.04	3.53E+06 ± 2.5E+05
K11	31	1546	1.55E+00	1.804E+00 ± 2.82E-02	62.1	13.92 ± 0.02	3.37E+06 ± 5.3E+04
K11	32	1092	1.09E+00	1.779E+00 ± 4.54E-02	55.2	12.51 ± 0.02	3.32E+06 ± 8.5E+04
K11	33	716	7.16E-01	1.823E+00 ± 7.08E-02	62.4	14.28 ± 0.03	3.41E+06 ± 1.3E+05
K11	34	796	7.96E-01	1.797E+00 ± 5.89E-02	66.8	16.85 ± 0.03	3.36E+06 ± 1.1E+05
K11	35	691	6.91E-01	1.760E+00 ± 2.74E-02	64.4	11.91 ± 0.03	3.29E+06 ± 5.2E+04
K11	149	718	7.18E-01	1.916E+00 ± 7.00E-02	55.8	13.95 ± 0.04	3.58E+06 ± 1.3E+05
K15			J =0.00103666±0.00000268				
K15	46	2568	2.57E+00	1.710E+00 ± 1.93E-02	75.8	9.12 ± 0.01	3.20E+06 ± 3.7E+04
K15	47	1221	1.22E+00	1.603E+00 ± 6.38E-02	83.2	8.24 ± 0.01	3.00E+06 ± 1.2E+05
K15	48	1329	1.33E+00	1.692E+00 ± 2.27E-02	75.9	7.68 ± 0.01	3.16E+06 ± 4.3E+04
K15	49	446	4.46E-01	1.779E+00 ± 8.05E-02	83.3	8.01 ± 0.03	3.32E+06 ± 1.5E+05
K15	50	698	6.98E-01	1.886E+00 ± 5.88E-02	69.8	7.96 ± 0.02	3.52E+06 ± 1.1E+05
K22			J =0.00103666±0.00000268				
K22	1	491	4.91E-01	2.002E+00 ± 2.08E-01	62.5	22.49 ± 0.10	3.74E+06 ± 3.9E+05
K22	2	808	8.08E-01	1.898E+00 ± 1.10E-01	70.9	22.53 ± 0.05	3.55E+06 ± 2.1E+05
K22	3	831	8.31E-01	1.923E+00 ± 1.81E-01	72.7	25.83 ± 0.08	3.59E+06 ± 3.4E+05
K22	4	412	4.12E-01	1.846E+00 ± 2.54E-01	70.8	21.42 ± 0.10	3.45E+06 ± 4.7E+05
K22	5	454	4.54E-01	2.129E+00 ± 2.20E-01	74.4	26.32 ± 0.08	3.98E+06 ± 4.1E+05
K22	6	194	1.94E-01	2.636E+00 ± 4.06E-01	56.8	21.18 ± 0.12	4.92E+06 ± 7.6E+05
K22	7	304	3.04E-01	2.018E+00 ± 2.33E-01	61.7	19.40 ± 0.09	3.77E+06 ± 4.3E+05
K22	8	353	3.53E-01	1.660E+00 ± 3.90E-01	77.1	26.63 ± 0.15	3.10E+06 ± 7.3E+05
K22	9	630	6.30E-01	1.856E+00 ± 1.65E-01	69.1	23.86 ± 0.06	3.47E+06 ± 3.1E+05
K22	10	540	5.40E-01	1.901E+00 ± 2.20E-01	72.8	22.86 ± 0.08	3.55E+06 ± 4.1E+05
K31			J =0.00103666±0.00000268				
K31	93	1791	1.79E+00	1.853E+00 ± 4.90E-02	65.8	10.45 ± 0.02	3.46E+06 ± 9.2E+04
K31	94	1021	1.02E+00	1.935E+00 ± 5.33E-02	67.7	11.14 ± 0.02	3.61E+06 ± 1.0E+05
K31	95	744	7.44E-01	1.914E+00 ± 8.84E-02	71.6	10.96 ± 0.02	3.58E+06 ± 1.7E+05
K31	96	773	7.73E-01	2.047E+00 ± 6.49E-02	64.9	10.58 ± 0.02	3.82E+06 ± 1.2E+05
K31	97	837	8.37E-01	1.999E+00 ± 5.99E-02	65.3	10.15 ± 0.02	3.73E+06 ± 1.1E+05
K38			J =0.0010318±0.0000002035				
K38	165	194	1.94E-01	6.272E+00 ± 7.38E-01	64.8	22.28 ± 0.14	1.16E+07 ± 1.4E+06
K38	166	368	3.68E-01	7.266E+00 ± 9.15E-01	92.5	26.45 ± 0.10	1.35E+07 ± 1.7E+06
K38	33	238	2.38E-01	7.299E+00 ± 3.35E-01	38.3	15.69 ± 0.11	1.35E+07 ± 6.2E+05
K38	34	170	1.70E-01	7.299E+00 ± 3.19E-01	47.7	13.76 ± 0.12	1.35E+07 ± 5.9E+05
K38	35	540	5.40E-01	6.613E+00 ± 1.50E-01	67.4	19.98 ± 0.09	1.23E+07 ± 2.8E+05

K38 36 533	5.33E-01	6.810E+00 ± 2.19E-01	42.7	24.22 ± 0.10	1.26E+07 ± 4.0E+05
K38 37 453	4.53E-01	6.912E+00 ± 2.78E-01	75.2	21.38 ± 0.09	1.28E+07 ± 5.1E+05
K38 38 593	5.93E-01	6.602E+00 ± 2.54E-01	77.7	17.44 ± 0.10	1.22E+07 ± 4.7E+05
K38 39 695	6.95E-01	6.972E+00 ± 2.81E-01	88.5	20.35 ± 0.06	1.29E+07 ± 5.2E+05
K38 40 1226	1.23E+00	6.646E+00 ± 2.19E-01	76.2	26.28 ± 0.07	1.23E+07 ± 4.1E+05
K38 P 91 931	9.31E-01	6.417E+00 ± 2.05E-01	70.8	17.13 ± 0.07	1.19E+07 ± 3.8E+05
K43	J=0.0010318±0.0000002035				
K43 156 561	5.61E-01	6.085E+00 ± 8.92E-02	37.5	8.14 ± 0.02	1.13E+07 ± 1.7E+05
K43 152 546	5.46E-01	5.960E+00 ± 6.79E-02	49.3	7.63 ± 0.03	1.11E+07 ± 1.3E+05
K43 153 501	5.01E-01	6.125E+00 ± 9.48E-02	35.9	7.98 ± 0.02	1.14E+07 ± 1.8E+05
K43 154 628	6.28E-01	5.959E+00 ± 6.59E-02	33.1	7.23 ± 0.02	1.11E+07 ± 1.2E+05
K43 155 662	6.62E-01	5.886E+00 ± 6.10E-02	41.4	8.04 ± 0.03	1.09E+07 ± 1.1E+05
K43 156 810	8.10E-01	5.914E+00 ± 4.25E-02	33.4	7.59 ± 0.02	1.10E+07 ± 8.2E+04
K43 157 1010	1.01E+00	6.013E+00 ± 4.47E-02	37.2	7.34 ± 0.02	1.12E+07 ± 8.6E+04
K43 158 744	7.44E-01	5.930E+00 ± 7.20E-02	35.1	7.58 ± 0.02	1.10E+07 ± 1.3E+05
K5	J=0.00103666±0.00000268				
K5 181 377	3.77E-01	2.102E+00 ± 3.87E-01	43.5	35.83 ± 0.17	3.93E+06 ± 7.2E+05
K5 182 490	4.90E-01	1.948E+00 ± 5.50E-01	53.1	51.60 ± 0.21	3.64E+06 ± 1.0E+06
K5 118 1965	1.97E+00	1.818E+00 ± 5.95E-02	50.3	48.48 ± 0.17	3.40E+06 ± 1.1E+05
K5 119 768	7.68E-01	1.338E+00 ± 3.04E-01	71.9	46.62 ± 0.15	2.50E+06 ± 5.7E+05
K5 120 484	4.84E-01	2.245E+00 ± 4.37E-01	62.4	46.43 ± 0.17	4.19E+06 ± 8.2E+05
K5 121 313	3.13E-01	2.033E+00 ± 3.41E-01	76.2	33.71 ± 0.14	3.80E+06 ± 6.4E+05
K5 122 484	4.84E-01	1.412E+00 ± 2.08E-01	76.6	35.66 ± 0.14	2.64E+06 ± 3.9E+05
K5 Po 21 1132	1.13E+00	1.938E+00 ± 2.19E-01	49.2	46.37 ± 0.11	3.62E+06 ± 4.1E+05
K5 Po 22 1114	1.11E+00	1.720E+00 ± 1.97E-01	31.3	40.08 ± 0.10	3.21E+06 ± 3.7E+05
Ma152	J=0.00103451±0.00000196				
MA152 171 210	2.10E-01	1.385E+00 ± 3.25E-01	76.6	8.27 ± 0.04	2.58E+06 ± 6.0E+05
MA152 172 496	4.96E-01	1.317E+00 ± 7.96E-02	80.2	8.06 ± 0.01	2.46E+06 ± 1.5E+05
Ma152 154 1624	1.62E+00	1.418E+00 ± 4.41E-02	86.1	8.02 ± 0.01	2.65E+06 ± 8.2E+04
Ma152 155 890	8.90E-01	1.311E+00 ± 4.79E-02	83.0	8.25 ± 0.02	2.45E+06 ± 8.9E+04
Ma152 156 1319	1.32E+00	1.524E+00 ± 5.75E-02	86.0	7.84 ± 0.01	2.84E+06 ± 1.1E+05
Ma152 157 1296	1.30E+00	1.405E+00 ± 3.21E-02	77.2	7.48 ± 0.02	2.62E+06 ± 6.0E+04
Ma170	J=0.00103451±0.00000196				
MA170 169 341	3.41E-01	1.849E+00 ± 1.13E-01	50.6	5.70 ± 0.02	3.45E+06 ± 2.1E+05
MA170 170 524	5.24E-01	1.903E+00 ± 9.78E-02	53.8	6.41 ± 0.02	3.55E+06 ± 1.8E+05
Ma170 149 763	7.63E-01	1.795E+00 ± 6.43E-02	60.1	5.61 ± 0.01	3.35E+06 ± 1.2E+05
Ma170 150 1106	1.11E+00	1.791E+00 ± 4.43E-02	60.1	6.06 ± 0.01	3.34E+06 ± 8.3E+04
Ma170 151 827	8.27E-01	1.880E+00 ± 5.34E-02	60.2	5.92 ± 0.01	3.50E+06 ± 1.0E+05
Ma170 152 827	8.27E-01	1.853E+00 ± 5.27E-02	59.5	5.69 ± 0.01	3.46E+06 ± 9.8E+04
MA170 45 834	8.34E-01	1.686E+00 ± 3.94E-02	58.1	6.06 ± 0.01	3.14E+06 ± 7.4E+04
MA203	J=0.00103666±0.00000268				
MA203 173 231	2.31E-01	4.540E+00 ± 1.37E+00	52.8	100.8 ± 1.24	8.47E+06 ± 2.6E+06
MA203 174 305	3.05E-01	2.452E+00 ± 1.30E+00	62.3	78.99 ± 0.48	4.58E+06 ± 2.4E+06
Ma203 11 573	5.73E-01	1.766E+00 ± 2.63E-01	82.3	41.65 ± 0.13	3.30E+06 ± 4.9E+05
Ma203 12 228	2.28E-01	2.369E+00 ± 9.86E-01	77.5	68.54 ± 0.54	4.42E+06 ± 1.8E+06
Ma203 13 167	1.67E-01	9.529E-01 ± 1.40E+00	95.5	96.48 ± 0.67	1.78E+06 ± 2.6E+06
Ma203 14 263	2.63E-01	1.273E-01 ± 1.15E+00	99.5	78.83 ± 0.59	2.38E+05 ± 2.1E+06
Ma203 15 314	3.14E-01	2.353E+00 ± 9.53E-01	94.6	64.95 ± 0.34	4.39E+06 ± 1.8E+06

Ma208	J =0.00103451±0.00000196					
Ma208 16 986	9.86E-01	2.202E+00	± 4.14E-02	68.6	8.04 ± 0.02	4.10E+06 ± 7.7E+04
Ma208 17 754	7.54E-01	2.179E+00	± 6.32E-02	66.7	8.58 ± 0.02	4.06E+06 ± 1.2E+05
Ma208 18 1115	1.12E+00	2.167E+00	± 3.75E-02	63.4	7.78 ± 0.02	4.04E+06 ± 7.0E+04
Ma208 19 1110	1.11E+00	2.218E+00	± 3.49E-02	62.0	7.95 ± 0.02	4.13E+06 ± 6.5E+04
Ma208 20 1015	1.02E+00	2.223E+00	± 4.45E-02	68.7	8.24 ± 0.01	4.14E+06 ± 8.3E+04
MA208 144 506	5.06E-01	2.139E+00	± 1.11E-01	60.1	8.33 ± 0.05	3.99E+06 ± 2.1E+05
Ma227	J =0.00103666±0.00000268					
MA227 190 557	5.57E-01	1.943E+00	± 1.18E-01	82.3	10.96 ± 0.02	3.63E+06 ± 2.2E+05
Ma227 41 698	6.98E-01	2.170E+00	± 9.79E-02	80.1	11.13 ± 0.03	4.05E+06 ± 1.8E+05
Ma227 42 1880	1.88E+00	1.987E+00	± 8.47E-02	89.8	15.24 ± 0.03	3.71E+06 ± 1.6E+05
Ma227 43 952	9.52E-01	2.107E+00	± 6.99E-02	76.1	10.33 ± 0.02	3.94E+06 ± 1.3E+05
Ma227 44 876	8.76E-01	2.147E+00	± 5.48E-02	83.0	10.97 ± 0.02	4.01E+06 ± 1.0E+05
Ma227 45 1085	1.09E+00	2.086E+00	± 5.45E-02	77.1	11.23 ± 0.02	3.90E+06 ± 1.0E+05
MA227 143 1404	1.40E+00	2.093E+00	± 4.02E-02	73.2	9.80 ± 0.02	3.91E+06 ± 7.6E+04
Ma37	J =0.00103451±0.00000196					
MA37 167 194	1.94E-01	1.114E+00	± 2.11E-01	81.7	8.05 ± 0.03	2.08E+06 ± 3.9E+05
MA37 168 313	3.13E-01	9.513E-01	± 1.17E-01	74.6	4.86 ± 0.02	1.77E+06 ± 2.2E+05
Ma37 143 659	6.59E-01	6.512E-01	± 6.26E-02	84.9	4.76 ± 0.01	1.22E+06 ± 1.2E+05
Ma37 144 540	5.40E-01	7.069E-01	± 7.78E-02	79.6	5.33 ± 0.01	1.32E+06 ± 1.5E+05
Ma37 145 858	8.58E-01	7.349E-01	± 3.21E-02	84.5	5.44 ± 0.02	1.37E+06 ± 6.0E+04
Ma37 146 556	5.56E-01	9.555E-01	± 7.96E-02	82.6	7.43 ± 0.02	1.78E+06 ± 1.5E+05
Ma37 147 753	7.53E-01	8.678E-01	± 5.46E-02	76.9	4.73 ± 0.01	1.62E+06 ± 1.0E+05
MA37 44 1613	1.61E+00	7.258E-01	± 2.35E-02	80.1	5.22 ± 0.01	1.35E+06 ± 4.4E+04
MA37 42 1088	1.09E+00	6.834E-01	± 4.83E-02	78.1	4.85 ± 0.01	1.28E+06 ± 9.0E+04
MA37 43 1348	1.35E+00	8.075E-01	± 2.74E-02	79.2	6.34 ± 0.01	1.51E+06 ± 5.1E+04
Ma85	J =0.00103666±0.00000268					
Ma85 52 1233	1.23E+00	8.129E-02	± 3.37E-02	97.4	11.27 ± 0.02	1.52E+05 ± 6.3E+04
Ma85 53 798	7.98E-01	9.311E-02	± 4.60E-02	97.7	6.56 ± 0.01	1.74E+05 ± 8.6E+04
Ma85 55 632	6.32E-01	2.128E-01	± 8.38E-02	93.8	12.81 ± 0.03	3.98E+05 ± 1.6E+05
Ma85 56 2019	2.02E+00	5.032E-02	± 3.33E-02	98.7	7.53 ± 0.01	9.41E+04 ± 6.2E+04
Ma85 57 1343	1.34E+00	7.004E-02	± 5.39E-02	98.1	12.41 ± 0.02	1.31E+05 ± 1.0E+05
Ma85 60 669	6.69E-01	4.286E-02	± 5.62E-02	99.3	9.85 ± 0.02	8.02E+04 ± 1.1E+05
MA85 138 1002	1.00E+00	2.007E-01	± 3.32E-02	93.5	11.48 ± 0.04	3.75E+05 ± 6.2E+04
MA85 139 736	7.36E-01	1.352E-01	± 4.79E-02	95.4	8.43 ± 0.02	2.53E+05 ± 9.0E+04
MA85 140 971	9.71E-01	4.905E-02	± 3.87E-02	98.5	9.92 ± 0.02	9.17E+04 ± 7.2E+04
MA85 141 691	6.91E-01	4.714E-02	± 7.62E-02	98.2	12.07 ± 0.03	8.82E+04 ± 1.4E+05
Ma75	J =0.00103451±0.00000196					
MA75 165 127	1.27E-01	1.564E+00	± 3.59E-01	93.0	7.14 ± 0.05	2.92E+06 ± 6.7E+05
MA75 166 371	3.71E-01	9.997E-01	± 1.90E-01	96.5	6.82 ± 0.02	1.86E+06 ± 3.6E+05
Ma75 140 904	9.04E-01	1.274E+00	± 1.28E-01	97.2	7.31 ± 0.02	2.38E+06 ± 2.4E+05
Ma75 141 429	4.29E-01	6.829E-01	± 1.77E-01	98.5	7.05 ± 0.03	1.27E+06 ± 3.3E+05
MA75 40 509	5.09E-01	7.332E-01	± 2.47E-01	96.6	14.35 ± 0.07	1.37E+06 ± 4.6E+05
MA75 41 916	9.16E-01	8.749E-01	± 8.30E-02	97.1	8.54 ± 0.02	1.63E+06 ± 1.5E+05

Chapter 3: Isotope correlation diagrams for Ar isotope compositions of fused plagioclase phenocryts, glass and whole rock samples of Madeira

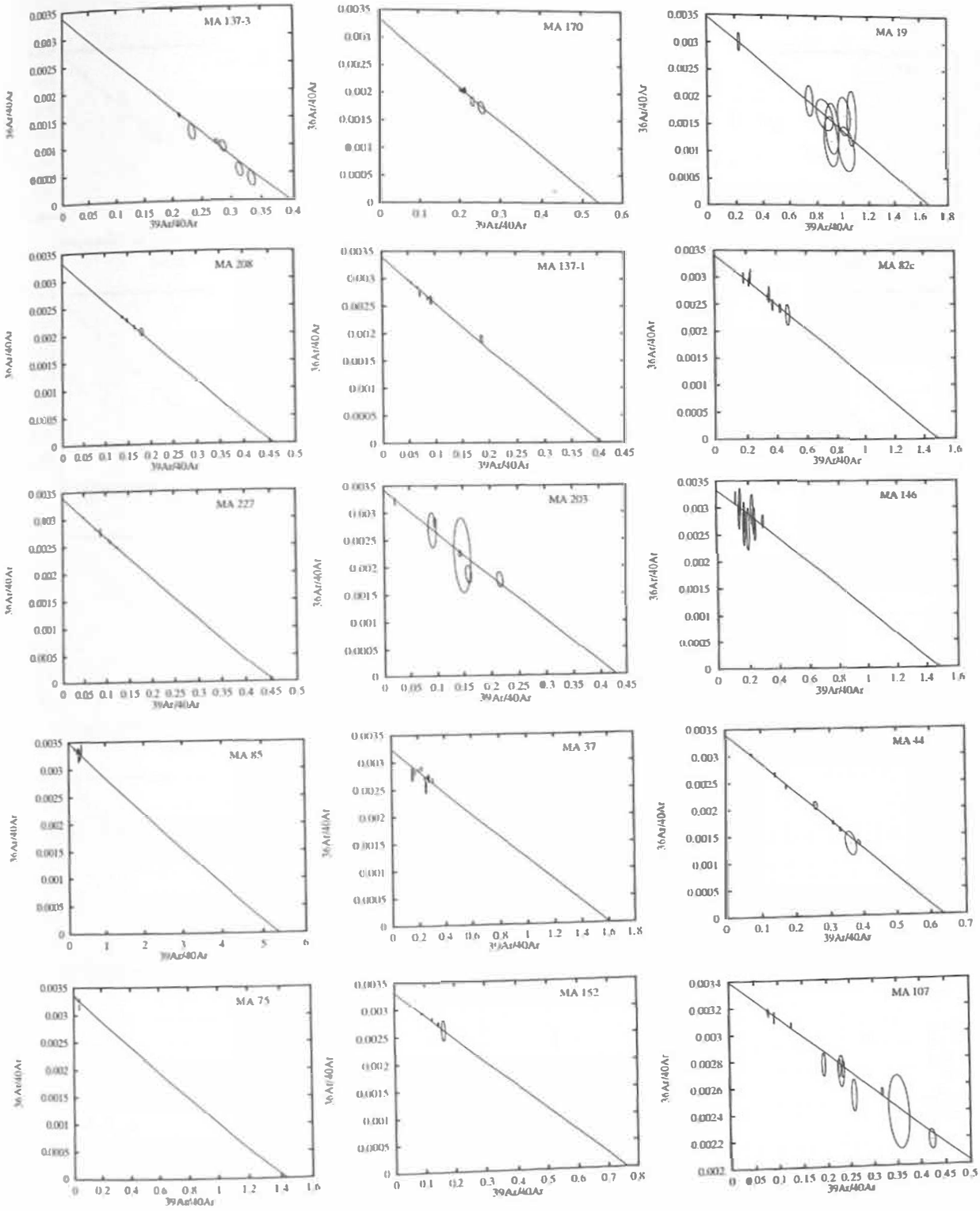

Chapter 3: Isotope correlation diagrams for Ar isotope compositions of fused plagioclase phenocryst and whole rock samples from Porto Santo

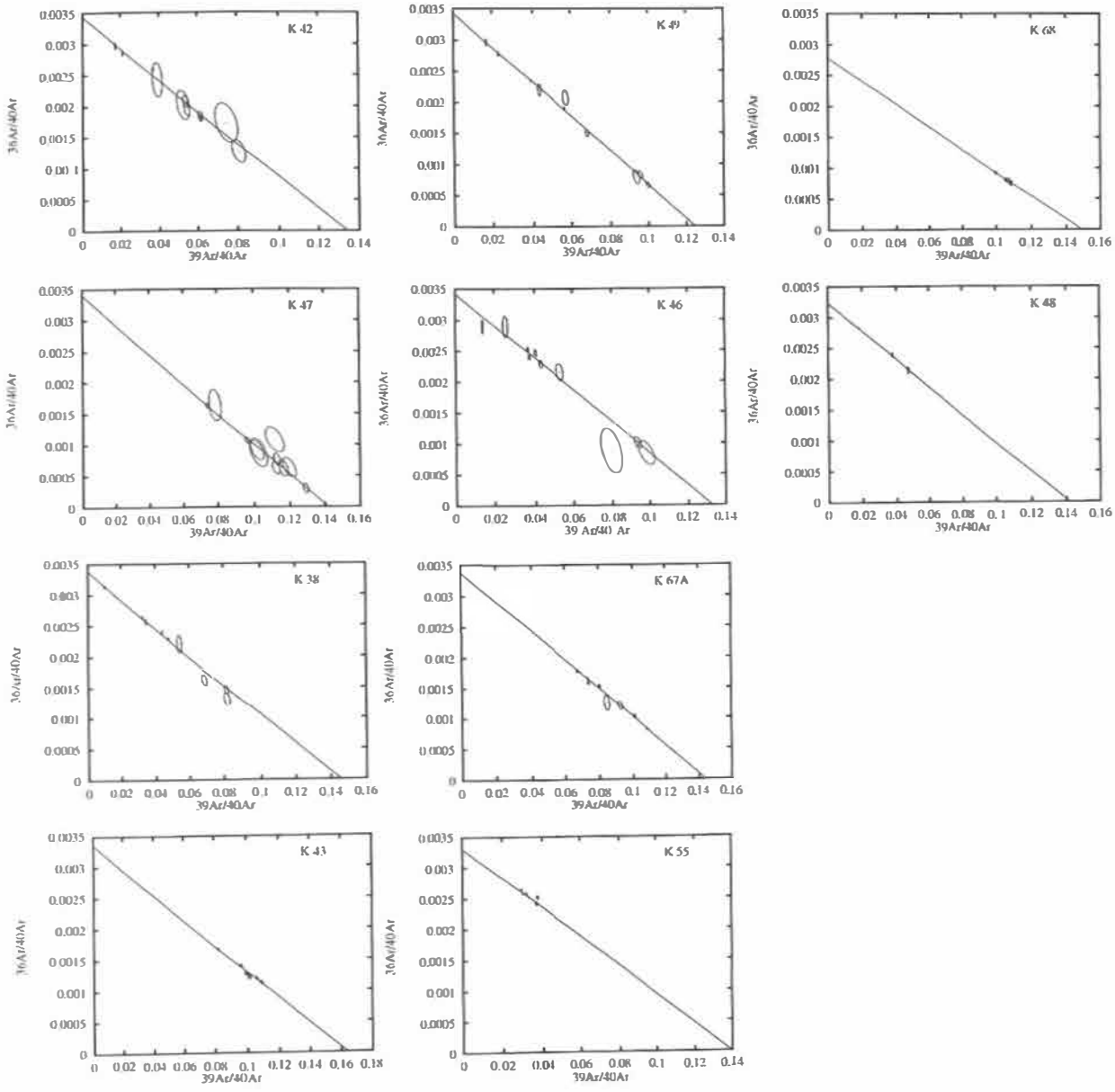

Chapter 3: Isotope correlation diagrams for Ar isotope compositions of fused whole rock and plagioclase phenocryst samples from the Desertas Islands and Ampère Seamount

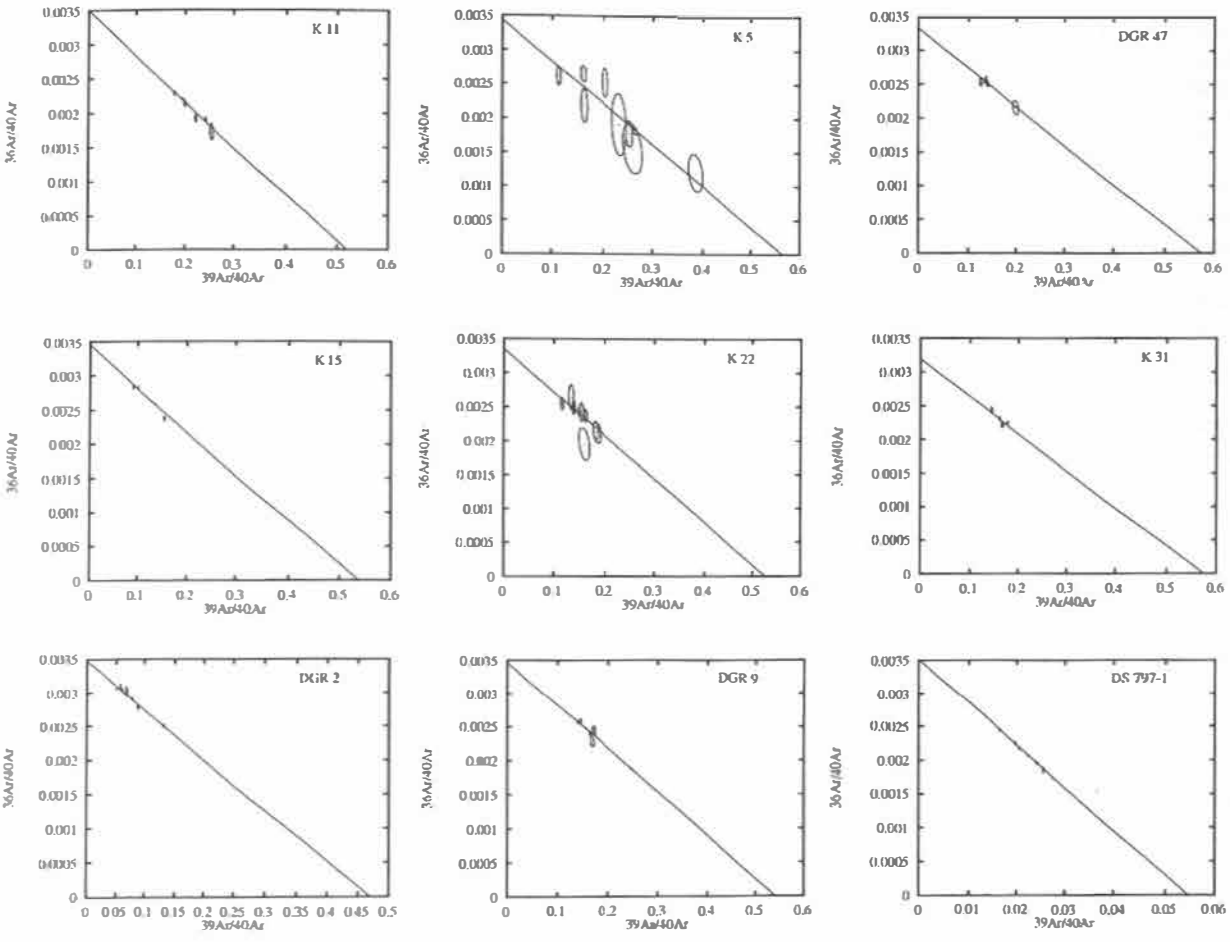

Appendix to Chapter 4 (The geochemical evolution of the Madeira hotspot)

Table A: XRF data

Sample	Md-33	191292-5	191292-6	191292-8	MA-67	MA-68	MA-77	MA-78a	MA-84
Unit/type	PE/flow	PE/flow	PE/flow	PE/flow	PE/dike	PE/dike	PE/cone	PE/cone	PE/flow
Site	32°48'08"	32°51'43"	32°49'09"	32°48'08"	32°46'00"	32°46'00"	32°45'26"	32°45'25"	32°46'43"
	17°02'28"	17°09'38"	17°05'44"	17°02'27"	17°03'48"	17°03'48"	17°00'50"	17°00'50"	17°02'27"
SiO_2	42.72	43.33	43.01	43.22	43.38	43.89	42.45	42.46	42.97
TiO_2	2.25	2.57	2.53	2.35	2.64	2.30	2.31	2.40	2.36
Al_2O_3	11.83	13.25	12.33	12.05	13.85	13.32	11.56	12.02	12.01
$Fe_2O_3^T$	12.23	12.44	12.18	12.33	12.80	12.28	12.58	12.44	12.42
MnO	0.19	0.19	0.19	0.19	0.19	0.18	0.19	0.19	0.19
MgO	15.40	11.96	13.65	15.00	11.51	12.25	15.05	14.68	14.67
CaO	11.26	11.17	11.55	11.41	11.06	11.26	10.48	10.96	11.17
Na_2O	2.43	3.06	2.96	2.71	2.68	3.10	2.04	2.13	2.96
K_2O	0.78	0.99	0.95	0.82	0.79	0.88	0.62	0.57	0.85
P_2O_5	0.45	0.56	0.53	0.50	0.74	0.57	0.53	0.53	0.51
CO_2	0.05	0.06	0.03	0.03	0.02	0.02	0.04	0.03	0.02
H_2O	0.12	0.41	0.17	0.09	0.52	0.44	1.14	1.26	0.18
Total	99.71	99.99	100.08	100.70	100.18	100.49	98.99	99.67	100.31

Sample	MA-85	MA-86	MA-87	MA-88	MA-89	MA-90	MA-91	MA-94	MA-97
Unit/type	PE/flow	PE/cone	PE/flow	PE/flow	PE/flow	PE/dike	PE/flow	PE/cone	PE/flow
Site	32°48'08"	32°47'53"	32°49'10"	32°49'00"	32°49'01"	32°47'53"	32°48'45"	32°51'00"	32°51'53"
	17°02'27"	17°06'32"	17°05'55"	17°06'23"	17°06'23"	17°06'32"	17°06'19"	17°09'44"	17°10'00"
SiO_2	42.89	43.93	43.84	43.48	43.29	43.39	43.33	41.10	42.97
TiO_2	2.34	2.47	2.45	2.46	2.54	2.47	2.47	2.50	2.53
Al_2O_3	12.14	12.75	13.01	12.75	12.01	12.58	12.29	12.42	12.90
$Fe_2O_3^T$	12.18	12.05	11.82	12.41	12.34	12.10	12.04	12.66	12.43
MnO	0.19	0.19	0.20	0.18	0.19	0.19	0.19	0.21	0.19
MgO	14.37	13.13	12.02	13.18	14.31	13.48	12.74	12.34	11.96
CaO	11.23	11.23	10.85	11.26	11.35	11.06	11.10	13.31	11.40
Na_2O	3.09	2.92	3.05	2.61	2.88	2.85	2.94	2.45	2.86
K_2O	0.88	1.06	1.08	0.69	0.87	0.94	1.03	0.58	0.94
P_2O_5	0.52	0.51	0.53	0.51	0.51	0.53	0.52	1.21	0.56
CO_2	0.03	0.04	0.03	0.01	0.03	0.02	0.02	0.02	0.05
H_2O	0.15	0.26	0.10	0.18	0.12	0.22	0.26	0.94	0.14
Total	100.01	100.54	98.98	99.72	100.44	99.83	98.93	99.74	98.93

Sample	MA-105	MA-117	MA-133	MA-139	MA-143	MA-168	MA217	MA218a	Md-1
Unit/type	PE/intr.	PE/cone	PE/flow	PE/cone	PE/cone	PE/cone	PE/intr.	PE/cone	LRP/dike
Site	32°44'57"	32°39'54"	32°39'13"	32°44'32"	32°38'19"	32°47'53"	32°45'05"	32°45'05"	32°45'19"
	17°06'46"	16°50'04"	16°51'53"	16°43'41"	16°56'04"	17°06'33"	17°03'10"	17°03'10"	16°56'19"
SiO_2	43.15	40.86	42.97	43.24	43.65	43.70	44.20	44.94	47.50
TiO_2	2.49	3.27	2.52	2.38	2.99	2.54	2.62	2.14	2.38
Al_2O_3	14.01	14.80	12.76	12.54	13.13	12.76	14.36	15.25	18.45
$Fe_2O_3^T$	12.56	14.73	12.83	12.97	12.93	11.97	12.81	11.80	10.89
MnO	0.20	0.21	0.18	0.23	0.19	0.19	0.20	0.20	0.24
MgO	11.51	9.50	11.32	12.19	10.88	12.77	10.22	10.60	3.36
CaO	11.37	8.49	11.27	11.05	11.36	11.25	10.53	9.53	9.00
Na_2O	2.82	1.63	2.67	2.12	2.73	3.23	2.82	2.59	4.10
K_2O	0.77	0.87	0.75	0.63	0.78	1.07	0.87	0.83	1.35
P_2O_5	0.73	0.61	0.54	0.54	0.52	0.55	0.71	0.55	1.18
CO_2	0.03	0.16	0.02	0.05	0.03	0.03	0.02	0.10	0.06
H_2O	0.28	3.37	0.84	1.58	1.33	0.14	0.46	1.41	1.64
Total	99.92	98.50	98.67	99.52	100.52	100.20	99.82	99.94	100.15

Appendix

Sample	Md-2	Md-3	Md-4	Md-5	Md-6	Md-9	Md-12	Md-13	Md-14
Unit/type	LRP/dike	LRP/dike	LRP/dike	LRP/dike	LRP/dike	LRP/dike	LRP/dike	LRP/dike	LRP/flow
Site	32°45'16"	32°45'16"	32°45'05"	32°45'04"	32°45'03"	32°44'30"	32°44'11"	32°44'11"	32°46'24"
	16°56'09"	16°56'09"	16°56'07"	16°56'07"	16°56'07"	16°56'00"	16°56'06"	16°56'06"	16°49'47"
SiO_2	44.05	44.39	43.50	43.77	42.60	52.94	43.19	42.58	45.11
TiO_2	2.94	2.73	2.49	2.87	3.04	1.74	3.54	3.57	2.44
Al_2O_3	14.09	13.76	13.78	13.84	14.72	18.89	14.59	14.52	12.97
$Fe_2O_3^t$	13.46	13.35	12.93	13.40	13.11	7.40	13.99	14.19	12.28
MnO	0.19	0.18	0.19	0.20	0.19	0.24	0.19	0.19	0.17
MgO	10.48	11.62	12.18	10.64	9.52	2.04	9.20	9.30	10.64
CaO	10.17	9.86	10.80	10.88	11.66	7.25	10.31	9.95	11.69
Na_2O	2.93	2.93	2.71	2.75	2.27	5.84	2.94	2.06	2.38
K_2O	0.88	0.87	0.78	0.92	0.86	1.88	0.96	1.03	0.57
P_2O_5	0.53	0.51	0.50	0.80	0.84	0.52	0.53	0.52	0.38
CO_2	0.04	0.02	0.15	0.12	0.06	0.07	0.04	0.10	1.26
H_2O	0.42	0.20	0.65	0.76	1.37	0.56	0.53	1.84	0.91
Total	100.18	100.42	100.66	100.95	100.24	99.37	100.01	99.85	100.80

Sample	Md-15	Md-16	Md-17b	Md-18	Md-21	171292-1	171292-5	181292-1	MA-15
Unit/type	LRP/flow	LRP/flow	LRP/flow	LRP/flow	LRP/flow	LRP/flow	LRP/flow	LRP/flow	LRP/flow
Site	32°46'08"	32°49'00"	32°51'38"	32°51'27"	32°40'00"				32°44'51"
	16°49'32"	17°05'57"	17°09'40"	17°10'06"	17°03'40"				17°01'32"
SiO_2	43.52	44.38	43.94	44.20	43.39	42.90	44.41	43.30	44.33
TiO_2	2.25	2.62	2.70	2.49	4.08	3.82	2.60	2.52	2.49
Al_2O_3	13.24	12.15	12.06	13.99	15.45	14.31	13.48	12.95	13.68
$Fe_2O_3^t$	12.73	12.75	13.07	12.37	14.81	13.76	12.86	13.63	11.79
MnO	0.18	0.17	0.19	0.19	0.20	0.18	0.19	0.19	0.24
MgO	11.85	13.07	13.74	11.36	6.49	8.21	11.48	12.51	7.89
CaO	11.65	10.66	10.37	11.05	9.50	10.88	11.10	10.69	11.14
Na_2O	2.78	2.02	2.10	2.74	3.73	3.48	2.81	2.50	2.96
K_2O	0.60	0.70	0.87	0.82	1.14	1.51	0.80	0.71	0.97
P_2O_5	0.54	0.47	0.55	0.68	0.92	0.54	0.54	0.55	0.53
CO_2	0.05	0.22	0.04	0.03	0.04	0.02	0.04	0.07	1.97
H_2O	0.77	1.32	0.87	0.47	0.59	0.35	0.20	0.43	0.62
Total	100.16	100.53	100.50	100.39	100.34	99.96	100.51	100.05	98.61

Sample	MA-16	MA-17	MA-20	MA-23	MA-25	MA-26	Ma-27	MA-28	MA-29
Unit/type	LRP/flow	LRP/flow	LRP/flow	LRP/flow	LRP/flow	LRP/flow	LRP/flow	LRP/flow	LRP/flow
Site	32°44'51"	32°44'50"	32°44'47"	32°44'38"	32°44'40"	32°44'40"	32°44'40"	32°44'40"	32°44'40"
	17°01'32"	17°01'33"	17°01'35"	17°01'51"	17°02'00"	17°02'02"	17°02'02"	17°02'03"	17°02'04"
SiO_2	48.30	45.24	47.97	46.36	47.69	45.05	45.92	45.29	45.37
TiO_2	2.52	2.34	2.57	2.52	2.77	2.80	2.96	2.80	2.85
Al_2O_3	16.09	13.95	16.13	14.42	16.52	14.37	14.97	14.82	14.60
$Fe_2O_3^t$	10.40	11.72	11.30	12.24	11.91	13.07	12.53	12.64	12.93
MnO	0.17	0.18	0.19	0.18	0.19	0.18	0.18	0.19	0.19
MgO	5.80	10.71	5.66	9.69	5.00	9.46	7.61	9.12	8.36
CaO	9.48	10.05	9.63	10.28	9.17	10.78	11.16	10.16	10.00
Na_2O	3.71	2.33	3.63	2.89	3.55	2.52	2.99	3.03	3.10
K_2O	1.49	0.95	1.19	0.98	1.10	0.75	0.98	1.09	1.01
P_2O_5	0.71	0.50	0.57	0.55	0.65	0.50	0.53	0.60	0.54
CO_2	0.04	0.06	0.28	0.01	0.03	0.03	0.02	0.02	0.01
H_2O	1.30	1.88	1.13	0.46	0.37	0.63	0.38	0.44	0.33
Total	100.01	99.91	100.25	100.58	98.95	100.14	100.23	100.20	99.29

Sample	MA-32	MA-33	MA-37	MA-38	MA-40	MA-41	MA-42	MA-46	MA-50
Unit/type	LRP/dike	LRP/dike	LRP/flow	LRP/flow	LRP/flow	LRP/flow	LRP/flow	LRP/flow	LRP/flow
Site	32°44'16"	32°44'16"	32°43'59"	32°43'51"	32°43'51"	32°43'51"	32°43'51"	32°43'48"	32°43'37"
	17°02'30"	17°02'30"	17°02'45"	17°02'56"	17°02'56"	17°02'57"	17°02'58"	17°02'55"	17°03'09"
SiO_2	44.01	42.89	47.11	46.60	43.90	44.59	56.78	47.91	42.43
TiO_2	3.01	2.38	3.05	2.46	2.65	2.84	1.54	2.49	2.72
Al_2O_3	14.22	13.09	17.01	15.29	12.89	15.45	19.47	15.91	13.34
Fe_2O_3'	12.88	12.19	11.93	11.75	13.29	13.02	6.83	11.65	13.61
MnO	0.20	0.18	0.19	0.19	0.20	0.20	0.16	0.18	0.19
MgO	9.30	13.00	5.13	7.90	11.76	8.02	1.16	6.04	13.59
CaO	9.98	11.43	9.31	10.01	10.42	10.08	3.77	9.75	10.05
Na_2O	2.64	2.97	4.11	3.42	2.85	3.08	5.66	3.60	1.38
K_2O	1.13	0.99	1.34	0.99	0.80	0.90	2.71	0.82	0.65
P_2O_5	0.75	0.53	0.89	0.85	0.80	0.84	0.54	0.63	0.44
CO_2	0.07	0.02	0.01	0.01	0.03	0.03	0.06	0.03	0.04
H_2O	1.26	0.43	0.42	0.34	0.51	0.47	2.13	0.84	2.49
Total	99.45	100.10	100.50	99.81	100.10	99.52	100.81	99.85	100.93

Sample	MA-51	MA-52	MA-53	MA-54	MA-55	MA-66	MA-71	MA-72b	MA-74
Unit/type	LRP/flow	LRP/flow	LRP/flow	LRP/flow	LRP/flow	LRP/flow	LRP/intr.	LRP/flow	LRP/flow
Site	32°43'51"	32°43'51"	32°43'50"	32°43'56"	32°44'51"	32°45'56"	32°44'08"	32°40'00"	32°40'02"
	17°03'15"	17°03'16"	17°03'17"	17°03'21"	17°03'12"	17°04'11"	17°02'25"	17°02'36"	17°02'34"
SiO_2	44.11	44.12	43.69	45.56	43.82	43.22	46.35	43.83	45.17
TiO_2	3.12	2.58	3.03	2.57	2.67	2.59	2.97	3.75	2.66
Al_2O_3	15.59	13.43	14.25	13.90	14.17	13.62	16.53	15.48	14.50
Fe_2O_3'	13.60	12.81	13.09	11.97	12.96	12.65	12.13	14.23	12.32
MnO	0.22	0.20	0.19	0.19	0.21	0.19	0.20	0.22	0.19
MgO	6.35	11.05	10.12	10.19	10.63	11.36	5.52	5.77	9.32
CaO	9.68	10.33	10.63	9.95	10.51	11.17	9.78	9.46	11.60
Na_2O	4.13	3.38	3.02	3.19	2.50	3.21	3.88	3.78	2.95
K_2O	1.41	0.92	0.97	1.08	0.83	0.88	1.28	1.13	0.87
P_2O_5	1.10	0.88	0.79	0.62	0.73	0.78	1.24	1.13	0.52
CO_2	0.01	0.02	0.01	0.03	0.02	0.02	0.02	0.02	0.01
H_2O	0.42	0.41	0.73	0.84	1.01	0.27	0.53	0.66	0.31
Total	99.74	100.13	100.52	100.09	100.06	99.96	100.43	99.46	100.42

Sample	MA-75b	MA-76	MA-80a	MA-81	MA-82a	MA-82c	MA-83	MA-102	MA-106
Unit/type	LRP/intr.	LRP/dike	LRP/intr.	LRP/intr.	LRP/intr.	LRP/intr.	LRP/intr.	LRP/intr.	LRP/flow
Site	32°45'06"	32°45'06"	32°45'34"	32°45'34"	32°47'32"	32°47'32"	32°47'32"	32°47'19"	32°39'30"
	17°01'10"	17°01'10"	17°01'16"	17°01'16"	17°02'00"	17°02'00"	17°02'00"	16°50'49"	16°48'50"
SiO_2	46.38	44.97	68.41	49.82	66.29	68.08	41.87	45.82	43.61
TiO_2	2.80	2.91	0.41	2.18	0.53	0.50	3.22	2.70	2.72
Al_2O_3	16.00	14.58	17.64	15.13	17.06	16.08	15.54	13.99	12.98
Fe_2O_3'	11.97	12.63	1.25	9.61	2.75	2.65	13.08	12.01	13.14
MnO	0.18	0.19	0.01	0.17	0.18	0.12	0.14	0.19	0.18
MgO	5.77	8.29	0.12	5.57	0.36	0.35	5.85	8.59	11.67
CaO	9.42	10.33	1.12	8.28	1.46	1.52	8.39	9.60	10.40
Na_2O	3.23	3.14	6.99	4.33	5.83	5.95	3.31	3.78	2.43
K_2O	0.96	1.09	3.68	1.58	3.50	3.38	1.09	1.29	0.87
P_2O_5	0.63	0.60	0.04	0.46	0.10	0.10	0.71	0.79	0.53
CO_2	0.11	0.13	0.03	2.21	0.06	0.06	4.79	0.01	0.08
H_2O	1.33	0.68	0.62	0.91	1.04	0.89	2.33	0.32	0.73
Total	98.78	99.54	100.32	100.25	99.16	99.68	100.32	99.09	99.34

Sample	MA-108	MA-109	MA-110	MA-113	MA-114	MA-115	MA-118a	MA-118b	MA-137
Unit/type	LRP/flow	LRP/flow	LRP/flow	LRP/flow	LRP/flow	LRP/flow	LRP/flow	LRP/flow	LRP/flow
Site	32°39'30"	32°39'30"	32°39'30"	32°39'30"	32°39'30"	32°39'29"	32°46'03"	32°46'03"	32°44'24"
	16°48'30"	16°48'28"	16°48'26"	16°48'25"	16°48'50"	16°48'30"	16°49'23"	16°49'23"	16°42'03"
SiO_2	43.82	43.75	42.82	43.91	44.71	44.43	53.42	53.54	43.37
TiO_2	2.53	2.83	3.81	3.35	2.54	3.61	1.78	1.82	2.70
Al_2O_3	13.25	13.50	14.45	14.22	13.55	15.91	18.84	19.15	11.64
$Fe_2O_3^t$	12.63	12.95	13.81	13.61	12.67	14.39	7.36	7.49	12.81
MnO	0.19	0.19	0.18	0.19	0.19	0.21	0.24	0.24	0.19
MgO	11.13	11.40	8.14	8.55	10.51	5.67	1.98	1.96	13.86
CaO	11.01	10.87	10.90	10.54	10.49	8.79	7.10	6.85	11.07
Na_2O	2.56	3.26	3.38	3.24	2.67	4.13	6.09	5.66	3.03
K_2O	0.80	1.03	1.49	0.92	0.84	1.35	1.91	1.88	0.93
P_2O_5	0.56	0.53	0.55	0.57	0.65	0.84	0.54	0.53	0.46
CO_2	0.03	0.03	0.02	0.02	0.04	0.02	0.02	0.05	0.02
H_2O	0.21	0.19	0.41	0.44	0.61	0.48	0.44	1.13	0.36
Total	98.72	100.53	99.96	99.56	99.47	99.83	99.72	100.30	100.44

Sample	MA-142	MA-145	MA-151	MA-152	MA-156	MA-160	MA-162	MA-171	MA-179
Unit/type	LRP/cone	LRP/cone	LRP/flow	LRP/flow	LRP/flow	LRP/flow	LRP/flow	LRP/flow	LRP/dike
Site	32°38'20"	32°38'42"	32°43'46"	32°43'48"	32°43'48"	32°43'46"	32°43'46"	32°42'32"	32°45'16"
	16°56'10"	16°56'25"	17°11'51"	17°11'51"	17°11'48"	17°11'43"	17°11'39"	16°45'40"	16°56'13"
SiO_2	42.96	47.20	45.13	46.13	42.92	43.20	42.85	41.89	43.82
TiO_2	2.95	2.75	2.50	2.60	2.59	2.93	2.87	3.24	2.77
Al_2O_3	13.24	16.33	13.47	14.75	12.16	13.62	13.21	13.34	13.87
$Fe_2O_3^t$	13.40	11.54	12.30	12.06	13.33	13.20	13.06	13.88	13.66
MnO	0.18	0.19	0.19	0.20	0.19	0.18	0.18	0.17	0.18
MgO	10.47	5.43	10.81	7.64	13.54	10.35	10.69	10.50	11.27
CaO	11.32	9.49	10.21	9.80	10.69	11.03	10.81	11.26	9.80
Na_2O	2.01	3.69	3.09	3.51	2.60	2.80	3.09	2.76	2.69
K_2O	0.82	1.06	0.96	1.04	0.74	0.79	0.86	0.77	0.81
P_2O_5	0.52	0.78	0.61	0.69	0.40	0.53	0.57	0.83	0.50
CO_2	0.07	0.04	0.03	0.03	0.04	0.03	0.03	0.02	0.04
H_2O	1.31	0.82	0.48	0.41	0.21	0.34	0.23	0.73	0.45
Total	99.25	99.32	99.78	98.86	99.41	99.00	98.45	99.39	99.86

Sample	MA-183	MA-229	DGR-2	DGR-8	DGR 14	DGR-18	DGR 23	DGR-26	DGR-29
Unit/type	LRP/cone	LRP/flow	DRP/flow	DRP/dike	DRP/dike	DRP/dike	DRP/flow	DRP/flow	DRP/flow
Site	32°44'56"	32°44'24"	32°30'30"	32°30'35"	32°30'44"	32°30'46"	32°30'30"	32°30'25"	32°30'25"
	16°56'01"	17°02'25"	16°30'19"	16°30'16"	16°30'17"	16°30'17"	16°30'18"	16°30'11"	16°30'10"
SiO_2	43.41	47.24	45.04	44.15	44.68	44.87	45.79	45.12	44.53
TiO_2	2.74	2.40	2.84	2.13	2.42	3.41	2.87	2.52	2.98
Al_2O_3	14.42	14.60	13.48	9.32	11.17	15.37	14.09	12.34	13.74
$Fe_2O_3^t$	13.19	11.21	13.55	13.58	13.38	13.95	13.22	13.71	13.81
MnO	0.19	0.19	0.18	0.18	0.18	0.19	0.18	0.18	0.19
MgO	10.04	8.61	9.60	17.72	13.57	6.90	8.05	11.90	9.53
CaO	10.98	9.08	10.95	10.38	11.20	10.76	11.22	11.20	10.80
Na_2O	2.13	3.53	2.24	1.68	2.05	3.02	2.71	2.08	2.72
K_2O	0.81	1.56	0.75	0.57	0.61	1.03	0.77	0.57	0.85
P_2O_5	0.66	0.61	0.44	0.33	0.34	0.56	0.44	0.38	0.49
CO_2	0.02	0.02	0.03	0.02	0.02	0.01	0.03	0.02	0.02
H_2O	1.50	0.64	1.40	0.44	0.21	0.34	0.42	0.44	0.36
Total	100.09	99.69	100.50	100.50	99.83	100.41	99.79	100.46	100.02

Sample	DGR 32	DGR-34	DGR 41	DGR-42	DGR 43	DGR 45a	DGR 46	DGR-47	DGR-49
Unit/type	DRP/flow	DRP/flow	DRP/flow	DRP/flow	DRP/flow	DRP/dike	DRP/flow	DRP/flow	DRP/flow
Site	32°30'24"	32°30'24"	32°30'30"	32°30'30"	32°30'30"	32°30'24"	32°32'15"	32°32'23"	32°34'06"
	16°30'10"	16°30'09"	16°30'04"	16°30'04"	16°30'04"	16°30'09"	16°31'18"	16°31'21"	16°32'06"
SiO_2	44.68	45.17	45.10	45.63	45.48	43.90	45.61	44.09	46.83
TiO_2	2.46	3.18	2.45	2.94	2.60	3.23	2.91	3.22	2.92
Al_2O_3	11.77	15.14	12.01	13.92	12.89	16.31	15.06	14.00	14.82
Fe_2O_3*	13.46	13.84	13.88	14.14	13.65	13.79	13.47	14.45	12.74
MnO	0.18	0.18	0.18	0.16	0.17	0.20	0.18	0.19	0.18
MgO	12.22	6.47	12.20	7.75	9.81	5.70	7.20	9.00	7.10
CaO	11.61	11.55	10.55	10.73	10.64	10.93	9.88	10.42	10.54
Na_2O	2.06	2.96	2.08	2.46	2.29	2.69	2.95	2.56	3.06
K_2O	0.58	0.94	0.63	0.72	0.67	0.84	0.89	0.94	1.07
P_2O_5	0.39	0.54	0.35	0.43	0.37	0.63	0.50	0.59	0.61
CO_2	0.01	0.03	0.04	0.03	0.03	0.02	0.03	0.03	0.02
H_2O	0.40	0.39	0.87	1.13	0.98	1.65	0.59	0.81	0.55
Total	99.82	100.39	100.34	100.04	99.58	99.89	99.27	100.30	100.44

Sample	DGR-51	DGR-52	DGR-54	K-2	K-6	K-8	K-9	K-11	K-12
Unit/type	DRP/flow	DRP/flow	DRP/flow	DRP/sill	DRP/dike	DRP/cobble	DRP/cobble	DRP/cobble	DRP/cobble
Site	32°34'03"	32°34'03"	32°34'03"	32°24'24"	32°24'24"	32°24'24"	32°24'24"	32°25'56"	32°25'56"
	16°32'03"	16°32'03"	16°32'03"	16°28'27"	16°28'27"	16°28'26"	16°28'26"	16°29'17"	16°29'17"
SiO_2	45.49	45.03	45.51	45.62	45.08	45.25	46.43	45.31	46.53
TiO_2	2.81	2.94	2.59	2.88	3.53	3.26	3.43	2.74	3.27
Al_2O_3	14.04	13.60	12.41	14.61	16.38	16.23	15.68	12.17	16.96
Fe_2O_3*	13.50	13.63	13.43	12.89	13.79	13.30	14.21	13.68	13.30
MnO	0.18	0.18	0.18	0.16	0.18	0.18	0.19	0.18	0.19
MgO	9.17	9.50	11.13	8.21	4.35	6.06	4.58	11.10	4.51
CaO	10.24	11.18	11.27	10.06	10.82	10.10	10.15	11.61	9.77
Na_2O	2.65	2.57	2.27	2.66	2.93	3.47	3.30	2.20	3.54
K_2O	0.85	0.82	0.64	0.76	1.03	1.12	1.08	0.67	1.16
P_2O_5	0.49	0.47	0.34	0.43	0.57	0.65	0.56	0.38	0.59
CO_2	0.03	0.03	0.00	0.04	0.03	0.01	0.01	0.03	0.01
H_2O	0.61	0.48	0.43	1.51	1.49	0.38	0.53	0.29	0.44
Total	100.06	100.43	100.20	99.83	100.18	100.01	100.15	100.36	100.27

Sample	K-13	K-15	K 16	K-18	K 19	K-21	K 22	K-25	K 26
Unit/type	DRP/cobble	DRP/dike	DRP/flow	DRP/flow	DRP/cone	DRP/flow	DRP/flow	DRP/flow	DRP/flow
Site	32°25'56"	32°25'56"	32°35'10"	32°34'38"	32°34'38"	32°34'38"	32°34'38"	32°30'35"	32°30'00"
	16°29'17"	16°29'17"	16°32'30"	16°32'27"	16°32'27"	16°32'27"	16°32'27"	16°30'06"	16°29'44"
SiO_2	56.68	46.07	48.18	43.97	47.78	44.73	45.17	46.11	44.03
TiO_2	1.49	2.80	2.49	2.73	2.43	1.74	1.77	2.43	3.17
Al_2O_3	17.68	14.98	17.48	13.37	17.60	14.32	14.40	12.16	14.62
Fe_2O_3*	7.60	13.00	13.03	13.40	11.77	13.23	13.54	13.72	14.10
MnO	0.18	0.17	0.19	0.18	0.21	0.19	0.19	0.17	0.18
MgO	2.00	7.32	3.07	10.72	2.94	9.29	10.16	11.34	8.25
CaO	6.01	9.95	7.41	11.10	8.61	11.13	10.47	10.68	10.59
Na_2O	5.01	3.10	4.38	2.16	4.46	2.53	2.77	2.10	2.98
K_2O	1.89	1.01	1.24	0.73	1.52	0.48	0.38	0.62	0.92
P_2O_5	0.53	0.64	0.93	0.73	1.24	0.47	0.40	0.37	0.61
CO_2	0.01	0.16	0.01	0.01	0.01	0.52	0.00	0.00	0.01
H_2O	0.57	0.79	1.16	1.08	0.52	1.53	0.53	0.90	0.53
Total	99.65	99.99	99.57	100.18	99.09	100.16	99.78	100.60	99.99

Sample	K-28	K-31	K-33	K-34	K-36	MA-4	MA-6	MA-11	MA-120
Unit/type	DRP/flow	DRP/flow	DRP/flow	DRP/dike	DRP/dike	ERP/congl.	ERP/congl.	ERP/congl.	ERP/congl.
Site	32°29'52"	32°31'55"	32°31'55"	32°31'55"	32°31'55"	32°47'38"	32°47'38"	32°47'38"	32°45'49"
	16°29'40"	16°31'23"	16°31'23"	16°31'23"	16°31'23"	17°01'09"	17°01'09"	17°01'09"	16°48'49"
SiO_2	42.95	45.24	43.99	45.14	46.44	42.47	42.90	41.63	46.14
TiO_2	3.75	2.90	2.53	2.81	2.59	3.75	3.43	3.76	2.62
Al_2O_3	15.62	14.13	10.65	13.25	13.87	16.80	15.59	17.14	14.79
Fe_2O_3'	15.52	13.41	13.31	12.71	12.52	15.18	13.33	10.76	12.07
MnO	0.17	0.18	0.18	0.18	0.17	0.09	0.12	0.10	0.16
MgO	5.71	8.65	14.42	9.32	8.38	6.29	6.29	4.88	7.53
CaO	10.72	11.06	11.17	11.01	10.36	6.01	10.26	10.06	9.21
Na_2O	1.90	2.94	1.72	2.58	3.00	2.07	2.28	2.68	2.48
K_2O	0.82	0.85	0.59	0.97	0.88	1.00	1.00	0.98	0.12
P_2O_5	0.53	0.57	0.40	0.47	0.52	0.74	1.00	1.06	0.38
CO_2	0.02	0.02	0.01	0.02	0.02	0.44	1.18	2.73	1.91
H_2O	2.10	0.41	0.73	0.98	0.68	5.02	2.80	3.69	3.85
Total	99.81	100.36	99.70	99.44	99.43	99.86	100.18	99.47	101.26

Sample	MA-123	MA-188	MA-197	MA-199	MA-201	Ma-202	MA-203	MA-206	MA-207
Unit/type	ERP/dike	ERP/congl.	ERP/congl.	ERP/flow	ERP/flow	ERP/flow	ERP/flow	ERP/flow	ERP/flow
Site	32°45'49"	32°45'49"	32°46'01"	32°43'50"	32°43'43"	32°43'41"	32°43'41"	32°43'40"	32°43'39"
	16°48'19"	16°48'50"	16°49'19"	17°02'51"	17°02'45"	17°02'47"	17°02'47"	17°02'45"	17°02'44"
SiO_2	44.06	44.80	43.94	55.52	48.87	46.51	45.02	43.39	52.80
TiO_2	2.80	2.64	1.45	1.65	2.51	2.77	2.65	3.44	1.83
Al_2O_3	13.57	15.06	8.39	18.27	18.17	17.42	16.17	15.89	17.96
Fe_2O_3'	11.49	12.20	13.50	7.33	9.35	11.80	12.27	13.99	10.13
MnO	0.20	0.16	0.17	0.16	0.20	0.19	0.17	0.17	0.22
MgO	5.52	6.98	22.07	1.99	3.07	5.04	8.23	6.29	2.47
CaO	11.05	9.30	7.14	4.24	8.91	9.95	10.38	11.66	5.51
Na_2O	2.53	1.99	1.50	5.64	5.14	3.36	2.38	2.43	5.28
K_2O	0.21	0.11	0.42	2.71	1.63	1.16	0.79	0.71	1.82
P_2O_5	0.56	0.38	0.28	0.68	0.89	0.81	0.60	0.55	0.72
CO_2	3.66	2.26	0.02	0.02	0.07	0.00	0.01	0.02	0.03
H_2O	3.07	3.94	0.76	0.85	0.55	0.95	1.11	1.09	0.92
Total	98.72	99.82	99.64	99.06	99.36	99.96	99.78	99.63	99.69

Sample	MA-208	MA-215	MA-216	MA-220	MA-224	MA-227	MA-228	M-30b	M-37/1
Unit/type	ERP/flow	ERP/flow	ERP/flow	ERP/flow	ERP/flow	ERP/congl.	ERP/congl.	PS/dike	PS/intr.
Site	32°43'37"	32°43'26"	32°43'26"	32°43'26"	32°43'26"	32°43'58"	32°43'58"	33°04'40"	33°05'24"
	17°02'43"	17°01'43"	17°01'43"	16°57'45"	16°57'45"	16°57'53"	16°57'53"	16°19'43"	16°19'09"
SiO_2	45.47	45.08	42.41	44.56	45.53	43.95	44.96	70.50	65.13
TiO_2	3.18	2.64	2.72	2.20	3.08	2.03	2.60	0.18	0.69
Al_2O_3	17.25	13.30	15.12	13.59	17.02	10.29	14.58	16.38	18.02
Fe_2O_3'	12.51	12.79	12.47	11.63	11.42	11.90	11.96	1.28	3.25
MnO	0.17	0.17	0.18	0.17	0.19	0.20	0.23	0.11	0.18
MgO	5.19	9.58	7.93	9.03	4.10	16.95	7.53	0.05	0.45
CaO	9.96	10.16	10.67	11.24	9.69	10.10	11.75	0.51	2.13
Na_2O	3.15	2.57	2.94	2.63	3.43	1.60	2.60	6.96	7.40
K_2O	0.98	0.58	0.87	0.63	0.97	0.66	0.88	3.17	2.57
P_2O_5	0.74	0.35	0.50	0.57	0.60	0.45	0.62	0.03	0.11
CO_2	0.01	2.06	3.11	2.72	2.55	0.40	0.33	0.04	0.16
H_2O	0.85	0.71	0.76	0.87	1.26	1.37	1.54	0.59	0.51
Total	99.46	99.99	99.68	99.84	99.84	99.90	99.58	99.80	100.60

Appendix

Sample	M-37/2	M-36	M-40	M-41	M-53	161292-2	161292-5	PS-2	PS-3
Unit/type	PS/intr.	PS/dike	PS/dike	PS/intr.	PS/intr.	PS/dike	PS/dike	PS/dike	PS/dike
Site	33°05'24"	33°05'24"	33°05'32"	33°05'32"	33°02'49"			33°05'03"	33°05'03"
	16°19'09"	16°19'09"	16°18'18"	16°18'18"	16°21'40"			16°18'04"	16°18'04"
SiO_2	65.09	46.52	45.63	54.72	53.30	44.77	44.51	58.14	44.86
TiO_2	0.69	2.43	1.90	1.38	1.68	1.88	2.94	1.21	3.72
Al_2O_3	17.97	15.23	9.33	18.48	18.39	11.26	14.59	18.76	16.46
$Fe_2O_3^t$	3.12	11.92	11.65	7.88	8.38	11.87	12.80	5.92	12.11
MnO	0.19	0.18	0.16	0.19	0.20	0.18	0.20	0.21	0.22
MgO	0.38	7.58	15.00	1.97	2.37	14.06	8.56	1.25	5.37
CaO	2.11	10.84	12.96	7.41	7.92	11.96	10.97	5.66	10.09
Na_2O	7.39	2.91	1.33	5.08	5.00	1.55	2.57	6.28	3.69
K_2O	2.57	0.76	0.52	1.31	1.10	0.42	0.75	1.80	0.89
P_2O_5	0.12	0.52	0.31	0.66	0.60	0.27	0.67	0.43	1.24
CO_2	0.15	0.19	0.08	0.19	0.04	0.27	0.06	0.19	0.23
H_2O	0.53	1.17	1.47	1.09	0.85	2.59	2.09	0.63	1.28
Total	100.31	100.25	100.34	100.36	99.83	101.08	100.71	100.48	100.16

Sample	PS-4	DS792-1	DS795-1	DS797-1a	DS797-1b	DS797-2	DS797-3	DS 797-4	DS 797-5
Unit/type	PS/dike	Ampere	Ampere	Ampere	Ampere	Ampere	Ampere	Ampere	Ampere
Site	33°05'03"	35°01'21"	35°02'25"	35°03'12"	35°03'12"	35°03'12"	35°03'12"	35°03'12"	35°03'12"
	16°18'04"	12°52'22"	12°53'51"	12°54'00"	12°54'00"	12°54'00"	12°54'00"	12°54'00"	12°54'00"
SiO_2	43.65	37.53	36.30	46.91	47.66	45.79	45.41	46.90	48.25
TiO_2	3.33	2.77	3.07	4.38	4.46	4.71	4.60	4.21	3.53
Al_2O_3	16.08	8.66	9.81	14.85	15.26	15.31	15.59	17.12	18.52
$Fe_2O_3^t$	14.46	12.58	12.92	11.01	10.50	12.81	12.05	9.90	11.14
MnO	0.20	0.16	0.18	0.12	0.10	0.11	0.11	0.08	0.07
MgO	6.41	11.70	7.60	4.46	4.27	3.46	3.80	3.38	1.46
CaO	10.82	16.10	17.94	9.34	9.25	8.84	8.71	7.60	5.71
Na_2O	2.66	1.46	1.70	3.07	3.33	3.49	3.49	3.70	4.40
K_2O	0.66	0.73	1.30	1.72	1.73	1.47	1.56	1.91	1.75
P_2O_5	0.58	0.45	0.55	0.83	0.86	0.89	0.94	1.01	1.15
CO_2	0.10	4.86	6.25	1.58	0.09	0.17	0.58	0.66	0.48
H_2O	1.39	3.07	2.28	1.61	1.86	1.99	2.18	3.26	3.30
Total	100.34	100.07	99.90	99.88	99.37	99.04	99.02	99.73	99.76

Sample	DS 797-6	DS 797-7	DS 797-10	VH-97-103	VH-97-76	SDC-1	
Unit/type	Ampere	Ampere	Ampere	Ampere	Ormonde	Standard	Deviation
Site	35°03'12"	35°03'12"	35°03'12"	35°03'01"	36°46'08"	n = 7	(2 σ)
	12°54'00"	12°54'00"	12°54'00"	12°54'02"	11°05'53"		
SiO_2	45.27	47.82	48.20	47.89	72.84	66.12	0.44
TiO_2	4.37	3.99	4.78	4.39	0.12	0.99	0.03
Al_2O_3	16.94	17.05	16.80	18.25	14.65	15.90	0.16
$Fe_2O_3^t$	15.41	10.74	14.40	10.09	1.27	6.87	0.15
MnO	0.11	0.10	0.14	0.05	0.01	0.11	0.01
MgO	2.08	2.90	1.32	2.19	0.15	1.74	0.12
CaO	5.68	7.10	5.04	6.38	2.86	1.41	0.01
Na_2O	3.55	3.91	3.28	4.14	2.63	2.14	0.29
K_2O	1.67	1.97	1.02	1.74	4.63	3.27	0.02
P_2O_5	0.94	1.03	0.97	0.89	0.07	0.15	0.01
CO_2	0.17	0.14	0.32	0.64	0.6	n. d.	
H_2O	3.30	2.14	3.62	2.69	0.46	n. d.	
Total	99.49	98.89	99.89	99.34	100.29		

For abbreviations see Table C

Appendix to Chapter 4 (The geochemical evolution of the Madeira hotspot)

Table B : Electron microprobe (EMP) data

Sample	13796-1	13796-2	13796-3	Ma 127	Ma 128	Ma 131b
Unit/type	ERP/dike	ERP/dike	ERP/dike	ERP/dike	ERP/dike	ERP/dike
Site	32°44'53"	32°44'53"	32°44'53"	32°45'00"	32°44'55"	32°45'49"
	16°48'42"	16°48'42"	16°48'42"	16°49'08"	16°49'06"	16°48'19"
Mean of n =	12	10	8	9	10	11
SiO_2	49.13	49.30	49.35	49.00	49.21	48.31
TiO_2	2.70	2.74	2.71	2.85	2.83	3.02
Al_2O_3	14.93	14.94	15.05	15.02	14.99	15.15
FeO'	11.83	11.68	11.55	11.43	11.72	12.50
MnO	0.19	0.20	0.19	0.20	0.16	0.21
MgO	6.14	6.12	6.14	6.14	6.02	5.39
CaO	11.11	10.92	11.27	11.39	11.16	10.72
Na_2O	3.00	3.04	3.04	2.94	2.55	3.40
K_2O	0.65	0.54	0.57	0.56	0.73	0.92
P_2O_5	0.37	0.37	0.37	0.47	0.42	0.50
SO_2	0.08	0.03	0.03	0.10	0.08	0.08
Total	100.11	99.86	100.26	100.09	99.86	100.19

For abbreviations see Table C

Appendix to Chapter 4 (The geochemical evolution of the Madeira hotspot)

Table C: Trace element data

Sample	Md 33	191292-5	191292-6	191292-8	MA-85	MA-87	MA-88	MA-97	MA-218a	M-1
Unit/type	PE/flow	PE/flow	PE/flow	PE/flow	PE/flow	PE/flow	PE/flow	PE/flow	PE/cone	LRP/flow
Ni*	391	233	277	381	350	252	261	268	234	4
Cr*	1039	619	781	977	959	634	717	650	562	<18
Co*	68	56	57	59	59	54	50	52	47	17
Ga*	18	21	16	16	16	21	20	19	19	23
V*	322	331	352	336	338	312	334	332	263	167
Zn*	84	91	86	85	87	89	89	89	101	126
Cs	0.17	0.31	0.29	0.17	0.20	0.32	0.25	0.20	0.37	0.17
Pr	7.07	9.46	8.26	7.48	7.58	9.32	8.24	9.18	10.3	16.6
Hf	4.37	4.83	4.79	4.42	4.41	5.81	5.11	5.33	5.60	7.73
W	1.10	0.85	0.61	0.52	n.d.	n.d.	n.d.	n.d.	n.d.	0.45
Tl	0.01	0.02	0.02	0.01	n.d.	0.01	0.02	0.01	n.d.	0.02
Y	18.1	22.3	20.8	18.9	19.0	20.6	18.4	19.4	26.3	37.0
Pb	16.4	23.4	24.5	17.2	18.3	25.3	18.6	18.1	25.4	27.7
Ba	226	332	307	235	233	318	274	306	409	597
Th	2.57	4.38	3.40	2.64	3.14	4.58	3.84	4.98	5.56	6.92
Nb	40.3	56.2	52.1	42.3	45.3	52.1	43.9	45.7	62.5	101
Ta	2.00	2.61	2.53	2.09	2.27	3.18	2.76	2.87	3.11	4.65
U	0.72	1.17	0.91	0.71	0.91	1.31	1.05	1.37	1.51	1.30
La	28.7	44.5	35.3	31.4	30.0	38.7	31.4	39.1	46.1	77.8
Ce	58.6	81.5	70.6	62.6	60.1	77.8	65.4	78.5	86.9	147
Pb	1.45	2.94	2.05	1.42	2.27	2.22	1.91	2.12	3.01	3.56
Nd	29.0	37.4	33.6	30.7	29.9	37.3	33.3	37.0	38.6	63.8
Sr	575	707	659	600	588	633	543	616	716	1413
Sm	6.03	7.42	6.92	6.34	6.38	7.67	6.96	7.71	7.66	11.7
Zr	186	214	209	191	195	225	196	185	261	387
Eu	1.88	2.24	2.08	1.96	1.96	2.31	2.12	2.32	2.34	3.51
Tb	0.76	0.90	0.85	0.77	0.77	0.94	0.86	0.96	0.97	1.40
Gd	5.57	6.88	6.35	5.94	5.65	6.56	6.06	6.73	6.87	10.70
Tb	0.76	0.90	0.85	0.77	0.77	0.94	0.86	0.96	0.97	1.40
Dy	3.94	4.75	4.42	4.03	4.07	4.90	4.48	4.97	5.33	7.34
Ho	0.68	0.83	0.78	0.70	0.70	0.89	0.80	0.88	0.97	1.33
Er	1.75	2.15	1.98	1.80	1.78	2.32	1.99	2.28	2.68	3.55
Tm	0.21	0.26	0.25	0.22	0.23	0.29	0.25	0.27	0.36	0.45
Yb	1.28	1.60	1.50	1.33	1.36	1.82	1.58	1.70	2.28	2.85
Lu	0.18	0.22	0.20	0.18	0.19	0.26	0.22	0.24	0.33	0.40

Appendix

Sample Unit/type	M-3 LRP/flow	Md-5 LRP/flow	Md-9 LRP/flow	Md-12 LRP/flow	Md-21 LRP/flow	MA-16 LRP/flow	MA-17 LRP/flow	MA-23 LRP/flow	MA-29 LRP/flow	MA-41 LRP/flow
Ni*	301	173	4	123	28	61	225	188	145	124
Cr*	494	388	62	250	30	141	485	400	257	225
Co*	65	52	8	50	38	30	51	51	46	43
Ga*	17	14	22	21	17	26	22	22	16	20
V*	296	326	93	358	334	245	276	274	273	290
Zn*	104	106	114	102	100	104	102	105	117	112
Cs	0.31	0.41	0.39	0.26	0.28	0.35	0.23	0.20	0.22	0.23
Pr	8.74	11.5	18.9	9.24	14.0	13.2	9.18	9.70	10.2	13.7
Hf	4.89	5.55	11.1	5.37	7.43	8.11	5.77	5.88	6.89	7.33
W	1.13	0.48	1.53	0.95	2.44	n.d.	n.d.	n.d.	n.d.	n.d.
Tl	0.02	0.03	0.08	0.02	0.03	0.01	0.02	0.02	0.02	0.02
Y	25.0	28.6	41.5	26.8	33.9	27.1	22.3	22.0	23.9	27.0
Rb	23.8	24.5	42.8	23.4	24.1	32.4	23.2	20.5	22.6	16.9
Ba	297	393	534	303	386	427	308	295	278	327
Th	3.87	3.98	6.53	3.25	4.65	7.61	4.39	5.32	4.95	6.41
Nb	53.2	64.6	132	56.5	73.2	69.9	49.2	48.9	50.7	58.5
Ta	2.48	2.90	6.10	2.69	3.44	4.59	2.98	3.29	3.39	3.83
U	1.00	0.88	1.71	0.80	1.09	1.60	1.24	1.43	1.37	1.54
La	40.2	47.6	81.8	39.3	60.1	56.1	38.3	38.8	41.0	58.3
Ce	75.5	98.4	166	76.8	117	114	76.9	80.8	85.9	116
Pb	2.49	2.34	4.08	4.44	3.50	3.47	2.25	2.53	2.98	2.47
Nd	34.8	45.9	72.9	37.5	56.0	51.5	36.3	39.3	41.9	54.4
Sr	670	903	1376	758	1110	642	547	575	638	829
Sm	7.03	9.05	13.3	7.74	11.0	9.88	7.71	8.06	8.80	10.5
Zr	225	254	578	250	372	311	233	206	246	278
Eu	2.23	2.78	3.95	2.44	3.39	2.95	2.37	2.44	2.68	3.21
Tb	0.93	1.13	1.54	1.02	1.34	1.28	0.94	1.05	1.13	1.31
Gd	6.71	8.27	11.6	7.47	10.12	8.56	6.76	7.04	7.57	9.01
Tb	0.93	1.13	1.54	1.02	1.34	1.28	0.94	1.05	1.13	1.31
Dy	4.97	5.92	8.15	5.40	6.90	6.85	5.25	5.64	6.02	6.83
Ho	0.90	1.05	1.48	0.98	1.23	1.26	0.96	1.03	1.08	1.24
Er	2.36	2.75	3.97	2.55	3.17	3.35	2.40	2.69	2.89	3.24
Tm	0.29	0.34	0.51	0.32	0.39	0.42	0.32	0.33	0.36	0.40
Yb	1.76	2.09	3.13	1.95	2.38	2.68	1.95	2.11	2.21	2.42
Lu	0.25	0.29	0.44	0.27	0.33	0.38	0.27	0.30	0.31	0.35

Appendix

Sample Unit/type	MA-42 LRP/flow	MA-53 LRP/flow	MA-66 LRP/flow	MA-75b LRP/intr.	MA-106 LRP/flow	MA-110 LRP/flow	MA-115 LRP/flow	MA-137 LRP/flow	MA-142 LRP/cone	MA-152 LRP/flow
Ni*	<2	207	223	47	316	99	24	424	159	150
Cr*	<18	341	506	71	566	187	25	840	471	276
Co*	10	47	56	38	61	48	40	65	51	42
Ga*	21	15	21	19	18	22	20	18	20	24
V*	82	304	304	275	308	361	275	318	366	286
Zn*	101	103	101	114	94	97	118	95	107	114
Cs	0.37	0.26	0.24	0.14	n.d.	n.d.	n.d.	0.21	0.21	n.d.
Pr	24.5	13.3	11.4	10.2	9.36	8.66	18.9	7.84	9.17	12.7
Hf	12.8	6.56	5.83	5.67	5.18	5.83	7.16	5.14	5.75	7.36
W	n.d.	n.d.	n.d.	n.d.	0.42	0.24	0.69	n.d.	n.d.	0.79
Tl	0.05	0.02	0.02	n.d.	0.32	0.29	0.43	0.01	0.02	0.38
Y	42.8	25.8	23.8	28.6	25.9	24.1	34.2	19.8	21.2	29.5
Rb	78.3	20.2	18.5	23.2	18.2	27.3	32.5	19.0	16.0	27.6
Ba	725	391	329	286	287	299	452	262	273	341
Th	21.9	6.79	5.46	4.06	3.87	2.40	9.30	3.01	3.38	7.16
Nb	121	67.4	48.5	57.3	47.4	68.4	102	46.7	45.3	65.0
Ta	8.72	4.25	2.96	2.90	2.55	4.19	5.18	2.98	2.77	3.50
U	6.55	1.88	1.38	1.19	0.91	0.54	2.47	0.83	0.93	1.79
La	137	57.7	49.5	40.2	39.6	29.6	95.6	27.8	33.5	58.9
Ce	181	114	97.7	81.6	76.7	64.9	171	60.3	70.9	111
Pb	6.53	2.79	2.24	2.13	1.87	1.19	2.91	1.56	1.82	2.99
Nd	86.8	51.7	46.3	39.7	37.7	36.7	70.0	32.2	37.9	48.7
Sr	694	798	703	644	680	687	1156	495	595	815
Sm	14.2	10.0	9.32	8.38	7.86	8.10	12.7	7.00	8.39	9.54
Zr	538	243	212	244	212	231	313	195	217	328
Eu	4.00	2.99	2.85	2.60	2.40	2.45	3.72	2.15	2.56	2.89
Tb	1.68	1.26	1.19	1.10	1.03	1.01	1.48	0.90	1.01	1.19
Gd	11.75	8.53	8.23	7.67	7.16	7.10	10.86	6.32	7.18	8.54
Tb	1.68	1.26	1.19	1.10	1.03	1.01	1.48	0.90	1.01	1.19
Dy	8.84	6.42	6.13	6.02	5.40	5.26	7.45	4.72	5.33	6.30
Ho	1.65	1.16	1.11	1.08	0.98	0.92	1.32	0.85	0.92	1.14
Er	4.56	3.04	2.83	2.89	2.58	2.36	3.46	2.11	2.25	3.01
Tm	0.59	0.37	0.35	0.37	0.32	0.29	0.43	0.26	0.28	0.38
Yb	3.73	2.30	2.12	2.28	1.96	1.70	2.66	1.63	1.68	2.42
Lu	0.56	0.33	0.30	0.32	0.27	0.23	0.37	0.23	0.23	0.34

Appendix

Sample Unit/type	MA-160 LRP/flow	MA-162 LRP/flow	DGR-2 DRP/flow	DGR-14 DRP/dike	DGR-47 DRP/flow	DGR-49 DRP/flow	K-11 DRP/cobble	K-12 DRP/cobble	K-18 DRP/flow	K-22 DRP/flow
Ni*	198	251	159	363	160	98	216	14	212	295
Cr*	419	466	412	740	288	222	552	<18	540	411
Co*	54	58	53	61	53	42	59	41	46	55
Ga*	21	22	20	15	22	21	16	22	18	21
V*	366	328	332	312	330	294	323	326	297	255
Zn*	104	100	110	102	137	124	108	134	105	108
Cs	n.d.	0.20	0.26	0.13	0.29	0.26	0.12	0.30	0.17	0.08
Pr	8.23	9.07	8.08	6.63	13.1	13.0	7.40	10.9	16.8	8.39
Hf	5.24	5.62	5.30	4.33	6.37	7.54	4.88	6.77	5.39	3.71
W	0.39	n.d.	n.d.	n.d.	n.d.	n.d.	n.d.	n.d.	n.d.	n.d.
Tl	0.30	0.01	n.d.	n.d.	n.d.	n.d.	n.d.	n.d.	n.d.	n.d.
Y	24.0	22.9	25.9	21.6	86.2	31.4	23.2	31.0	47.4	24.0
Pb	15.9	16.2	18.2	14.2	23.3	27.8	14.5	26.4	15.2	7.70
Ba	224	268	199	164	298	319	173	290	327	218
Th	2.81	3.53	2.70	2.31	3.91	5.05	2.27	3.92	5.22	4.04
Nb	37.6	44.2	41.9	35.4	58.7	69.0	36.1	59.0	59.7	39.1
Ta	2.09	2.58	2.13	1.77	2.92	3.47	1.82	3.10	2.84	1.86
U	0.71	0.92	0.74	0.67	1.07	1.43	0.64	1.13	1.36	1.03
La	30.9	34.9	29.1	24.1	57.0	55.1	25.7	41.1	72.5	39.0
Ce	64.1	72.9	61.4	50.7	107	107	55.6	85.1	120	72.3
Pb	1.52	1.83	1.89	1.34	2.09	2.94	1.50	2.44	2.35	1.59
Nd	34.4	36.9	33.2	26.9	53.3	49.7	30.6	43.5	67.4	31.5
Sr	637	606	526	462	716	736	486	719	737	509
Sm	7.66	8.12	7.52	6.07	11.4	10.1	6.90	9.26	13.8	6.31
Zr	207	215	234	191	294	358	213	305	239	169
Eu	2.37	2.56	2.35	1.87	3.80	3.00	2.13	2.87	4.29	1.97
Tb	0.99	1.02	1.00	0.81	1.95	1.26	0.90	1.21	1.92	0.88
Gd	6.95	7.31	7.03	5.71	13.1	8.97	6.44	8.43	13.9	5.91
Tb	0.99	1.02	1.00	0.81	1.95	1.26	0.90	1.21	1.92	0.88
Dy	5.24	5.53	5.51	4.40	11.6	6.65	4.89	6.53	10.3	4.86
Ho	0.93	0.99	0.97	0.78	2.44	1.16	0.87	1.17	1.82	0.90
Er	2.39	2.40	2.54	2.05	6.93	2.99	2.25	3.07	4.60	2.45
Tm	0.30	0.31	0.32	0.26	0.89	0.38	0.29	0.40	0.57	0.32
Yb	1.83	1.90	1.95	1.60	4.93	2.29	1.73	2.47	3.38	2.00
Lu	0.25	0.26	0.27	0.22	0.76	0.31	0.24	0.35	0.45	0.28

Appendix

Sample	K-26	K-31	MA-120	MA-123	MA-127	13796-1	MA-208	MA-215	MA-227	M-30 b
Unit/type	DRP/flow	DRP/flow	ERP/congl.	ERP/dike	ERP-glass	ERP-glass	ERO/flow	ERO/flow	ERP/congl.	PS/dike
Ni*	164	177	88	55	n.d.	n.d.	40	258	512	<2
Cr*	282	314	116	42	n.d.	n.d.	20	531	1218	<18
Co*	46	47	41	34	n.d.	n.d.	38	51	57	<4
Ga*	21	18	25	23	n.d.	n.d.	21	16	14	27
V*	328	323	311	318	n.d.	n.d.	329	289	236	<12
Zn*	140	118	97	102	n.d.	n.d.	110	107	87	116
Cs	0.24	0.13	0.05	0.02	0.17	0.19	0.15	0.11	0.14	0.28
Pr	9.86	9.56	6.44	13.4	11.0	7.24	12.5	6.08	8.30	10.9
Hf	6.54	6.47	5.13	8.91	6.94	4.90	7.14	4.63	4.42	4.81
W	n.d.	n.d.	n.d.	n.d.	n.d.	n.d.	n.d.	n.d.	n.d.	0.97
Tl	0.02	0.01	0.00	0.00	n.d.	n.d.	0.02	0.00	n.d.	0.13
Y	25.9	25.9	21.5	29.9	32.8	27.0	28.8	21.5	18.2	22.1
Pb	17.8	17.2	0.60	1.80	12.2	14.5	20.2	11.6	16.2	87.8
Ba	290	248	82.0	170	175	174	356	150	223	985
Th	3.23	3.33	3.27	3.00	2.33	2.45	5.45	1.96	4.03	15.6
Nb	46.2	45.0	28.1	54.7	53.2	35.8	66.1	29.8	49.2	196
Ta	2.98	2.68	1.89	4.29	3.26	1.83	3.95	1.79	2.52	8.39
U	0.88	0.90	1.17	0.78	0.63	0.72	1.27	0.53	1.05	5.14
La	35.3	35.5	23.7	45.6	35.6	25.7	51.1	19.7	34.9	61.4
Ce	76.0	75.6	50.8	106	80.5	55.0	102	44.6	68.2	105
Pb	1.69	1.98	1.29	1.61	1.48	1.75	2.44	1.18	2.00	7.43
Nd	41.5	39.4	27.6	53.9	44.1	29.8	47.5	25.9	31.8	32.7
Sr	624	547	358	590	728	479	876	427	608	156
Sm	9.21	8.74	6.54	10.9	9.55	6.92	9.72	6.11	6.36	5.16
Zr	250	253	177	365	352	211	293	186	196	110
Eu	2.85	2.73	2.20	3.47	2.95	2.22	3.07	1.95	1.90	1.41
Tb	1.17	1.11	0.96	1.42	1.24	1.01	1.22	0.89	0.76	0.58
Gd	8.09	7.80	6.11	9.56	8.66	6.77	8.84	5.96	5.57	4.08
Tb	1.17	1.11	0.96	1.42	1.24	1.01	1.22	0.89	0.76	0.58
Dy	6.36	6.23	5.35	7.73	6.70	5.62	6.43	4.82	4.03	3.45
Ho	1.12	1.11	1.01	1.39	1.23	1.02	1.20	0.89	0.70	0.65
Er	2.80	2.81	2.60	3.70	3.23	2.69	2.90	2.22	1.82	1.91
Tm	0.36	0.37	0.34	0.46	0.41	0.35	0.38	0.29	0.23	0.30
Yb	2.13	2.28	2.06	2.77	2.53	2.17	2.38	1.80	1.38	1.90
Lu	0.30	0.31	0.29	0.39	0.36	0.30	0.32	0.24	0.19	0.28

Appendix

Sample	M-36	M-37	M-40	M-41	M-53	161292-2	PS-2	PS-3	PS-4	DS 790-1
Unit/type	PS/dike	PS/intr.	PS/dike	PS/intr.	PS/intr.	PS/dike	PS/dike	PS/dike	PS/dike	Coral Patch
Ni*	98	<2	361	<2	<2	283	<2	6	9	n.d.
Cr*	258	36	1288	<18	<18	850	<18	<18	23	n.d.
Co*	45	<4	66	63	15	64	39	49	63	n.d.
Ga*	17	21	11	28	24	17	24	16	23	n.d.
V*	299	34	266	94	116	285	63	225	367	n.d.
Zn*	96	104	78	116	124	80	133	101	99	n.d.
Cs	0.05	0.07	0.09	0.39	0.43	0.05	0.14	0.21	0.05	0.15
Pr	9.55	23.0	8.38	16.4	17.2	5.27	22.1	16.2	10.4	10.7
Hf	5.20	11.1	3.28	9.49	9.77	3.26	13.0	5.87	4.74	6.66
W	0.49	1.73	0.10	577	0.98	0.21	531	432	306	n.d.
Tl	0.02	0.05	0.01	0.06	0.07	0.01	0.05	0.09	0.19	0.02
Y	28.1	94.1	26.2	39.2	40.4	19.3	47.9	37.6	29.3	29.9
Rb	16.2	49.8	9.50	33.8	23.8	8.40	42.4	18.3	9.70	6.70
Ba	216	1101	365	402	404	135	622	473	867	84.0
Th	3.85	14.26	1.84	6.00	6.77	1.90	8.99	6.77	4.72	3.11
Nb	54.2	151	28.0	80.1	86.8	28.2	160	86.7	56.2	63.3
Ta	2.52	8.00	1.37	4.79	4.24	1.42	9.23	4.64	3.05	3.93
U	0.95	2.23	0.47	1.64	1.40	0.42	1.90	1.46	1.09	1.81
La	43.2	128	43.2	74.1	78.3	21.1	107	73.9	48.5	45.4
Ce	83.0	221	59.3	142	153	42.9	200	147	92.5	74.3
Pb	2.21	6.86	1.04	3.55	3.98	1.10	4.73	2.45	1.80	1.38
Nd	37.8	79.0	34.0	63.7	66.5	21.9	81.1	64.3	40.9	43.9
Sr	611	829	502	1032	1149	329	1178	1266	847	411
Sm	7.49	13.1	6.79	11.6	12.3	4.76	14.0	12.2	8.11	9.29
Zr	245	464	140	484	488	137	712	283	221	275
Eu	2.28	3.94	1.98	3.50	3.61	1.51	4.01	3.73	2.50	2.85
Tb	0.99	1.80	0.92	1.40	1.47	0.68	1.61	1.52	1.07	1.13
Gd	7.14	12.5	6.58	10.4	10.9	4.67	11.9	11.3	7.79	8.33
Tb	0.99	1.80	0.92	1.40	1.47	0.68	1.61	1.52	1.07	1.13
Dy	5.39	11.2	4.99	7.41	7.72	3.78	8.55	7.95	5.87	5.85
Ho	1.00	2.59	0.93	1.37	1.42	0.71	1.60	1.43	1.09	1.04
Er	2.72	8.54	2.46	3.68	3.90	1.91	4.51	3.72	2.91	2.48
Tm	0.36	1.26	0.31	0.48	0.51	0.25	0.61	0.46	0.37	0.31
Yb	2.22	8.84	1.94	3.07	3.26	1.53	3.95	2.82	2.33	1.82
Lu	0.31	1.43	0.27	0.44	0.47	0.22	0.57	0.39	0.33	0.26

Sample	DS 797-1	DS 797-2	DS 797-7	VH 97-103	VH-97-76	VH-97-77	BE-N	
Unit/type	Ampere	Ampere	Ampere	Ampere	Ormonde	Ormonde	(n=3)	dev. (2 σ)
Ni*	38	31	26	n.d.	n.d.	n.d.	n.d.	
Cr*	103	83	<18	n.d.	n.d.	n.d.	n.d.	
Co*	34	37	26	n.d.	n.d.	n.d.	n.d.	
Ga*	25	27	26	n.d.	n.d.	n.d.	n.d.	
V*	375	387	342	n.d.	n.d.	n.d.	n.d.	
Zn*	88	97	82	n.d.	n.d.	n.d.	n.d.	
Cs	0.80	0.33	0.59	1.61	0.20	0.51	0.77	0.01
Pr	15.7	14.9	16.1	13.4	2.63	3.20	17.4	0.60
Hf	9.74	10.4	10.8	10.0	0.88	2.54	5.98	0.45
W	n.d.	n.d.	n.d.	n.d.	n.d.	n.d.	n.d.	
Tl	n.d.	0.03	0.04	0.06	0.58	0.33	0.03	0.00
Y	32.9	32.8	32.0	25.5	1.35	30.8	27.3	1.08
Rb	37.2	25.2	39.0	52.4	95.3	53.3	49.9	3.17
Ba	417	365	478	403	1545	206	1092	64.4
Th	5.51	4.86	6.42	5.29	0.67	0.37	10.4	1.14
Nb	89.6	67.4	86.5	71.7	1.69	5.14	112	5.97
Ta	4.55	4.16	5.24	4.56	0.05	0.34	5.30	0.46
U	1.87	2.40	2.48	2.16	0.13	2.70	2.46	0.36
La	58.2	48.6	60.4	50.8	19.2	8.50	86.0	5.90
Ce	122	109	128	107	27.4	19.1	156	11.9
Pb	3.57	2.61	2.59	2.10	14.9	2.60	3.97	0.26
Nd	62.9	63.7	63.8	53.6	8.36	15.3	66.1	3.15
Sr	1063	878	992	926	315	209	1492	125
Sm	13.1	13.8	13.2	112	0.99	4.40	12.2	0.75
Zr	457	437	467	374	31.6	96.4	277	11.0
Eu	3.89	4.04	3.97	3.47	0.81	1.26	3.60	0.18
Tb	1.47	1.61	1.47	1.23	0.06	0.85	1.32	0.11
Gd	11.0	11.4	10.9	9.07	0.61	5.05	10.2	0.68
Tb	1.47	1.61	1.47	1.23	0.06	0.85	1.32	0.11
Dy	7.42	8.22	7.63	6.49	0.28	5.48	6.41	0.43
Ho	1.25	1.41	1.35	1.13	0.05	1.12	1.07	0.06
Er	3.14	3.49	3.26	2.76	0.14	3.15	2.62	0.24
Tm	0.39	0.43	0.43	0.36	0.02	0.44	0.31	0.02
Yb	2.30	2.60	2.63	2.22	0.14	2.74	1.82	0.09
Lu	0.31	0.36	0.36	0.30	0.02	0.40	0.25	0.02

Table C: All data in ppm. (* = Trace elements determined by XRF) Abbreviations: PE= Post-Erosional, LRP= Late Madeira Rift Phase, DRP= Desertas Rift Phase, ERP= Early Madeira Rift Phase, PS= Porto Santo.

Appendix to Chapter 5 (Evolution of the Selvagen archipelago and neighboring seamounts)

Sample description and sampling sites:

Sample	Location	Description/ phenocryst phases	Latitude/ Longitude
Selvagen Grande			
J 1	200 m east from Ponta do Risco	Lava flow, 10 % ol, 5-10 % cpx, 5 % mgt	30°09´05"N/ 15°51´45"W
J 2	Slope over Desembarcadouro	Breccia, 15 % fsp, 1-2 % hbl	30°08´23"N/ 15°52´05"W
J 3	Slope over Desembarcadouro,	Breccia, 20 % fsp and 1-2 % cpx	30°08´23"N/ 15°52´05"W
J 4	Top of Portinho das Cagarras	Bomb in scoria deposits, 10 % ol, 3 % cpx	30°08´24"N/ 15°52´03"W
J 6	Top of Portinho das Cagarras	Bomb in scoria, 5 % ol, 3 % cpx	30°08´24"N/ 15°52´03"W
J 7	Portinho das Cagarras	Flow, vesicular, 5% ol, 3 % cpx, 5 % mgt	30°08´24"N/ 15°51´58"W
J 8a	Portinho das Cagarras	Flow, vesicular, 5 % ol, 3 % cpx, 5 % mgt	30°08´24"N/ 15°52´03"W
J 9	Portinho das Cagarras	Block, 10% neph, 5% fsp, 3 % amph	30°08´26"N/ 15°52´02"W
J 10	Trail going up to Pico da Atalaia	Block, 15 % ol	30°08´28"N/ 15°52´03"W
J 11	Trail going up to Pico da Atalaia	Block, 1% fsp	30°08´28"N/ 15°52´03"W
J 12	Above Cisterna Nova	Flow, vesicular, 2% ol, 1 % opx	30°08´29"N/ 15°52´04"W
J 13	Above Cisterna Nova	Bomb, vesicular, 2-3% ol, 1 % opx	30°08´29"N/ 15°52´05"W
J 14	Above Cisterna Nova	Bomb, 5% ol, 3 % opx	30°08´29"N/ 15°52´05"W
J 15	Above Cisterna Nova	Flow, 2% ol, 1 % cpx	30°08´32"N/ 15°52´10"W
J 16	Above Cisterna Nova	Flow, 5% ol, 1 % cpx,	30°08´35"N/ 15°52´13"W
J 18	Pico da Atalaia	Flow, 5 % ol, 1 % mgt	30°08´40"N/ 15°52´15"W
J 19 a	Trail at Ponta dos Moinhos	Dike, 5 % cpx	30°08´16"N/ 15°52´05"W
J 21	Trail at Ponta dos Moinhos,	Calcareous dike,	30°08´21"N/ 15°52´02"W
J 23	Enseada da Fonte das Galinhas	Dike, 10% neph, 5 % amph, 5 % fsp	30°08´17"N/ 15°51´58"W
J 24	Enseada da Fonte das Galinhas	Intrusion, 15% neph, 5-10 % amph, 3 % fsp	30°08´16"N/ 15°51´54"W
J 25	Enseada da Fonte das Galinhas	Clast, 5% amph, fsp, mgt	30°08´17"N/ 15°51´53"W
J 26	Enseada da Fonte das Galinhas	Bomb, 3 % ol	30°08´17"N/ 15°51´53"W
J 27	Enseada da Fonte das Galinhas	Flow, 5% ol, 1 % opx, 1 % mgt	30°08´17"N/ 15°51´50"W
J 28	Cabeço do Inferno	Bomb, 1-2% ol, mgt, opx	30°08´14"N/ 15°51´44"W
J 29	Cabeço do Inferno	Bomb, 1% ol, mgt, opx	30°08´14"N/ 15°51´44"W

J 30	Cabeço do Inferno	Flow, 5 % ol, 1 % opx, mgt	30°08´13"N/ 15°51´43"W
J 31	Bay between Ponta do Inferno a. Ponta de Leste	Dike, 5-10 % amph, 5-10 % fsp	30°08´11"N/ 15°51´30"W
J 32	Between Ponta do Inferno a. Ponta de Leste	Intrusion, 15 % amph, 10-15% fsp and neph	30°08´16"N/ 15°51´29"W
J 33	Ponta de Leste	Bomb, 1-3 % amph, 1 % opx, 1 % mgt	30°08´18"N/ 15°51´32"W
J 34	Ponta de Leste	Bomb, 1-3 % amph, 1 % opx, mgt	30°08´18"N/ 15°51´32"W
J 35 b	Ponta dos Moinhos	Clast, 5 % amph , 1-3 opx, mgt	30°08´19"N/ 15°51´56"W
J 35 f	Ponta dos Moinhos	Clast, 3-5% 1-3 % amph, 1 % mgt	30°08´19"N/ 15°51´56"W
J 35 g	Ponta dos Moinhos	Clast, 3 % amph, 1 % mgt	30°08´19"N/ 15°51´56"W
J 36	Ponta dos Moinhos , river bed	Dike, 3-5 % ol, 1 % mgt	30°08´21"N/ 15°51´37"W
J 37	Pond, SE of the island	Dike, 5 % ol	30°08´22"N/ 15°51´30"W
J 38	Pond, SE of the island	Dike, vesicular, 5 % ol, 3 % neph	30°08´22"N/ 15°51´30"W
J 39	Pond, SE of the island	Dike, vesicular, 5 % ol,	30°08´22"N/ 15°51´30"W
J 41 a	Pond, SE of the island	Intrusion, 5 % ol, 3-5 % amph	30°08´22"N/ 15°51´30"W
J 42	Pond, SE of the island	Dike, 5-10 % ol	30°08´22"N/ 15°51´30"W
J 43	Pond, SE of the island	Dike, 5-10 % ol	30°08´22"N/ 15°51´30"W
J 45	Enseada dos Pedreiras	Flow, vesicular, 5-10 % ol	30°08´25"N/ 15°51´30"W
J 46	Vicinity of Pico dos Tornozelos	Bomb, 10 % ol	30°08´27"N/ 15°51´31"W
J 47 b	Pico dos Tornozelos	Flow, 10 % ol	30°08´41"N/ 15°51´34"W
J 48	Ponta Espinha	Flow, 5 % ol	30°08´49"N/ 15°51´26"W
J 49	Ponta Espinha	flow, 5% ol,	30°08´49"N/ 15°51´26"W
J 59 a	Cliff above Enseada da Fonte das Galinhas	Calcareous sediment and carbonate clasts, sample from base of bank	30°08´17"N/ 15°51´58"W
J 59 b	Cliff above Enseada da Fonte das Galinhas	Calcareous sediment and carbonate clasts, sample from middle of bank	30°08´17"N/ 15°51´58"W
J 59 c	Cliff above Enseada da Fonte das Galinhas	Calcareous sediment and carbonate clasts, sample from top of bank	30°08´17"N/ 15°51´58"W
SG-1 b	Cliff above Ponta dos Moinhos	Dike, 5 % fsp, 3 % ol, 3 % cpx	30°08´28"N/ 15°52´03"W
SG-3	Cliff above Ponta dos Moinhos	Breccia, 10 % ol	30°08´28"N/ 15°52´03"W
SG-4	Cliff above Ponta dos Moinhos	Breccia, 5 % fsp, 1 % amph	30°08´28"N/ 15°52´03"W
SG-5	Cliff above Ponta dos Moinhos	Breccia, 5 % fsp, 5 % sod, 1 % amph	30°08´28"N/ 15°52´03"W
SG-6	Cliff above Ponta dos Moinhos	Breccia, 5 % fsp, 5 % sod, 1 % amph	30°08´28"N/ 15°52´03"W
SG-7	Cliff above Ponta dos Moinhos	Intrusion, 5 % fsp, 1 % sod, 1 % amph	30°08´28"N/ 15°52´03"W
SG-8	Cliff above Ensada da F. d. Galinhas	Intrusion, 15 % fsp, 5 % amph	30°08´28"N/ 15°52´03"W
SG-10	Above Ponta dos Moinhos	Flow, 5 % ol	30°08´40"N/ 15°52´15"W
SG-12	Above Ponta dos Moinhos	Dike, vesicular, 5 % ol	30°08´40"N/ 15°52´15"W

SG-13	Cisterna Nova	Block, 10 % ol	30°08´40"N/ 15°52´15"W
Selvagen Pequena			
J 50	Eastern slope of Pico do Veado	Breccia, 5-10 % amph	30°18'00" N/ 16°17'05"W
J 51	Eastern slope of Pico do Veado	Dike, 1% ol, 1% cpx	30°18'00" N/ 16°17'05"W
J 52	Beach at Ponta do Norte	Beach cobble, 5-10% plg, 3-5 % amph ± cpx	30°18'58"N/ 16°15'00"W
J 53	Beach at Ponta do Norte	Beach cobble ca. 10% fsp, 3-5 % amph	30°18'58"N/ 16°15'00"W
J 54	Beach at Ponta do Norte	Beach cobble, ca. 1% large amph. 1% plg	30°18'58"N/ 16°15'00"W
J 55	Northern slope of Marco Ne	Dike, 10% fsp, 3-5 % amph	30°16'40"N/ 16°13'00"W
J 56	NE sector of the island	Dike, 5 % amph, 3-5 % cpx	30°18'00"N/ 16°10'05"W
J 57	NE sector of the island	Dike, 4 % ol, 1 % amph/cpx	30°18'00"N/ 16°10'05"W
J 58	SE of Marco Cal VII	Dike, 1-3 % ol	30°18'00"N/ 16°19'10"W
SP 1	Beach at SW coast	Beach cobble, 10 % amph, 5 % ol	30°17'00"N/ 16°18'00"W
SP 2	Beach at SW coast	Dike, 15 % fsp, 5 % amph	30°17'00"N/ 16°18'00"W
Seamounts			
Dacia Seamount			
DS 809-1	Eastern top between 590 and 580 m water depths	Angular clast, 30 % ol	31°08'31"N/ 13°31'06"W
Conception Seamount			
DS 822-1	Southern slope between 990 and 650 m depths	Subrounded boulder, 30 % ol, 5 % cpx	29°49' 21"N/ 12°39'42"W
DS 822-2	s.a.	Subrounded boulder, 30 % small ol, 15 % small cpx, 15% small plg.	s.a.
DS 822-3	s.a.	Rounded pebble, 20% plg, 20 % cpx	s.a.
DS 822-4	s.a.	Pebble, 14 % ol, 20 % plg, 20 % cpx	s.a.
DS 822-5	s.a.	Pebble, 8 % ol, 1 % cpx, 1 % plg	s.a.
DS 822-6	s.a.	Rounded pebble, 30% cpx, 25 % plg, 5 % ol	s.a.
DS 822-7	s.a.	Pebble, 25 % plg, 15 % cpx, 10 % ol	s.a.
DS 822-8	s.a.	Pebble, 25 % plg, 18 % cpx, 12 % ol	s.a.
DS 822-9	s.a.	Rounded pebble, 22 % cpx, 20 % plg, 8 % ol	s.a.
DS 822-11	s.a.	Pebble, 22 % plg, 20 % cpx, 19 % ol	s.a.
DS 822-12	s.a.	Pebble, 20 % ol	s.a.
DS 822-13	s.a.	Pebble, 20 % ol, 20 % cpx, 12 % plg	s.a.
DS 822-15	s.a.	Pebble, vesicular, 5 % ol	s.a.
DS 822-28	s.a.	Pebble, vesicular, 5 % ol	s.a.
DS 822-30	s.a.	Clast, vesicular, 5 % ol	s.a.

Nico Seamount			
DS 830-2	Northern slope between 740 and 600 m depths	Pebble, vesicular, apyric	30°26'26"N/ 13°20'33"W
Lars Seamount			
DS 832-2	Northern top, between 1350 and 1280 m depths	Clast, 10 % cpx	32°48'05"N/ 13°17'10"W
Last Minute Seamount			
DS 836-2	Summit, between 1230 and 1110 m depths	Fragment, 20 % fsp, with large amph xenolithe	30°09'32"N/ 14°44'35"W

Appendix to Chapter 5 (Evolution of the Selvagen archipelago and neighboring seamounts)

Radiometric ages

Sample	N	Mean apparent age (Ma)	MSWD	Isochron age (Ma)	MSWD (isochron)	Initial $^{40}Ar/^{36}Ar$
Selvagen Grande						
Pliocene lavas						
J 49 (wr) Flow, Tornozelous complex	11	**3.44 ± 0.10**	0.83	3.40 ± 0.52	0.91	295.5 ± 8
J 30 (wr) Flow, Inferno complex	11	**3.37 ± 0.10**	1.50	3.03 ± 0.32	1.15	304.0 ± 10
J 8a (wr) Flow, Atalaia complex	8	**3.36 ± 0.16**	1.79	2.07 ± 1.20	1.14	315.9 ± 19.6
Miocene dikes						
J 43 (wr) Basanitic dike	14	**8.3 ± 0.08**				
J 36 (wr) Basanitic dike	14	**9.9 ± 0.40**				
J 42 (wr) Basanitic dike	12	**11.7 ± 0.50**				
Oligocene basement						
J 32 (kfsp) Phonolitic intrusion	10	**24.19 ± 0.08**	2.13	24.27 ± 0.14	2.60	287.0 ± 8
J 9 (kfsp) Phonolitic boulder	11	24.75 ± 0.18	11.20	**24.61 ± 0.12**	1.85	325.6 ± 7.6
J 23 (kfsp) Phonolitic intrusion	9	**24.62 ± 0.08**	2.09	24.60 ± 0.20	3.71	308.0 ± 122
J 2 (kfsp) Ponolitic clast in breccia	15	**24.77 ± 0.28**	32	25.25 ± 0.30	29.2	239.0± 24
J 35f (amph) Phonotephr. clast in Unit III	10	**25.23 ± 0.22**	1.29	24.91 ± 0.78	1.33	334.0 ± 98.0
J 35g (amph) Tephritic clast in Unit III	9	25.29 ± 0.20	4.76	**24.84 ± 0.34**	2.24	352.2 ± 39.4
J 41a (amph) Phonotephritic intrusion	10	**25.76 ± 0.20**	1.22	25.71 ± 0.24	1.38	296.2 ± 3.0
Selvagen Pequena						
SP 2 (wr) Tephriphonolitic dike	14	**28.7 ± 0.40**				
J 54 (amph) Tephritic boulder		**28.9 ± 0.4**				
J 54 (kfsp) Tephritic boulder		**29.8 ± 0.2**				
J 56B (amph) Tephritic dike		**28.9 ± 0.2**				
J 56A (amph) Tephritic dike		**29.2 ± 0.3**				
J 50 (amph) Breccia		**29.5 ± 1.6**				
J 55 (amph) Phonolitic dike		**29.5 ± 0.20**				

(continued):

Sample	N	Mean apparent age (Ma)	MSWD	Isochron age (Ma)	MSWD (isochron)	Initial $^{40}Ar/^{36}Ar$
Dacia Seamount DS 809-1 (wr) Basanitic clast	11	**9.16 ± 0.30**	0.98	9.80 ± 0.74	0.67	293.6 ± 1.8
Conception Seamount DS 822-4 (wr) Alkali basaltic pebble	9	**16.64 ± 0.20**	1.07	16.80 ± 1.40	1.16	294.3 ± 9.4
DS 822-2 (wr) Alkali basaltic boulder	3	**17.50 ± 0.60**	1.32	18.10 ± 3.20	2.24	291.6 ± 18.6
Lars Seamounmt DS 832-2 (wr) Tephritic clast	10	**67.70 ± 0.20**	1.43	68.20 ± 2.0	2.29	289.3 ± 13.9

Radiometric ages calculated from $^{40}Ar/^{39}Ar$ isotope composition of whole rocks (wr), alkali feldspar and amphibole phenocrysts (kfsp, amph). N = Number of single crystals / whole rock particles analyzed. Errors are quoted at the 2 σ-level. Accepted ages, based on the criteria discussed in the Analytical Techniques chapter, are printed in bold letters. Samples given without isochrone ages and initial Ar ratio are preliminiary data. MSWD = Mean square weighted deviates.